Complex bottle-brush copolymers by reversible addition fragmentation chain transfer polymerisation: synthesis and applications

Andrew Kerr

A thesis submitted in partial fulfilment of the requirements for the degree of

Doctor of Philosophy in Chemistry

Department of Chemistry

University of Warwick

February 2019

Table of Contents

Declaration v

Acknowledgements vi

Abbreviations vii

List of Figures x

List of Tables xiv

List of Publications xv

Abstract xvi

Chapter 1: Introduction 1

1.1 Reversible-deactivation radical polymerisation (RDRP) techniques 2

1.2 RAFT Polymerisation 3

1.3 RAFT polymerisation kinetics 6

1.4 Choice of RAFT agent 8

1.5 Polymeric architectures 11

1.6 Synthetic approaches to bottle-brushes 12

1.7 Analysis and applications of bottle-brush copolymers 17

1.7.1 Analysis by microscopy and scattering techniques 18

1.7.2 Bottle-brush self-assembly 21

1.7.3 Bottle-brushes as encapsulating agents 23

1.7.4 Templating and hollow bottle-brush materials 25

1.8 Conclusion 27

1.9 References 28

Chapter 2: The RAFT 'grafting from' shuttle CTA approach as a means to access complex bottle-brush polymeric architectures 35

2.1 Introduction 36

2.2 Results and discussion 39

2.2.1 Synthesis of poly(hydroxyethylacrylamide) backbones 39

2.2.2 Functionalisation of PHEAm backbone with CTA units....42
2.2.3 RAFT grafting from with shuttle CTA....44
2.2.4 Characterisation of bottle-brush architecture....48
2.2.5 Grafting from of multiblock side chains....52
2.2.6 Multiblock backbone bottle-brushes....54
2.2.7 Incorporation of multiblocks among the ‘x’ and ‘y’-axis....59
2.3 Conclusion....60
2.4 Experimental....62
2.5 References....71
Chapter 3: Anchor group bottle-brush polymers as oil additive friction modifiers....73
3.1 Introduction....74
3.2.1 Poly(laurylacrylate) bottle-brush synthesis....78
3.2.2 Low grafting density comb polymers....81
3.2.3 Anchor group bottle-brushes....84
3.2.5 RAFT End group removal....89
3.2.6 Quartz crystal microbalance with dissipation (QCM-D).....93
3.2.7 Mini traction machine testing....96
3.2.8 Viscosity testing....101
3.3 Conclusion....103
3.4 Experimental....104
3.5 References....112
Chapter 4: Polymeric nanotubes as drug delivery vectors – comparison of a covalently and supramolecularly assembled construct....114
4.1 Introduction....115
4.2 Results and discussion....121
4.2.1 Design and synthesis....121
4.2.2 Fluorescence and radioactive tag labelling....126

4.2.3 Cell viability 130
4.2.4 Cell Association 131
4.2.5 Spacial coincidence with Lysosomal tracker 132
4.2.6 *In vivo* pharmacokinetics 135
4.2.7 Biodistribution 139
4.3 Conclusion 141
4.4 Experimental 142
4.5 References 153
Chapter 5: Conclusion and outlook 156
Appendix A 160
Appendix B 174
Appendix C 182

Declaration

Experimental work contained in this thesis is original research carried out by the author, unless otherwise stated, in the Department of Chemistry at the University of Warwick, in the Department of Drug Delivery, Disposition and Dynamics at the Monash Institute of Pharmaceutical Sciences, or at Lubrizol Chemical Synthesis department, Hazelwood, Derbyshire between March 2015 and February 2019. No material herein has been submitted for any other degree, or at any other institution.

Results from other authors are referenced in the usual manner throughout the text.

Signed:_____ Date:_____

Andrew Kerr

Acknowledgements

Firstly I would like to thank my supervisor Professor Sebastien Perrier for giving me the opportunity to pursue a PhD, his guidance, support and advice throughout the years.

Next thank you to Lubrizol for the opportunity to collaborate together, in particular to Dr. Tim Smith, Dr. Paul Kirkman and Dr. Paul O'Hora for their help and guidance on the project.

I would like to acknowledge all the Perrier group members over my time at Warwick who have made this a great experience. Firstly Guillaume Gody for his tutoring on RAFT and all of the postdocs who have helped me along the way (Johannes B., Sylvain C., Ed Mansfield, Matthias H., Raoul P.). All of my colleagues in the lab or offices: Guillaume M., Caroline B., Majda A., Liam M., Julia R., Sophie L., Tammie B., Alex C., Pratik G., Junliang Z., Joji, T., Daniel L., Andy L., Agnès K., Tom F., Satu H., Robert R., Qiao S., Jie Y., Sean E., Fannie B., Philip D., Hall S., Maria K..

Special thanks to Ximo for his discussions on brushes and supervising me during my stay in Melbourne, much gratitude to Erny S. for all her help on the project there and the other members of the group Carlos and Cheng.

Finally I would like to thank my family for all their support over the years.

Abbreviations

ACVA	4,4’-Azobis(4-cyanovaleric acid)
ABC	Accelerated blood clearance effect
AFM	Atomic force microscopy
AIBN	Azobisisobutyronitrile
ATRP	Atom transfer radical polymerisation
AUC	Area under the curve
BA	Butyl acrylate
C14	Carbon 14 isotope
Cl	Clearance rate
CP	Cyclic peptide
CTA	Chain transfer agent
CTA Acid	2-(((dodecylthio)carbonothioyl)thio)-2-methylpropanoic acid
CTA-1	Butyl 2-(((dodecylthio)carbonothioyl)thio)-2-methylpropanoate
C_{tr}	Chain transfer constant
$Đ$	Dispersity
DCM	Dichloromethane
DLS	Dynamic light scattering
DMA	Dimethylacrylamide
DMF	Dimethylformamide
DMSO	Dimethylsulfoxide
DP	Degree of polymerisation
EPHP	Ethyl piperidine hypophosphite
EPR	Enhanced permeation and retention
ESI MS	Electrospray mass spectrometry
GMO	Glyceryl monooleate
HEA	Hydroxyethylacrylate
HEAm	Hydroxyethylacrylamide
HOPG	Highly ordered pyrolytic graphite
HPLC	High performance liquid chromatography

LA	Lauryl acrylate
LAM	Less activated monomer
LPO	Lauroyl peroxide
MALDI-ToF	Matrix assisted laser desorption/ionisation - time of flight
MAM	More activated monomer
MHEAm	Methyl-hydroxyethylacrylamide
MMA	Methyl methacrylate
M_n	Number average molecular weight
$M_{n\ theo}$	Theoretical number average molecular weight
MRI	Magnetic resonance imaging
MTM	Mini traction machine
MTT	3-(4,5-dimethylthiazol-2-yl)-2,5-diphenyltetrazolium bromide
M_w	Weight average molecular weight
MW	Molecular weight
MWD	Molecular weight distribution
NAS	N-acryloxysuccinimide
NHS	N-hydroxysuccinimide
NMP	Nitroxide mediated polymerisation
NMR	Nuclear magnetic resonance
PABTC	2-(((butylthio)carbonothioyl)thio) propanoic acid
PDI	Polydispersity index
PEG	Poly(ethylene glycol)
PMA	Poly(alkylmethacrylate)
PMBTC	Methyl 2-(((butylthio)carbonothioyl)thio)propanoate
QCM-D	Quartz crystal microbalance - dissipation
RAFT	Reversible addition fragmentation chain transfer
RDRP	Reversible deactivation radical polymerisation
R_h	Hydrodynamic radius
RI	Refractive index

SANS	Small angle neutron scattering
SAXS	Small angle x-ray scattering
SEC	Size exclusion chromatography
$t_{1/2}$	Half-life time
TEM	Transmission electron microscopy
THF	Tetrahydrofuran
UV	Ultraviolet
V601	Dimethyl 2,2'-azobis(2-methylpropionate)
VA-044	2,2'-Azobis[2-(2-imidazolin-2-yl)propane]dihydrochloride
V_d	Volume of distribution
VI	Viscosity index
α	Mark-Houwink parameter

List of Figures

Figure 1.1: Scheme outlining the proposed mechanism of RAFT, adapted from Ref[10]. 3
Figure 1.2: Top – scheme showing pre-equilibrium step mechanism and the associated rate constant, adapted from Ref[12]. a) Equation for calculation of chain transfer coefficient. b) Equation for determining the chain transfer rate constant in the RAFT process. Bottom – scheme for the main equilibrium step. c) Equation for calculation of interchain chain transfer coefficient. b) Equation for evaluation of k_{ex}. 4
Figure 1.3: Top- scheme showing order of activity of various R groups and the range of monomers that can be polymerised effectively with each. Bottom –a similar scheme for the choice of Z group. Adapted from Ref[12]. 9
Figure 1.4: Top - examples of commonly used CTAs in academic literature (1, 2, 3). Bottom – structures of three CTAs produced on industrial scale by the companies Lubrizol, Solvay and Arkema. 10
Figure 1.5: Scheme showing a variety of possible polymeric architectures. 11
Figure 1.6: Scheme outlining the three different approaches to graft polymer synthesis, adapted from Ref[62]. 13
Figure 1.7: Schemes showing the mechanisms of the three RAFT 'grafting from' approaches, adapted from Ref[87]. 16
Figure 1.8: Scheme showing the structure of a selection of bottle-brush copolymers that have been described in literature – diblock,[92] triblock[93] and statistical heterografts,[94] core-shell[95-97], dumbbell[98] and ABA backbones.[99, 100] 17
Figure 1.9: I – Bottle-brush with an end block containing a UV-labile protecting group. Upon UV irradiation hydrogen intramolecular hydrogen bonding interactions induce folding of the tail as imaged by AFM height profiles, adapted from ref[115]. **II** – AFM height profile images of a 6-arm star brush of varying arm length and side chain thickness, adapted from ref[114]. **III** – Image of cyclic brush polymers derived from a ring closure strategy, adapted from Ref[117]. **IV** – Scheme for macromonomer REMP and a representative AFM image, adapted from Ref[118]. 19
Figure 1.10: I – Upon increasing the side chain length in from a) DP12 to b) DP120 a transition from semi-flexible to rigid rod is observed, adapted from Ref[119]. II – Backbone scission monitored at various time-points for a bottle-brush deposited as a surface monolayer. III – Scission of the brush backbone is observed as the size of the cationic shell is increased from top to bottom, adapted from Ref[121]. 20
Figure 1.11: A – Scheme showing self-assembly of block and statistical heterograft bottle-brushes, adapted from Ref[129]. B – Assembly of a PLA/PS diblock images by SEM, adapted from Ref[109]. C – ROMP polymerisation of an AB macromonomer to form a Janus brush and its assembly in AFM and SAXS, adapted from Ref[130]. 21
Figure 1.12: I – a poly(lactide)-b-PS diblock heterograft brush assembled to give photonic crystals, adapted from Ref[134]. II – By mixing different ratios of brushes with varying block sizes the domain size can be controlled, leading to reflection of light over a broad range of wavelengths. Adapted from Ref[133]. 22
Figure 1.13: A – Scheme for a drug loaded brush by ROMPO 'grafting through', adapted from Ref[144]. B – aqueous self-assembly and drug loading of an amphiphilic bottle-brush, adapted from Ref[138]. C – Unimolecular bottle-brush for theranostic applications and kinetics of drug release (right), adapted from Ref[145]. 24
Figure 1.14: A – Approach to synthesis of hollow nanotube through a bottle-brush templating approach, adapted from Ref[111]. B – TEM image of a cyclic bottle-brush

copolymer loaded with gold, adapted from Ref[157]. C – Synthetic approach and TEM imaging of inorganic silica nanotubes, adapted from Ref[156]. 26
Figure 2.1: The RAFT 'R' group grafting from approach to graft polymer synthesis involving three steps – polymerisation of the backbone, modification of monomer units with CTA and thirdly the grafting from polymerisation. 37
Figure 2.2: Schemes and SEC molecular weight distributions for PHEAm backbones synthesised by RAFT. SEC performed in DMF eluent conditions, number above SEC trace designates target DP. A – CTA Acid controlled polymerisations targeting DPs between 100 – 4000 in H_2O at 2M monomer concentration. B – PMBTC controlled polymerisations targeting DPs between 50 – 1000 in dioxane/H_2O at 2M monomer concentration. 40
Figure 2.3: ^{1}H-NMR spectrum in DMSO-d_6 of the DP50 PHEAm (**A**) and ^{1}H NMR spectrum in $CDCl_3$ of the functionalised PolyCTA backbone (**B**)..... 42
Figure 2.4: DMF SEC molecular weight distributions of backbones before and after modification with PABTC. 42
Figure 2.5: A & C – Kinetic plot and DMF SEC molecular weight distributions of grafting from polymerisation of NAM in absence of shuttle CTA. B & D Kinetic plot and DMF SEC traces of grafting from polymerisation of NAM in presence of 0.5 equivalents shuttle CTA. For clarity the linear shuttle CTA derived polymers have been omitted from the SEC trace, see Figure 2.7A for a representative SEC trace of both distributions. E – pseudo first order linear kinetic profile for reactions with and without shuttle CTA. 45
Figure 2.6: Possible termination steps in a grafting from polymerisation considering only bimolecular termination by recombination. A – Terminations for a standard R group RAFT grafting from polymerisation. B – Additional possible terminations during a shuttle CTA mediated grafting from procedure, these will occur in addition to those described in A. 47
Figure 2.7: A – DMF SEC molecular weight distribution of a PNAM bottle-brush synthesised with addition of 1 equivalent shuttle CTA showing two separate species – the high MW bottle-brush and low MW linear polymer derived from the shuttle CTA. B – SEC trace of bottle-brush synthesised in absence of shuttle CTA, leading to a high molecular weight shoulder. The brush was hydrolysed to cleave side chains and analysed again by SEC. 48
Figure 2.8: SANS data of A – brushes with DP50 side chains of DP100 and 1000 backbones fitted to a rigid cylinder model. B – DP500 backbone brush with DP20 side chains fitted to a flexible cylinder model. 49
Figure 2.9: A, B – AFM images of a $(PBA_{47})_{500}$ bottle-brush polymer dipped onto a mica subtrate. Inset shows 100nm scale bars. C – Typical height profile of two brush molecules from image B. D – Small section of an AFM image of PHEAm bottle-brush with worm-like species apparent. 51
Figure 2.10: Grafting from polymerisation to generate hexablock side chain bottle-brush polymers. The RAFT end group of the PolyCTA backbone will chain extend in the same manner to form a hexablock, however this may been omitted for clarity. 52
Figure 2.11: A and B – SEC analysis of DP50 backbone bottle-brush hexablock targeting DP15 per block. Linear polymer omitted from SEC traces for clarity, shown in Figure A.11 A. C and D – SEC analysis of DP100 backbone bottle-brush hexablock targeting DP10 per block. Linear polymer omitted from SEC traces for clarity, shown in Figure A.11 B. 53
Figure 2.12: A and B – DMF SEC molecular weight distributions of the nonablock copolymer backbone. C and D - DMF SEC chromatograms analysis of the nonablock copolymer backbone. 55

Figure 2.13: Scheme showing synthesis of the nonablock copolymer backbone bottle-brush **23** and AFM imaging of the compound. Sample deposited onto mica sheets by dipping into a dilute chloroform solution. 58
Figure 2.14: Scheme and SEC analysis for the grafting from of pentablock side to synthesise compound **24**. 60
Figure 3.1: A – Mechanism of film formation for organic friction modifiers, adapted from Ref. [1]. B – Density of polymers onto a surface affects the conformation – a brush regime is preferable for lubrication over the 'mushroom' adapted from Ref. [1]. C –Usage of a surface active polymer additives maintains a film even at low entrainment speeds adapted from Ref. [3]. D – Friction coefficients determined by mini traction machine testing of various functionalised viscosity index modifiers, adapted from Ref. [3]. 75
Figure 3.2: A – Scheme of synthesis of PolyCTA with CTA Acid performed in two steps with a solvent switch. **B** – ^{1}H NMR spectra of the partially functionalised product after the first reaction in DMF. **C** – ^{1}H NMR spectra of the final product after the second step. 79
Figure 3.3: A – SEC molecular weight distributions of the grafting from step of the DP100 PolyCTA with varying quantities of shuttle CTA. **B** – The same experiment with the DP500 PolyCTA backbone. **C and D** – AFM height images of the short and long bottle-brushes deposited onto an HOPG substrate. 81
Figure 3.4: Top – scheme for grafting from step from the comb precursor PolyCTA. Bottom – SEC molecular weight distributions of the starting backbone copolymer, the modified PolyCTA and the derived PLA comb copolymer. For the comb polymer trace the recorded $M_{n\,SEC}$ and $Đ$ values disregard the low molecular weight linear polymer species. 82
Figure 3.5: Mark-Houwink α values determined by SEC triple detection. 84
Figure 3.6: A –Synthetic scheme for diblock anchor group bottle brush polymer using a RAFT grafting from approach. B – Structural representation of the 5 brush materials studied in this work. C – Possible conformations of anchor group materials when interacting with a surface. 84
Figure 3.7: ^{1}H NMR analysis of a) polymerisation mixture of the first PHEAm block performed in D_2O. Monomer conversion was determined to be 95% and the polymer was purified by precipitation prior to chain extension, b) polymerisation mixture of ABA triblock copolymer backbone in D_2O, c) PolyCTA ABA backbone in $CDCl_3$. 85
Figure 3.8: SEC molecular weight distributions of A – PLA brush, B – Statisical brush, C – Diblock brush, D – ABA Triblock brush, E – BAB triblock brush. The backbones and PolyCTA polymers were analsyed in DMF SEC conditions, whereas the final PLA bottle-brushes were analysed in $CHCl_3$ SEC due to differences in solubility. The PLA bottle-brushes contain shuttle CTA derived linear polymer chains which have been omitted for clarity. 86
Figure 3.9: Scheme for synthesis of the ABA and BAB triblock backbone bottle-brushes. 88
Figure 3.10: DLS analysis of diblock anchor group bottle-brushes with varying DP of the PNAM anchor group. DP = A – 100, B -200, C – 400. 89
Figure 3.11: Scheme for RAFT agent end group removal by radical reduction leading to two main potential products – either capped with an H or an initiator fragment. 90
Figure 3.12: MALDI-ToF spectra of PNAM species. A – DP13 PNAM synthesised with PABTC. B – PNAM reacted with V601/LPO reagents. C – Reaction performed with AIBN/LPO reagents. D – Reaction performed with VA-044/EPHP. 91
Figure 3.13: Decomposition and termination by disproportionation of V601 to produce methylmethacrylate (MMA) as a side product. 92

Figure 3.14: Potential mechanism for the RAFT end group removal of the $PNAM_{13}$ with the V601 / LPO reaction conditions. Usage of AIBN / LPO yielded only products in the upper red outlined box. 92
Figure 3.15: The Sauerbrey equation where Δf = change in resonance frequency, Δm = change in mass adsorbed onto QCM surface, f_0 = fundamental resonance frequency, A = piezoelectrically active area, p_q = quartz density and μ_q = quartz shear-modulus. 94
Figure 3.16: A - QCM analysis of the linear PLA, brush PLA and anchor group diblock brush compounds. B – Relationship of ΔD *vs* Δf over time for the brush compounds. C – Layer thicknesses calculated by the Voigt model. 95
Figure 3.17: Stribeck curve with schemes at top outlining each regime. 97
Figure 3.18: MTM testing of compounds at a treatment of 1 wt. % at various temperatures comparing performance of anchor group brushes against base oil, unfunctionalised polymers and the commercial friction modifier (GMO). 98
Figure 3.19: MTM testing of polymer at a treatment of 1 wt. % at various temperatures comparing the performance of differing bottle-brush acrhitectures 101
Figure 4.1. **A** – scheme showing dimensions of a sphere and rod shaped silica nanoparticle. **B** – TEM images of each nanoparticle. **C** – Bar charts showing increased tumour transport and distribution of the rod nanoparticle. Adapted from Ref [29]. 117
Figure 4.2: A – chemical structure of an octacylic peptide demonstrating the hydrogen bonding interactions between each molecule. Adapted from Ref [40]. **B** – Structure and image of expected morphology of a cyclic peptide polymer conjugate. Adapted from Ref [44]. **C** – AFM image of a PEG-cyclic peptide conjugate dried onto a mica substrate, scale bar = 100 nm. 119
Figure 4.3: Scheme and chemical structures of the 5 compounds studied in this work. 121
Figure 4.4: SEC molecular weight distributions using DMF eluent system of each synthetic step for **A** – the short PNAM brush, **B** – the long PNAM brush. Atomic force microscopy images prepared for drop casting a dilute aqueous solution onto mica substrate. **C** – SB AFM image, **D** – LB AFM image. 123
Figure 4.5: MALDI mass spectra of: **A** - $PNAM_{13}$ polymer synthesised with a RAFT agent end group, **B** – $PNAM_{13}$ polymer post reaction with ACVA / LPO revealing full removal of the RAFT end group. 124
Figure 4.6: A – synthetic approach to the labelling of the 2-arm CP conjugate by chain extension with NAS units. **B** – SEC chromatograms in DMAc eluent system showing clear chain extension of the conjugate with the NAS containing block. **C** – Schematic for the mixing approach of labelled CP with the starting material. 128
Figure 4.7: A – HPLC traces of polymers after modification with Alexa-488 monitored by fluorescent intensity at the 490 nm / 525 nm excitation/emission wavelengths. **B** – HPLC traces of the CP before and after chain extension and functionalisation with dye. **C** – Image of the dye-labelled SB, under long wavelength UV irradiation a green emission is observed. 129
Figure 4.8: Left – PD10 column purification performed of crude reaction mixture showing separation of polymer and the free label. Right – G25 SEC column with PBS eluent of the dialysis purified radiolabelled SB material showing presence of only the high MW brush species. Radioactive counts determined by scintillation counting. 130
Figure 4.9: MTT assay data for four cell lines for the five compounds studied. 131
Figure 4.10: Flow cytometry data for left – MDA and right – 3T3 cell lines. Experiments were performed in triplicate for each set of conditions. Error bars show standard deviation. 132

Figure 4.11: Confocal microscopy images of MDA cell cultures incubated with the labelled compounds for 24 h at 37°C prior to imaging and with Lysotracker red / Hoechst blue stains shortly before. Channels show the Alexa-488 labelled compounds at 490 / 530 nm excitation / emission, lysotracker at / nm and Hoechst blue at / nm. 134
Figure 4.12: Confocal microscopy showing still images of a time lapse experiment at various time points of MDA cells treated with the dye labelled CP conjugate. 135
Figure 4.13: Plasma concentration profiles as a % of initial dose against time for the 5 radiolabelled compounds. 136
Figure 4.14: The pharmacokinetic parameters listed in table 4.2 visualised in bar chart format. 137
Figure 4.15: Biodistribution data in major organs of the 5 compounds determined after 24 h IV dosage. Blank organs were spiked to determine counting efficiencies. Left - % dose found in each organ. Right - % dose per gram tissue of each organ. 139

List of Tables

Table 2.1: Polymerisation conditions for PHEAm backbones, M_n and $Đ$ determined by DMF SEC. 41
Table 2.2: PolyCTA backbone samples used in this work, M_n and $Đ$ determined by DMF SEC against linear PMMA calibration standards 44
Table 2.3: Synthesised brush compounds, M_n and $Đ$ determined by DMF SEC. The PHEAm compounds were analysed by SANS and fitted with a combination of cylinder with gaussian chain models, the fitted parameters of cylinder radius, length, kuhn length and radius of gyration of the gaussian chain are shown in the table. 50
Table 2.4: Mulitblock backbone samples and the bottle-brushes polymers grafted therefrom, M_n and $Đ$ determined by DMF SEC. 56
Table 3.1: Summary of SEC analysis data performed with $CHCl_3$ eluent system on a linear, comb, short and long bottle-brush consisting of PLA. The α values and $M_{n\ DALS}$ were determined by triple detection with dual angle light scattering detectors. 83
Table 3.2: Summary of brush compounds synthesised in this study. Triple detection SEC with dual angle light scattering analysis performed with instrument using $CHCl_3$ eluent at 30 °C with 2 % TEA additive. 87
Table 3.3: Viscosity of various polymer-blends at 1wt. % determined at 40 and 100°C. .. 102
Table 4.1: Chemical strucutre and abbreviations of the synthesised compounds in this study. $M_{n\ SEC}$ and $Đ$ was determined using a DMF eluent system. [a] Activities of the labelled materials were determined after reaction of the NAS units with C14-ethanolamine by liquid scintillation counting. 125
Table 4.2: Pharmacokinetic parameters determined by the non-compartment model showing the average and standard deviation across n=3 in vivo plasma concentration experiments. 137

List of Publications

The following publications have been produced from the work detailed in this thesis:

Chapter 2:

Complex multiblock bottle-brush architectures by RAFT polymerization

A. Kerr, M. Hartlieb, J. Sanchis, T. Smith, S. Perrier.

Chemical communications, **2017**, 87, 11901-11904.

Chapter 3:

Anchor group bottle-brush polymers as oil additive friction modifiers

A. Kerr, P. Kirkman, P. O'Hora, T. Smith, S. Perrier.

Manuscript in preparation.

Chapter 4:

Polymeric nanotubes as drug delivery vectors – comparison of a covalently and supramolecularly assembled construct

A. Kerr, E. Sagita, J. Sanchis, T. H. Nguyen, C. J. H. Porter, S. Perrier.

Manuscript in preparation.

Abstract

This thesis aims to investigate the synthesis of bottle-brush polymers through the use of the reversible addition fragmentation chain transfer (RAFT) polymerisation technique and probe their applications in a range of fields.

In the first chapter the synthetic methodology is optimised by building on a previously described 'shuttle CTA' approach, where the advantages of this technique to access high monomer conversions is exploited. Initially the synthesis of high molecular weight backbone bottle-brushes with extended cylindrical morphologies is demonstrated, and characterised by techniques including SANS and AFM. The ability of RAFT to access multiblock copolymers is then utilised for densely grafted bottle-brush systems to create novel materials of high complexity by one pot polymerisations to high monomer conversions.

The versatility of the materials and their synthesis are then illustrated through the use of apolar and polar brushes, for two very different applications, as oil modifiers and drug delivery vectors, respectively.

Synthesis of oil soluble bottle-brush systems through the established technique is performed, where a variety of structures with surface active polar blocks are then studied as friction / viscosity modifier additives. Significant improvement in friction reduction efficacy is obtained by the addition of a polar segment and the copolymer composition is also shown to play an important role. The high performing materials have potential for industrial applications, although initial synthesis was only performed on a 10 g scale.

The versatility of bottle-brush nanomaterials are then displayed by work in the fourth chapter where they are studied as unimolecular drug delivery vectors. Size and morphology control enabled by the precise synthesis allows the effect of these parameters to be studied in biological systems. A comparison of the covalently bound brushes with a supramolecular assembled tube of similar dimensions is also carried out to further improve understanding of nanocarrier capabilities.

Chapter 1

Introduction

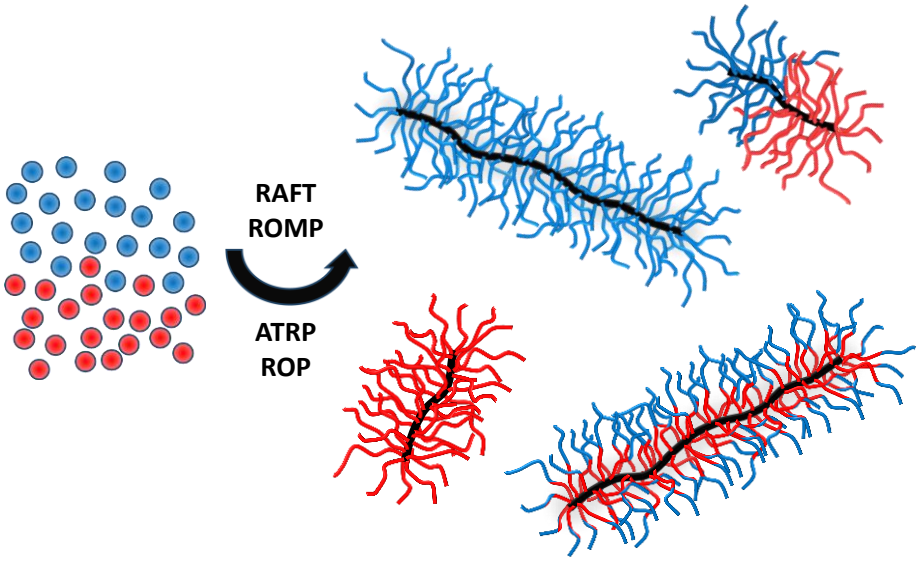

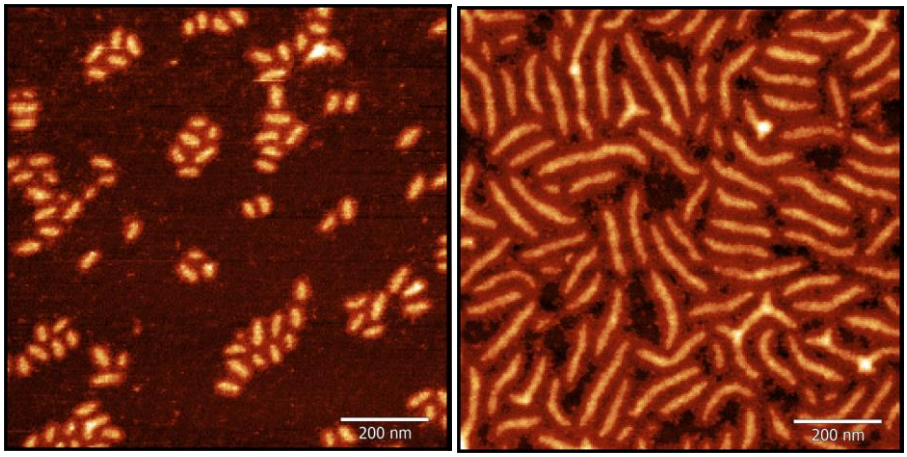

1.1 Reversible-deactivation radical polymerisation (RDRP) techniques

Since the development of RDRP in the 1990s there has been a huge amount of academic research into the area, and strong industrial interest with the development of several products through this technology. RDRP offers vast potential for the synthesis of a new generation of polymeric materials, by means of controlling molecular weight (MW), dispersity, architecture and incorporation of a variety of monomers. While anionic polymerisation has long been recognised as a living polymerisation, and thus can be used to create high fidelity polymeric materials, the reaction conditions and array of monomers are rather stringent. In this regard RDRP is far more flexible and in some cases is not significantly more challenging than performing a traditional free radical polymerisation (FRP), which is responsible for ~40 % of polymer production worldwide.[1] As a result RDRP has been established as an invaluable tool for modern polymer science.

Among the most popular RDRP techniques are nitroxide mediated polymerisation (NMP),[2] metal mediated living radical polymerisations (atom transfer radical polymerisation (ATRP)[3] and single electron transfer living radical polymerisation (SET-LRP)[4]) and reversible addition fragmentation chain transfer polymerisation (RAFT).[5] RAFT was simultaneously discovered in 1998 by CSIRO[6] and by Rhodia, working in collaboration with Zard, who named the process macromolecular design via the interchange of xanthates (MADIX), since it uses xanthate chain transfer agents (CTA).[7] Since then RAFT has established itself as one of the most versatile and convenient RDRP methods.[8] In a FRP the propagating radical is highly reactive and readily undergoes terminations with other radical species, necessitating the slow feeding of radical production, fundamentally making the polymerisation challenging to control and leading to a broad molecular weight distribution. RDRP approaches circumvent this issue by the reversible termination of the propagating radical into a dormant species end group, which can be later reactivated to resume propagation, although the exact method of achieving this varies between techniques. By maintaining a low concentration of active radical species the rate of propagation is favoured over termination, while the reversible activation ensures polymer chains grow equally throughout the course of the polymerisation and thus enables living-like behaviour. RAFT works through a degenerative transfer mechanism, whereby a small number of propagating radicals rapidly undergoes transfer between CTAs, causing equal polymerisation growth of each

chain with a CTA group (Figure 1.1). Since the discovery of RAFT there has been a huge number of research publications in the field (871 in 2018 alone, source: Web of Science) with the technique routinely used for polymer synthesis in a broad range of applications.[9]

1.2 RAFT Polymerisation

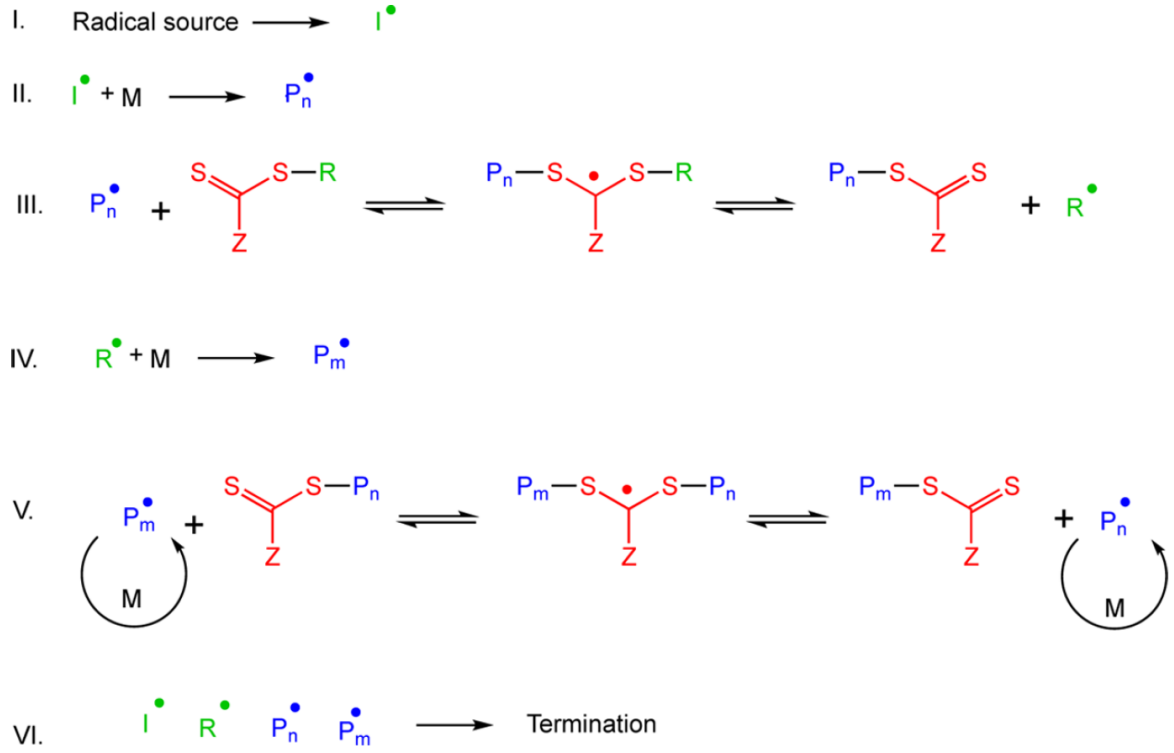

Figure 1.1: Scheme outlining the proposed mechanism of RAFT, adapted from Ref[10].

Compared to FRP, where the lifetime of a radical can be considered to exist on a single polymeric chain which continually propagates to a very high molecular weight until eventual termination, in RAFT the radical spends a short amount of time propagating on each chain, rapidly transferring between the CTAs so that effectively all chains grow evenly. Through this procedure polymers of narrow dispersity and of targeted molecular weight can be obtained, and block copolymer architectures can be synthesised by sequential chain extension of a CTA capped polymer. Compositional drift in free radical copolymerisations can additionally be avoided, instead resulting in the formation of gradient copolymers in RDRP systems.

As *per* the principles of a living polymerisation system, significantly faster initiation than propagation is necessary to acquire low dispersities. In regards to RAFT this refers firstly to the initial pre-equilibrium step where a propagating oligomeric radical attacks the C=S bond of the CTA to form a short lived intermediate, which can then undergo

fragmentation back to the starting material or to the R group (Figure 1.2 top). For successful chain transfer this fragmentation must occur towards the R group and the R radical must then propagate before re-addition to the CTA. The rate of this process with respect to propagation is defined by the chain transfer constant (C_{tr}), where a high value (at least > 10)[11] is therefore vital to ensure rapid consumption of the CTA at the beginning of the polymerisation to yield the desired MW and is required to achieve narrow dispersity materials.

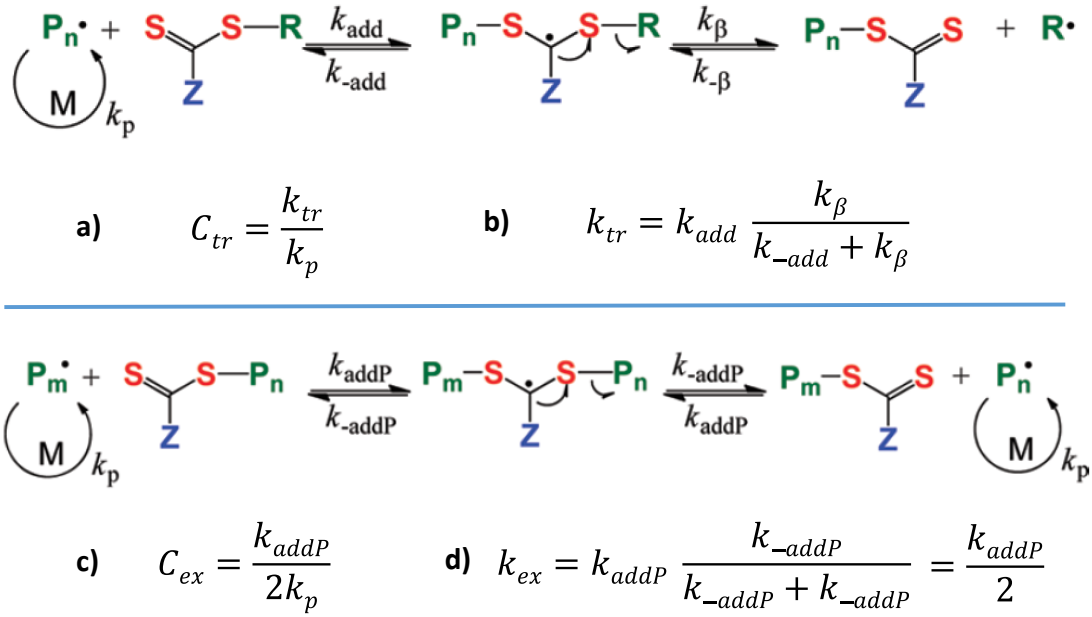

Figure 1.2: Top – scheme showing pre-equilibrium step mechanism and the associated rate constant, adapted from Ref[12]. a) Equation for calculation of chain transfer coefficient. b) Equation for determining the chain transfer rate constant in the RAFT process. Bottom – scheme for the main equilibrium step. c) Equation for calculation of interchain chain transfer coefficient. b) Equation for evaluation of k_{ex}.

After consumption of the starting RAFT agent the polymerisation process enters the main equilibrium stage, where chain transfer continues to occur between the propagating species and polymers capped with the CTA end group. At this step the rate of addition will be primarily determined by the nature of the Z group, while the R group of the CTA no longer affects the fragmentation as a result of its position at the opposite end of the polymeric chain. A separate chain transfer constant (C_{ex}) for this interchain exchange can therefore be defined (Figure 1.2 bottom). The essentially identical reactivity of the P_n and P_m species results in a symmetrical intermediate radical where the k_{addP} and k_{-addP} should be of equal values. If the CTA is rapidly consumed within low monomer conversions, the dispersity and molecular weight distributions of the polymeric product will be predominantly affected by the magnitude of C_{ex}.

Unlike in ATRP and NMP, which both involve reversible recombination of a radical species, it is worth noting that RAFT does not directly change radical concentration or prevent termination events when compared to FRP, but rather alters the distribution of monomer species. Such terminations will result in the formation of polymeric chains without the RAFT end group and can be thus be considered 'dead' and unable to undergo further chain extension, however, the number of CTA will not be affected by this and a certain number of 'living' chains will always remain in absence of further side reactions. For this reason RAFT (and other RDRP) cannot be considered a truly living polymerisation and are instead commonly referred to with the terminology RDRP or 'controlled radical polymerisation', to differentiate from techniques such as anionic polymerisation which under some conditions can be considered completely devoid of irreversible chain transfers and terminations. As a result of this, theoretically the M_n of a RAFT controlled polymerisation must always be lower than that of the corresponding FRP, although there are a number of experimental procedures that have been shown to allow access to ultra-high M_n products with RAFT.[13-15]

For a typical RAFT procedure an external source of radical initiation is required, often a thermally decomposing azo or peroxide compound. If room temperature polymerisation conditions are favourable redox pairs can also be an effective choice,[16, 17] and in recent years there has been substantial interest in the use of photo-mediated polymerisations.[18] In this technique either a photocatalyst is used (PET-RAFT),[19] or the RAFT agent is activated directly where it functions as a photoiniferter.[20, 21] With the use of an external radical source the number of initiation events can be determined according to the moles of initiating compound and thus the number of possible end group terminations known. A potential advantage of recognising the number of termination events in RAFT is the ability to estimate the livingness of the polymer – *i.e.* what percentage of chains in the product contain the desired end group. Since every radical that enters the system will inevitably terminate, the number of dead chains formed throughout the process will be equal to the number of radicals produced (assuming a disproportionation mechanism – half the number would be expected if termination occurring purely by recombination). This value can then be tailored by careful selection of the polymerisation conditions, most notably the initiator concentration, which is of increased importance for syntheses involving further block extensions where high RAFT end group fidelity is essential. A

commonly reported parameter is the CTA / I ratio which gives a convenient value to plan experiments and give a handle on the expected livingness, although the true parameter of pertinence is ratio to the initiator *consumed*, which will depend on the time, temperature and decomposition rate of the selected initiating species. Livingness can be calculated from the following equation:

$$L\ (\%) = \frac{[CTA]}{[CTA] + 2f \times [I]_0 \times (1 - e^{-k_d \times t}) \times (1 - \frac{f_c}{2})}$$

Where [CTA] is the initial concentration of CTA, f is the initiation efficiency (typically assumed to be 50%), $[I]_0$ is the initial initiator concentration, k_d is the rate coefficient of decomposition, t is time and f_c is the coupling factor referring to whether the terminations occur by combination ($f_c = 1$) or disproportionation ($f_c = 0$).

The targeted molecular weight (ratio of CTA to monomer) can also be corrected in a similar manner, since the number of chains will be increased by the initiator derived species the actual targeted molecular weight (ratio of number of chains to monomer) will be reduced. In practice with the use of low initiator quantities this difference is often negligible.

$$M_{n\ theo} = \frac{[M]_0 \times Conv. \times M_{n\ monomer}}{[CTA] + 2f \times [I]_0 \times (1 - e^{-k_d \times t}) \times (1 - \frac{f}{2})} + M_{n\ CTA}$$

Where is the initial monomer concentration, Conv. Is the monomer conversion into polymer, M_n monomer is the molecular weight of the monomer and M_n CTA is the molecular weight of the CTA.

1.3 RAFT polymerisation kinetics

Assuming instantaneous chain transfer and absence of side reactions the RAFT process should not affect polymerisation kinetics and thus behave identically to FRP, although in practice inhibition periods and rate retardation are often observed, most significantly for the dithiobenzoate class of CTAs.[22, 23] These kinetic effects have been attributed to a range of phenomenon including presence of impurities, unsuitable choice of R/Z group,[24] extended lifetime of the intermediate radical[25] and intermediate termination events.[26] Additionally the high molecular weights associated with FRP often lead to the rate accelerating Trommsdorff effect which is not significant in RAFT as a result of the

lowered molecular weights obtained. Molecular weight dependence of propagation and termination rate coefficients for the propagating species may also cause a variation between RAFT and FRP for the same reason. Disregarding these possibilities, the RAFT process should behave the same kinetically as FRP.

In NMP and ATRP the initiating species should remain at constant concentration throughout the course of the polymerisation, meaning the rate equation can be simplified to only being proportional to the [M]. The occurrence of terminations will reduce this concentration of propagating species, thus slowing down the propagation rate and causing a deviation from first order rate kinetics – if the polymerisation follows the model it therefore provides evidence of a successful living polymerisation. While RAFT is a RDRP technique, when using an external source of initiator, however, in the same manner as FRP the radical concentration will reach a constant value as a result of stationary state kinetics, as long as the rate of initiator decomposition remains constant. The kinetics will therefore also observe the pseudo first order relationship even with the occurrence of terminations:

$$-\frac{d[M]}{dt} = k_p[\mathrm{M}][R^*] = k_p[\mathrm{M}]\sqrt{\frac{f k_d[\mathrm{I}]_o e^{-k_d \mathrm{t}}}{k_t}}$$

$$= k_{obs}[\mathrm{M}]$$

Where k_p is the rate constant for propagation, [R*] is the radical concentration, k_t is the rate constant for termination, $[I]_0$ is the initial initiator concentration and k_{obs} is the observed rate constant.

Since a thermally decomposing azo initiator does so in an exponential manner the initiation rate will only follow a linear relationship for a short period at the start of the polymerisation – e.g. AIBN at 66 °C has a half-life of 10 hours, in which case the assumption of stationary state may only be valid for the initial few hours of polymerisation, after which the [R·] will drop substantially enough to cause deviation. While adherence to the linear first order relationship in RAFT is useful to provide evidence of expected polymerisation behaviour, it does not necessitate that the polymerisation is 'living' and that terminations are not occurring. Indeed at longer

reaction times with an azo initiator a deviation is expected, this dropoff can be accounted for by considering the radical concentration within the rate equation.[27]

1.4 Choice of RAFT agent

The RAFT process has good tolerance of reaction conditions and chemical functionalities, with a wide range of polymerisable monomers available including the so called 'more activated monomers' (MAMs) and 'less activated monomers' (LAMs). In both cases the selection of a suitable RAFT agent is essential, where the functionality of the R and Z group play an important role in the activity of a RAFT agent with a specific monomer.[12] A range of CTA structures have been studied to determine compatibilities (Figure 1.3), generally the stability of the R group must be matched with the stability of the propagating monomer radical to promote efficient fragmentation and ensure a high chain transfer constant during pre-equilibrium (Step III, Figure 1.1). An equivalent R group structure to the propagating radical is often not sufficient to achieve good control of the polymerisation (especially for methacrylate monomers) due to penultimate unit effects on radical stability, however, if the R group is too stable, control of high propagation rate monomers (e.g. acrylamides) is reduced due to slow reinitiation rate of the R· species with respect to propagation. Figure 1.3 shows recommended R groups for a variety of MAM/LAMs – for methacrylates/methacrylamides tertiary R groups with cyano or phenyl groups are required, whereas less substituted groups are suitable for LAMs such as vinyl acetate. After the pre-equilibrium step and establishment of the main RAFT process, the R group no longer plays a role in the mechanism, but the Z group still has an effect on the intermediate radical stability / fragmentation and thus chain transfer constant throughout the course of the polymerisation.

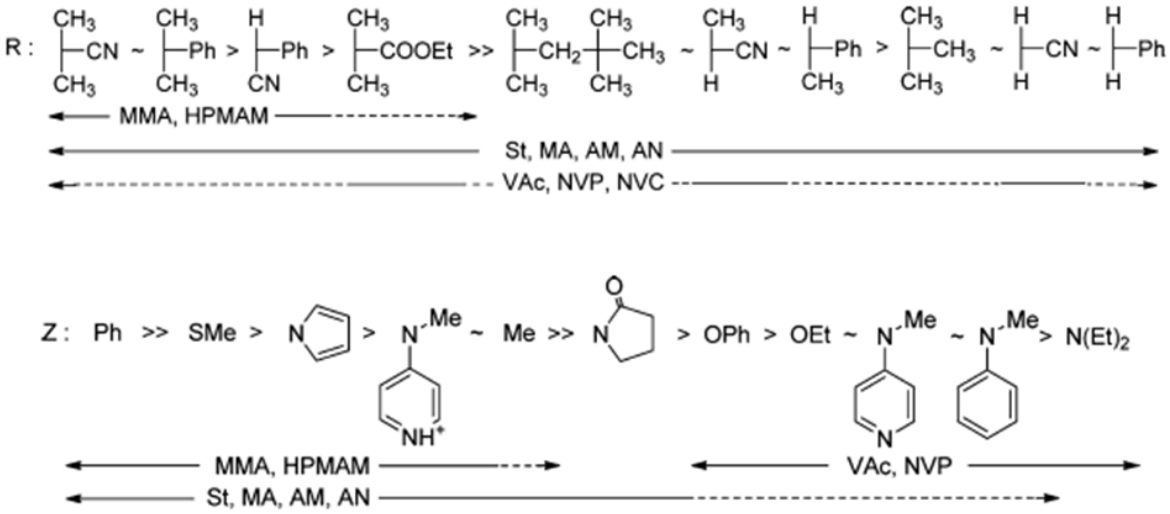

Figure 1.3: Top- scheme showing order of activity of various R groups and the range of monomers that can be polymerised effectively with each. Bottom –a similar scheme for the choice of Z group. Adapted from Ref[12].

Among the classes of Z groups, dithiobenzoates (Z = Ph) possess the highest chain transfer constants and are therefore particularly useful for the polymerisation of meth-acrylate/methacrylamide monomers, however, are prone to rate retardation effects most significantly for the higher k_p acrylates, acrylamides and LAMs. They are more reactive which can be useful in end group removal chemistries but also makes them more susceptible to hydrolysis[28] which is inconvenient for aqueous polymerisation conditions (although use of acidic buffers can mitigate this[29]). Trithiocarbonates (Z = S-alkyl) have therefore become more popular as they possess higher stabilities, respectable chain transfer constants, are often easier to synthesise and are suitable for the polymerisation of a wide range of monomers.[30] The use of xanthates (Z = O-alkyl) is typically reserved for the polymerisation of LAMs such as vinyl acetate, where the use of other CTAs causes significant rate retardation. The low chain transfer constants of xanthates generally makes them poor choices for MAMs, although with careful selection of Z group this can be improved.[31] They have been shown to control the typically challenging polymerisation of ethylene[32] and the narrow dispersity photo-RAFT polymerisation of acrylamides with xanthates has also been reported.[13] Finally the other major class of Z group are the dithiocarbamates,[33] which have been utilised with pH responsive switching to polymerise diblocks of MAMs and LAMS in direct sequence, a difficult feat for most other CTAs.[34] Placement of a pyridine on the Z group allows for alteration of the chain transfer constant

by protonation of the 'N' atom, where in the protonated state the CTA displays superior control of MAMs.

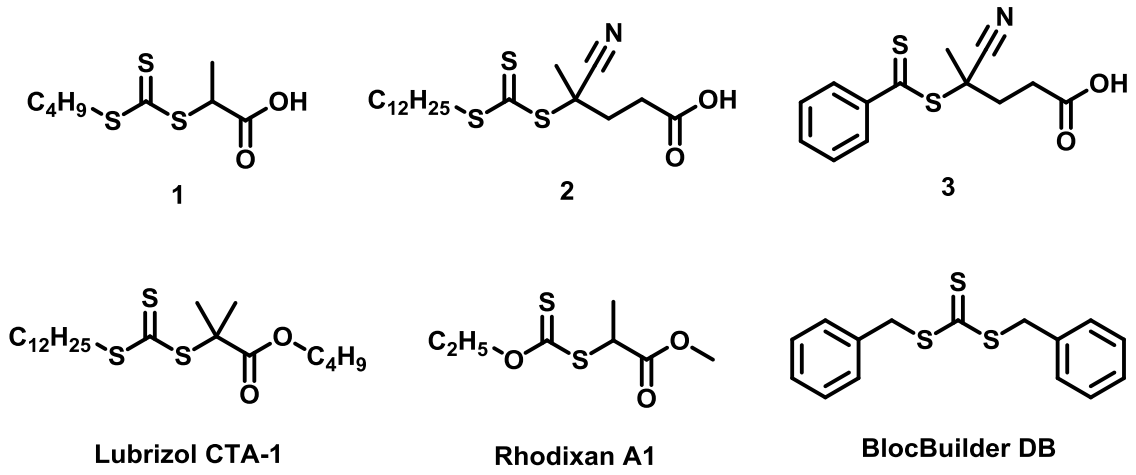

Figure 1.4: Top - examples of commonly used CTAs in academic literature (1, 2, 3). Bottom – structures of three CTAs produced on industrial scale by the companies Lubrizol, Solvay and Arkema.

One major advantage of the RAFT approach is the similarity in experimental setup with that of FRP, with the only change in many cases being the addition of the CTA in relatively small quantities. It is therefore highly amenable to industrial scale up processes and has captured the attention of a number of companies such as Lubrizol,[35] Solvay, Dupont and Arkema (Figure 1.4). Lubrizol have utilised RAFT in the multi-tonne scale production of poly(alkylmethacrylate) star copolymers (Asteric^{TM}) to produce viscosity modifiers for lubrication fluids, where the star architecture provides superior shear stability over traditional linear alternatives. A number of CTAs are also now produced on commercial scale by the company Boron Molecular, a spin off from CSIRO. The presence of the RAFT end group can be undesirable in many applications, however, due to colouration of polymeric materials and potential for further side reactions releasing odorous compounds such as thiols. A range of reactions to cleave the RAFT agent end group or use it to incorporate further functionalities onto the polymer have been developed which makes this less problematic.[36] Impurities present in the CTA from synthesis can also be highly odorous and thus, depending on the application, high purities are often required which can make CTA production expensive on a commercial scale.

1.5 Polymeric architectures

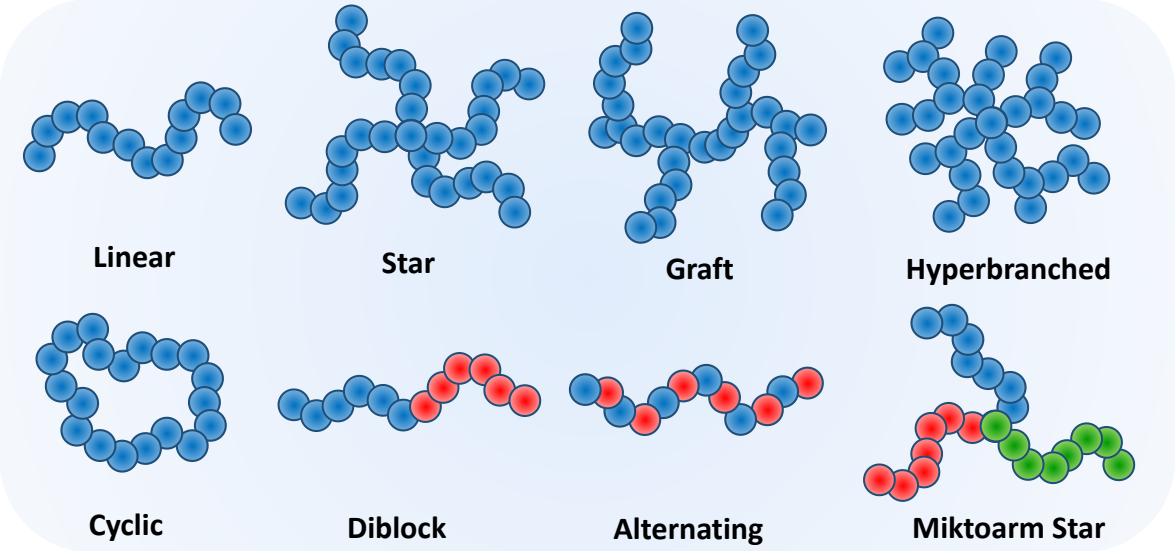

Figure 1.5: Scheme showing a variety of possible polymeric architectures.

Control of polymeric architecture has a profound impact on material properties and the use of RDRP techniques allows for exquisite control of a vast range of complex structures including multiblock,[37] cyclic,[38] alternating,[39] star,[40] graft and hyperbranched materials[41] (Figure 1.5). RAFT has been utilised for the synthesis of all of these architectures,[42] for example the iterative polymerisation of monomers to full conversion allows for facile synthesis of multiblocks,[43-45] while the RAFT end group can be used for chemistries such as intramolecular end to end Diels-Alder to form cyclic polymers[46] or reduction to thiol and subsequent protein coupling.[47, 48] There are often multiple approaches to access each architecture – in star polymer synthesis for instance the individual arms can be first isolated and then crosslinked together,[49] or alternatively multi-functional CTAs can be used to allow for direct star formation in a single core first polymerisation step.[50] Such flexibility allows for a great deal of creativity in polymer synthesis and furthermore by combination with other controlled polymerisation techniques a huge range of potential structures are available.[51] In particular the synthesis of miktoarm star copolymers is facilitated by the use of multiple orthogonal polymerisation techniques, as has been demonstrated in the case of sequential RAFT then ATRP from a multi-initiator core to yield an A_2B_2 arm star,[52] and additionally by combination of RAFT, ROP and click chemistry to create a 4-arm ABCD structure.[53] Other possibilities include exploiting the alternating copolymerisation behaviour of monomers combinations such as styrene/maleic anhydride, which forms an almost perfect AB repeat unit polymer. RAFT

can be used to control the MW or enable synthesis of multiblock copolymers which can then be selectively functionalised at the maleic anhydride units to form novel precision graft structures.[54, 55] Additionally the RAFT polymerisation of vinylbenzylchloride with maleic anhydride and subsequent ATRP of the chloride groups has been demonstrated to create grafted glycopolymers in several architectural designs.[56]

1.6 Synthetic approaches to bottle-brushes

Among the multitude of polymeric architectures bottle-brushes are particularly challenging to synthesise (first shown in the 1980s[57]) but offer many novel properties. Graft copolymers consist of polymeric backbone with numerous grafted side chains, of which bottle-brush polymers are considered a subset characterised by a very high grafting density. Upon increasing the packing of side arms a transition from a comb to bottle-brush is observed, where the high steric hindrance causes the backbone to stretch out into an extended conformation and forces the molecule to adopt a cylindrical morphology. This endows the polymer with a number of unique properties compared to other architectures including high entanglement molecular weight,[58] unusual bulk rheological properties[59, 60] and versatile options for chemical functionalisation.[61]

Graft polymers can be synthesised through three general approaches: 'grafting to', 'grafting through' and 'grafting from' (Figure 1.6).[62, 63] Each method has advantages and disadvantages.

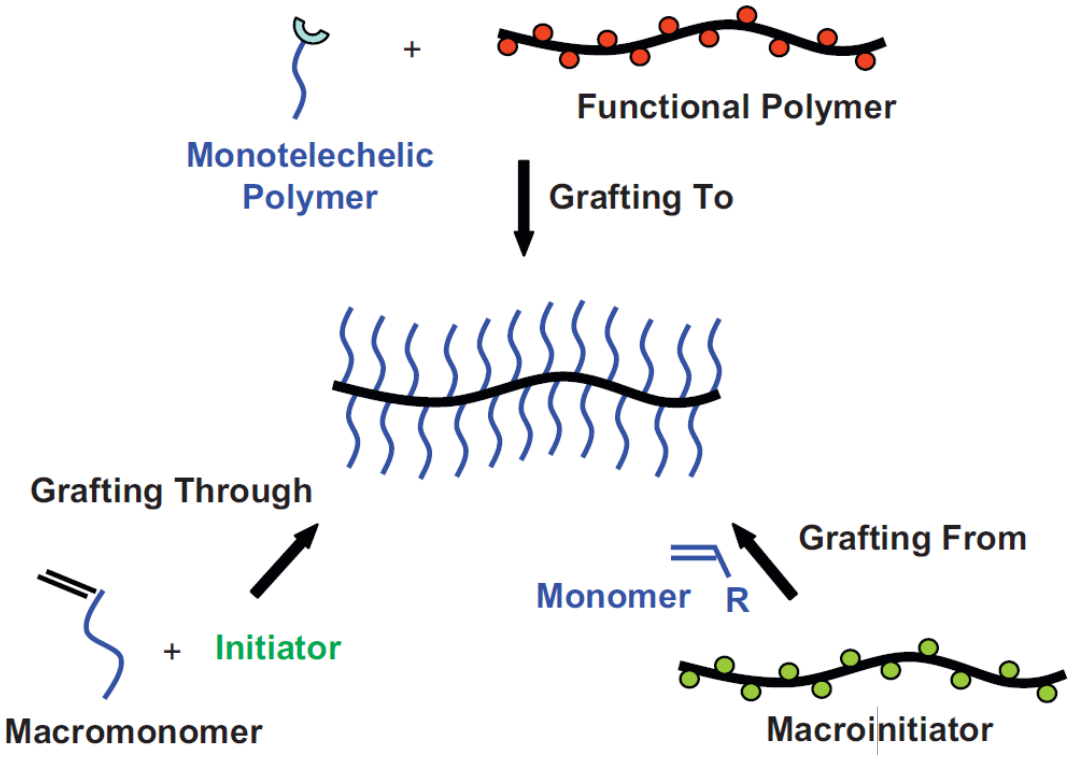

Figure 1.6: Scheme outlining the three different approaches to graft polymer synthesis, adapted from Ref[62].

The 'grafting through' technique involves taking a polymer with a reactive chain end, also known as a macromonomer, and polymerising them together to form a bottle-brush polymer. The advantage of this approach is that it ensures a high grafting density – every monomer unit of the backbone will have a grafted side chain attached. However the low reactivity of the macromonomer can make it challenging to achieve a high degree of polymerisation of the backbone, especially for radical polymerisations.[64-66] This approach has been used effectively in the synthesis of bottle-brushes in particular with ring opening metathesis polymerisation (ROMP),[67-69] facilitating the polymerisation of norbornene macromonomers where backbone lengths of > DP500 with side chains of 10,000 g mol^{-1} have been obtained.[70] The macromonomers are often synthesised by combination with another controlled polymerisation technique and can also be modified to introduce other functionalities such as dyes and drug moieties.[71, 72] The ROMP 'grafting through' is particularly useful for the synthesis of heterograft bottle-brushes with two distinct

regimes by the sequential polymerisation of two different norbornene macromonomers to yield Janus nanoparticles.

The ‘grafting to’ approach involves preparing the polymer backbone and side arms separately, then attaching the arms through a coupling reaction. This allows for exact characterisation and high control of the degree of polymerisation of both the side chain and backbone polymers. However, steric hindrance means it is difficult to reach high conversion in the coupling reaction, therefore the grafting density is typically lowered.[73] Additionally excess unconjugated linear polymer must be separated from the bottle-brush to reach a high purity product which can be challenging depending on the nature of the polymer used. Most examples of this approach use click chemistry methods to maximise the efficiency of the coupling although the ‘grafting to’ is generally less popular for the synthesis of dense graft copolymers.[74-76]

In the ‘grafting from’ approach a polymer backbone functionalised with initiator groups is synthesised, from which the side chains are directly grafted *via* a polymerisation step. This method allows for the preparation of bottle-brush polymers with very long backbones and high grafting densities. The drawbacks of this approach are that the side chains are more difficult to analyse and if the initiators are added to the backbone via a coupling reaction the grafting density may be lowered depending on the yield of this reaction. Alternatively synthesising the backbone from a monomer with an initiator group already attached would require two orthogonal polymerisation techniques which complicates the approach, but has been demonstrated successfully for combinations of ring opening polymerisations (ROP), ATRP and RAFT.[77, 78] Initiation efficiency from the backbone may also be sub-quantitative depending on reaction conditions which would lead to a reduction in the side chain density.[79, 80] The ‘grafting from’ technique has been used most extensively with atom transfer radical polymerisation (ATRP),[81-83] with which the structure of the bottle-brushes can be controlled in terms of the grafting density, side chain and backbone length, and choice of monomer.

In RAFT specifically the ‘grafting from’ approach is complicated by the choice of whether to attach the CTA to the polymer through the R or Z group, such a decision will have a profound effect on the polymerisation step due to the fragmentation of the R-Sulphur bond during polymerisation (Figure 1.7). In the case of the Z group approach the trithiocarbonate will remain attached to the polymer backbone at all times and the

propagating radical will be removed into solution – this can be advantageous at preventing terminations involving the high molecular weight bottle-brushes, however, in practice functions similarly to the 'grafting to' approach, whereby steric hindrance of the grafts makes it increasing difficult for radicals to diffuse and activate the trithiocarbonates at the core. This reduces the potential MW of the side chains and can lower the grafting density. For the R group approach on the other hand, the propagating radical remains attached to the polymeric backbone throughout the process, therefore maintaining a high grafting density although with the possibility for formation of cross-linked networks by excessive terminations. The R group approach can be considered a true 'grafting from' analogous to techniques such as ATRP. Early attempts with this methodology had limited success due to extensive intermolecular cross-coupling side reactions.[50] While further studies have been reported, in this application RAFT has been infrequently used compared to ARTP.[84-86]

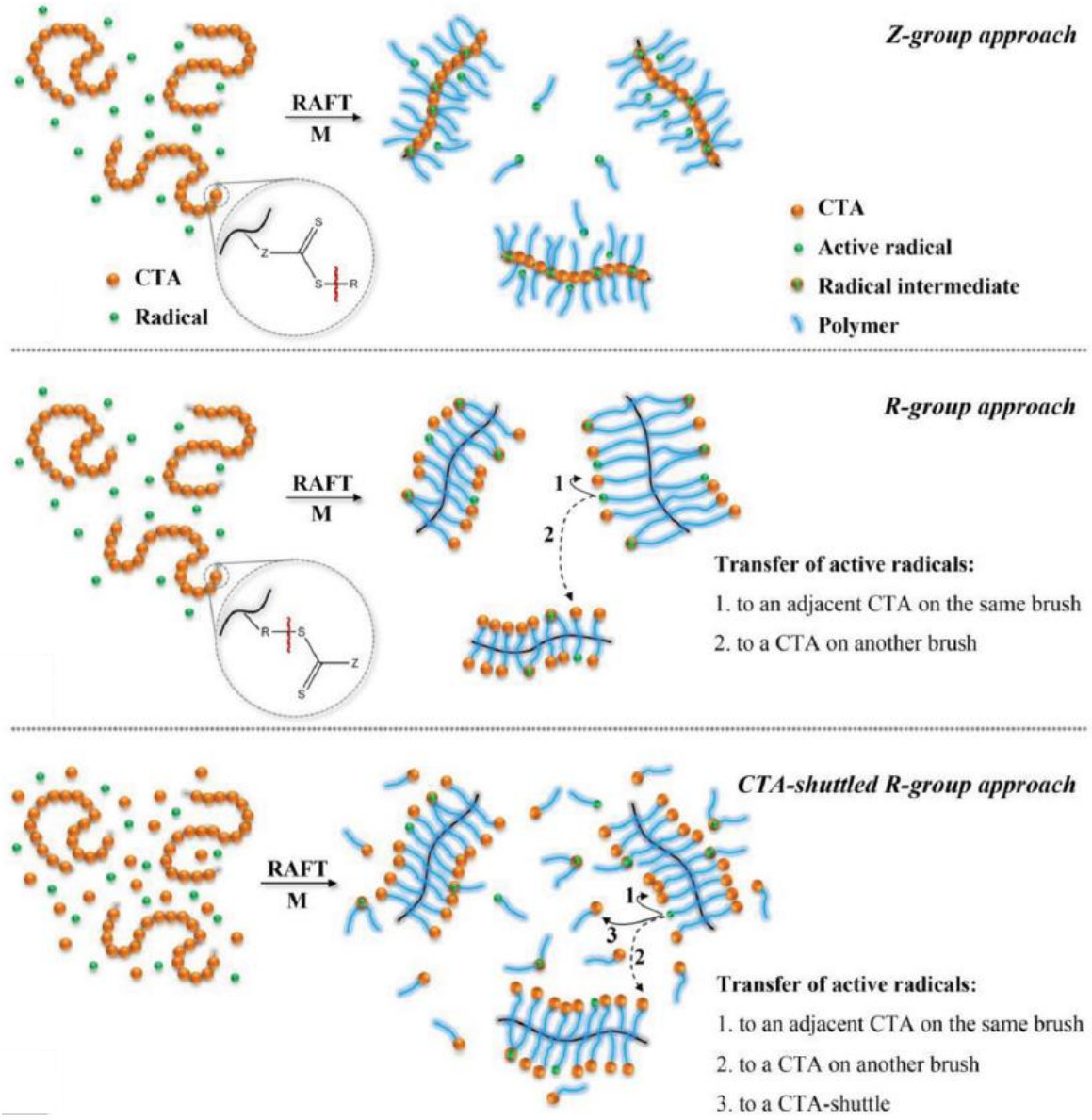

Figure 1.7: Schemes showing the mechanisms of the three RAFT 'grafting from' approaches, adapted from Ref[87].

Recently, an elegant solution to this problem when utilising the RAFT 'grafting from' approach was published by Müller and co-workers, using the addition of free, ungrafted chain transfer agent (CTA), which was shown to improve control over the polymerisation.[87] This 'Shuttle CTA approach' was reported to utilize the linear polymers to shuttle radicals between bottle-brushes, helping to activate CTAs in the sterically hindered environment of the side chains and thus lowering the polydispersity of the final compound (Figure 1.7). A similar technique has been reported for the RAFT grafting from in heterogeneous conditions off a cellulose substrate where the addition of free 'sacrificial' free CTA was necessary to control the polymerisation by compensating for a reduced CTA concentration at the surface.[88] For the initial shuttle CTA approach

poly(vinylbenzyl chloride) was used as the bottle-brush backbone which is limited to relatively low degrees of polymerisation (DP100) and therefore only short cylindrical molecules were synthesised. A recent publication adapted this technique to synthesise bottle-brush of DP1000 backbones with polystyrene side chains, although required multiple additional reaction steps.[89] Photo-RAFT has also been suggested to improve the control of the grafting from step, where a typical azo initiator thermally induced polymerisation displayed significantly worse control than an equivalent reaction performed by initiation solely with light.[90, 91]

1.7 Analysis and applications of bottle-brush copolymers

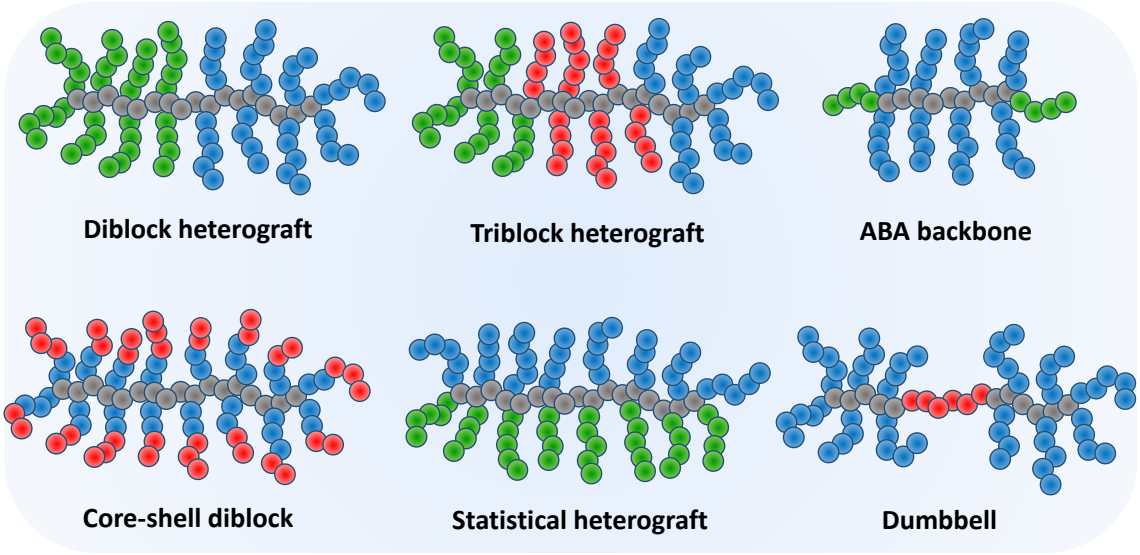

Figure 1.8: Scheme showing the structure of a selection of bottle-brush copolymers that have been described in literature – diblock,[92] triblock[93] and statistical heterografts,[94] core-shell[95-97], dumbbell[98] and ABA backbones.[99, 100]

Excellent synthetic control of bottle-brushes allows these unimolecular species to be made to precise specifications, creating nanoparticle size objects with tailored size in terms of cylinder length and thickness. An array of complex structures have been described in the literature which introduce further functionality and enables a number of possible applications for bottle-brush materials (Figure 1.8).[101-103] Other variations of structural parameters include v-shaped side chains,[104] very high density grafts[105], gradient backbones[106], and bimodal length bristles.[107] Heterograft bottle-brushes are of particular interest for introducing amphiphilicity to form Janus-type macromolecules. Perhaps the most facile route to block copolymer heterograft brushes is sequential macromonomer polymerisations by ROMP, however, several papers have also reported the synthesis of

these architectures by multiple orthogonal polymerisations grafting from a block copolymer backbone - for diblocks combinations of two of ROP, RAFT and ATRP have been performed,[108-111] and even a triblock bottle-brush was realised by the reaction of all three in sequence.[93] It is worth noting that norbornene ROMP derived backbones have a repeat unit per side chain of 5 C atoms, whereas a vinyl monomer derived backbone potentially has a side chain every 2 C atoms and therefore a significant difference in grafting density can be obtained from the two methods.

1.7.1 Analysis by microscopy and scattering techniques

Microscopy techniques have proven highly useful for the characterisation of such compounds, most notably atomic force microscopy (AFM) where height profile images of bottle-brushes deposited onto substrates are highly effective for analysing molecular size and morphology.[112, 113] The extended conformation of the backbone can be readily observed from this analysis, for example the polymeric side chain length has been shown to have a large impact on the backbone flexibility and the successful synthesis of complex 6-arm star brushes could be confirmed by direct visualisation of the expected structure (Figure 1.9).[114] Tadpole-like brushes with a stimuli-responsive hydrogen bonding end block could be observed to coil on a mica surface[115] and AFM has even been used to measure molecular weight by analysing the area of individual macromolecules where it showed good agreement with MALLS-SEC.[116] Ultrahigh molecular weight macrocyclic bottle-brush have been synthesised via a ring closure coupling reaction[117] or through ring expansion metathesis polymerisation of a macromonomer,[118] where in both cases the cyclic morphology could be revealed by AFM (Figure 1.9).

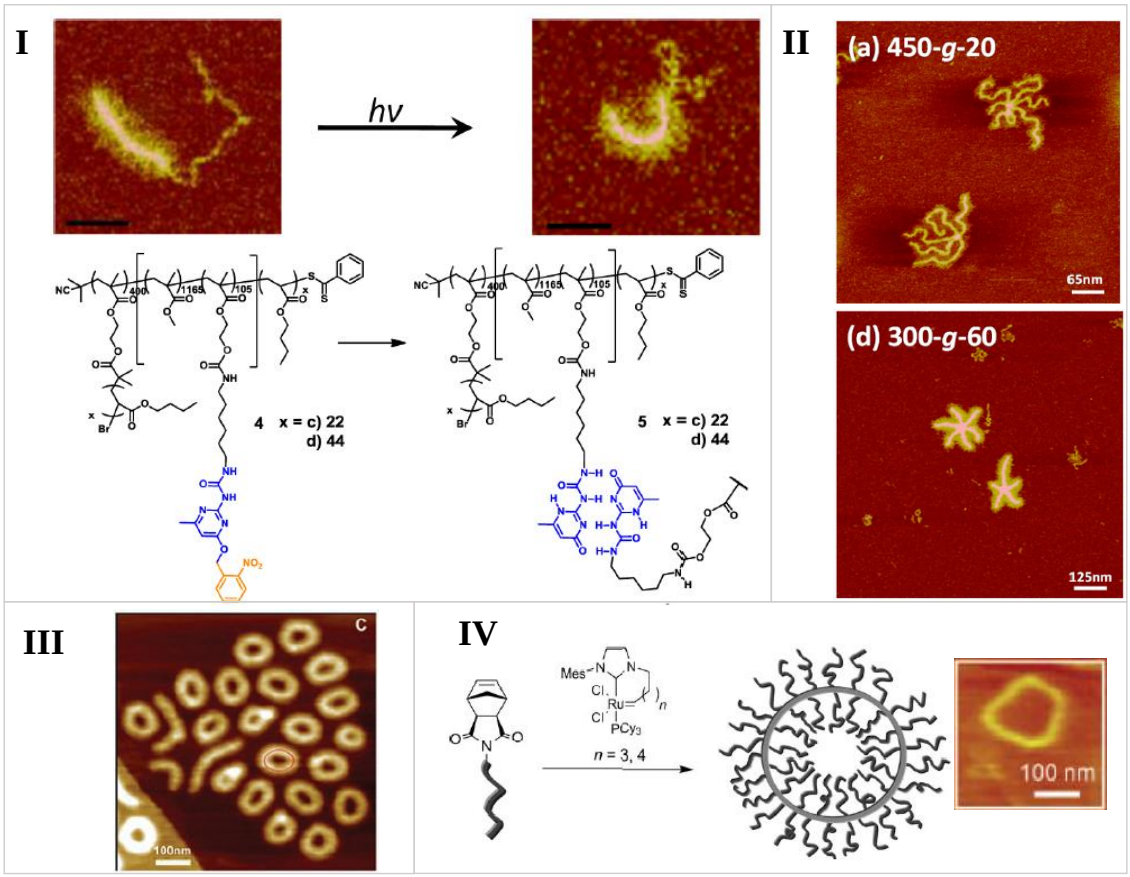

Figure 1.9: I – Bottle-brush with an end block containing a UV-labile protecting group. Upon UV irradiation hydrogen intramolecular hydrogen bonding interactions induce folding of the tail as imaged by AFM height profiles, adapted from ref[115]. **II** – AFM height profile images of a 6-arm star brush of varying arm length and side chain thickness, adapted from ref[114]. **III** – Image of cyclic brush polymers derived from a ring closure strategy, adapted from Ref[117]. **IV** – Scheme for macromonomer REMP and a representative AFM image, adapted from Ref[118].

Scission of the carbon-carbon bond backbone of bottle-brush molecules has been reported when the polymer is deposited onto a surface.[119, 120] A monolayer of a poly(n-butylacrylate) side chain brush deposited by a Langmuir Blodgett trough onto a liquid surface (water/propanol) caused backbone degradation over the course of several hours to days (Figure 1.10). This phenomenon was attributed to stretching interactions of the side chain across the substrate inducing force along the already extended bottle-brush backbone, at sufficiently high quantities to cause bond scission. The cleavage could be monitored by dipping an AFM substrate into the monolayer and imaging the individual bottle-brush molecules, where a continual reduction in molecular size was observed over the course of 42 hours. Additionally a core-shell diblock bottle-brush consisting of a poly(oligo(ethyleneglycol)methacrylate) core and a positively charged poly(2-[dimethylamino]ethyl methacrylate) shell displayed rapid backbone scission when

deposited onto mica and silica substrates in the dry state.[121] Increased decomposition rate was observed for diblocks with higher cationic shell content and therefore electrostatic interactions with the substrate were suggested to be the main driving force for increasing backbone stress. The remarkable ability to break covalent bonds through individually weak polymer interactions is a novel property for densely grafted bottle-brushes.

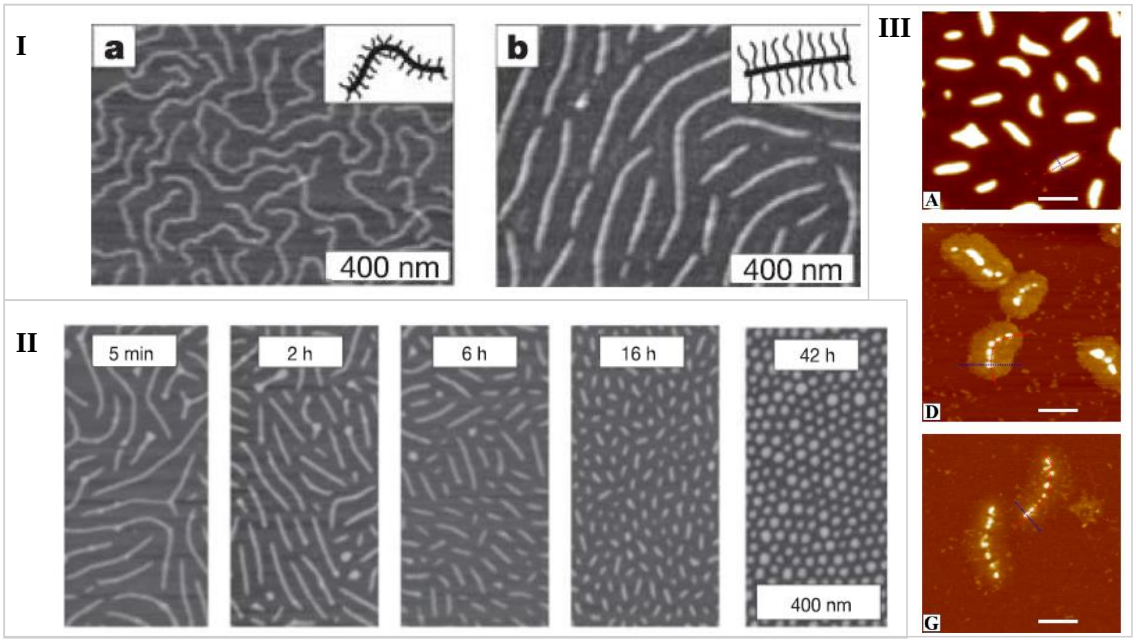

Figure 1.10: I – Upon increasing the side chain length in from a) DP12 to b) DP120 a transition from semi-flexible to rigid rod is observed, adapted from Ref[119]. II – Backbone scission monitored at various time-points for a bottle-brush deposited as a surface monolayer. III – Scission of the brush backbone is observed as the size of the cationic shell is increased from top to bottom, adapted from Ref[121].

Small angle scattering techniques (x-ray or neutron) are highly complementary to microscopy analysis and are useful for elucidation of bottle-brush size and conformation. Several studies have focused on the effect of variation of structural parameters (side chain DP, grafting density, type of monomer) on the polymer morphology in solution[122, 123] - as AFM is typically performed in the dry state it may not be representative of the behaviour in solution and therefore scattering provides valuable information for many applications. Worm-like cylindrical models generally provide a good fit for bottle-brush scattering data, consistent with the extended backbone morphology observed by microscopy. The polymeric side chains are known to be slightly extended compared to a typical linear polymer, although not to the same extent as the backbone - experimental and theoretical studies suggest a dependence of $N^{3/4}$ for the radius of a bottle-brush (where N is DP) in contrast to the $N^{3/5}$ relationship expected for a free linear polymer.[124-126]

1.7.2 Bottle-brush self-assembly

In the same manner as linear diblock copolymers, melts of heterograft bottle-brushes will phase separate into varying morphologies to minimise interfacial interactions of opposing polymer blocks (Figure 1.11). Domain size and nature of the morphology are dictated by the volume fraction and segregation parameter of each block component. The densely grafted side chains of bottle-brushes reduce interpenetration and causes high entanglement molecular weights, promoting rapid phase separation. Compared to linear species, therefore, bottle-brush melts possess faster dynamics of self-assembly, while the domains can also be significantly larger (> 100 nm) by virtue of increased molecular size of each component.[92, 127, 128]

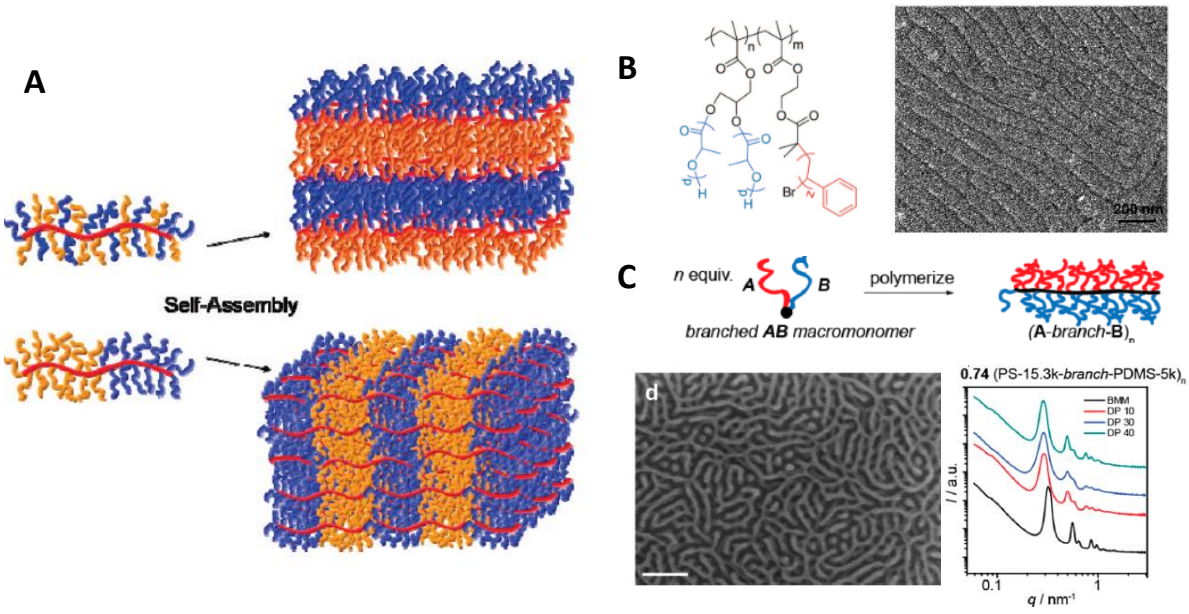

Figure 1.11: A – Scheme showing self-assembly of block and statistical heterograft bottle-brushes, adapted from Ref[129]. B – Assembly of a PLA/PS diblock images by SEM, adapted from Ref[109]. C – ROMP polymerisation of an AB macromonomer to form a Janus brush and its assembly in AFM and SAXS, adapted from Ref[130].

Larger domain sizes achieved through bottle-brush assemblies can provide them with optical properties and enable their use as photonic crystals.[131] A poly(styrene) (PS) brush with an poly(n-butylacrylate) (BA) side chain displayed spherical, lamellar and cylindrical morphologies depending on MW and sample preparation conditions. Furthermore the film appeared in bright colours as a result of reflecting selective visible light wavelengths.[132] Changing the linear block to a brush, as demonstrated by Grubbs et al.,[129] allowed access to different size regimes to yield a broader spectrum of colours (Figure 1.12). [133, 134] By mixing various sizes of bottle-brushes an entire range of colours

could be accessed, and in further work by the group they were able to synthesis photonic crystal materials in the infra-red region through incorporation of polyisocyanate macromonomers, which form rigid, helical structures.[135] ROMP of an AB difunctional macromonomer offered another approach to higher density Janus bottle-brush materials which showed unique assembly into the gyroid morphology.[130]

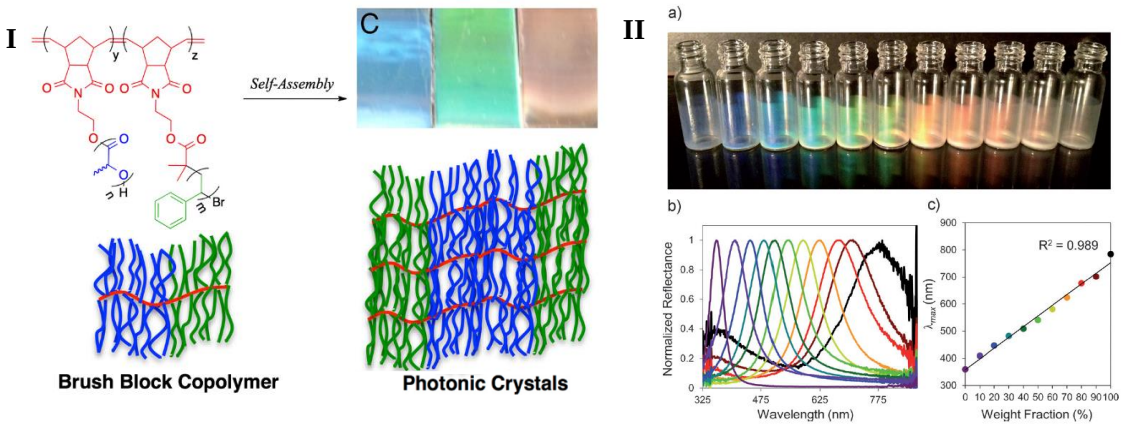

Figure 1.12: I – a poly(lactide)-b-PS diblock heterograft brush assembled to give photonic crystals, adapted from Ref[134]. II – By mixing different ratios of brushes with varying block sizes the domain size can be controlled, leading to reflection of light over a broad range of wavelengths. Adapted from Ref[133].

ABA triblock copolymer backbones have also been used to induce self-assembly behaviour, where the 'B' block is the bottle-brush core and the 'A' block ends aggregate with one another. Disk shaped morphologies with a highly ordered pattern were formed as a result of the stiffer central block provided by the use of a PBA-b-PS graft bottle-brush segment with poly(N-(2-methacryloyloxyethyl)pyrrolidone) 'A' block tails.[136] Additionally the introduction of a crystallisable 'A' block onto the ends of a PBA bottle-brush core promoted network formation through physical crosslinking as evidenced by AFM.[100]

The self-assembly of amphiphilic bottle-brushes in dilute solution again display unique behaviour when compared to their linear based counterparts, where they function as giant surfactants.[92, 102, 137] They generally exhibit lower critical micelle concentrations on the order of 1 nM and have a tendency to form micelles of larger hydrodynamic volume. Diblock heterograft bottle-brushes consisting of hydrophobic poly(lactide) and hydrophilic poly(ethylene oxide) (PEO) of combined molecular weights 0.7-4.4 $*10^6$ g mol^{-1} formed large micelles with 55 nm core radii and, including the corona, hydrodynamic diameters of 250 nm.[138] Altering block asymmetry affects size and

morphology of the assemblies as predicted by packing parameters, which further enabled formation of cylindrical micelles several micrometres in length. In other work vesicular structures of several hundred nm were observed for bottle-brushes composed of heterografts with three different polymers blocks.[86, 139]

1.7.3 Bottle-brushes as encapsulating agents

Bottle-brushes have received interest for usage as nanocarriers to deliver drugs, signal or detect in solution.[140] Encapsulation of the desired agents can be approached in a number of ways, firstly by the use of the previously described amphiphilic micellar brush assemblies. In this case hydrophobic small molecules can be loaded into the core by physical interactions, which can be useful for the slow release of drug molecules.[141] A range of polymeric micelles from 50-150 nm in hydrodynamic diameter consisting of poly(lactide)-b-PEO bottle brushes were loaded with the anticancer drug paclitaxel, allowing for effective solubilisation in aqueous solution and reaching loading capacities of 6.5 wt. % (Figure 1.13 B). [142] Incorporation of coumarin units into the hydrophobic brush block enabled cross-linking in response to UV irradiation to lock the assembled structure in place, where it was found loading with paclitaxel actually improved crosslinking efficiencies, implying structural alterations within the micelle cores. An amphiphilic bottle-brush composed of a cholesterol functional macromonomer as the hydrophobic segment displayed micellisation in water and effective loading of doxorubicin (22.1 wt. %).[143] Slow release kinetics of doxorubicin were observed (~25 % after 14 days) under biologically relevant conditions, while the materials also showed cell

cytotoxicity in *vitro* and extended plasma circulation times in *vivo* when compared to the administration of free drug.

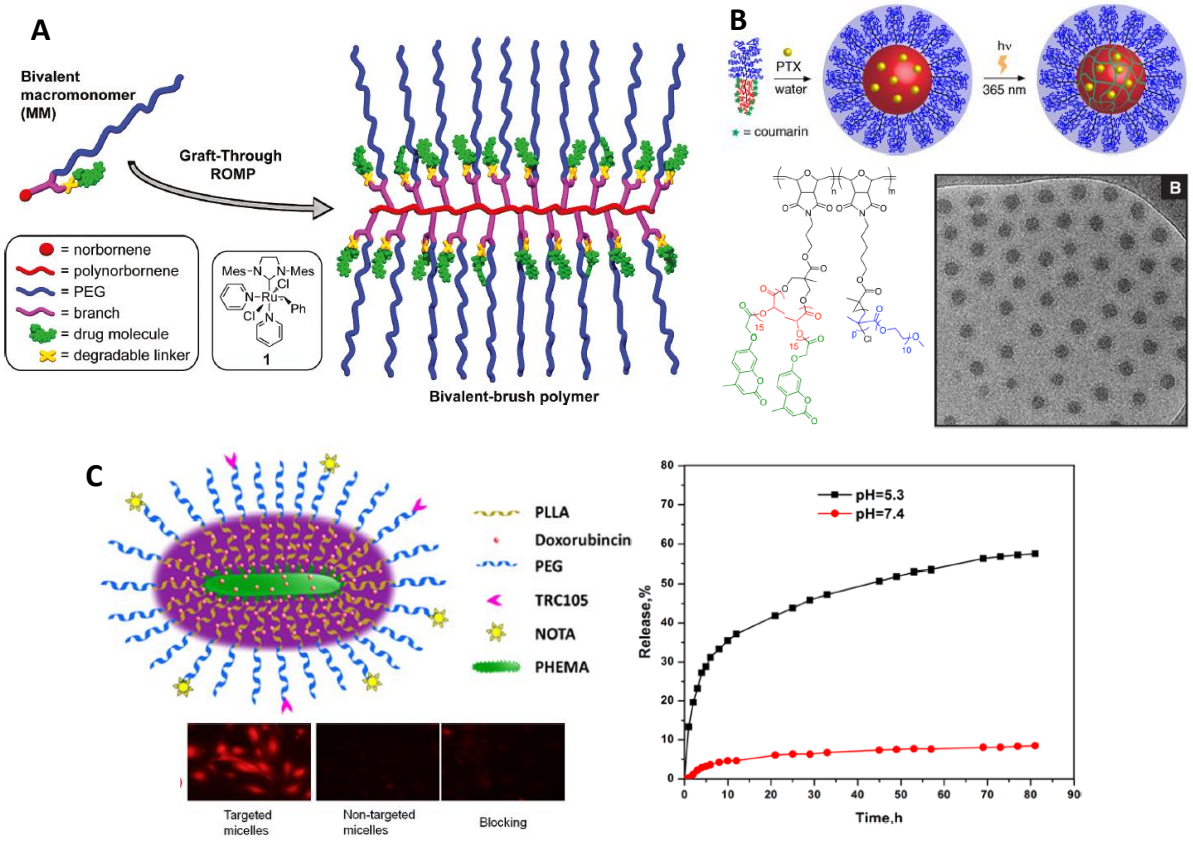

Figure 1.13: A – Scheme for a drug loaded brush by ROMPO 'grafting through', adapted from Ref[144]. B – aqueous self-assembly and drug loading of an amphiphilic bottle-brush, adapted from Ref[138]. C – Unimolecular bottle-brush for theranostic applications and kinetics of drug release (right), adapted from Ref[145].

Alternatively the use of unimolecular bottle-brushes as encapsulation agents has been explored, where the dimensions of the nanocarrier will be determined by the brush length and thickness and thus be much smaller than those of micellar constructs. Agent loading can be achieved either by covalent binding into the brush at selective positions,[146, 147] or by the synthesis of an amphiphilic core-shell brush architecture, in which case encapsulation can be performed in a similar manner to solution self-assemblies.[148-150] Advantages of bottle-brushes compared to other nanoparticle systems include the robust choice of chemical functionalisation which can be performed at distinct locations such as the backbone, side chain and periphery. This was exemplified in a study by Grubbs et al. in which a TEMPO-label was inserted either at the end of the backbone, in the centre or on the exterior of a bottle-brush, whereby electron paramagnetic resonance (EPR) revealed substantial differences in mobility.[61] A polymeric quencher was ineffective for

the TEMPO labels among the backbone as a result of reduced access from side chain steric hindrance, but showed a much high quenching rate for the exterior TEMPO units. In drug delivery applications, a core-shell brush loaded with doxorubicin was functionalised with antibodies and macrocyclic chelators onto the exterior to facilitate targeting behaviour and positron emission tomography imaging (Figure 1.13 C).[145] Such combinations of labels make bottle-brushes an effective platform for theranostic treatments.[151] Drug labelled ROMP macromonomers, attached *via* a degradable linker (Figure 1.13 A), were used to synthesise brushes and were demonstrated as therapeutically effective in *vitro*,[144] while an identical approach was used to access novel MRI contrast and fluorescent agent functional brushes, which were used for redox responsive imaging in *vivo*.[152]

1.7.4 Templating and hollow bottle-brush materials

The compartmentalised nature of side chain block copolymer bottle-brushes makes them suitable for templating processes where they can be used to fabricate hollow nanotube materials or to form polymer-inorganic hybrid nanoparticles of specific size and morphology.[101] Typically a core-shell architecture is designed to load inorganic material into the interior block while retaining a polymeric shell which can mitigate aggregation through steric stabilisation.[153, 154] This approach has been carried out for a number of aniostropic nanoparticles such as loading of a high aspect ratio core-shell bottle-brush with $HAuCl_4$ into the poly(vinyl pyridine) centre.[155] Varying nanoparticles dependent on the loading quantities of gold into the core were obtained - extended nanowire structures were acquired for high amounts, whereas smaller nanoclusters for lower loadings.[155] In a similar fashion a brush template consisting of a poly(caprolactone) core and poly((2-dimethylamino) ethyl methacrylate) polycationic shell underwent silica deposition into the amine functional block, where subsequent treatment with acid or calcination degraded the polyester interior to yield a hollow silica nanotube with high surface area (Figure 1.14 C).[156] Donut shaped hybrid nanoparticles of a organo-silica or gold containing internal segment were synthesised from a cyclic bottle-brush polymer and TEM analysis confirmed the expected structure (Figure 1.14 B).[157]

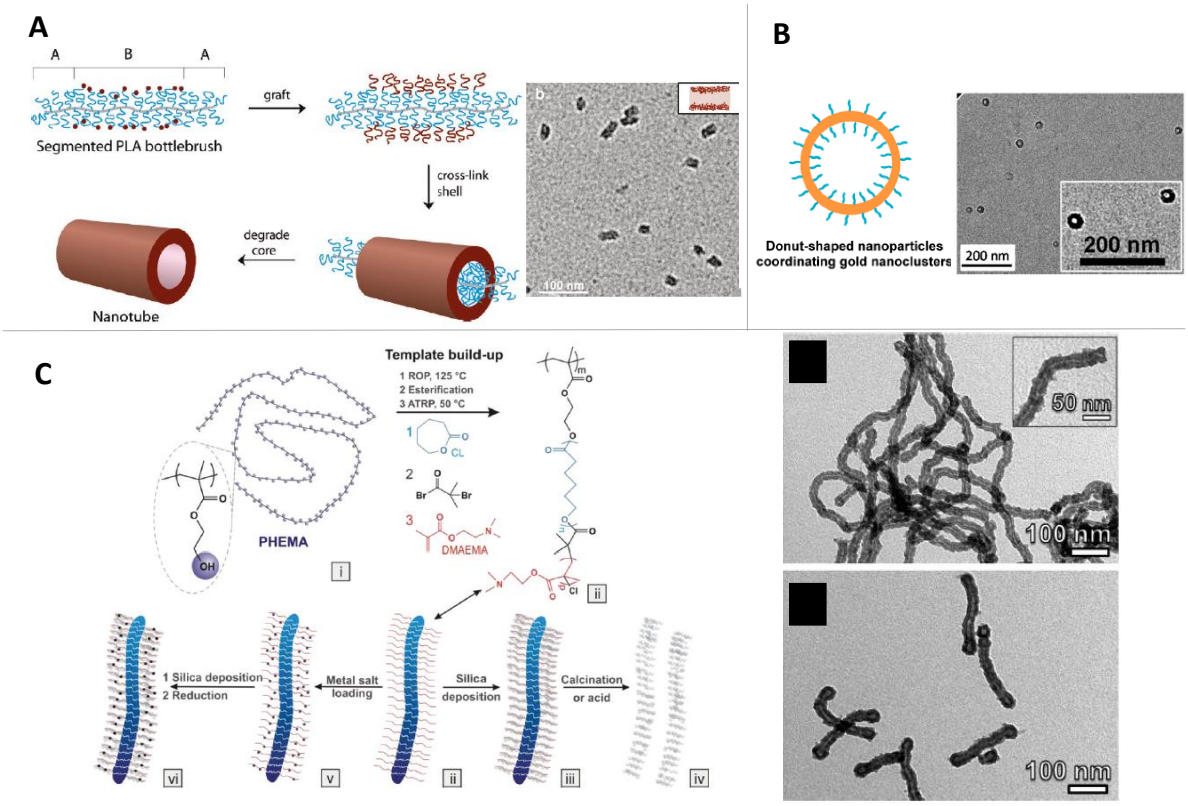

Figure 1.14: A – Approach to synthesis of hollow nanotube through a bottle-brush templating approach, adapted from Ref[111]. B – TEM image of a cyclic bottle-brush copolymer loaded with gold, adapted from Ref[157]. C – Synthetic approach and TEM imaging of inorganic silica nanotubes, adapted from Ref[156].

Open-ended nanotubes could be derived from a bottle-brush templating approach (Figure 1.14 A) from a triblock copolymer backbone.[111] Extension of the central block with firstly a degradable poly(lactone) core, and secondly a cross-linkable 4-(3-butenyl)styrene containing segment was performed, followed by cross-metathesis under dilute conditions and subsequent acid treatment. The dimensions of the resulting nanotube were shown to be consistent with the molecular size of an individual bottle-brush thus allowing for precise structural control.[158] In further work by the same group a hollow nanocapsule with readily modifiable surface chemistry was synthesised by a similar technique by incorporating an additional poly(styrene-co-maleic anhydride) periphery block.[159] Studies of cellular uptake on varying surface functionalised nanotubes showed efficient internalisation for the anionic charged surface materials, with the presence of hydrophobic groups also important for effective uptake. The internal cavity was suggested to be useful for potential encapsulation of therapeutic agents.

1.8 Conclusion

Developments in synthetic polymer chemistry over the last 25 years, such as RDRP and ROMP, have led to huge progress in the realisation of well-defined macromolecular structures. Among these techniques RAFT has established itself as one of the most robust and versatile, due to the facile experimental set up and tolerance to a wide range of functional groups and reaction conditions. The broad range of monomers that can be polymerised by a radical process can also mostly be controlled by RAFT, enabling introduction of diverse functionalities into a variety of polymeric architectures. Bottle-brushes in particular offer a highly versatile platform for development of new nanotechnologies, where their unique properties and vast potential for structural/compositional variations allow them to be tailored to many applications. Despite the advancements, bottle-brushes remain challenging to synthesise with several limitations from each preparation process and therefore further need to develop new synthetic protocols remains. The general underutilisation of RAFT in the 'grafting from' approach and its inherent amenability with industrial processes make it an appealing option with which to explore optimisation of graft copolymer synthesis, in particular with the use of the newly reported 'shuttle CTA' technique.

This thesis aims to investigate the usage of this synthetic approach and drive to the limits of achievable structural complexity. The versatility of the synthesis is demonstrated through polymerisation of apolar and polar monomers, to generate bushes with very different applications, as oil additives and as drug delivery vectors respectively, to illustrate the wide range of applications available to these materials.

1.9 References

1. G. Odian, *Principles of polymerization*, John Wiley & Sons, 2004.
2. J. Nicolas, Y. Guillaneuf, C. Lefay, D. Bertin, D. Gigmes and B. Charleux, *Prog. Polym. Sci.*, 2013, **38**, 63-235.
3. K. Matyjaszewski and J. Xia, *Chem. Rev.*, 2001, **101**, 2921-2990.
4. V. Percec, T. Guliashvili, J. S. Ladislaw, A. Wistrand, A. Stjerndahl, M. J. Sienkowska, M. J. Monteiro and S. Sahoo, *J. Amer. Chem. Soc.*, 2006, **128**, 14156-14165.
5. G. Moad, E. Rizzardo and S. H. Thang, *Aust. J. Chem.*, 2009, **62**, 1402-1472.
6. J. Chiefari, Y. Chong, F. Ercole, J. Krstina, J. Jeffery, T. Mayadunne, G. F. Meijs, C. L. Moad and G. Moad, *Macromolecules*, 1998, **31**, 5559-5562.
7. D. Charmot, P. Corpart, H. Adam, S. Zard, T. Biadatti and G. Bouhadir, *Macromol. Symp.*, 2000, **150**, 23-32.
8. M. R. Hill, R. N. Carmean and B. S. Sumerlin, *Macromolecules*, 2015, **48**, 5459-5469.
9. G. Moad, E. Rizzardo and S. H. Thang, *Chem.–An Asian Jour.*, 2013, **8**, 1634-1644.
10. S. Perrier, *Macromolecules*, 2017, **50**, 7433-7447.
11. A. H. Mueller, R. Zhuang, D. Yan and G. Litvinenko, *Macromolecules*, 1995, **28**, 4326-4333.
12. D. J. Keddie, G. Moad, E. Rizzardo and S. H. Thang, *Macromolecules*, 2012, **45**, 5321-5342.
13. R. N. Carmean, T. E. Becker, M. B. Sims and B. S. Sumerlin, *Chem*, 2017, **2**, 93-101.
14. N. P. Truong, M. V. Dussert, M. R. Whittaker, J. F. Quinn and T. P. Davis, *Polymer Chemistry*, 2015, **6**, 3865-3874.
15. E. Read, A. Guinaudeau, D. J. Wilson, A. Cadix, F. Violleau and M. Destarac, *Polymer Chemistry*, 2014, **5**, 2202-2207.
16. W. Bai, L. Zhang, R. Bai and G. Zhang, *Macromol. Rapid Commun.*, 2008, **29**, 562-566.
17. L. Martin, G. Gody and S. Perrier, *Polymer Chemistry*, 2015, **6**, 4875-4886.
18. T. G. McKenzie, Q. Fu, M. Uchiyama, K. Satoh, J. Xu, C. Boyer, M. Kamigaito and G. G. Qiao, *Advanced Science*, 2016, **3**, 1500394.
19. J. Xu, S. Shanmugam, H. T. Duong and C. Boyer, *Polymer Chemistry*, 2015, **6**, 5615-5624.
20. R. Ran, Y. Yu and T. Wan, *J. Appl. Polym. Sci.*, 2007, **105**, 398-404.
21. H. Wang, Q. Li, J. Dai, F. Du, H. Zheng and R. Bai, *Macromolecules*, 2013, **46**, 2576-2582.
22. Y. Kwak, A. Goto, Y. Tsujii, Y. Murata, K. Komatsu and T. Fukuda, *Macromolecules*, 2002, **35**, 3026-3029.
23. C. Barner-Kowollik, J. F. Quinn, T. U. Nguyen, J. P. Heuts and T. P. Davis, *Macromolecules*, 2001, **34**, 7849-7857.
24. M. Destarac, *Polymer Reviews*, 2011, **51**, 163-187.

25. G. Moad, J. Chiefari, Y. K. Chong, J. Krstina, R. T. A. Mayadunne, A. Postma, E. Rizzardo and S. H. Thang, *Polym. Int.*, 2000, **49**, 993-1001.
26. M. J. Monteiro and H. de Brouwer, *Macromolecules*, 2001, **34**, 349-352.
27. F. D'Agosto, M. T. Charreyre, L. Veron, M. F. Llauro and C. Pichot, *Macromol. Chem. Phys.*, 2001, **202**, 1689-1699.
28. D. B. Thomas, A. J. Convertine, R. D. Hester, A. B. Lowe and C. L. McCormick, *Macromolecules*, 2004, **37**, 1735-1741.
29. C. W. Scales, Y. A. Vasilieva, A. J. Convertine, A. B. Lowe and C. L. McCormick, *Biomacromolecules*, 2005, **6**, 1846-1850.
30. R. T. Mayadunne, E. Rizzardo, J. Chiefari, J. Krstina, G. Moad, A. Postma and S. H. Thang, *Macromolecules*, 2000, **33**, 243-245.
31. M. Destarac, W. Bzducha, D. Taton, I. Gauthier-Gillaizeau and S. Z. Zard, *Macromol. Rapid Commun.*, 2002, **23**, 1049-1054.
32. C. Dommanget, F. D'Agosto and V. Monteil, *Angew. Chem. Int. Ed.*, 2014, **53**, 6683-6686.
33. M. Destarac, D. Charmot, X. Franck and S. Zard, *Macromol. Rapid Commun.*, 2000, **21**, 1035-1039.
34. M. Benaglia, J. Chiefari, Y. K. Chong, G. Moad, E. Rizzardo and S. H. Thang, *J. Amer. Chem. Soc.*, 2009, **131**, 6914-6915.
35. A. J. Brzytwa and J. Johnston, *Polym. Prepr.*, 2011, **52**, 533-534.
36. H. Willcock and R. K. O'Reilly, *Polymer Chemistry*, 2010, **1**, 149-157.
37. J.-F. Lutz, M. Ouchi, D. R. Liu and M. Sawamoto, *Science*, 2013, **341**, 1238149.
38. T. Josse, J. De Winter, P. Gerbaux and O. Coulembier, *Angew. Chem. Int. Ed.*, 2016, **55**, 13944-13958.
39. H. De Brouwer, M. A. Schellekens, B. Klumperman, M. J. Monteiro and A. L. German, *J. Polym. Sci., Part A: Polym. Chem.*, 2000, **38**, 3596-3603.
40. X. Zhang, J. Xia and K. Matyjaszewski, *Macromolecules*, 2000, **33**, 2340-2345.
41. K. Matyjaszewski, S. G. Gaynor, A. Kulfan and M. Podwika, *Macromolecules*, 1997, **30**, 5192-5194.
42. A. Gregory and M. H. Stenzel, *Prog. Polym. Sci.*, 2012, **37**, 38-105.
43. G. Gody, T. Maschmeyer, P. B. Zetterlund and S. Perrier, *Nat. Comm.*, 2013, **4**, 2505.
44. J. Zhang, G. Gody, M. Hartlieb, S. Catrouillet, J. Moffat and S. Perrier, *Macromolecules*, 2016, **49**, 8933-8942.
45. N. G. Engelis, A. Anastasaki, G. Nurumbetov, N. P. Truong, V. Nikolaou, A. Shegiwal, M. R. Whittaker, T. P. Davis and D. M. Haddleton, *Nature Chemistry*, 2017, **9**, 171.
46. Q. Tang, Y. Wu, P. Sun, Y. Chen and K. Zhang, *Macromolecules*, 2014, **47**, 3775-3781.
47. M. Li, P. De, H. Li and B. S. Sumerlin, *Polymer Chemistry*, 2010, **1**, 854-859.
48. C. Boyer, V. Bulmus, J. Liu, T. P. Davis, M. H. Stenzel and C. Barner-Kowollik, *J. Amer. Chem. Soc.*, 2007, **129**, 7145-7154.
49. G. Zheng and C. Pan, *Polymer*, 2005, **46**, 2802-2810.
50. J. F. Quinn, R. P. Chaplin and T. P. Davis, *J. Polym. Sci., Part A: Polym. Chem.*, 2002, **40**, 2956-2966.
51. Y. Kwak, R. Nicolaÿ and K. Matyjaszewski, *Aust. J. Chem.*, 2009, **62**, 1384-1401.

52. W. Zhang, W. Zhang, J. Zhu, Z. Zhang and X. Zhu, *J. Polym. Sci., Part A: Polym. Chem.*, 2009, **47**, 6908-6918.
53. G. Moriceau, G. Gody, M. Hartlieb, J. Winn, H. Kim, A. Mastrangelo, T. Smith and S. Perrier, *Polymer Chemistry*, 2017, **8**, 4152-4161.
54. G. Moriceau, J. Tanaka, D. Lester, G. S. Pappas, A. B. Cook, P. O'Hora, J. Winn, T. Smith and S. Perrier, *Macromolecules*, 2019.
55. R. Fleet, E. T. van den Dungen and B. Klumperman, *Macromol. Chem. Phys.*, 2011, **212**, 2191-2208.
56. P. Rempp, P. Lutz, P. Masson, P. Chaumont and Physics, *Macromolecular Chemistry*, 1985, **13**, 47-66.
57. M. Wintermantel, M. Gerle, K. Fischer, M. Schmidt, I. Wataoka, H. Urakawa, K. Kajiwara and Y. Tsukahara, *Macromolecules*, 1996, **29**, 978-983.
58. S.-i. Namba, Y. Tsukahara, K. Kaeriyama, K. Okamoto and M. Takahashi, *Polymer*, 2000, **41**, 5165-5171.
59. M. Hu, Y. Xia, G. B. McKenna, J. A. Kornfield and R. H. Grubbs, *Macromolecules*, 2011, **44**, 6935-6943.
60. Y. Xia, Y. Li, A. O. Burts, M. F. Ottaviani, D. A. Tirrell, J. A. Johnson, N. J. Turro and R. H. Grubbs, *J. Amer. Chem. Soc.*, 2011, **133**, 19953-19959.
61. S. S. Sheiko, B. S. Sumerlin and K. Matyjaszewski, *Prog. Polym. Sci.*, 2008, **33**, 759-785.
62. M. Zhang and A. H. Müller, *J. Polym. Sci., Part A: Polym. Chem.*, 2005, **43**, 3461-3481.
63. Y. Tsukahara, K. Tsutsumi, Y. Yamashita and S. Shimada, *Macromolecules*, 1990, **23**, 5201-5208.
64. S. Sheiko, M. Gerle, K. Fischer, M. Schmidt and M. Möller, *Langmuir*, 1997, **13**, 5368-5372.
65. P. Dziezok, K. Fischer, M. Schmidt, S. S. Sheiko and M. Möller, *Angew. Chem. Int. Ed.*, 1997, **36**, 2812-2815.
66. Y. Xia, J. A. Kornfield and R. H. Grubbs, *Macromolecules*, 2009, **42**, 3761-3766.
67. D. Grande, J. L. Six, S. Breunig, V. Héroguez, M. Fontanille and Y. Gnanou, *Polym. Adv. Technol.*, 1998, **9**, 601-612.
68. K. Nomura, S. Takahashi and Y. Imanishi, *Macromolecules*, 2001, **34**, 4712-4723.
69. S. Jha, S. Dutta and N. B. Bowden, *Macromolecules*, 2004, **37**, 4365-4374.
70. A. Li, J. Ma, G. Sun, Z. Li, S. Cho, C. Clark and K. L. Wooley, *J. Polym. Sci., Part A: Polym. Chem.*, 2012, **50**, 1681-1688.
71. C. Cheng and N.-L. Yang, *Macromolecules*, 2010, **43**, 3153-3155.
72. M. Schappacher and A. Deffieux, *Macromolecules*, 2005, **38**, 7209-7213.
73. Y. Yan, Y. Shi, W. Zhu and Y. Chen, *Polymer*, 2013, **54**, 5634-5642.
74. H. Gao and K. Matyjaszewski, *J. Amer. Chem. Soc.*, 2007, **129**, 6633-6639.
75. A. C. Engler, H. i. Lee and P. T. Hammond, *Angew. Chem.*, 2009, **121**, 9498-9502.
76. A. Nese, Y. Kwak, R. Nicolaÿ, M. Barrett, S. S. Sheiko and K. Matyjaszewski, *Macromolecules*, 2010, **43**, 4016-4019.
77. H.-i. Lee, W. Jakubowski, K. Matyjaszewski, S. Yu and S. S. Sheiko, *Macromolecules*, 2006, **39**, 4983-4989.
78. D. Neugebauer, B. S. Sumerlin, K. Matyjaszewski, B. Goodhart and S. S. Sheiko, *Polymer*, 2004, **45**, 8173-8179.

79. B. S. Sumerlin, D. Neugebauer and K. Matyjaszewski, *Macromolecules*, 2005, **38**, 702-708.
80. K. L. Beers, S. G. Gaynor, K. Matyjaszewski, S. S. Sheiko and M. Möller, *Macromolecules*, 1998, **31**, 9413-9415.
81. D. Neugebauer, *Polymer*, 2015, **72**, 412-421.
82. D. Neugebauer, K. Matyjaszewski, M. Da Silva and S. S. Sheiko, *ACS Polym. Prepr.*, 2002, **43**, 239-240.
83. D. Wu, X. Song, T. Tang and H. Zhao, *J. Polym. Sci., Part A: Polym. Chem.*, 2010, **48**, 443-453.
84. T. Krivorotova, J. Jonikaite-Svegzdiene, P. Radzevicius and R. Makuska, *React. Funct. Polym.*, 2014, **76**, 32-40.
85. X. Lian, D. Wu, X. Song and H. Zhao, *Macromolecules*, 2010, **43**, 7434-7445.
86. Z. Zheng, J. Ling and A. H. Müller, *Macromol. Rapid Commun.*, 2014, **35**, 234-241.
87. M. Semsarilar, V. Ladmiral and S. Perrier, *J. Polym. Sci., Part A: Polym. Chem.*, 2010, **48**, 4361-4365.
88. Y. Wang, Z. Zheng, Z. Huang and J. Ling, *Polymer Chemistry*, 2017, **8**, 2659-2665.
89. K. J. Arrington and J. B. Matson, *Polymer Chemistry*, 2017, **8**, 7452-7456.
90. S. Shanmugam, J. Cuthbert, T. Kowalewski, C. Boyer and K. Matyjaszewski, *Macromolecules*, 2018, **51**, 7776-7784.
91. Z. Li, J. Ma, C. Cheng, K. Zhang and K. L. Wooley, *Macromolecules*, 2010, **43**, 1182-1184.
92. J. Bolton and J. Rzayev, *Macromolecules*, 2014, **47**, 2864-2874.
93. V. Heroguez, E. Amedro, D. Grande, M. Fontanille and Y. Gnanou, *Macromolecules*, 2000, **33**, 7241-7248.
94. G. Cheng, A. Böker, M. Zhang, G. Krausch and A. H. Müller, *Macromolecules*, 2001, **34**, 6883-6888.
95. M. Zhang, T. Breiner, H. Mori and A. H. Müller, *Polymer*, 2003, **44**, 1449-1458.
96. H. G. Börner, K. Beers, K. Matyjaszewski, S. S. Sheiko and M. Möller, *Macromolecules*, 2001, **34**, 4375-4383.
97. A. Li, Z. Li, S. Zhang, G. Sun, D. M. Policarpio and K. L. Wooley, *ACS Macro Letters*, 2011, **1**, 241-245.
98. S. Qin, K. Matyjaszewski, H. Xu and S. S. Sheiko, *Macromolecules*, 2003, **36**, 605-612.
99. W. F. Daniel, G. Xie, M. Vatankhah Varnoosfaderani, J. Burdynska, Q. Li, D. Nykypanchuk, O. Gang, K. Matyjaszewski and S. S. Sheiko, *Macromolecules*, 2017, **50**, 2103-2111.
100. T. Pelras, C. S. Mahon and M. Müllner, *Angew. Chem. Int. Ed.*, 2018, **57**, 6982-6994.
101. R. Verduzco, X. Li, S. L. Pesek and G. E. Stein, *Chem. Soc. Rev.*, 2015, **44**, 2405-2420.
102. M. Müllner and A. H. Müller, *Polymer*, 2016, **98**, 389-401.
103. Y. Wu, Q. Tang, M. Zhang, Z. Li, W. Zhu and Z. Liu, *Polymer*, 2018, **143**, 190-199.
104. J. M. Bak, G. Jha, E. Ahn, S.-H. Jung, H. M. Jeong, B.-S. Kim and H. Lee, *Polymer*, 2012, **53**, 3462-3468.
105. S. J. Lord, S. S. Sheiko, I. LaRue, H.-I. Lee and K. Matyjaszewski, *Macromolecules*, 2004, **37**, 4235-4240.

106. J. Burdyńska, W. Daniel, Y. Li, B. Robertson, S. S. Sheiko and K. Matyjaszewski, *Macromolecules*, 2015, **48**, 4813-4822.
107. J. Bolton and J. Rzayev, *ACS Macro Letters*, 2011, **1**, 15-18.
108. J. Rzayev, *Macromolecules*, 2009, **42**, 2135-2141.
109. M. Xie, J. Dang, H. Han, W. Wang, J. Liu, X. He and Y. Zhang, *Macromolecules*, 2008, **41**, 9004-9010.
110. K. Huang, D. P. Canterbury and J. Rzayev, *Macromolecules*, 2010, **43**, 6632-6638.
111. S. S. Sheiko and M. Möller, *Chem. Rev.*, 2001, **101**, 4099-4124.
112. J. Seog, D. Dean, A. Plaas, S. Wong-Palms, A. Grodzinsky and C. Ortiz, *Macromolecules*, 2002, **35**, 5601-5615.
113. J. Burdynska, Y. Li, A. V. Aggarwal, S. Höger, S. S. Sheiko and K. Matyjaszewski, *J. Amer. Chem. Soc.*, 2014, **136**, 12762-12770.
114. P. J. Stals, Y. Li, J. Burdyńska, R. Nicolaÿ, A. Nese, A. R. Palmans, E. Meijer, K. Matyjaszewski and S. S. Sheiko, *J. Amer. Chem. Soc.*, 2013, **135**, 11421-11424.
115. S. S. Sheiko, M. da Silva, D. Shirvaniants, I. LaRue, S. Prokhorova, M. Moeller, K. Beers and K. Matyjaszewski, *J. Amer. Chem. Soc.*, 2003, **125**, 6725-6728.
116. M. Schappacher and A. Deffieux, *Science*, 2008, **319**, 1512-1515.
117. Y. Xia, A. J. Boydston and R. H. Grubbs, *Angew. Chem. Int. Ed.*, 2011, **50**, 5882-5885.
118. S. S. Sheiko, F. C. Sun, A. Randall, D. Shirvanyants, M. Rubinstein, H. Lee and K. Matyjaszewski, *Nature*, 2006, **440**, 191-194.
119. I. Park, A. Nese, J. Pietrasik, K. Matyjaszewski and S. S. Sheiko, *J. Mater. Chem.*, 2011, **21**, 8448-8453.
120. Z. Zheng, M. Müllner, J. Ling and A. H. Müller, *ACS nano*, 2013, **7**, 2284-2291.
121. S. L. Pesek, X. Li, B. Hammouda, K. Hong and R. Verduzco, *Macromolecules*, 2013, **46**, 6998-7005.
122. S. Rathgeber, T. Pakula, A. Wilk, K. Matyjaszewski and K. L. Beers, *Jour. Chemical Physics*, 2005, **122**, 124904.
123. S. Rathgeber, T. Pakula, A. Wilk, K. Matyjaszewski, H.-I. Lee and K. L. Beers, *Polymer*, 2006, **47**, 7318-7327.
124. I. Potemkin, A. Khokhlov and P. Reineker, *Euro. Physic. Jour. E*, 2001, **4**, 93-101.
125. T. Birshtein, O. Borisov, Y. B. Zhulina, A. Khokhlov and T. Yurasova, *Polymer Science USSR*, 1987, **29**, 1293-1300.
126. A. Steinhaus, T. Pelras, R. Chakroun, A. H. Gröschel and M. Müllner, *Macromol. Rapid Commun.*, 2018, **39**, 1800177.
127. M. B. Runge, C. E. Lipscomb, L. R. Ditzler, M. K. Mahanthappa, A. V. Tivanski and N. B. Bowden, *Macromolecules*, 2008, **41**, 7687-7694.
128. Y. Xia, B. D. Olsen, J. A. Kornfield and R. H. Grubbs, *J. Amer. Chem. Soc.*, 2009, **131**, 18525-18532.
129. K. Kawamoto, M. Zhong, K. R. Gadelrab, L.-C. Cheng, C. A. Ross, A. Alexander-Katz and J. A. Johnson, *J. Amer. Chem. Soc.*, 2016, **138**, 11501-11504.
130. D.-P. Song, T. H. Zhao, G. Guidetti, S. Vignolini and R. M. Parker, *ACS nano*, 2019.
131. M. B. Runge and N. B. Bowden, *J. Amer. Chem. Soc.*, 2007, **129**, 10551-10560.
132. G. M. Miyake, V. A. Piunova, R. A. Weitekamp and R. H. Grubbs, *Angew. Chem. Int. Ed.*, 2012, **51**, 11246-11248.

133. B. R. Sveinbjörnsson, R. A. Weitekamp, G. M. Miyake, Y. Xia, H. A. Atwater and R. H. Grubbs, *Proceedings of the National Academy of Sciences*, 2012, **109**, 14332-14336.
134. G. M. Miyake, R. A. Weitekamp, V. A. Piunova and R. H. Grubbs, *J. Amer. Chem. Soc.*, 2012, **134**, 14249-14254.
135. Y. Shi, W. Zhu, D. Yao, M. Long, B. Peng, K. Zhang and Y. Chen, *ACS Macro Letters*, 2013, **3**, 70-73.
136. H. Luo, J. L. Santos and M. Herrera-Alonso, *Chem. Commun.*, 2014, **50**, 536-538.
137. R. Fenyves, M. Schmutz, I. J. Horner, F. V. Bright and J. Rzayev, *J. Amer. Chem. Soc.*, 2014, **136**, 7762-7770.
138. L. Su, G. S. Heo, Y. N. Lin, M. Dong, S. Zhang, Y. Chen, G. Sun and K. L. Wooley, *J. Polym. Sci., Part A: Polym. Chem.*, 2017, **55**, 2966-2970.
139. M. Müllner, *Macromol. Chem. Phys.*, 2016, **217**, 2209-2222.
140. B. Xu, G. Gu, C. Feng, X. Jiang, J. Hu, G. Lu, S. Zhang and X. Huang, *Polymer Chemistry*, 2016, **7**, 613-624.
141. H. Unsal, S. Onbulak, F. Calik, M. Er-Rafik, M. Schmutz, A. Sanyal and J. Rzayev, *Macromolecules*, 2017, **50**, 1342-1352.
142. T.-H. Tran, C. T. Nguyen, L. Gonzalez-Fajardo, D. Hargrove, D. Song, P. Deshmukh, L. Mahajan, D. Ndaya, L. Lai and R. M. Kasi, *Biomacromolecules*, 2014, **15**, 4363-4375.
143. J. A. Johnson, Y. Y. Lu, A. O. Burts, Y. Xia, A. C. Durrell, D. A. Tirrell and R. H. Grubbs, *Macromolecules*, 2010, **43**, 10326-10335.
144. J. Guo, H. Hong, G. Chen, S. Shi, T. R. Nayak, C. P. Theuer, T. E. Barnhart, W. Cai, S. Gong, *ACS Appl. Mat. Int.*, 2014, **6**, 21769-21779.
145. J. Zou, Y. Yu, Y. Li, W. Ji, C.-K. Chen, W.-C. Law, P. N. Prasad and C. Cheng, *Biomaterials science*, 2015, **3**, 1078-1084.
146. Y. Yu, C.-K. Chen, W.-C. Law, J. Mok, J. Zou, P. N. Prasad and C. Cheng, *Mol. Pharm.*, 2012, **10**, 867-874.
147. H. Luo, M. Szymusiak, E. A. Garcia, L. L. Lock, H. Cui, Y. Liu and M. Herrera-Alonso, *Macromolecules*, 2017, **50**, 2201-2206.
148. P. Zhao, L. Liu, X. Feng, C. Wang, X. Shuai and Y. Chen, *Macromol. Rapid Commun.*, 2012, **33**, 1351-1355.
149. Y. Huang, L. Li and Y. e. Fang, *J. Mater. Sci. Mater. Med.*, 2010, **21**, 557-565.
150. C. Yang, S. Huang, X. Wang and M. Wang, *Polymer Chemistry*, 2016, **7**, 7455-7468.
151. M. A. Sowers, J. R. McCombs, Y. Wang, J. T. Paletta, S. W. Morton, E. C. Dreaden, M. D. Boska, M. F. Ottaviani, P. T. Hammond and A. Rajca, *Nature Comm.*, 2014, **5**, 5460.
152. M. Müllner, T. Lunkenbein, M. Schieder, A. H. Gröschel, N. Miyajima, M. Förtsch, J. Breu, F. Caruso and A. H. Müller, *Macromolecules*, 2012, **45**, 6981-6988.
153. M. Müllner, J. Yuan, S. Weiss, A. Walther, M. Förtsch, M. Drechsler and A. H. Müller, *J. Amer. Chem. Soc.*, 2010, **132**, 16587-16592.
154. R. Djalali, S.-Y. Li and M. Schmidt, *Macromolecules*, 2002, **35**, 4282-4288.
155. M. Müllner, T. Lunkenbein, J. Breu, F. Caruso and A. H. Müller, *Chem. Mater.*, 2012, **24**, 1802-1810.

156. L. Xiao, L. Qu, W. Zhu, Y. Wu, Z. Liu and K. Zhang, *Macromolecules*, 2017, **50**, 6762-6770.
157. S. Onbulak and J. Rzayev, *Polymer Chemistry*, 2015, **6**, 764-771.
158. K. Huang, A. Jacobs and J. Rzayev, *Biomacromolecules*, 2011, **12**, 2327-2334.

Chapter 2

The RAFT ‘grafting from’ shuttle CTA approach as a means to access complex bottle-brush polymeric architectures

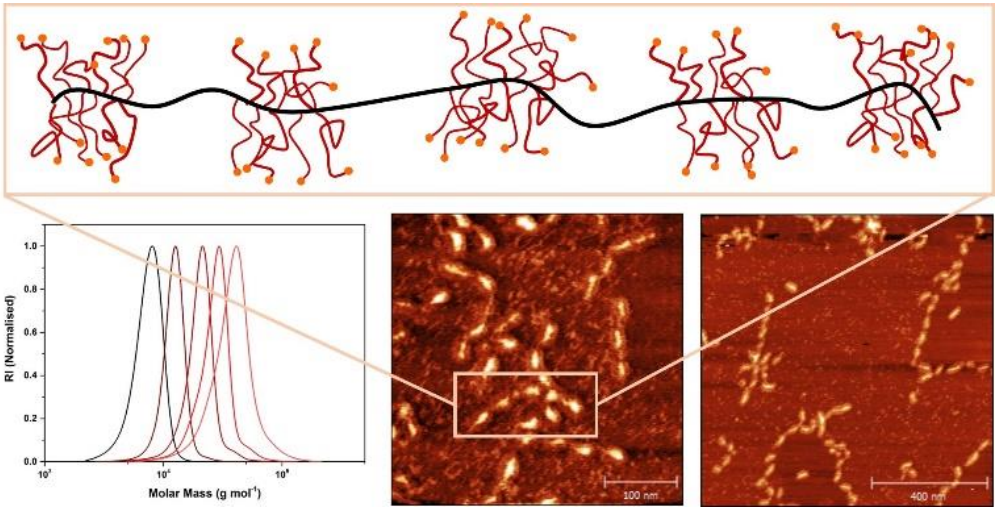

Molecular bottle-brush polymers are promising materials for a number of applications, however, their synthesis via RAFT has been seldom used. In this chapter the RAFT polymerization R-group grafting from approach with addition of CTA ‘shuttle’ is used to access densely grafted bottle-brush copolymers with excellent control. The synthesis of unique multiblock brush polymeric architectures is investigated with this approach. The combination of this technique with RAFT acrylamide multiblock methodology allows high monomer conversions to be achieved with minimal brush-brush coupling terminations, therefore block copolymer grafted side chains can be synthesised in a one-pot process. Instalment of non-functional linker blocks into the backbone gives microstructure control to yield multi-segmented bottle-brushes. The use of both approaches is demonstrated to access highly complex brush macromolecules, incorporating multiblocks along both the polymer backbone and grafted side chains.

2.1 Introduction

The high versatility and functionality of biological macromolecules such as proteins or DNA is ultimately a result of the perfect control over the sequence of these polymers.[160] As synthetic chemists strive to mimic this feature, the control of monomer sequence in synthetic polymers has attracted increasing interest in recent years, as the arrangement of monomer units has a fundamental effect on the properties and functions of the material.[37] The development of new methodologies to yield sequence controlled polymers or multiblock copolymers has brought the scientific community closer to mimicking the high structural control nature demonstrates. In particular, RDRP techniques have proven to be versatile and effective for the synthesis of complex polymeric architectures such as star[40, 161], graft[50, 54] and multiblocks.[43, 44, 162] While synthetic precision to the extent of proteins is still unattainable, RDRP may be useful for filling a niche between low fidelity free radical derived materials and truly sequence controlled macromolecules. An interesting example of biomacromolecules with a complex structure required for their functionality are mucins, which exhibit a bottle-brush architecture and are responsible for a range of tasks including lubrication.[163-166] Recent work has attempted to mimic these biological structures with synthetic molecular bottle-brushes, often by incorporation of linear ungrafted blocks which possess surface affinity.[167, 168]

There are three approaches to synthesize bottle-brush polymers – 'grafting to', 'grafting through' and 'grafting from'. Each method entails advantages and limitations, however the grafting from technique is arguably the most versatile, as high molecular weight backbones and high grafting densities can be accessed.[62, 102] A range of polymerisation techniques and combinations have been used,[81, 111, 169-172] of which ATRP has been used most extensively,[62, 82] with fewer examples in literature utilising RAFT (Figure 2.1).[77] The 'grafting from' approach using a radical polymerisation technique is inherently challenging due to the inevitability of bimolecular terminations, which can rapidly lead to gelation if occurring between large bottle-brush macromolecules. To avoid this issue low monomer concentrations and conversions are typically required.[81] An initial report by Muller et al demonstrated the use of the shuttle CTA RAFT grafting from approach to be an effective technique for bottle-brush synthesis.[87]

The use of controlled polymerisation techniques enables the dimensions and structure of bottle-brushes to be precisely altered by changing parameters such as backbone length,

side chain length, grafting density and chemical composition.[123] Techniques to control the sequence of the backbone in bottle-brush polymer synthesis offers another aspect for modification of the macromolecular architecture of brush copolymers. Alternating copolymerisation of maleimide / maleic anhydride with styrene derivatives has been employed in the synthesis of several graft copolymer systems.[56, 173] This method offers a lower grafting density combined with sequence regulation that cannot be achieved by statistical copolymerisation. The radical copolymerisation of terpene and maleimide derivatives in fluorinated alcoholic solvents has also been used to yield 1:2 or 2:1 sequence regulated graft copolymers[174] and the alternating anionic copolymerisation of 1,1-diphenylethylene derivatives and styrene in various feeding ratios was utilised to synthesise sequence-determined bottle-brushes.[175]

For biomimetic lubricant applications a triblock copolymer ABA backbone where 'B' is the bottle-brush block and 'A' is a polymer with a strong surface affinity has been identified to possess excellent lubrication properties,[168] and in a different report using a RAFT based approach a penta-block backbone bottle-brush was synthesised.[85] While these examples demonstrate the potential of RDRP techniques in this context, they are still far away from the structural complexity of mucins.[176]

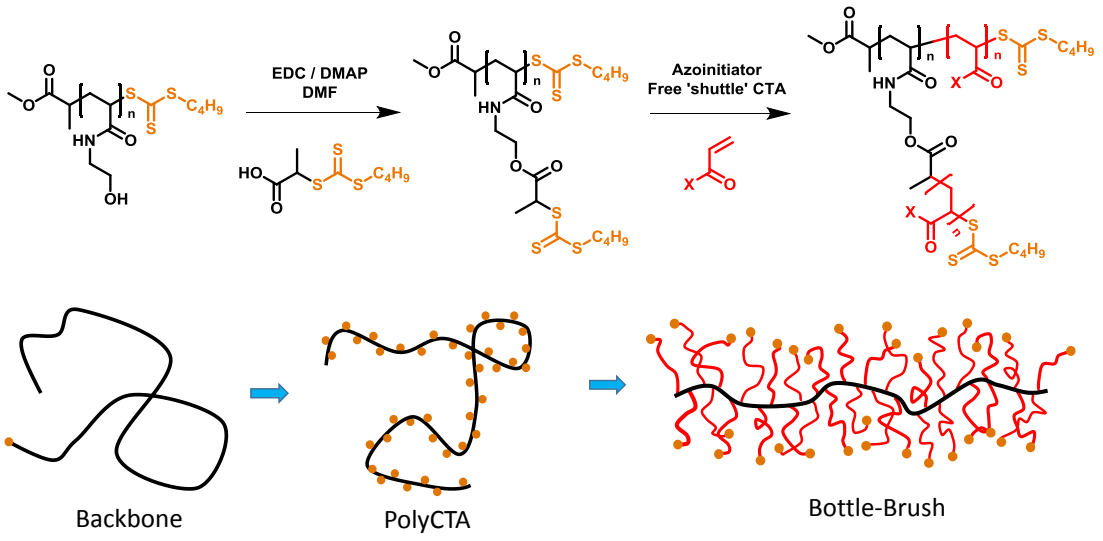

Figure 2.1: The RAFT 'R' group grafting from approach to graft polymer synthesis involving three steps – polymerisation of the backbone, modification of monomer units with CTA and thirdly the grafting from polymerisation.

As shown by the Perrier group, the RAFT process is highly suitable for the synthesis of multiblock copolymers, especially when acrylamide monomers are used in aqueous

conditions. By exploiting the high propagation rate of these monomers, quantitative conversions after short reaction times are possible and thus one-pot multiblock synthesis is feasible. The one-pot methodology avoids time consuming purification steps and even challenging dodecablock structures can be synthesised in under 24h.[177]

Within this chapter, firstly the reported shuttle CTA procedure is modified to be used with polyacrylamide based backbones (Figure 2.1). This enables much longer bottle-brushes to be accessed and during this the shuttle CTA process is optimised to take advantage of the improvement in control offered. Then the utilisation of this technique for the synthesis of complex bottle brush architectures using RAFT polyacrylamide multiblock methodology is shown. The incorporation of multiblocks in either the backbone or side chain of a brush polymer is demonstrated. Control of the microstructure can be achieved by creating brush segments placed at precise locations in the linear backbone, separated by non-functional monomer blocks mimicking the structure of naturally occurring lubricants. Alternatively the introduction of multiblock side chains is demonstrated to create a core-shell like structure with multiple layers. Finally, the combination of both approaches gives rise to a multi segmented macromolecule with 29 separate polymeric domains.

2.2 Results and discussion

2.2.1 Synthesis of poly(hydroxyethylacrylamide) backbones

Firstly the optimisation of the polymerisation of hydroxethylacrylamide (HEAm) was investigated with the aim of reaching relatively high molecular weights in order to enable the synthesis of long cylindrically shaped bottle-brushes. Initially polymerisations were mediated with CTA Acid, a compound produced by Lubrizol on a tonne scale. Polymerisations of acrylamide monomers are known to proceed faster under aqueous conditions and therefore initial experiments were performed in water to attempt to access the highest molecular weight backbones possible, while also offering the advantage of being a green, non-toxic solvent. In the case of CTA Acid the C12 alkyl chain leads to poor aqueous solubility, however, upon deprotonation of the carboxylic acid in basic conditions at elevated temperatures, the solubility is high, although a surfactant effect causes effervescence during the degassing step pre-reaction. The azo initiator azobis-cyanovaleric acid (ACVA) was selected for its solubility in basic aqueous conditions.

At monomer concentrations of 2 M, almost quantitative monomer conversions were obtained in 5 h reaction time at 70 °C, yielding polymers of narrow dispersity (<1.2) from DP100 – 500 (Figure 2A). Targeting higher DPs of 1000 / 4000 causes a large increase in dispersity up to values of ~1.7, this loss of control is attributed to the decreased CTA / I ratio (2 and 0.5 respectively) and thus chain end livingness for these reactions. Across the experiments the initiator concentration was kept constant to ensure similar kinetics, therefore for the high DP polymerisations where the CTA concentration is very low, the number of terminated chains is comparatively high (Table 2.1). The low CTA concentration may also lead to a lower effective chain transfer rate which would contribute to increasing dispersity. While the polymerisations could be controlled, the acid functional end group may lead to side reactions in the subsequent esterification step and therefore a CTA with a methyl ester protecting group would be preferable. The use of PMBTC was studied as the shorter C4 Z-group allowed mixtures of water/dioxane to be used as solvent for polymerisation, whereas the C12 alkyl chain with an ester R group offered no solubility under such conditions.

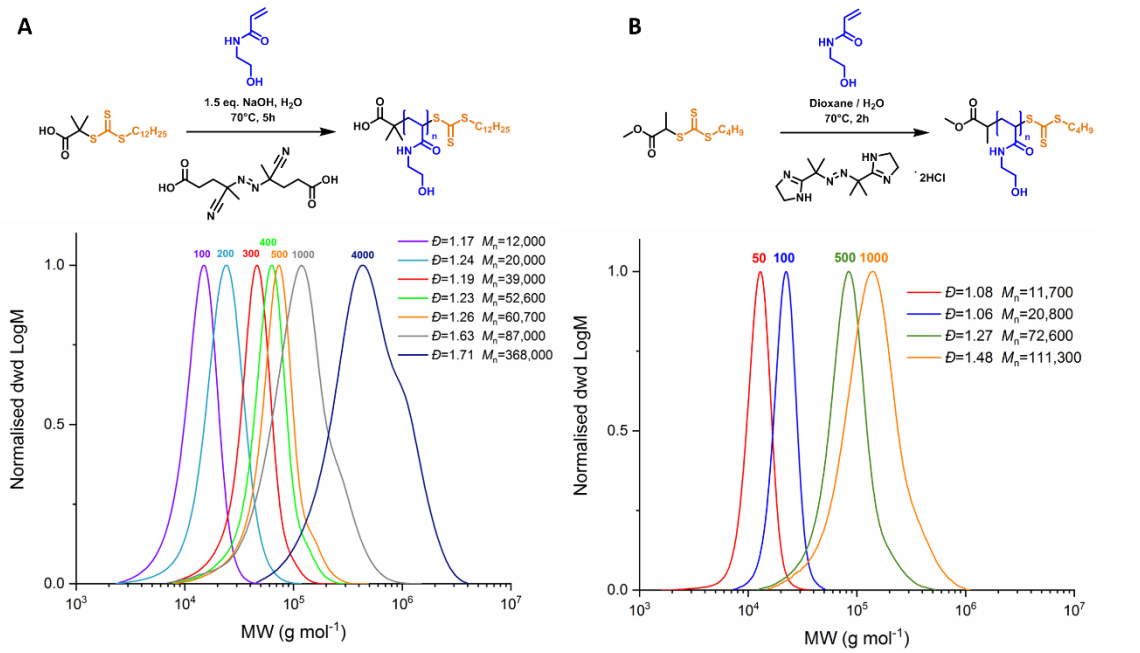

Figure 2.2: Schemes and SEC molecular weight distributions for PHEAm backbones synthesised by RAFT. SEC performed in DMF eluent conditions, number above SEC trace designates target DP. A – CTA Acid controlled polymerisations targeting DPs between 100 – 4000 in H_2O at 2M monomer concentration. B – PMBTC controlled polymerisations targeting DPs between 50 – 1000 in dioxane/H_2O at 2M monomer concentration.

The use of azo initiator VA-044 with a calculated half-life of 15 minutes at 70°C allows for rapid polymerisation reactions of 2h to full monomer conversion with the use of PMBTC (Figure 2.2B). This azoinitiator is insoluble under basic conditions and therefore could not be used in combination with the previously described CTA Acid mediated polymerisations. Narrower dispersities were obtained through this methodology although the same trend of increasing PDI with targeted MW was observed. The fast reaction times provided convenient synthesis of polymeric backbones in partially aqueous conditions up to DP1000, with the ester end group reducing likelihood of side reactions in the post-polymerisation functionalisation.

Table 2.1: Polymerisation conditions for PHEAm backbones, M_n and $Đ$ determined by DMF SEC.

Entry	Target DP	CTA	Solvent	Initiator	T (°C)	Time	CTA:I	Conv. (%)	$M_{n\ theo}$ ($gmol^{-1}$)	$M_{n\ sec}$ ($gmol^{-1}$)	$Đ$
1	100	CTA Acid	H_2O	ACVA	70	5h	20	98	11,900	12,000	1.17
2	200	CTA Acid	H_2O	ACVA	70	5h	10	>99	23,400	20,000	1.24
3	300	CTA Acid	H_2O	ACVA	70	5h	6.6	>99	34,900	39,000	1.19
4	400	CTA Acid	H_2O	ACVA	70	5h	5	99	46,400	53,000	1.23
5	500	CTA Acid	H_2O	ACVA	70	5h	4	95	57,900	61,000	1.26
6	1000	CTA Acid	H_2O	ACVA	70	5h	2	>99	115,000	87,000	1.63
7	4000	CTA Acid	H_2O	ACVA	70	5h	0.5	98	460,000	368,000	1.71
8	50	PMBTC	H_2O/Dioxane	VA-044	70	2h	80	98	6,000	11,700	1.08
9	100	PMBTC	H_2O/Dioxane	VA-044	70	2h	40	97	11,900	20,800	1.06
10	500	PMBTC	H_2O/Dioxane	VA-044	70	2h	8	99	57,900	72,600	1.27
11	1000	PMBTC	H_2O/Dioxane	VA-044	70	2h	5	98	115,000	111,300	1.48

The molecular weights, as determined by SEC against linear calibration standards, were significantly higher for the PMBTC derived polymers than the $M_{n\ theo}$ (Table 2.1). This trend of overestimated $M_{n\ SEC}$ was found in future work using PHEAm and is likely an effect of substantial difference in hydrodynamic volume of the highly polar PHEAm compared to the calibration standards. In the case of the initial CTA Acid mediated polymerisations, however, lower $M_{n\ SEC}$ values very close to the $M_{n\ theo}$ were obtained. These differences could potentially be explained from variations in performance of the SEC instrument across different column calibrations at which the two sets of reactions were performed. Otherwise it is perhaps a result of the observed surfactant effect, where the assembly of deprotonated CTA Acid molecules into micelles may affect its chain transfer constant and thus lead to variations in the obtained $\underline{M}_n$. Due to the preference of using an ester protected CTA this effect was not studied in more detail.

2.2.2 Functionalisation of PHEAm backbone with CTA units

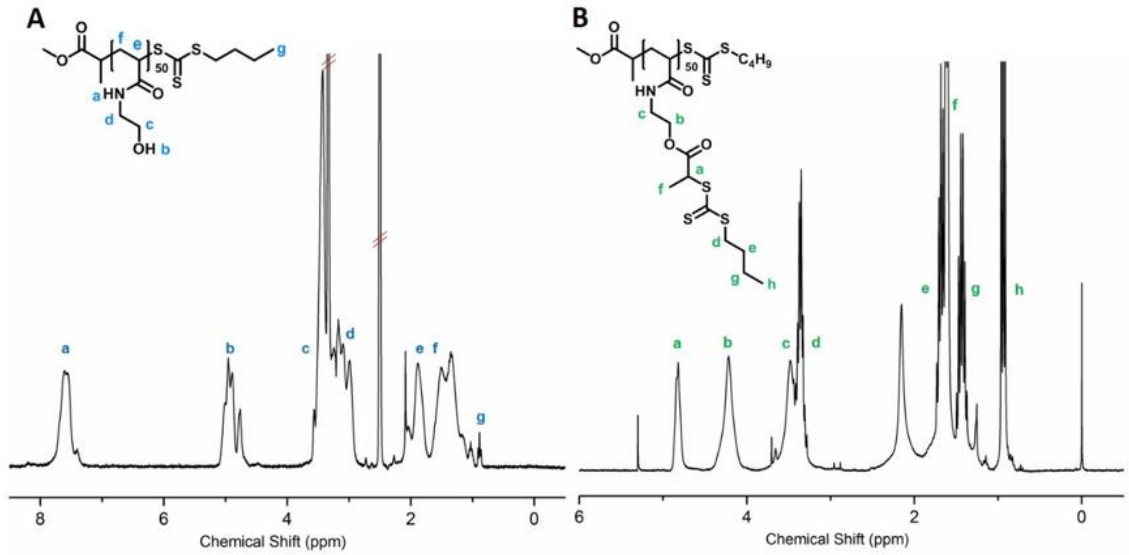

Figure 2.3: ^{1}H-NMR spectrum in DMSO-d_6 of the DP50 PHEAm (**A**) and ^{1}H NMR spectrum in $CDCl_3$ of the functionalised PolyCTA backbone (**B**).

In the next step the pendant alcohol units of the monomer were functionalised with PABTC *via* EDC / DMAP catalysed Steglich esterification. An excess of 1.5 eq. PABTC with respect to the alcohol units was used to drive the reaction to high conversion, confirmed by ^{1}H NMR analysis showing almost quantitative consumption of the alcohol peak at ~5.0 ppm with the presence of CH_2 ester at 4.2 ppm and CH of CTA units at 4.8 ppm in the product PolyCTA NMR (Figure 2.3). Additionally elemental analysis was consistent with the introduction of 3 sulphur atoms per monomer unit.

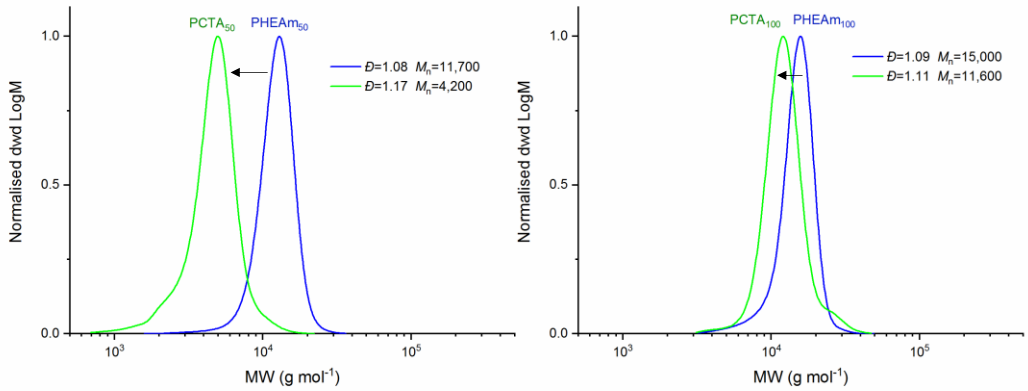

Figure 2.4: DMF SEC molecular weight distributions of backbones before and after modification with PABTC.

In SEC a shift to higher MW is expected after reaction, however for the DP50 / 100 backbones DMF SEC analysis actually shows a longer retention time post-modification

(Figure 2.4). Such a result is plausible considering the large change in polarity from the hydrophilic PHEAm to the hydrophobic butyl trithiocarbonate PolyCTA which will lead to different solubility of the polymer in DMF and thus varying hydrodynamic radius, the actual parameter measured by SEC. Presumably the hydrophobic PolyCTA has stronger polymer-polymer interactions than with solvent, causing the molecule to adopt a more tightly coiled conformation in solution perhaps driven by internal hydrogen bonding of amide units in the backbone.

Triple detection SEC is a technique that combines the usage of refractive index (RI), light scattering and viscosity detectors to obtain more accurate MW measurements and further information on polymer properties. The measurement of RI functions as a concentration detector with a response proportional to the refractive index increment (dn/dc) of the sample, while light scattering detectors enable determination of MW without the need to compare with calibration standards which are frequently of a different chemical composition to the sample of interest. Calculation of this molar mass is also reliant on an accurate value of dn/dc, which can be measured by the SEC instrument directly by injection of a sample of precisely known concentration, assuming full recovery of the sample though filtration and column elution. The SEC instrument is equipped with dual angle (15° and 90°) light scattering detectors which is important for the assessment of the angular dependence for larger polymers of R_g >~10 nm. Viscosity detectors can be utilised to elucidate polymer conformation and the extent of branching architectures through the Mark-houwink equation and also provides a method of R_h measurement. By combination with the R_g determined from light scattering, triple detection can therefore give detailed structural information in addition to improved MW measurements. The DP50 PolyCTA was analysed by triple detection SEC through which a non-relative MW was determined (Table 2.2), which does indeed corroborate with an increase in MW of the PolyCTA in addition to NMR spectroscopy which unambiguously confirms the success of the reaction.

Table 2.2: PolyCTA backbone samples used in this work, M_n and $Đ$ determined by DMF SEC against linear PMMA calibration standards.

Entry	Description	$M_{n\ theo}$ (gmol^{-1})	$M_{n\ sec}$ (gmol^{-1})	$M_{n\ DALS}$ (gmol^{-1})	$Đ$	dn/dc
12	$PCTA_{50}$	17,000	4,200	29,900	1.17	0.143
13	$PCTA_{100}$	33,800	11,600	-	1.11	-
14	$PCTA_{500}$	167,800	94,300	-	1.30	-
15	$PCTA_{1000}$	335,600	177,000	-	1.61	-

2.2.3 RAFT grafting from with shuttle CTA

The grafting from step was initially performed with 4-*N*,acryloylmorpholine (NAM) as monomer to synthesise bottle-brush polymers. Typically when using the grafting from, approach low monomer conversions over long reactions times are required to maintain low radical concentrations and thus minimise bimolecular terminations between bottle-brush macromolecules, which quickly leads to extensive cross-coupling. The high k_p of NAM allows for low initiator concentrations to be used which is particularly vital to reduce the number of termination events while also attaining near quantitative monomer conversions, an essential parameter for facile multiblock copolymer synthesis. In order to improve control of the polymerisation, the addition of free 'shuttle' CTA was investigated during this step.

Two kinetic experiments were performed, targeting a degree of polymerisation of 75 for the side chains in the presence and absence of shuttle CTA. 0.5 equivalents of shuttle CTA per grafted CTA were added while maintaining the same overall target DP. PABTC was used as the shuttle CTA which is identical to the grafted CTA and therefore should not display a difference in activation or chain transfer constant. Relatively high monomer concentrations of 2M (27 wt. %) were used. SEC analysis (Figure 2.5) of the polymerisation in absence of shuttle CTA shows the formation of a high molecular weight shoulder leading to substantial increase in dispersity once the monomer conversion exceeds ~70%. However, up to moderate conversions of ~50% the dispersity remains narrow and no high molecular weight shoulder is observed.

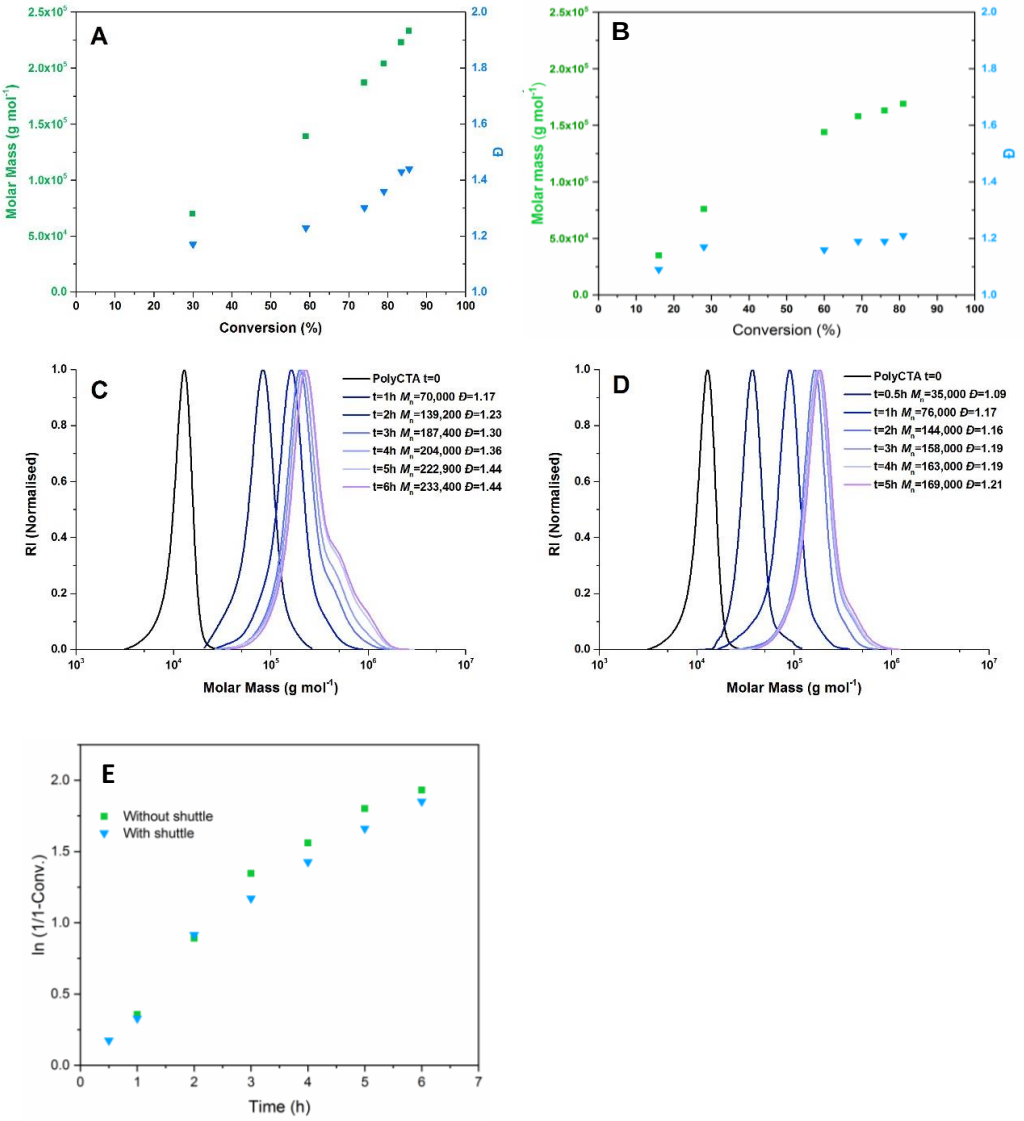

Figure 2.5: A & C – Kinetic plot and DMF SEC molecular weight distributions of grafting from polymerisation of NAM in absence of shuttle CTA. B & D Kinetic plot and DMF SEC traces of grafting from polymerisation of NAM in presence of 0.5 equivalents shuttle CTA. For clarity the linear shuttle CTA derived polymers have been omitted from the SEC trace, see Figure 2.7A for a representative SEC trace of both distributions. E – pseudo first order linear kinetic profile for reactions with and without shuttle CTA.

This degree of control is notably good considering the high monomer conversion achieved when compared to typical bottle brush grafting from procedures and even without the addition of shuttle CTA, the grafting from polymerisation is well controlled if full monomer consumption is not required. In the case of shuttle CTA addition, the distribution remains monomodal even when reaching full monomer conversion, however, an additional peak at low molecular weight is present which is attributed to the formation of a substantial amount of linear polymer (Figure 2.7A). The M_n of the linear shuttle CTA

derived chains is in good agreement the targeted side chain molecular weight and should represent the composition of the grafted side chains on the brush.

The addition of free shuttle CTA reduces the amount of cross coupling between brush macromolecules, however, it also leads to a substantial amount of linear polymer side product dependent on the equivalents added. It is worth noting that in a RAFT polymerisation process using an external source of initiating radicals, as in this case of thermally decomposing azo initiators, the initiator derived chains will be linear species unattached to the brush backbone and, as a result, linear polymer side products are always expected with the grafting from approach using RAFT[42] - the addition of shuttle CTA simply increases their quantity. The reduction of bimolecular termination of brush molecules appears to be mainly due to a dilution effect whereby having a linear polymer in solution reduces the likelihood of terminations occurring between brush macromolecules. In the absence of shuttle CTA, termination events of the bottle-brush side chain can occur either intramolecularly or intermolecularly, with only the latter leading to undesirable gelation (Figure 2.6).

In the shuttle CTA approach, additional routes of terminations involving linear/linear or brush/linear coupling can occur which also do not substantially affect the molecular weight of the bottle-brush compound. Therefore using shuttle CTA under equivalent conditions with the same radical production will lower the fraction of brush/brush coupling and thus improve control. As described in the work by Muller,[87] the free CTA may also perform a shuttling effect by aiding the transfer of radicals between brush macromolecules ensuring all CTAs are evenly activated and thus polymerise at the same rate. This may be expected to be particularly advantageous for bottle-brush synthesis due to the close packing of CTAs on the polymeric backbone leading to a very sterically hindered environment, which may reduce the rate of chain transfer and thus control of the polymerisation. However, for the system presented here, there is no substantial difference in dispersity of the main population of bottle-brushes synthesised with or without the shuttle CTA present and only a reduction in bimolecular termination is apparent. A similar improvement in control can be obtained by polymerising at low monomer concentrations and targeting low conversions. In this system the main advantage of the shuttle CTA technique is the ability to target quantitative monomer conversions in short

reaction times, allowing for convenient one pot multiblock polymerisations which would otherwise require time consuming purification steps between each block.

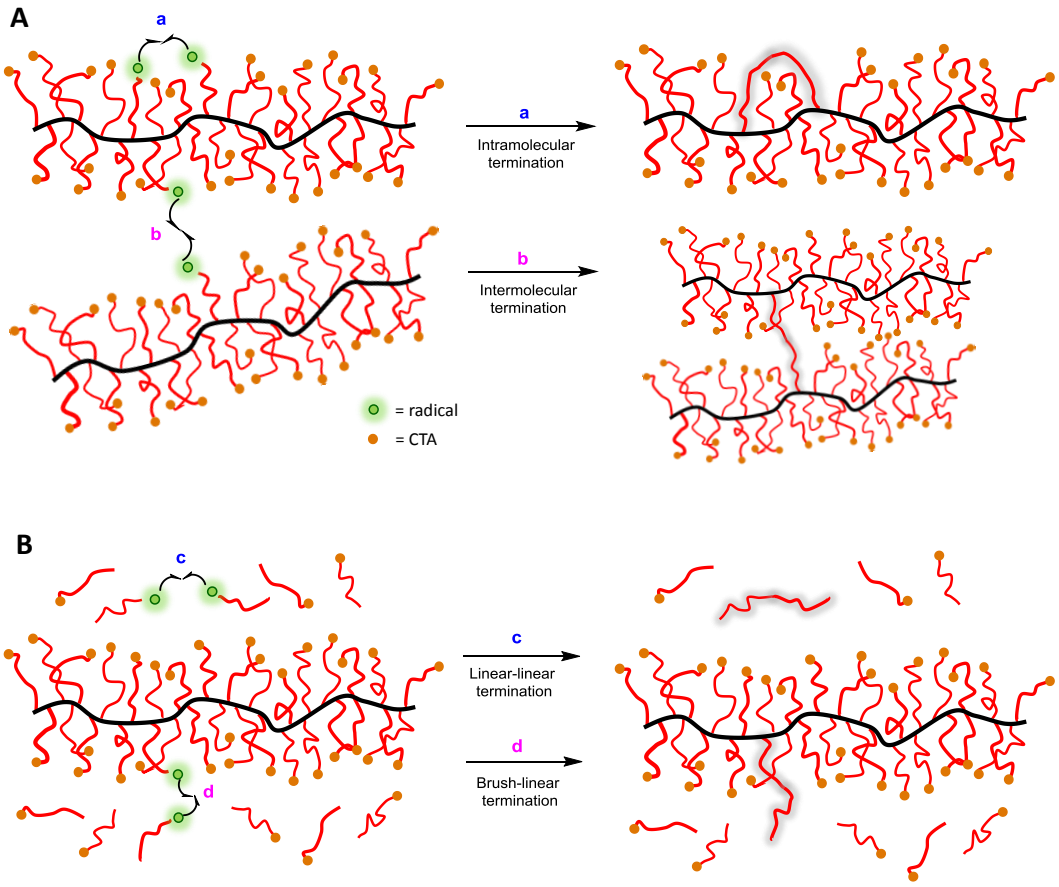

Figure 2.6: Possible termination steps in a grafting from polymerisation considering only bimolecular termination by recombination. A – Terminations for a standard R group RAFT grafting from polymerisation. B – Additional possible terminations during a shuttle CTA mediated grafting from procedure, these will occur in addition to those described in A.

Cleavage of the PNAM side chains from the bottle-brush backbone by hydrolysis of the ester linkage and subsequent SEC analysis of the polymer branches can be used to estimate the initiation efficiency of the PolyCTA.[80] Lower initiation efficiencies causes deviation of the side chain MW from the theoretical value – fewer side chains means each will be of a higher MW for a given monomer conversion. A $PNAM_{70}$ side chain bottle-brush was synthesised in absence of shuttle CTA to minimise the formation of linear chains which would interfere with analysis of the hydrolysed grafts (Figure 2.7B). The cleaved side chains gave $M_{n\ SEC}$ = 10,400, $Đ$ = 1.07, which is very close to $M_{n\ theo.}$ = 10,180, suggesting close to quantitative initiation efficiency. Analysis of PNAM homopolymers showed good agreement with $M_{n\ theo}$ and $M_{n\ SEC}$ using calibration against PMMA standards, so the quantification should be accurate. While the MWD of the main

brush peak may appear equivalent between the standard and shuttle CTA techniques, it is possible the dispersity of the side chains is better controlled under using the latter approach, however the narrow, PDI obtained even under standard conditions make this unlikely. This may be due to the relatively high monomer conversions achieved during these reactions which favour high initiation efficiency of CTA side groups - it is possible the shuttle CTA is more advantageous for side chain control under low monomer consumption conditions, although this is not explored here.

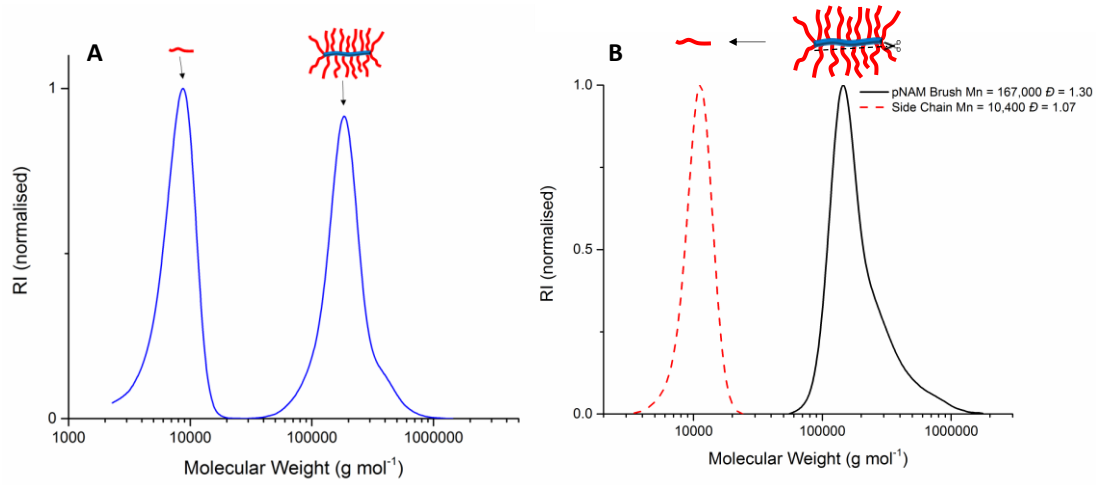

Figure 2.7: A – DMF SEC molecular weight distribution of a PNAM bottle-brush synthesised with addition of 1 equivalent shuttle CTA showing two separate species – the high MW bottle-brush and low MW linear polymer derived from the shuttle CTA. B – SEC trace of bottle-brush synthesised in absence of shuttle CTA, leading to a high molecular weight shoulder. The brush was hydrolysed to cleave side chains and analysed again by SEC.

2.2.4 Characterisation of bottle-brush architecture

The very large molecular weight, highly branched architecture and cylindrical conformation of bottle-brush polymers make them challenging to characterise with techniques such as SEC and DLS. Small angle neutron scattering (SANS) is a powerful technique that gives information on the size and shape of macromolecules in solution, and was used to confirm the structure of the synthesised bottle-brushes. Experimentally a neutron beam is passed through a dilute polymeric solution, where interactions of the neutron with the nuclei of the sample causes elastic scattering and the intensity is measured at varying angles. A deuterated solvent is typically used because the deuterium atom has a substantially larger scattering length density to that of hydrogen and therefore provides higher contrast between the solution and sample of interest than would be achieved by using a hydrogenated solvent.

Three bottle-brushes of varying molecular weights were analysed by this technique, two brushes of DP100 / 1000 backbone length with side chains of DP50 PHEAm (**16**, **17,** Table 3), and thirdly a DP500 backbone with DP20 side chains of the same monomer (**18**). These were prepared by the grafting from HEAm from the previously described PolyCTA samples with the corresponding backbone length, using ACVA as initiator in DMF. It is known that the length of the side chain is an integral factor for the adopted conformation of the bottle-brush, and a transition from a flexible comb to a stiff rod has been demonstrated upon increasing the molecular weight of the side chains due to excluded volume effects.[119] The increase in steric hindrance from lengthening the side chain from DP20 to 50 should therefore provide a measurable confirmation of this change.

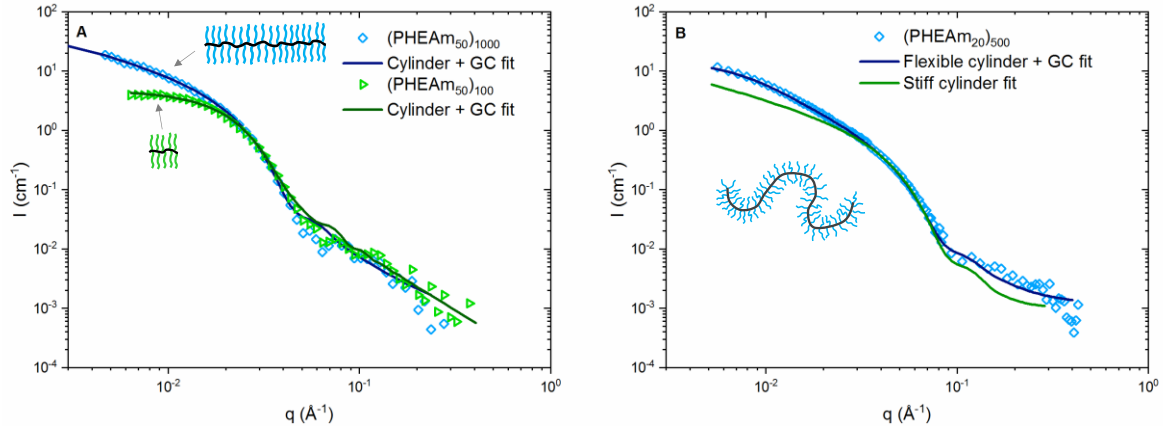

Figure 2.8: SANS data of A – brushes with DP50 side chains of DP100 and 1000 backbones fitted to a rigid cylinder model. B – DP500 backbone brush with DP20 side chains fitted to a flexible cylinder model.

The scattering vector 'q' is inversely proportional to the real-space intramolecular distances being probed, which can be considered the window of observation of the analysis. At high q values relating to a small window of observation, the individual side chains of the bottle-brush will be observed, which will produce a scattering response similar to a Gaussian polymer coil - although steric hindrance between chains means they are likely to be more extended than a typical linear polymer in solution. At low q values, however, the cylindrical conformation of the molecule will be observed. To account for both components the data was fitted to a model combining a cylindrical form factor with a Gaussian chain model. In the case of **16** and **17** the rigid cylindrical form factor model proves a good fit, as evidenced by the q^{-1} decay in scattering intensity at low q values, most evident for longer DP1000 brush (Figure 2.8), where the scattered intensity decay

of q^{-1} is characteristic of a stiff rod.[178] The fitted model proposes a similar radius of 7.5 – 8.0 nm for both compounds. For the DP100 backbone the model predicts a length of 21.5nm – considering the repeat unit of a monomer is 0.25nm in size, if the backbone is fully extended it should reach a maximum length of 25nm which is in reasonable agreement with the SANS determined value. Due to the configuration of the SANS instrument, the measurable q-range does not extend to small enough values to observe scattering corresponding to lengths of > 100 nm, therefore the precise length of the DP1000 sample could not be determined.

For sample **18** the profile does not display a q^{-1} relationship and instead changing to a flexible cylinder model produces a much improved fit to the experimental data, where the Kuhn length of 13.5 nm accounts for this change in conformation. As expected, a narrower radius of 4.3 nm is observed, correlating with the reduction in side chain length to DP20.

Table 2.3: Synthesised brush compounds, M_n and $Đ$ determined by DMF SEC. The PHEAm compounds were analysed by SANS and fitted with a combination of cylinder with gaussian chain models, the fitted parameters of cylinder radius, length, kuhn length and radius of gyration of the gaussian chain are shown in the table.

Entry	Description	$M_{n\ theo}$ ($gmol^{-1}$)	$M_{n\ sec}$ ($gmol^{-1}$)	$Đ$	Cyl. Radius (nm)	Cyl. Length (nm)	Kuhn Length (nm)	Rg SC (nm)
16	$(PHEAm_{50})_{100}$	608,000	228,000	1.21	7.5	21.5	-	3.0
17	$(PHEAm_{50})_{1000}$	6,407,000	1,430,000	1.71	8.0	>150	-	3.4
18	$(PHEAm_{20})_{500}$	1,390,000	532,000	1.40	4.3	>150	13.5	1.8
19	$(PBA_{47})_{500}$	3,179,000	333,000	1.33	-	-	-	-

The large molecular size of bottle-brushes also allows direct visualisation by microscopy techniques such as transmission electron microscopy and, in the case of polymer bottle-brushes, more commonly atomic force microscopy (AFM). This is highly useful for determining the molecular size, shape and parameters such as persistent length, without the necessity to fit the data to models. Under standard sample preparation conditions the compound is dried onto an atomically flat substrate such as graphite, mica or silica. Since the analysis is typically performed in the dry state it is worth noting the morphology of adsorbed polymer is dependent on interactions with the surface / air and may not be representative of properties in solution, in this regard SANS can give superior information.

Initial attempts to analyse the PHEAm side chain brushes by AFM on mica substrates proved challenging, with difficulty finding suitable sample preparation conditions. Evidence of worm like structures were observed (Figure 2.9D), but generally low quality images were obtained. Butyl acrylate side chains brushes have been extensively studied in literature and therefore from the PolyCTA$_{500}$ backbone butyl acrylate side chains were grafted to an intermediate DP47 length and characterised by AFM (**19**). Cylindrical shaped semi-flexible particles were observed (Figure 2.9A, B) with a length of approximately 140 nm, which matches closely with the expected theoretical length of 125 nm for a DP500 backbone, especially considering the additional size of side chains and the inherent tendency of AFM to overestimate dimensions of small objects. The combination of SANS / AFM provides strong evidence the shuttle CTA RAFT technique is effective for the preparation of cylindrically shaped molecular bottle-brushes.

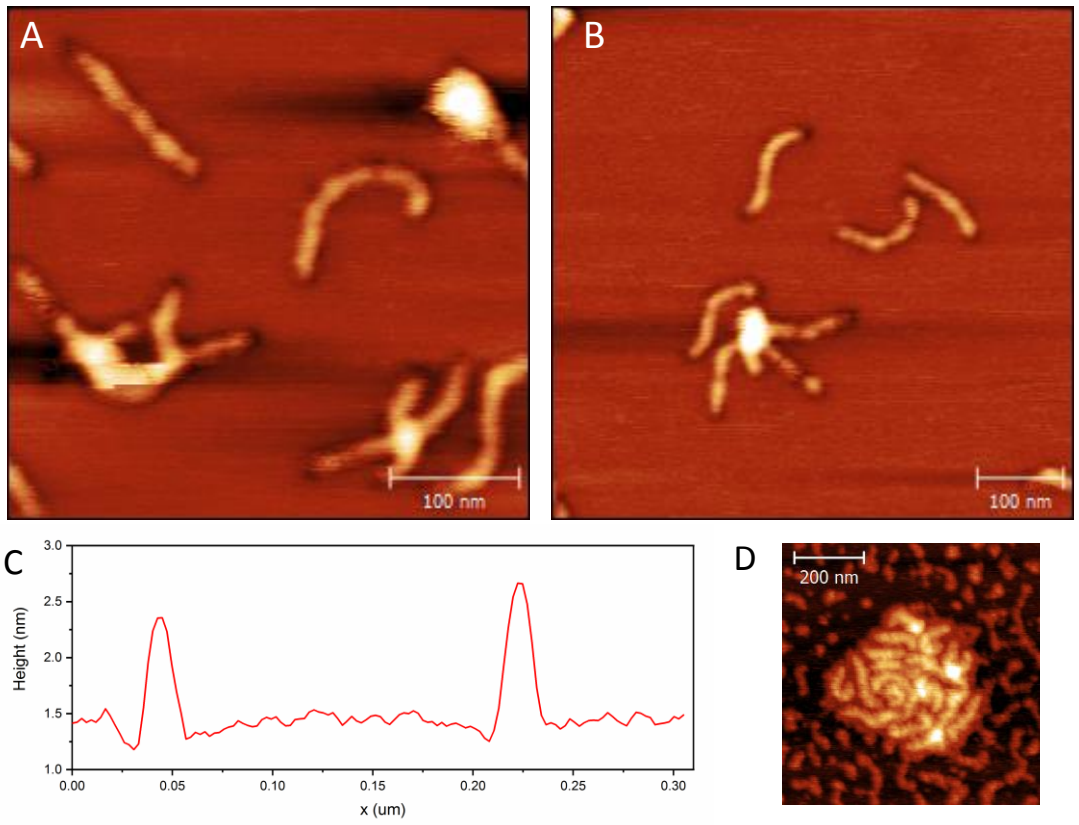

Figure 2.9: A, B – AFM images of a (PBA$_{47}$)$_{500}$ bottle-brush polymer dipped onto a mica subtrate. Inset shows 100nm scale bars. C – Typical height profile of two brush molecules from image B. D – Small section of an AFM image of PHEAm bottle-brush with worm-like species apparent.

2.2.5 Grafting from of multiblock side chains

To test the limits of the shuttle CTA technique, the continual chain extension of the grafts of the bottle-brush to high monomer conversions was attempted until a loss of control was observed, with the aim of preparing multiblock side chains. The monomers NAM and dimethylacrylamide (DMA) were polymerised in alternating order targeting a short DP of 15 per block (Figure 2.10). The PolyCTA backbone was completely insoluble in water and therefore the first PNAM block was polymerised in dioxane using the azoinitiator V601 over an 8 h reaction time. For subsequent blocks, monomers were added in aqueous solutions with the azoinitiator VA-044, heating at 70°C with a reaction time of 2 h per block. Such conditions yielded >95% monomer consumption for each polymerisation. Aliquots of NAM / DMA were sequentially added with extra initiator to chain extend a further 5 blocks from the PNAM brush backbone to synthesise a hexablock brush structure within 18 h total reaction time.

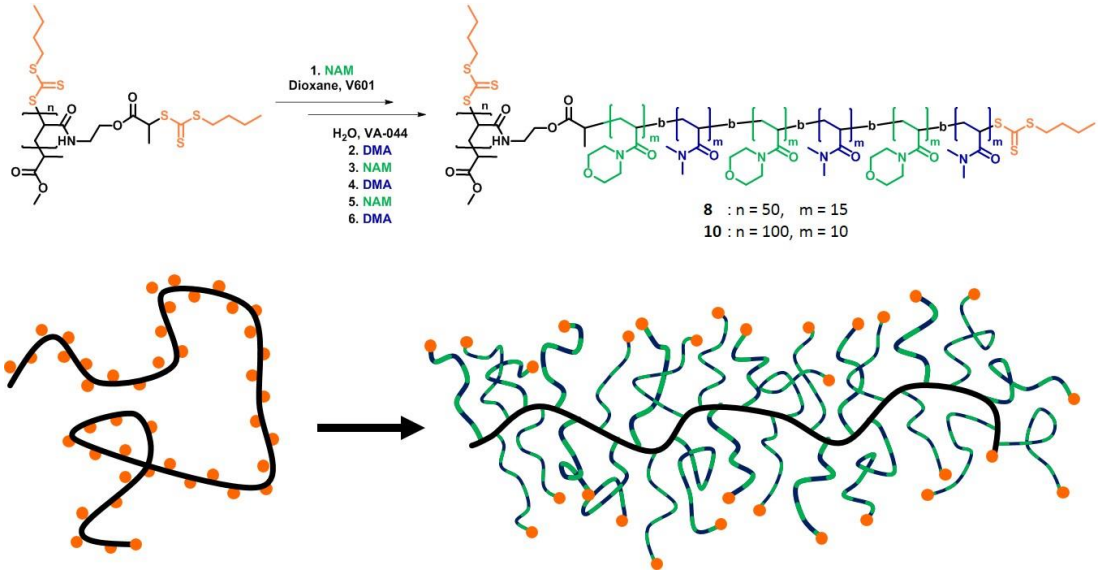

Figure 2.10: Grafting from polymerisation to generate hexablock side chain bottle-brush polymers. The RAFT end group of the PolyCTA backbone will chain extend in the same manner to form a hexablock, however this may been omitted for clarity.

By SEC analysis the distribution of the bottle-brush shifts to higher molecular weight after each chain extension with an increasingly large high molecular weight shoulder which is attributed to accumulating bimolecular terminations (Figure 2.11A). Despite this shoulder, the dispersity remains reasonably low at $Đ$=1.36 after 6 chain extensions, at which point no further blocks were attempted due to the substantial bimodality of the SEC

trace. In a linear multiblock polymerisation a low molecular weight tail is typically observed, caused by the formation of dead chains throughout the process which lack a CTA end group and thus are unable to chain extend. In comparison the brush system displays no such low molecular weight tail, with what appears to be near perfect re-initiation between blocks. With an average of 50 CTA groups per brush it is highly unlikely that all side chains of a single bottle-brush molecule will be terminated, therefore the majority of brush arms will continue to chain extend ensuring the molecule as whole is 'living' despite the occurrence of bimolecular termination.

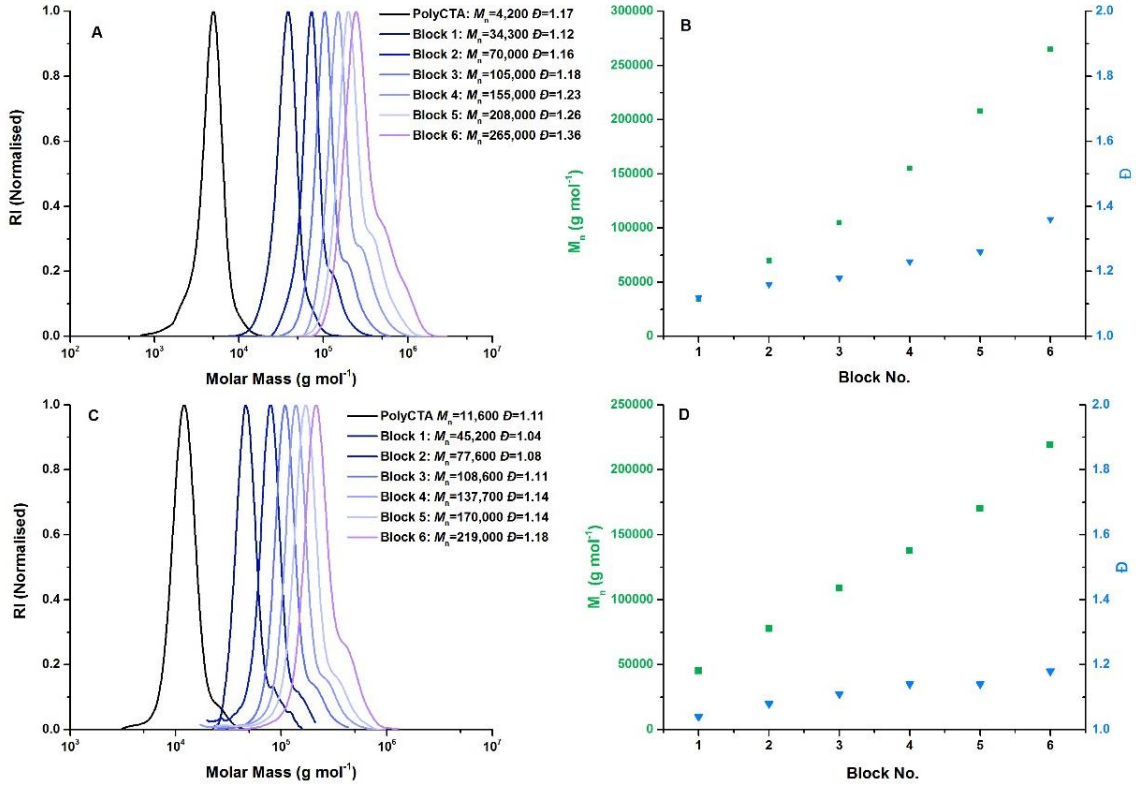

Figure 2.11: A and B – SEC analysis of DP50 backbone bottle-brush hexablock targeting DP15 per block. Linear polymer omitted from SEC traces for clarity, shown in Figure A.11 A. C and D – SEC analysis of DP100 backbone bottle-brush hexablock targeting DP10 per block. Linear polymer omitted from SEC traces for clarity, shown in Figure A.11 B.

The shuttle CTA derived chains can be clearly seen by SEC to chain extend for each block to form a hexablock linear polymer in solution (Appendix, Figure A.11). It would be expected to represent the same composition as the grafted chains of the bottle-brush, and indeed, after removal of the linear polymer by fractional precipitation and subsequent hydrolysis of the bottle-brush side chains an identical MWD to that of the linear polymer is observed. Attempting the same procedure in the absence of the shuttle CTA rapidly

leads to loss of control of the polymerisation with a very broad multimodal distribution observed after 3 blocks (Figure A.13). It is therefore evident that the addition of shuttle CTA is essential for the successful implementation of this technique.

The hexablock side chain structure is potentially of interest as a number of core-shell layers could be incorporated to give unique properties to the brush macromolecule. In this case the NAM / DMA units are both highly hydrophilic polymers, but it would be feasible to instead introduce alternating hydrophobic/hydrophilic blocks or responsive monomers into the chain. The short DP50 PolyCTA backbone used in these polymerisations would be expected to give a very short cylindrical conformation, similar to a star polymer. Therefore, the grafting from increasingly long backbones was investigated to access more bottle-brush like structures. Targeting DP10 blocks of NAM/DMA, a hexablock side chain off a longer DP100 PolyCTA backbone was synthesised with excellent control by SEC analysis (final block $Đ$=1.18). To aid control of the polymerisation the amount of shuttle CTA was increased to 2 equivalents per grafted CTA, which lowered the cross coupling between brushes but leads to increased quantity of linear polymer side products (Figure A.11 B). Additionally, the procedure was attempted with a DP500 backbone, however, significant brush coupling was observed even with the addition of 4 equivalents of shuttle CTA, therefore this approach is limited to relatively short backbones.

2.2.6 Multiblock backbone bottle-brushes

Using the same general synthetic approach as described for multi-block side chains, we further attempted to use the multiblock methodology to obtain alternative backbones that could yield novel polymeric architectures. It is known that the grafting density has a large impact on bottle-brush properties such as the stiffness of the backbone and the chain entanglement molecular weight.[39] Copolymerising a non-functional monomer into the PHEAm backbone in a random statistical distribution would reduce the grafting density of the brush and thus reduce the stiffness of the main chain while also affecting other properties. Instead, by using a multiblock approach, sequences of ungrafted linker chains can be placed periodically throughout the brush backbone, which alters the flexibility of the overall macromolecule while the grafting density in brush subunits remains high. This architecture could be considered similar to that of naturally occurring mucins. Structurally mucins are typically composed of a heavily glycosylated central bottle-brush region

separated by bare unglycosylated domains, which are believed to be important for surface interactions but also enable self-association between mucin macromolecules to form gels or multimers including 'train-of-brushes' structures.[11]

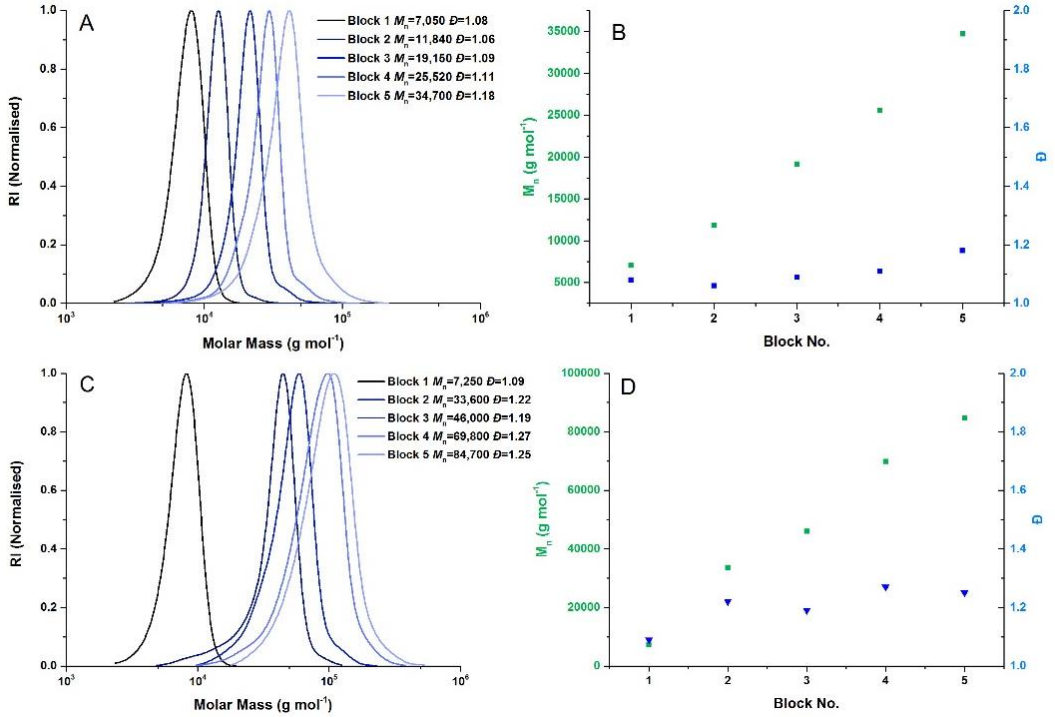

Figure 2.12: A and B – DMF SEC molecular weight distributions of the nonablock copolymer backbone. C and D - DMF SEC chromatograms analysis of the nonablock copolymer backbone.

NAM was used as the non-functional monomer as its polymerisation behaviour in block copolymerisations is well established. [43] A backbone consisting of alternating blocks of HEAm and NAM was synthesised, aiming for a high number of blocks to push the limits of structural complexity (Figure 2.13). By using a di-functional CTA linked by the 'R' group, two blocks can be polymerised simultaneously in an outwards symmetric fashion, which enabled a nonablock polymer to be quickly synthesised in just 5 steps rather than a 9 step synthesis as would be required with a standard CTA. Firstly, a MacroCTA of DP30 PHEAm was synthesised using DiPABTC in DMF, then purified and subsequently chain extended in water with VA-044 at 70°C by addition of 4 alternating aliquots of NAM / HEAm, targeting DP20 for each block. Monomer conversions of >92% were obtained and SEC analysis revealed a shift to higher molecular weight after each block extension to yield a polymer of narrow monomodal distribution (Table 3, **20**, M_n = 34,700, $Đ$ = 1.18) (Figure 2.12A). Functionalisation of the PHEAm units by esterification with PABTC was performed using the same procedure as described earlier. This gave a

copolymer containing blocks of PNAM sandwiched between PolyCTA blocks, which can be chain extended in a second polymerisation to form brush regions. The subsequent grafting from step using NAM as the side chain monomer proceeded as expected with excellent control by the addition of 0.5 equivalents shuttle CTA to yield bottle-brush **21** of M_n = 181,000 and $Đ$ = 1.29. The monomodal trace with no high molecular weight shoulder shows prevention of cross coupling in the grafting from step and thus the multiblock structure of the bottle-brushes should be maintained in high fidelity. Each macromolecule would be expected to contain 5 separate brush segments connected by 4 DP20 PNAM linker blocks. The highly branched nature of brush polymers means their hydrodynamic volume is much more compact compared to an equivalent molecular weight linear polymer, and therefore elutes at a later retention time. The use of triple detection analysis combining the refractive index trace with dual angle light scattering and viscosity detectors allows a non-relative molecular weight to be determined independent of standards. Doing so provides a M_n value closer to the expected theoretical (Table 4).

Table 2.4: Mulitblock backbone samples and the bottle-brushes polymers grafted therefrom, M_n and $Đ$ determined by DMF SEC.

Entry	Description	$M_{n\ theo}$ (g mol^{-1})	$M_{n\ SEC}$ (g mol^{-1})	$M_{n\ DALS}$ (g mol^{-1})	$Đ$	dn/dc
20	$PHEAm_{20}$-$PNAM_{20}$-$PHEAm_{20}$-$PNAM_{20}$-$PHEAm_{30}$-$PNAM_{20}$-$PHEAm_{20}$-$PNAM_{20}$- $PHEAm_{20}$ Nonablock Backbone	23,300	34,700	-	1.18	-
21	[$pNAM_{42}$] Graft from 20 PolyCTA	703,000	184,000	797,000	1.28	0.097
22	$PMHEAm_{50}$-$PNAM_{100}$-$PMHEAm_{50}$-$PNAM_{100}$-$PMHEAm_{50}$-$PNAM_{100}$-$PMHEAm_{50}$-$PNAM_{100}$-$PMHEAm_{50}$ Nonablock Backbone	88,300	84,700	-	1.25	-
23	[pBA_{50}] Graft from 22 PolyCTA	1,745,000	382,000	1,930,000	1.53	0.052
24	[$PNAM_{10}$-$PDMA_{10}$-$PNAM_{10}$-$PDMA_{10}$-$PNAM_{10}$] Graft from 20 PolyCTA	732,000	321,000	484,000	1.35	0.086

While successful, the use of short DP20 block linkers may have minimal effect on the flexibility of the brush in comparison to the bulky bottle-brush segments. The linker blocks would also only be several nanometres in size, which make it challenging to image the macromolecule and identify individual brush regions by techniques such as AFM.

Therefore, it was desirable to target higher molecular weight blocks to aid characterisation of the complex architecture. A nonablock with larger DP100 pNAM linkers and DP50 brush segments was synthesised using the same procedure but with an alternative alcohol functional acrylamide monomer. The methyl functionalised version of hydroxyethyl acrylamide polymerised at a slightly faster rate and proved easier to incorporate in multiblock polymerisations to high monomer conversion, especially when targeting higher molecular weights. A backbone with a total DP of 650 was accessed (**22**, M_n = 84,700 and $Đ$ = 1.25), with 5 alcohol functional segments of DP50 each separated by 4 DP100 PNAM linkers. The multiblock copolymer was used to synthesise bottle-brush **23** with n-butylacrylate side chains by the shuttle CTA RAFT technique (Figure 2.13A).

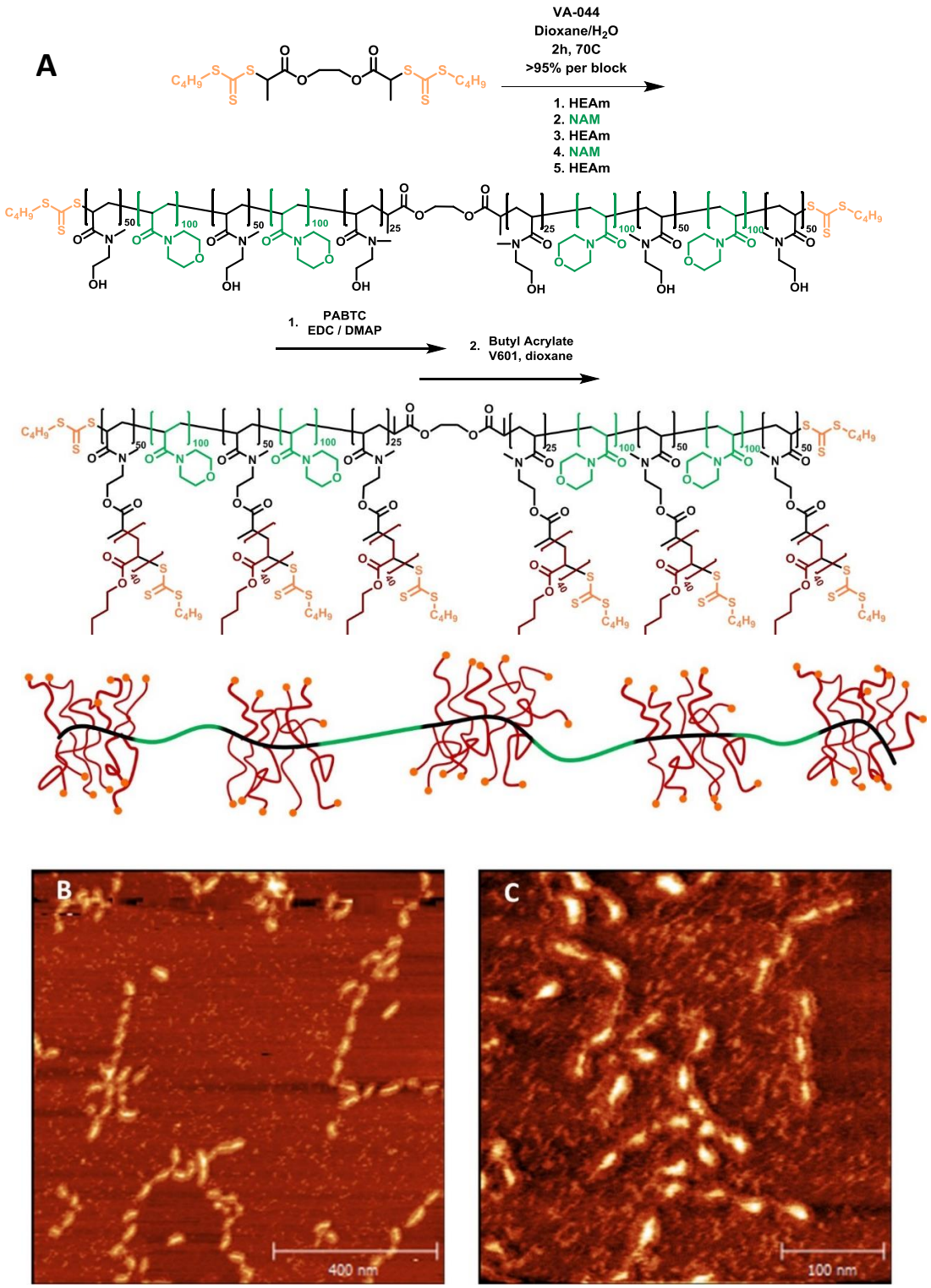

Figure 2.13: Scheme showing synthesis of the nonablock copolymer backbone bottle-brush **23** and AFM imaging of the compound. Sample deposited onto mica sheets by dipping into a dilute chloroform solution.

Imaging of compound **23** by AFM revealed the appearance of the expected 'sausage string' like structure with a clear tendency for the bottle-brushes to be linked together in groups (Figure 2.13B, C). A bottle-brush with a DP250 length backbone would be

expected to have a length of ~62.5 nm when fully extended, whereas each individual segment with DP50 would have a length of 12.5 nm. The average length of each brush segment is approximately 19 nm and fits more closely to that of separate segments, especially since AFM can overestimate the size of very small objects. Individual macromolecules with the ideal 5 brush segments are present in the AFM, although a number of defected molecules with fewer brushes are present, which could result from sample preparation but are also an expected side product from the synthetic procedure. During the initial backbone polymerisation a small number of dead chains will accumulate between blocks, leading to a number of defect brushes with less than 5 brush segments. However, the low concentration of initiator used in the polymerisations ensures a high livingness is achieved to minimise the formation of imperfect brush architectures. In this case AFM analysis provides a unique way of confirming the effectiveness of RAFT acrylamide multiblock chemistry, where individual macromolecules can be directly imaged to visualize the segmented block regions.

2.2.7 Incorporation of multiblocks among the 'x' and 'y'-axis

Once conditions for the introduction of multiblocks into the backbone and side chain had been established, the combination of the two approaches into one bottle-brush molecule was attempted to push the limits of structural complexity in the system. The nonablock backbone with short DP20 PHEAm was selected as the total number of brush units is equivalent to the DP100 backbone which had already been successfully used for the grafting from of a hexablock side chain, and therefore multiblock polymerisations would be expected to proceed with the same degree of control. Using one pot polymerisation conditions with 2 eq. shuttle CTA pentablock side chains of NAM/DMA were grafted from the multiblock backbone **20** (Figure 2.14). The dispersity of the nonablock PolyCTA was $Đ$ = 1.33, and this remains approximately constant throughout each block extension, indicating good control of the polymerisation. Theoretically this polymer possesses a structure consisting of five separate brush regions each composed of pentablock copolymer grafts, and therefore contains 29 separate polymeric domains, including spacers, within a single molecule.

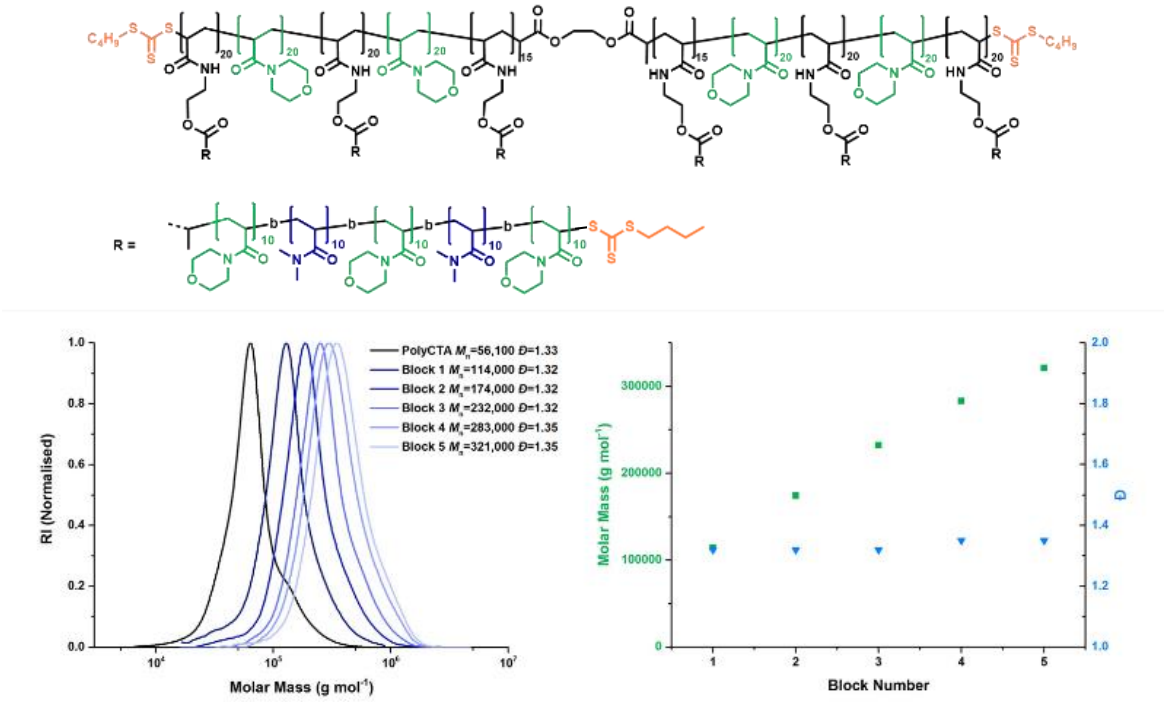

Figure 2.14: Scheme and SEC analysis for the grafting from of pentablock side to synthesise compound **24**.

2.3 Conclusion

In this work the application of multiblock RAFT acrylamide polymerisations for the synthesis of bottle-brush copolymers is demonstrated and its effectiveness to access complex architectures shown. In grafting from polymerisations the full consumption of monomer is very challenging, however, by a combination of rapidly propagating acrylamides and the addition of shuttle CTA this is achievable while still maintaining good control over the polymerisation process. This can be used to access long cylindrical brush molecules as evidenced by SANS / AFM, but also allows multiple blocks of acrylamide monomers to be grafted from the side chain of a precursor in a one pot process to synthesise advanced core-shell systems. Additionally, a nonablock copolymer backbone with alternating regions of grafted and linear segments was used to synthesise bottle-brushes with precise control of the microstructure. Using AFM it was possible to visualize multi-segmented bottle brush copolymers and elucidate the proposed structure. Combining the two methods, a multiblock backbone was generated with a multiblock side chain resulting in a macromolecule with a total of 29 separate domains produced in a one-pot synthesis.

Within this study, the scope of enormous structural complexity that can be achieved using an efficient RAFT grafting from methodology is outlined. The synthesized multi-segmented brush copolymers exhibit a highly promising method enabling the synthesis of biomimetic macromolecular analogues to complex naturally occurring bottle-brush molecules. Further investigations will focus on the application of these polymers for biomedical purposes and on probing their performance as lubricants.

2.4 Experimental

Materials

4-acryoylmorpholine (NAM, 97%), dimethylacrylamide (DMA, 99%) and N-hydroxyethyl acrylamide (HEAm, 97%) were obtained from Sigma-Aldrich and were passed through a basic alumina column before use. Dimethyl sulfoxide-d_6 (99.9% D atom), chloroform-*d* (99.8% D atom), deuterium oxide (99.9% D atom), methanol, dichloromethane (anhydrous), butanethiol, carbon disulphide, sodium hydroxide and 4-(Dimethylamino)pyridine (DMAP) were obtained from Sigma Aldrich and used as received. 1,4-dioxane and N,N-dimethylformamide (anhydrous) were obtained from fisher scientific and used as received. N-(3-Dimethylaminopropyl)-N′-ethylcarbodiimide hydrochloride (EDC) was obtained from Carbosynth and used as received. Initiators 2,2′-azobis[2-(2-imidazolin-2-yl)propane]dihydrochloride (VA-044, >98%, Wako), 4,4′-azobis(4-cyanovaleric acid) (V501, >98%, Aldrich) and dimethyl 2,2'-azobis(2-methylpropionate) (V601, >98%, Wako) were used as received. CTA Acid was supplied by the industrial sponsor Lubrizol and was recrystallized in hexane twice prior to use.

Instrumentation and Analysis

NMR Spectroscopy

^{1}H and ^{13}C NMR spectra were ran on either a Bruker DPX-300 or DPX-400 spectrometer using deuterated solvents (deuterated dimethyl sulfoxide, chloroform or water).

Size exclusion chromatography (SEC)

DMF-SEC: Agilent 390-LC MDS instrument equipped with differential refractive index (DRI), viscometry (VS), dual angle light scatter (LS) and dual wavelength UV detectors. The system was equipped with 2 x PLgel Mixed D columns (300 x 7.5 mm) and a PLgel 5 µm guard column. The eluent was DMF with 5 mmol NH_4BF_4 additive. Samples were run at 1 ml min^{-1} at 50°C. Poly(methyl methacrylate) standards (Agilent EasyVials) were used for calibration, MW ranging from 550 to $2.14*10^6$ g mol^{-1}. Analyte samples were filtered through a nylon membrane with 0.22 μm pore size before injection. Respectively,

experimental molar mass ($M_{n,SEC}$) and dispersity ($Đ$) values of synthesized polymers were determined by conventional calibration using Agilent GPC/SEC software.

Atomic Force Microscopy (AFM)

AFM images were acquired in AC mode on a Cypher S system (Asylum Research). The probes used were AC160TS from Olympus probes with a nominal resonant frequency of 300 kHz and a spring constant of approximately 40 N m^{-1} on a Multimode AFM (Asylum Research). Images were acquired at a pixel resolution of 512 and a scan rate of 1 Hz. Samples were diluted to 1 μg ml^{-1} in chloroform, and samples were prepared by dipping a freshly cleaved mica substrate into the solution. The data were analyzed by the Asylum Research software.

Small Angle Neutron Scattering (SANS)

SANS was carried out on the Sans2d small-angle diffractometer at the ISIS Pulsed Neutron Source (STFC Rutherford Appleton Laboratory, Didcot, U.K.)[44]. A collimation length of 4m and incident wavelength range of 1.75 – 16.5 Å was employed. Data were measured simultaneously on two 1 m^2 detectors to give a Q-range of 0.0045 – 1.00 $Å^{-1}$. The small-angle detector was position 4m from the sample and offset vertically 60 mm and sideways 100 mm. The wide-angle detector was position 2.4m from the sample, offset sideways by 980 mm and rotated to face the sample. Q is defined as:

$$Q = \frac{4\pi \sin\frac{\theta}{2}}{\lambda}$$

where θ is the scattered angle and λ is the incident neutron wavelength. The beam diameter was 8 mm. Each raw scattering data set was corrected for the detector efficiencies, sample transmission and background scattering and converted to scattering cross-section data ($\partial\Sigma/\partial\Omega$ vs. Q) using the instrument-specific software.[45] These data were placed on an absolute scale (cm^{-1}) using the scattering from a standard sample (a solid blend of hydrogenous and perdeuterated polystyrene) in accordance with established procedures. Data was fitted using SASfit software with a combination of cylinder and Gaussian chain model or combination of flexible cylinder and Gaussian chain.

Synthesis of 2-(((butylthio)carbonothioyl)thio) propanoic acid (PABTC)

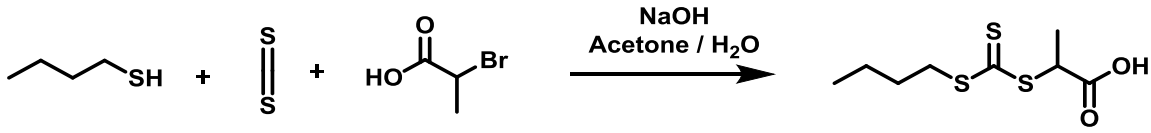

A 50% aqueous NaOH solution (16 g, 200 mmol) was added to a stirred mixture of butanethiol (18 g, 200 mmol) in 30 ml H_2O. Acetone (10 ml) was added to the flask and stirred for 30 minutes at room temperature, followed by addition of carbon disulphide (13.5 ml, 225 mmol) and stirred for 30 minutes. The reaction mixture was cooled with an ice bath, 2-bromopropionic acid (18.75 ml, 205 mmol) was added dropwise maintaining the temperature of the mixture at <30°C, followed by addition of 50% NaOH solution (16.4 g). The ice bath was removed, H_2O (30 ml) added and stirred at room temperature for 24h. The reaction mixture was diluted with a further 50 ml H_2O, cooled with an ice bath and 10M HCl solution (20 ml) was added dropwise. After leaving to stand at room temperature for 2h a solid was formed, this was collected by filtration, washed with cold water and dried, then suspended again in cold water, stirred for 15 minutes and refiltered. The yellow powder was recrystallized twice from hexane to yield the product as a bright yellow solid (42.4 g, 89%). ^{1}H NMR (400MHz, $CDCl_3$): δ 4.86 (1H, q, J = 7.3 Hz), 3.37 (2H, t, J = 7.3 Hz), 1.69 (2H, m), 1.63 (3H, d, J = 7.2 Hz), 1.45 (2H, m), 0.94 (3H, t, J = 7.3 Hz) . ^{13}C NMR (101 MHz, $CDCl_3$) δ 221.9, 177.0, 47.6, 37.1, 29.9. ESI MS -ve: Calcd for $C_8H_{13}O_2S_3Na$ $[M]^-$ 237.01. Found m/z 237.1. Melting point: 53.5 – 54.0 °C.

Synthesis of methyl 2-(((butylthio)carbonothioyl)thio)propanoate

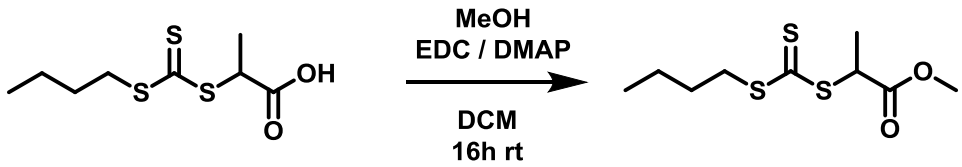

PABTC (1 g, 4.2 mmol) and methanol (0.537 g, 16.8 mmol) were dissolved in 10 ml anhydrous DCM in a dry 50 ml round bottom flask under nitrogen. The reaction mixture was cooled with an ice water bath followed by the addition of DMAP (62 mg, 0.50 mmol) and then EDC (0.965 g, 5.03 mmoL). After 30 minutes the ice bath was removed and stirred for a further 4h at room temperature. The reaction mixture was transferred to a separating funnel and the organic phase washed with 1M HCl solution, twice with

saturated $NaHCO_3$ solution, once with brine and then dried over $MgSO_4$, filtered and concentrated under vacuum. The crude product was purified with flash chromatography using a 25 g silica column with a hexane/ethyl acetate eluent gradient. The fractions were concentrated under vacuum to yield a yellow oil (780 mg, 74%). ^{1}H NMR (400MHz, $CDCl_3$): δ 4.84 (1H, q, J = 7.4 Hz), 3.75 (3H, s), 3.37 (2H, t, J = 7.4 Hz), 1.68 (2H, quin, J = 7.5 Hz), 1.60 (3H, d, J = 7.4 Hz), 1.43 (2H, sxt, J = 7.4 Hz), 0.94 (3H, t, J = 7.3Hz). ^{13}C NMR (101 MHz, $CDCl_3$) δ 222.1, 171.6, 52.9, 47.7, 37.0, 29.9, 22.1, 17.0, 13.6. ESI MS +ve: Calcd for $C_9H_{16}O_2S_3Na$ $[M+Na]^+$ 275.02. Found m/z 275.0.

Synthesis of ethane-1,2-diyl bis(2-(((butylthio)carbonothioyl)thio)propanoate) (DiPABTC)

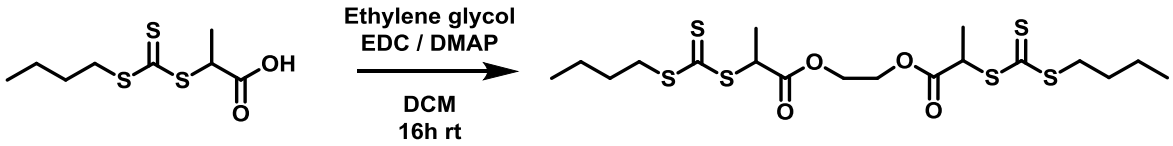

PABTC (500 mg, 2.01 mmol) and ethylene glycol (62.5 mg, 1.01 mmol) were dissolved in 5 ml anhydrous DCM in a dry 25 ml round bottom flask under nitrogen. The reaction mixture was cooled with an ice water bath followed by the addition of DMAP (25.6 mg, 0.21 mmol) and then EDC (442 mg, 2.31 mmoL). After 30 minutes the ice bath was removed and stirred for a further 4 h at room temperature. The reaction mixture was transferred to a separating funnel and the organic phase washed with 1M HCl solution, twice with brine and then dried over $MgSO_4$, filtered and concentrated under vacuum. The crude product was purified with flash chromatography using a 12 g silica column with a hexane/ethyl acetate eluent gradient. The fractions were concentrated under vacuum to yield a yellow oil (318 mg, 60%). ^{1}H NMR (300 MHz, $CDCl_3$) δ 4.84 (q, J = 7.2 Hz, 2H), 4.35 (s, 4H), 3.37 (t, J = 7.3 Hz, 4H), 1.69 (q, 4H), 1.61 (d, J = 7.2 Hz, 6H) 1.45 (dt, J = 14.6 Hz, 7.2 Hz, 4H), 0.94 (t, J = 7.3 Hz, 6H). ^{13}C NMR (101 MHz, $CDCl_3$) δ 221.9, 171.0, 63.1, 47.8, 37.0, 29.9, 22.1, 16.8, 13.6. ESI MS +ve: Calcd for $C_{18}H_{30}O_4S_6Na$ $[M+Na]^+$ 524.04. m/z 524.1 found.

Synthesis of PHEAm backbones

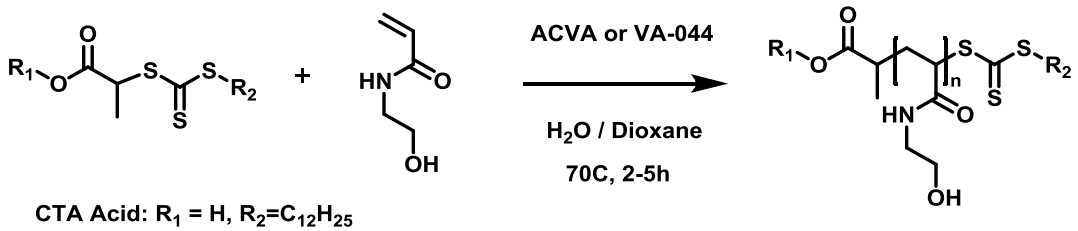

CTA Acid: R_1 = H, R_2=$C_{12}H_{25}$
PMBTC: R_1 = CH_3, R_2=C_4H_9

Synthesis with CTA Acid: HEAm (500 mg, 4.34 mmol, 100 to 4000 equivalents depending on target DP), CTA Acid (1 equivalent), ACVA (0.6 mg, $2.17*10^{-3}$ mmol, 122 µl of a basic aqueous 5 $mgml^{-1}$ solution), and distilled H_2O (1.3 ml) were added to a 3 ml vial with a stirrer bar, sealed with a rubber septum and degassed with nitrogen for 10 minutes. A solution of NaOH (5 $mgml^{-1}$ in H_2O, 1.7 equivalents with respect to CTA) was simultaneously degassed with nitrogen in a separate vial and then added via syringe to the reaction mixture. This procedure was to avoid excessive foaming during degas as the CTA Acid can act as a surfactant. The reaction vessel was then placed in an oil bath preheated to 70°C and heated with stirring for 5h, after which it was cooled under a stream of cold water, the septum removed and analysed with ^{1}H NMR and SEC (Figure 2.2 for example SEC). Typical ^{1}H NMR (300 MHz, DMSO-d6) δ 7.8-7.5 (1H, NH), 5.1-4.8 (1H, OH), 3.6 – 2.9 (4H, $NHCH_2CH_2OH$), 2.0 – 1.0 (3H, $CH_2CHC{=}O$).Synthesis with PMBTC: a similar procedure to as described above was used, except with a 50:50 dioxane / distilled water mixture as the solvent and with the use of azoinitiator VA-044 instead of ACVA. The reaction mixture was prepared as one solution and degassed in a 3 ml vial with a stirrer bar and rubber septum, after which heated for 2h at 70°C.

Synthesis of PolyCTA by esterification of pHEAm with PABTC

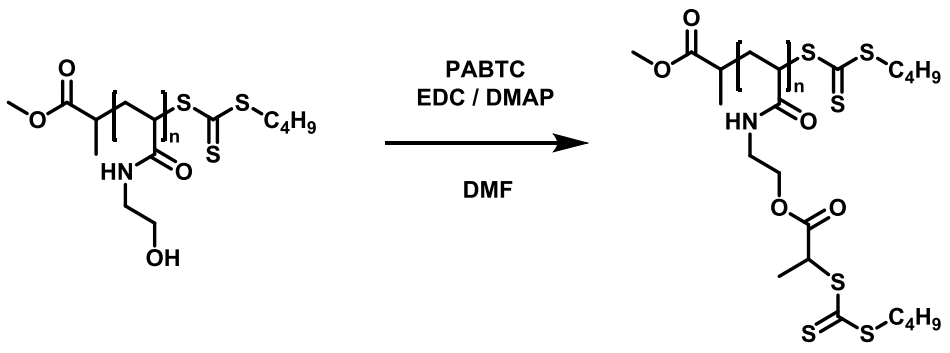

PHEAm (100 mg, 0.870 mmol with respect to alcohol groups) and PABTC (290 mg, 1.22 mmol) were dissolved in 10 ml DMF in a dry 50 ml round bottom flask under nitrogen, cooled with an ice bath followed by the addition of DMAP (21 mg, 0.17 mmol) and EDC (333 mg, 1.74 mmol). The reaction mixture was stirred for 30 minutes after which the ice bath was removed and stirred at room temperature for a further 2 4h. The reaction mixture was precipitated once into water, redissolved in dioxane and precipitated twice into 60:40 MeOH:water to remove unconjugated PABTC. The precipitate was collected by centrifugation and dried in a vacuum oven overnight at 45°C. ^{1}H NMR (300 MHz, $CDCl_3$): δ 4.9 -4.8 (1H, SC<u>H</u>(CH_3)), 4.4 – 4.1 (2H, C(O)OC<u>H</u>$_2$), 3.6 – 3.5 (2H, C(O)NHC<u>H</u>$_2$), 3.4 – 3.3 (2H, SC<u>H</u>$_2$), 2.2 – 1.2 (3H, C<u>H</u>$_2$C<u>H</u>), 1.66 (2H, t, $SCH_2C\underline{H}_2$), 1.62 (3H, d, SCH(C<u>H</u>$_3$)), 1.45 (2H, q, $SCH_2CH_2C\underline{H}_2$), 0.94 (3H, t, C<u>H</u>$_3$$CH_2$). Elemental analysis: Cald for $C_{13}H_{21}NO_3S_3$: C, 46.54; H, 6.31; N, 4.18; O, 14.31; S, 28.6. Found: C, 46.28; H, 6.28; N, 4.04; S, 27.1.

Grafting from kinetics of NAM from DP50 polyCTA

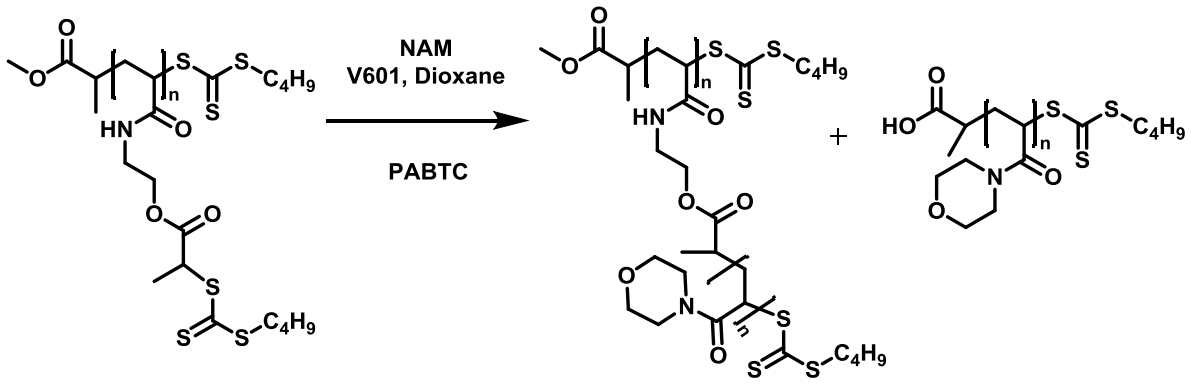

DP50 PolyCTA (19.8 mg, 0.057 mmol), NAM (600 mg, 4.25 mmol) and V601 (0.2 mg, 1.06 μmol) were dissolved in Dioxane (3.72 ml) in a 7 ml vial with a stirrer bar, sealed with a rubber septum and degassed with nitrogen for 10 minutes. The vial was then placed in an oil bath preheated to 65°C for 6 h. Periodically throughout the reaction 100 μl samples were withdrawn via a degassed syringe and analysed with ^{1}H NMR in $CDCl_3$ and DMF SEC to determine conversions, M_n and *Đ*. After 6 h the vial was removed and cooled under a stream of cold water before removing the septum to quench the polymerisation. For the polymerisation with the addition of shuttle CTA instead PolyCTA

(13.2 mg, 0.038 mmol) and PABTC (4.5mg, 0.019 mmol) were used, otherwise the same procedure was performed. Typical ^{1}H NMR (300 MHz, $CDCl_3$): δ 3.65 – 3.2 (8H, N[C$\underline{H}_2$C$\underline{H}_2$]$_2$O), 2.7 -2 .4 (1H, $CH_2C\underline{H}C$=O), 1.9 – 1.1 (2H, C$\underline{H}_2$CHC=O).

Cleavage of grafting polymer side chains by ester hydrolysis

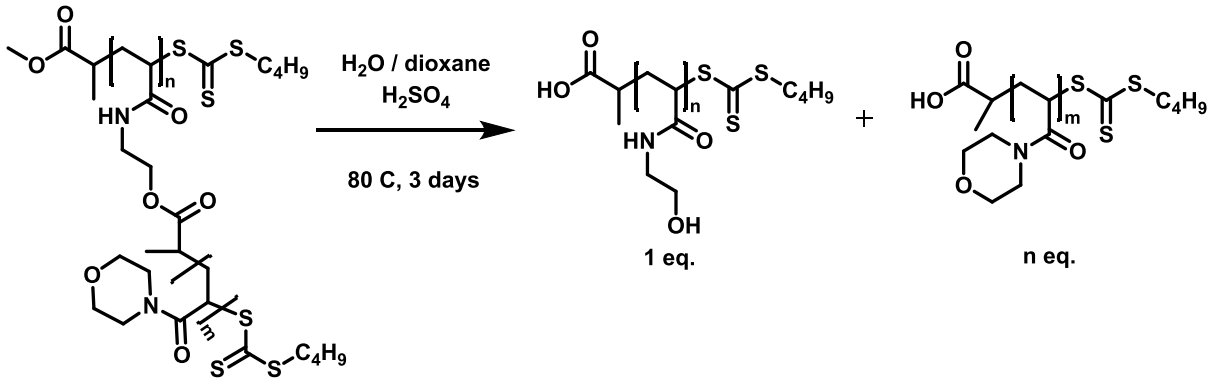

The PNAM side chain bottle-brush sample (100 mg) was dissolved in a mixture of distilled water (1 ml) and dioxane (0.5 ml), 3 drops of concentrated H_2SO_4 were added and the vial was heated at 80°C for 3 days. An aliquot of the reaction mixture was then analysed by DMF SEC to show full degradation of the brush and used for determination of the molecular weight of the linear side chains.

For the hydrolysis of the multiblock side chain brush, firstly the linear shuttle CTA derived polymer was removed by fractional precipitation. The polymer was dissolved in dioxane (50 mg ml^{-1}) and diethyl ether added dropwise until the reaction mixture became turbid, the precipitate was collected by centrifugation and the process repeated 4 times until no linear polymer was observed by SEC analysis. The ester hydrolysis was then performed on the purified multiblock bottle-brush using the procedure described above.

Multiblock side chain brush synthesis

The first PNAM brush block was synthesised by addition of PolyCTA (39.6 mg, 0.118 mmol), PABTC (28.1 mg, 0.118 mmol), NAM (500 mg, 3.54 mmol), V601 (0.6 mg, 2.36 μmol) and dioxane (3 ml) into a 7 ml vial equipped with a stirrer bar. The vial was sealed with a rubber septum, degassed for 10 minutes with nitrogen and placed in an oil bath preheated to 65°C for 10 h. The vial was removed, cooled under a stream of cold water, and analysed with ^{1}H NMR to determine a conversion of 91%. The reaction mixture was

precipitated into diethyl ether to yield a yellow solid. The polymer (180 mg) was placed in a vial with DMA (235 mg, 2.37 mmol), VA-044 (0.3 mg, 0.79 μmol), dioxane (0.56 ml) and water (0.25 ml), degassed with nitrogen and heated in an oil bath at 70°C for 2 h. Samples were withdrawn via degassed syringe and analysed by ^{1}H NMR / SEC to ensure full monomer conversion was achieved between blocks. A degassed solution of the next monomer block with initiator was then added to the vial via syringe. This process was continued for 4 subsequent aliquots to yield the hexablock brush copolymer. The monomer aliquots contained VA-044 (0.3 mg, 0.79 μmol), water (0.35 ml) and either NAM (334 mg, 2.37 mmol) or DMA (235 mg, 2.37 mmol).

Multiblock backbone brush

First a pHEAm$_{30}$ MacroCTA was synthesised. DiPABTC (73 mg, 0.15 mmol), HEAm (500 mg, 4.34 mmol), VA-044 (0.5 mg, 1.45 μmol), dioxane (1.4 ml) and water (0.34 ml) were mixed in a 3 ml vial equipped with a stirrer bar, sealed with a rubber septum and degassed for 10 minutes with nitrogen. The vial was placed in an oil bath at 70°C for 2h. The reaction mixture was precipitated twice in acetone and dried in a vacuum oven at 45°C overnight to yield the pHEAm$_{30}$ MacroCTA as a yellow powder. The DP of the polymer was determined by 1H NMR. The MacroCTA (174 mg, 0.044 mmol), NAM (250 mg, 1.77 mmol), VA-044 (0.2 mg, 0.59 μmol) and water (0.47 ml) were placed in a 3 ml vial, degassed with nitrogen for 10 minutes and placed in an oil bath heated to 70°C for 2 h. Samples were withdrawn via degassed syringe and analysed by ^{1}H NMR / SEC to ensure full monomer conversion was achieved between blocks. A degassed solution of the next monomer block with initiator was then added to the vial via syringe. This process was continued for 3 subsequent aliquots to yield the nonablock copolymer. The monomer aliquots contained VA-044 (0.2 mg, 0.59 μmol), Water (0.4 ml) and either HEAm (204mg, 2.37 mmol) or NAM (250 mg, 2.37 mmol). The reaction mixture was precipitated twice in acetone and dried in a vacuum oven overnight at 45°C. The HEAm units were esterified with PABTC using the same procedure as described for the synthesis of PolyCTA. The grafting from polymerisation was performed with 0.5 equiv. of shuttle CTA with NAM using the same procedure as described for the grafting from kinetics of DP50 PolyCTA.

For the second multiblock backbone (compound **22**) an identical approach was used except with the N-(2-hydroxyethyl)-N-methylacrylamide monomer and targeting higher molecular weights of each block.

Synthesis of N-(2-hydroxyethyl)-N-methylacrylamide

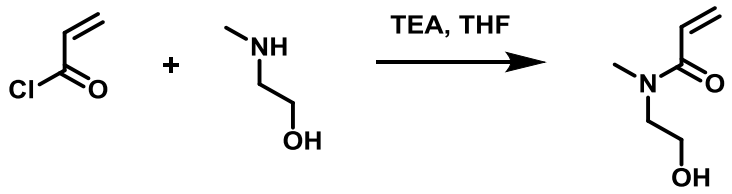

The monomer was synthesised adapting a previously reported procedure.[179] Acryloyl chloride (12 g, 0.133 mol) dissolved in 30 ml THF was added dropwise to a solution of methylethanolamine (19.9 g, 0.265 mol) in 200 ml THF under ice bath cooling and then stirred at room temperature for 3h. The reaction mixture was filtered, acidified with dropwise addition of concentrated H_2SO_4, and filtered again. The filtrate was concentrated under reduced pressure and the residue purified with column chromatography using an ethyl acetate / methanol eluent gradient to isolate the product as a colourless oil. ^{1}H NMR (300 MHz, $CDCl_3$) δ 6.66 (m, 1H), 6.29 (m, 1H), 5.69 (m, 1H), 3.78 (m, 2H), 3.60 (dt, J = 24 Hz, 5.4 Hz, 2H), 3.16, 3.02 (2 s, 3H). ^{13}C NMR (101 MHz, $CDCl_3$) δ 168.1, 128.6, 127.3, 61.05, 52.2, 37.0. ESI MS +ve: Calcd for $C_6H_{11}NO_2Na$, $[M+Na]^+$ 152.07. Found m/z 152.1.

2.5 References

1. C. M. Dobson, *Nature*, 2003, **426**, 884-890.
2. J.-F. Lutz, M. Ouchi, D. R. Liu and M. Sawamoto, *Science*, 2013, **341**, 1238149.
3. R. T. Mayadunne, J. Jeffery, G. Moad and E. Rizzardo, *Macromolecules*, 2003, **36**, 1505-1513.
4. X. Zhang, J. Xia and K. Matyjaszewski, *Macromolecules*, 2000, **33**, 2340-2345.
5. J. F. Quinn, R. P. Chaplin and T. P. Davis, *J. Polym. Sci., Part A: Polym. Chem.*, 2002, **40**, 2956-2966.
6. G. Moriceau, G. Gody, M. Hartlieb, J. Winn, H. Kim, A. Mastrangelo, T. Smith and S. Perrier, *Polymer Chemistry*, 2017, **8**, 4152-4161.
7. N. G. Engelis, A. Anastasaki, G. Nurumbetov, N. P. Truong, V. Nikolaou, A. Shegiwal, M. R. Whittaker, T. P. Davis and D. Haddleton, 2017, **9**, 171.
8. J. Zhang, G. Gody, M. Hartlieb, S. Catrouillet, J. Moffat and S. Perrier, *Macromolecules*, 2016, **49**, 8933-8942.
9. G. Gody, T. Maschmeyer, P. B. Zetterlund and S. Perrier, *Nature Comm.*, 2013, **4**, 2505.
10. R. Bansil and B. S. Turner, *Curr. Opin. Colloid Inter. Sci.*, 2006, **11**, 164-170.
11. J. An, A. Dėdinaitė, A. Nilsson, J. Holgersson and P. M. Claesson, *Biomacromolecules*, 2014, **15**, 1515-1525.
12. B. Zappone, M. Ruths, G. W. Greene, G. D. Jay and J. N. Israelachvili, *Biophys. J.*, 2007, **92**, 1693-1708.
13. A. Dėdinaitė, *Soft Matter*, 2012, **8**, 273-284.
14. X. Liu, A. Dedinaite, M. Rutland, E. Thormann, C. Visnevskij, R. Makuska and P. M. Claesson, *Langmuir*, 2012, **28**, 15537-15547.
15. X. Banquy, J. Burdynska, D. W. Lee, K. Matyjaszewski and J. Israelachvili, *J. Amer. Chem. Soc.*, 2014, **136**, 6199-6202.
16. S. S. Sheiko, B. S. Sumerlin and K. Matyjaszewski, *Prog. Polym. Sci.*, 2008, **33**, 759-785.
17. R. Verduzco, X. Li, S. L. Pesek and G. E. Stein, *Chem. Soc. Rev.*, 2015, **44**, 2405-2420.
18. S. Y. Yu-Su, S. S. Sheiko, H.-i. Lee, W. Jakubowski, A. Nese, K. Matyjaszewski, D. Anokhin and D. A. Ivanov, *Macromolecules*, 2009, **42**, 9008-9017.
19. K. L. Beers, S. G. Gaynor, K. Matyjaszewski, S. S. Sheiko and M. Möller, *Macromolecules*, 1998, **31**, 9413-9415.
20. J. Bernard, A. Favier, T. P. Davis, C. Barner-Kowollik and M. H. Stenzel, *Polymer*, 2006, **47**, 1073-1080.
21. K. Huang, D. P. Canterbury and J. Rzayev, *Macromolecules*, 2010, **43**, 6632-6638.
22. Z. Li, K. Zhang, J. Ma, C. Cheng and K. L. Wooley, *J. Polym. Sci., Part A: Polym. Chem.*, 2009, **47**, 5557-5563.
23. S. C. Radzinski, J. C. Foster and J. B. Matson, *Polymer Chemistry*, 2015, **6**, 5643-5652.
24. D. Neugebauer, *Polymer*, 2015, **72**, 412-421.
25. A. Nese, Y. Kwak, R. Nicolaÿ, M. Barrett, S. S. Sheiko and K. Matyjaszewski, *Macromolecules*, 2010, **43**, 4016-4019.
26. Z. Zheng, J. Ling and A. H. Müller, *Macromol. Rapid Commun.*, 2014, **35**, 234-241.

27. S. Rathgeber, T. Pakula, A. Wilk, K. Matyjaszewski and K. L. Beers, *J. Chem. Phys.*, 2005, **122**, 124904.
28. S. Li, C. Ye, G. Zhao, M. Zhang and Y. Zhao, *J. Polym. Sci., Part A: Polym. Chem.*, 2012, **50**, 3135-3148.
29. R. Fleet, E. T. van den Dungen and B. Klumperman, *Macromol. Chem. Phys.*, 2011, **212**, 2191-2208.
30. M. Matsuda, K. Satoh and M. Kamigaito, *Macromolecules*, 2013, **46**, 5473-5482.
31. Q. Wang, H. Ma, W. Sang, L. Han, P. Liu, H. Shen, W. Huang, X. Gong, L. Yang and Y. Wang, *Polymer Chemistry*, 2016, **7**, 3090-3099.
32. T. Krivorotova, P. Radzevicius and R. Makuska, *Eur. Pol. J.*, 2015, **66**, 543-557.
33. J. Perez-Vilar and R. L. Hill, *J. Bio. Chem.*, 1999, **274**, 31751-31754.
34. G. Gody, T. Maschmeyer, P. B. Zetterlund and S. Perrier, *Macromolecules*, 2014, **47**, 3451-3460.
35. A. Gregory and M. H. Stenzel, *Prog. Polym. Sci.*, 2012, **37**, 38-105.
36. B. S. Sumerlin, D. Neugebauer and K. Matyjaszewski, *Macromolecules*, 2005, **38**, 702-708.
37. S. S. Sheiko, F. C. Sun, A. Randall, D. Shirvanyants, M. Rubinstein, H. Lee and K. Matyjaszewski, *Nature*, 2006, **440**, 191-194.
38. B. Hammouda, *J. Appl. Crystallogr.*, 2010, **43**, 716-719.
39. S.-i. Namba, Y. Tsukahara, K. Kaeriyama, K. Okamoto and M. Takahashi, *Polymer*, 2000, **41**, 5165-5171.
40. Y. I. Estrin, V. Komratova, G. Estrina, V. Lodygina and B. Rozenberg, *Russ. J. Appl. Chem.*, 2008, **81**, 135-143.

Chapter 3

Anchor group bottle-brush polymers as oil additive friction modifiers

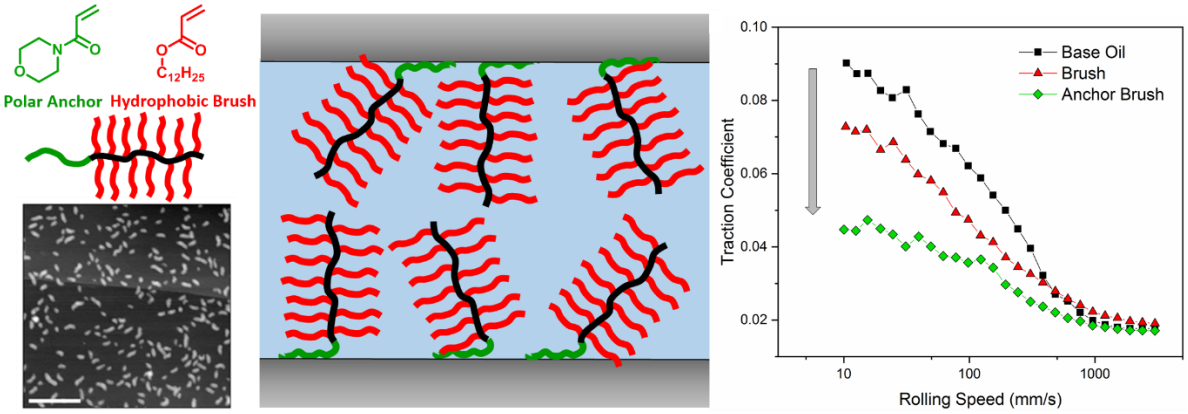

The friction reduction performance of molecular bottle-brushes consisting of a hydrophobic poly(laurylacrylate) core and an anchor group block of polar poly(acryloylmorpholine) was evaluated for oil-based lubrication. RAFT polymerisation was used to access diblock, ABA, BAB or statistical bottle-brush architectures via the jjgrafting from methodology with good control of the resulting materials. QCM-D analysis provided evidence of surface interaction by addition of the anchor group and mini traction machine testing displayed promising results with ≈50% reduction in friction coefficient at low polymer treatment rates (1 wt. %). The introduction of the anchor group is essential for effective friction reduction and in some cases the bottle-brush compounds gave superior performance to commercial additives.

3.1 Introduction

Engine oils contain a complex mixture of additives performing roles as anti-oxidants, wear resistance, viscosity modification and friction reduction. The use of friction modifier additives is essential for control of lubrication in many applications including automotive engines, where an increasing drive for higher efficiencies and use of lower viscosity base oils makes the development of new additives an important area of research. Base oils of lower viscosity can improve engine efficiency by reducing traction when a layer of fluid is maintained between the two moving surfaces, however, the thinner lubricant can be more readily squeezed from the contact and thus increase likelihood of surface contact between asperities at high temperatures, leading to durability issues. To solve this problem the usage of additives to induce the formation of a thin, highly viscous film localised at the metal surface would provide effective lubrication while not substantially impacting the bulk liquid properties. Currently applied commercial friction additives fall under the categories of small molecule organic friction modifiers and organo-molybdenum compounds,[1, 2] however, alternatives such as functionalised polymeric viscosity modifiers,[3] polymer brushes and nanoparticle formulations have received focus in recent years in attempts to reduce fuel consumption and meet increasing environmental regulations.[4-7]

Organic friction modifiers consist of an amphiphilic surfactant structure with a polar head group and aliphatic tail group. They are believed to function primarily through the formation of a monolayer onto the steel surface, whereby the polar head group is adsorbed onto the steel substrate by hydrogen bonding or dipole interactions and the hydrophobic tail provides oil solubility with van der Waals forces between chains (Figure 3.1 A).[8] Close packing of the molecules leads to a densely covered non-compressible film that effectively reduces friction between surface asperities. On the other hand organo-molybdenum based additives, such as molybdenum dialkylthiophosphates, provide a friction reduction only after an initial period in which surface rubbing occurs.[9] These additives are understood to degrade to form a molybdenum disulphide nanofilm, where the planar layered structure of this compound facilitates sliding between layers to dissipate energy and thus provide effective lubrication.

The direct modification of a surface by covalent attachment of a polymer brush layer (as opposed to a molecular bottle-brush) has been shown to drastically reduce friction

between two sliding surfaces.[10-12] For effective friction reduction the selected polymer must have good solubility in the required solvent, the grafting density of chains should be high (favouring the grafting 'from' over 'to' approach[13]), and the molecular weight of the graft also impacts performance. The dense packing of swollen polymer chains disfavours interpenetration of chains on opposing surfaces and the entrapment of solvent molecules within the brush side chains ensures a hydration layer is maintained even under high pressure conditions.[14] The use of zwitterionic monomers is particularly effective for aqueous lubrication due to the high affinity of water molecules to the charged monomer units, offering low friction up to high pressures of 150 MPa.[15, 16] In the case of oil lubrication the grafting from of dodecyl methacrylate onto mica substrates gives excellent friction reduction in hydrophobic solvents such as hexadecane and mineral oil.[17, 18] However, this approach requires pre-functionalisation of a surface, whereas in many commercial applications the preparation of an oil formulation containing a friction reduction additive is a more convenient and cost effective approach.

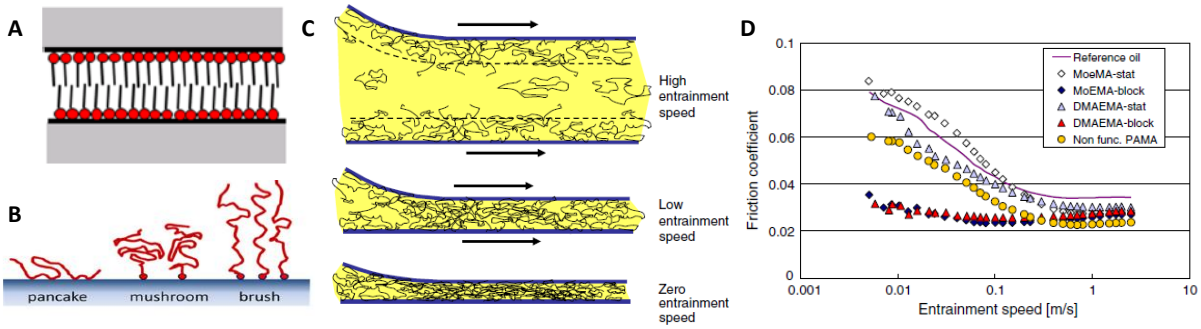

Figure 3.1: A – Mechanism of film formation for organic friction modifiers, adapted from Ref. [1]. B – Density of polymers onto a surface affects the conformation – a brush regime is preferable for lubrication over the 'mushroom', adapted from Ref. [1]. C –Usage of a surface active polymer additive maintains a surface film even at low entrainment speeds, adapted from Ref. [3]. D – Friction coefficients determined by mini traction machine testing of various functionalised viscosity index modifiers, adapted from Ref. [3].

Polyalkylmethacrylates are commonly used as viscosity index improvers in automotive oil formulations and the introduction of a polar polymer block has been shown to endow these materials with lubrication properties due to interaction of the polar block with steel surfaces to form reversibly bound polymer brush-like structures (Figure 3.1 C).[3, 19 -22] Studies were performed on diblocks copolymers consisting of an alkyl methacrylate hydrophobic block and a second polar methacrylate block incorporating a range of functionalities including morpholines, tertiary amines, ureas and short poly(ethylene oxide)s.[3] It was shown polymers with amine or morpholine functionalities were

particularly effective, displaying low friction coefficients (μ = 0.03) at slow entrainments speeds, and additionally an increase of molecular weight was associated with an improved lubrication performance. Statistical copolymers of the same composition offered no friction reduction, consistent with the suspected mechanism of adsorption of the polar block to the steel surface - this interaction is expected to be much stronger for a block architecture than for a statistical copolymer, where only a few monomer units may be able to adsorb at a given point. Being high molecular weight polymers, these additives are promising in that they offer both friction and viscosity improvements from one material.[23] ABA triblock copolymers with end groups introducing surface activity or UCST behaviour have also been investigated for oil based lubrication.[24, 25] Transitioning from a linear polymer to a molecular bottle-brush architecture may provide advantages in the formation of a more densely grafted polymeric film, reducing entanglement interactions.

The use of molecular bottle-brushes has been extensively studied for antifouling purposes and lubrication in aqueous systems,[26-29] often in an attempt to mimic the biological system of articular joints which display very low friction coefficients (μ = 0.001-0.01) over many repeat loading cycles.[30] The remarkable performance of synovial joints is attributed to the complex interaction of a number of components including lubricin, a biomacromolecule which possesses a heavily glycosylated bottle-brush core.[31] It has been shown that electrostatic anchor blocks attached to a solvated bottle-brush unit provide effective surface activity and an ABA triblock bottle-brush mimicking lubricin displayed excellent lubrication performance.[32, 33]

The majority of studies on molecular bottle-brush polymer lubrication has focused on aqueous solutions with comparatively little research into engine applicable oil systems. For friction reduction in this environment a polar anchor group with a hydrophobic, oil soluble bottle-brush segment is required to achieve surface activity analogous to the aqueous systems. Organic friction modifiers consist of a hydrophobic tail and a polar head group, typically a carboxylic acid, alcohol, amine, ester or amide functionality, which binds preferentially with the polar steel surface – incorporating these functionalities into the brush anchor group should be an effective strategy. To this end RAFT polymerisation was selected as the synthetic technique for anchor group bottle-brushes - the high tolerance for functional groups, solvent and reaction conditions make it a convenient

choice for accessing complex polymeric architectures by radical polymerisation. The RAFT grafting from approach with shuttle CTA control has been demonstrated to improve control of bottle-brush synthesis and the introduction of block copolymers into the backbone is facile.[34 - 36] Using this methodology a range of poly(laurylacrylate) (PLA) complex brush architectures were investigated as oil based friction reduction additives.

In Chapter 1 the synthesis of bottle-brush polymers with polyacrylamide side chains was established, leading to the formation of water soluble materials. By polymerising an alternative monomer into the side chain the system can be readily adapted to synthesise oil soluble bottle-brush compounds as required for engine based friction reduction applications, with almost no modification to the synthetic approach. During this chapter the use of PLA bottle-brushes are investigated, with the long C12 alkyl chain providing effective oil solubility, where typically at least a C8 monomer side chain is required for sufficient hydrophobicity.

3.2 Results and Discussion

3.2.1 Poly(laurylacrylate) bottle-brush synthesis

The RAFT 'grafting from' approach using the C12 alkyl chain transfer agent (CTA Acid) would be preferable since it is synthesised by Lubrizol on a large scale, and, as previously shown, it can be used to access poly(hydroxyethylacrylamide) (PHEAm) backbones (Chapter 2). The esterification of the hydroxyl functional backbone was attempted with DCC/DMAP catalysed reaction conditions but led to precipitation of the polymer product out of solution (DMF solvent). NMR analysis of the compound showed 81% functionalisation of the alcohol groups, determined by integration of the CH_2 ester units at 4 ppm compared to the 3.0 – 3.5 ppm region containing the CH_2 groups adjacent to the unmodified OH groups (Figure 3.2). The large difference in solubility between the highly polar PHEAm starting material and the hydrophobic C12 PolyCTA target structure makes it challenging for the reaction to proceed to completion. The use of dimethylacetamide as the reaction solvent increased the yield before reaching the insolubility issues, however, it was still not possible to reach quantitative conversions of the hydroxyl units in one pot. It was therefore necessary to perform a partial esterification in DMF, isolate the polymer, then repeat the conjugation in DCM to access full conversion to the PolyCTA. In

comparison to the procedure with the C4 alkyl PABTC, the process was far less efficient with respect to reagent quantities and time.

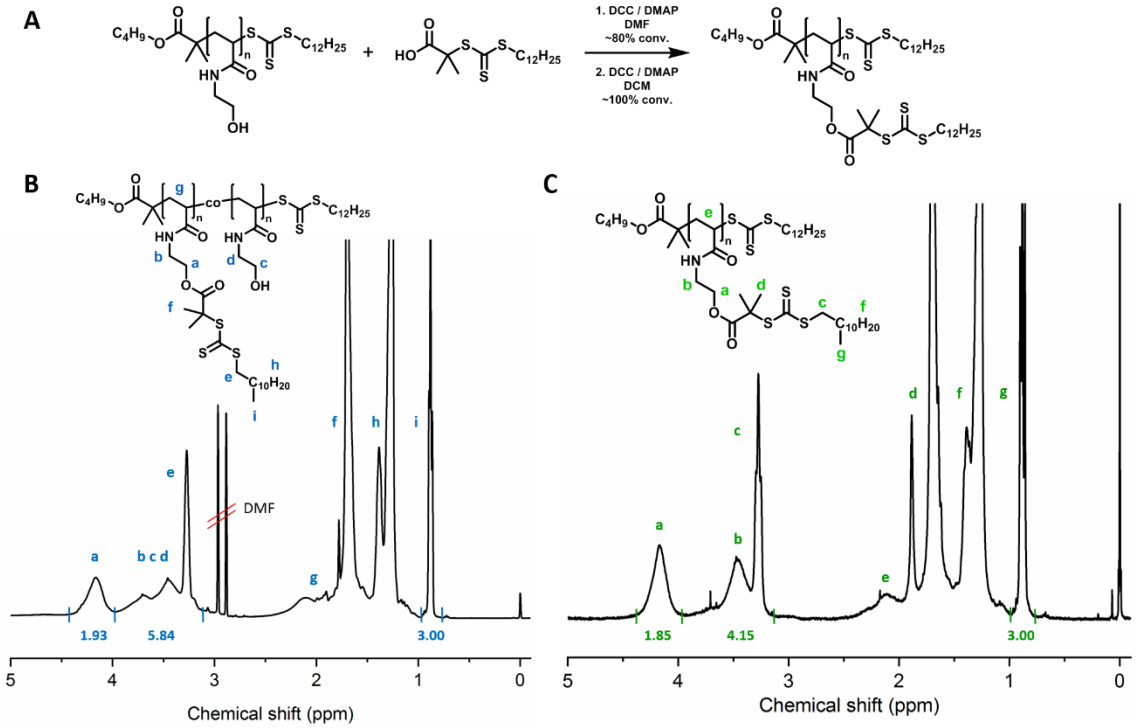

Figure 3.2: A – Scheme of synthesis of PolyCTA with CTA Acid performed in two steps with a solvent switch. **B** – ^{1}H NMR spectra of the partially functionalised product after the first reaction in DMF. **C** – ^{1}H NMR spectra of the final product after the second step.

The grafting from polymerisation of lauryl acrylate (LA) from the PolyCTA backbones to access oil soluble bottle-brush compounds was then attempted. While methacrylates are most commonly used in commercial applications, the higher propagation rate of acrylate monomers over the methacrylate was particularly desirable for the grafting from step of bottle-brush synthesis. Here the minimisation of radical production, mainly achieved by use of low initiator concentrations, is essential to prevent excessive brush-brush coupling terminations and therefore a monomer with faster polymerisation kinetics is preferable. The excellent control achieved through the polyacrylamide systems suggests a similar result could be obtained with the acrylate monomer family, as the determined k_p values are similar among the two families.[37] Furthermore the RAFT agent R group used for the PolyCTA compounds confers poor control of methacrylate monomers, where a significantly better leaving R group is required to obtain narrow dispersities. The preference for use of alkyl methacrylates in commercial viscosity modifiers is primarily due to typically being lower cost and having a higher hydrolytic stability than the corresponding acrylates. The main goal of this study was to identify

properties of various bottle-brush architectures and therefore the use of the synthetically facile acrylate monomer was deemed more suitable for this initial research.

The grafting from polymerisation was performed (target DP75 per side chain) with addition of varying equivalents of shuttle CTA with respect to the PolyCTA to establish the optimal quantity for good control over polymerisation. High monomer conversions were desirable as in industrial applications the full consumption of monomer is typically required to be cost effective and avoid difficult purification steps. Residual monomer in the final product can lead to problems such as toxicity and reduction of flashpoint, therefore must be registered as by-products. Compared to the previously studied acrylamide monomers, for LA significantly higher initiator concentrations were required to reach moderate monomer conversions ([I] = $1*10^{-3}$ mol) and, even with the addition of 1 equivalent shuttle CTA, polymerisations exceeding ~80 % monomer conversion caused significant high molecular weight shoulders in the SEC traces, while containing large amounts of linear polymer side product (Appendix, Figure B.1). It is theorised that this is a result of the lower propagation rate observed for LA necessitating higher radical production, thus reducing the side chain livingness. Even in the absence of shuttle CTA the formation of linear polymer was observed, caused by the production of initiator derived chains transferring the CTA group from the PolyCTA backbone into solution. This is more prevalent than in previous polymerisations as a result of the higher azo initiator concentrations used.

SEC molecular weight distributions revealed the formation of high molecular weight shoulders in the absence of shuttle CTA (Figure 3.3), most significantly for the longer DP500 backbone bottle-brush, while presence of shuttle CTA lead to the complete removal of this shoulder concomitant with increased production of linear polymer. Under these reaction conditions increasing equivalents of the shuttle CTA from 0.5 to 1 offers no improvement in control at the same monomer conversions of 70 %. Balancing the goal to reach high monomer conversions with the minimisation of linear polymer led to the selection of conditions with 0.5 eq. shuttle CTA targeting a monomer conversion of ~70 %. This procedure was carried out to synthesise PLA bottle-brushes of DP100 and DP500 backbones (Table 3.1), where AFM imaging confirmed the expected cylindrical structure

transitioning from a short to long worm-like morphology (Figure 3.3 C + D). The materials were found to be fully soluble in a range of mineral oils (groups II and III).

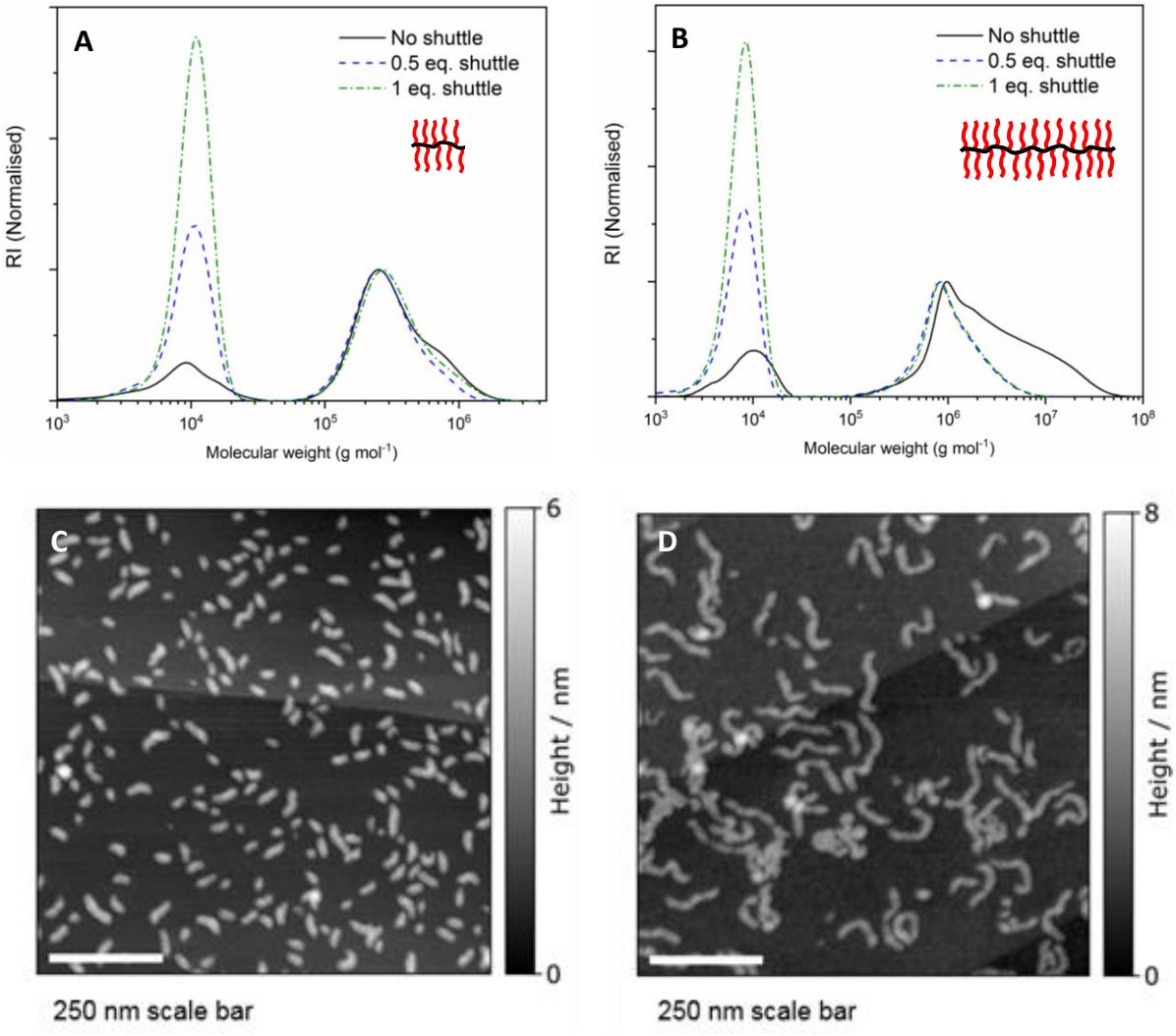

Figure 3.3: A – SEC molecular weight distributions of the grafting from step of the DP100 PolyCTA with varying quantities of shuttle CTA. **B** – The same experiment with the DP500 PolyCTA backbone. **C and D** – AFM height images of the short and long bottle-brushes deposited onto an HOPG substrate.

3.2.2 Low grafting density comb polymers

As an additional parameter to control the molecular architecture, the grafting density of the bottle-brush side chains can be readily altered by copolymerising a non-functional monomer into the hydroxylated backbone, leading to the formation of comb polymers. To investigate this LA was copolymerised with hydroxyethylacrylate (HEA), the change of monomer from the acrylamide to the acrylate version should ensure that a similar reactivity ratio between the LA and HEA is maintained and therefore a statistical copolymer will be synthesised. In this case the grafts will be randomly distributed along

the backbone and can therefore be considered a comb polymer, whereas if the monomers had significantly different reactivity ratios a gradient copolymer would be created.

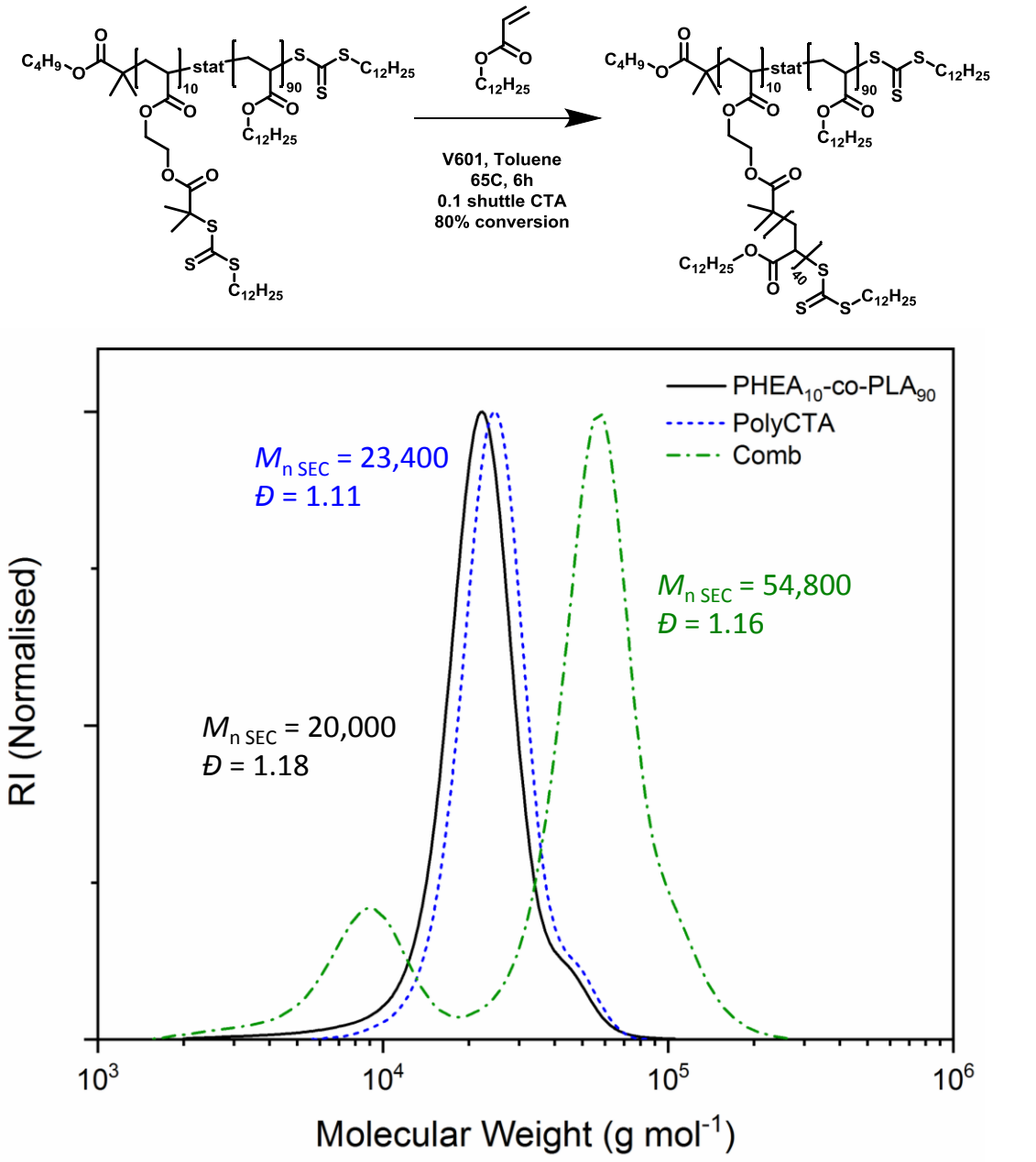

Figure 3.4: Top – scheme for grafting from step from the comb precursor PolyCTA. Bottom – SEC molecular weight distributions of the starting backbone copolymer, the modified PolyCTA and the derived PLA comb copolymer. For the comb polymer trace the recorded $M_{n\ SEC}$ and $Đ$ values disregard the low molecular weight linear polymer species.

The esterification with CTA units proceeded with no solubility issues and the grafting from polymerisation was significantly easier to control than the dense bottle-brushes, with only 0.1 eq. shuttle CTA required to prevent formation of high molecular weight shoulders in addition to reaching slightly higher monomer conversions of 80% (Figure

3.4). The improved control for the comb polymers is attributed to the reduction in the number of side chains per macromolecule, decreasing the number of potential sites that could cross-link through radical terminations.

Triple detection SEC was used to more accurately determine the molecular weights of the bottle-brush and comb polymers, both of which were significantly underestimated by the conventional poly(methylmethacrylate) calibration standards. The discrepancy in difference of $M_{n\ theo}$ and the $M_{n\ SEC}$ was greater for the bottle-brushes than for the comb polymer, reflecting the increased branching density of the brush system causing a more significant deviation in hydrodynamic volume between that of branched macromolecules with the linear calibration standards (Table 3.1).

Table 3.1: Summary of SEC analysis data performed with $CHCl_3$ eluent system on a linear, comb, short and long bottle-brush consisting of PLA. The α values and $M_{n\ DALS}$ were determined by triple detection with dual angle light scattering detectors.

Sample	$M_{n\ theo}$ (g mol^{-1})	$M_{n\ SEC}$ (g mol^{-1})	$M_{n\ DALS}$ (g mol^{-1})	Đ	α
Linear PLA	12,260	7,079	12,900	1.11	0.54
Comb	126,200	54,800	124,000	1.16	0.36
DP100 Brush	1,007,000	185,000	1,209,000	1.16	0.29
DP500 Brush	4,795,000	775,300	5,227,000	1.27	0.33

Furthermore, Mark-Houwink plots were used to determine the α values of each sample, where a trend of lower values for higher density structures (linear, comb, brush) was observed (Figure 3.5). The linear polymer displays the highest value (0.54), within the typical range of linear flexible polymers (0.5 – 0.8), perhaps on the lower side due to relatively bulky C12 alkyl side chain of PLA. Comparing a branched polymer to a linear polymer of the same molecular weight, it will exhibit a smaller hydrodynamic volume due to the denser packing of the material and thus a lower intrinsic viscosity. The low α values (<0.4) of the graft polymers is typical of branched structures suggesting their conformation in solution is closer to a hard sphere than a Gaussian coil, providing evidence for the successful synthesis of the targeted structures. Being architecturally identical the DP100 and DP500 traces overlay with very similar α values indicating reproducible control of the grafting from synthesis.

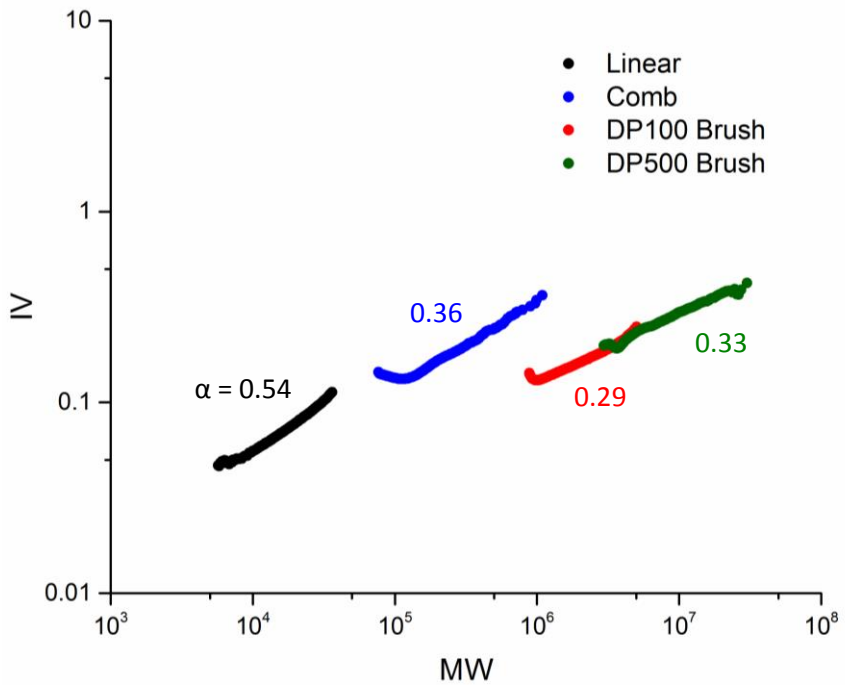

Figure 3.5: Mark-Houwink α values determined by SEC triple detection.

3.2.3 Anchor group bottle-brushes

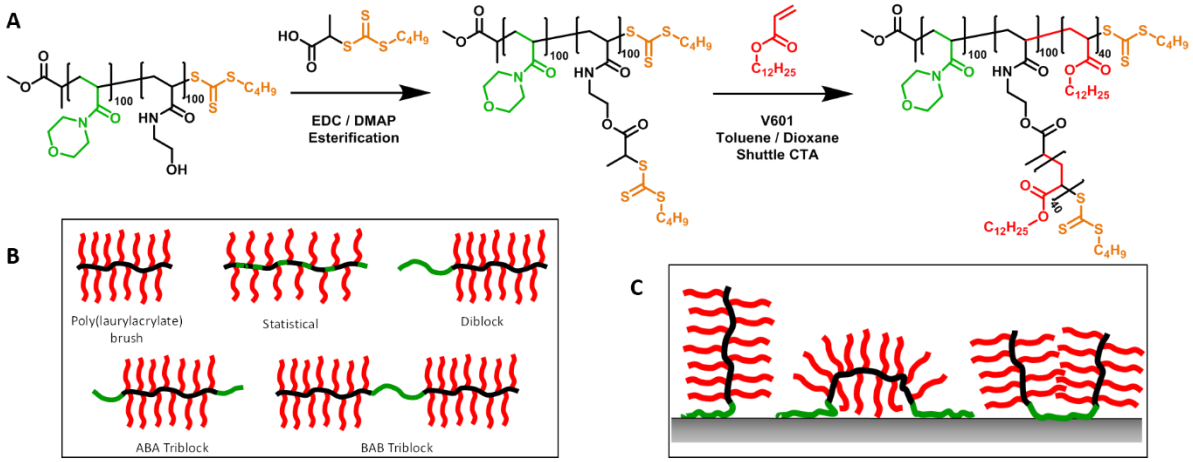

Figure 3.6: A –Synthetic scheme for diblock anchor group bottle brush polymer using a RAFT grafting from approach. B – Structural representation of the 5 brush materials studied in this work. C – Possible conformations of anchor group materials when interacting with a surface.

After demonstrating the success of the RAFT shuttle CTA grafting from approach for the synthesis of oil soluble poly(laurylacrylate) (PLA) based bottle-brush and comb polymers, the incorporation of a polar anchor group to form an amphiphilic material was attempted (Figure 3.6). Poly(*N*-acryloylmorpholine) (PNAM) was selected as the polar anchor group because block copolymers with HEAm can be readily prepared (Chapter 2), and the amide unit has been shown to possess good surface activity for lubrication applications.[38] While the use of the commercially produced CTA Acid proved possible

for bottle-brush synthesis, the esterification step was significantly more time consuming and inefficient than the previously studied PABTC RAFT agent, and therefore for the synthesis of the anchor group bottle-brushes on a larger scale (10 g) the use of PABTC was preferred. Firstly as a control an un-functionalised PLA bottle-brush with a molecular weight of ~1*10^6 g mol^{-1} was studied (DP100*46); this was synthesised by the standard grafting from approach with 0.5 equivalents of shuttle CTA in the final step.

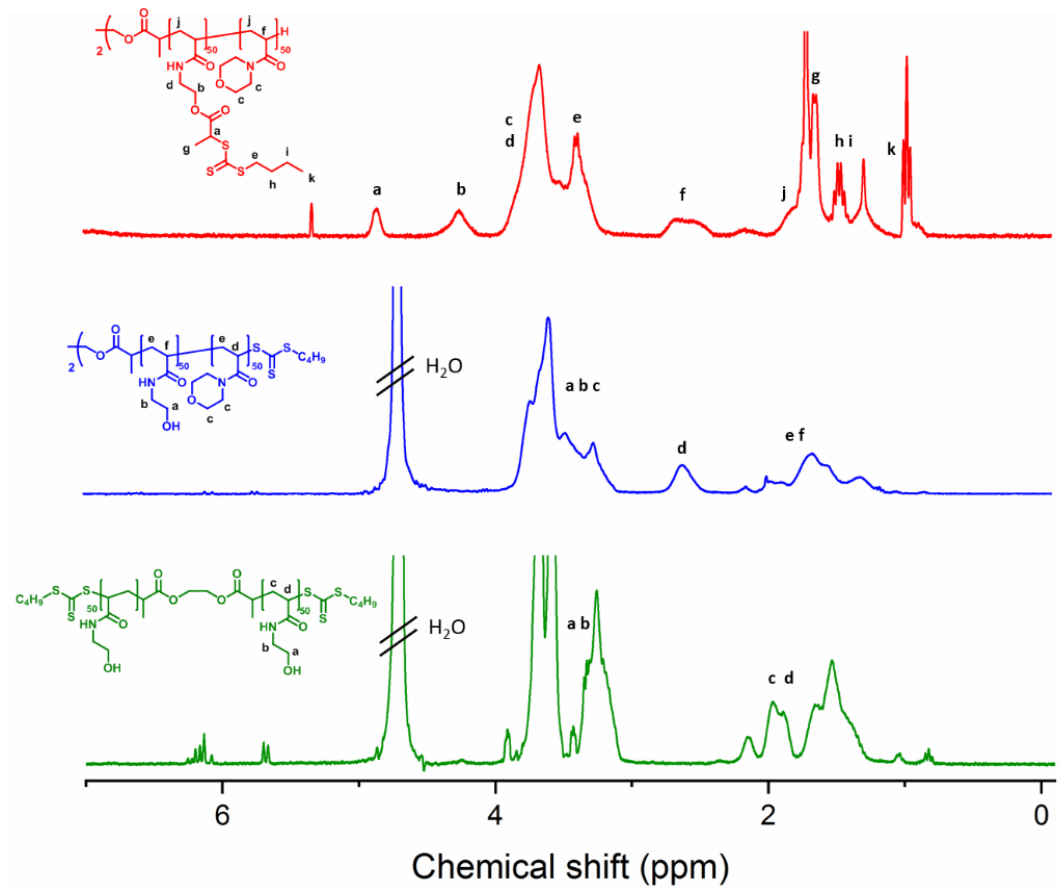

Figure 3.7: ^{1}H NMR analysis of a) polymerisation mixture of the first PHEAm block performed in D_2O. Monomer conversion was determined to be 95% and the polymer was purified by precipitation prior to chain extension, b) polymerisation mixture of ABA triblock copolymer backbone in D_2O, c) PolyCTA ABA backbone in $CDCl_3$.

Previous research shows the necessity of incorporating the polar group as a block to ensure effective surface activity. To confirm this trend also applied to bottle-brush materials, compounds with the PNAM anchor installed as a diblock and as a statistical copolymer among the backbone were synthesised. For these compounds the starting backbone material was prepared as either a diblock of NAM_{100}-b-$PHEAm_{100}$ or by copolymerising the same quantity of monomers in one step to access a statistical copolymer. Following the same synthetic procedure as before yielded oil soluble

amphiphilic bottle-brushes with the PNAM block as a diblock or statistically. ^{1}H NMR analysis of each step confirmed the presence of PNAM in the expected molar ratio to PHEAm as determined by comparison of integral at 2.5 ppm (PNAM backbone H) with either PHEAm or PolyCTA proton environments (Figure 3.7). We were also interested in investigating alternative architectures in addition to the diblock - using an ABA triblock copolymer backbone with two anchor groups may invoke formation of a loop conformation upon surface interaction, whereas the 'dumbbell' like BAB triblock could lead to formation of a film with denser surface coverage (Figure 3.6 C). For these bottle-brush backbones a di-functional CTA was used to access a symmetrical triblock copolymer in two polymerisation steps (Figure 3.9).

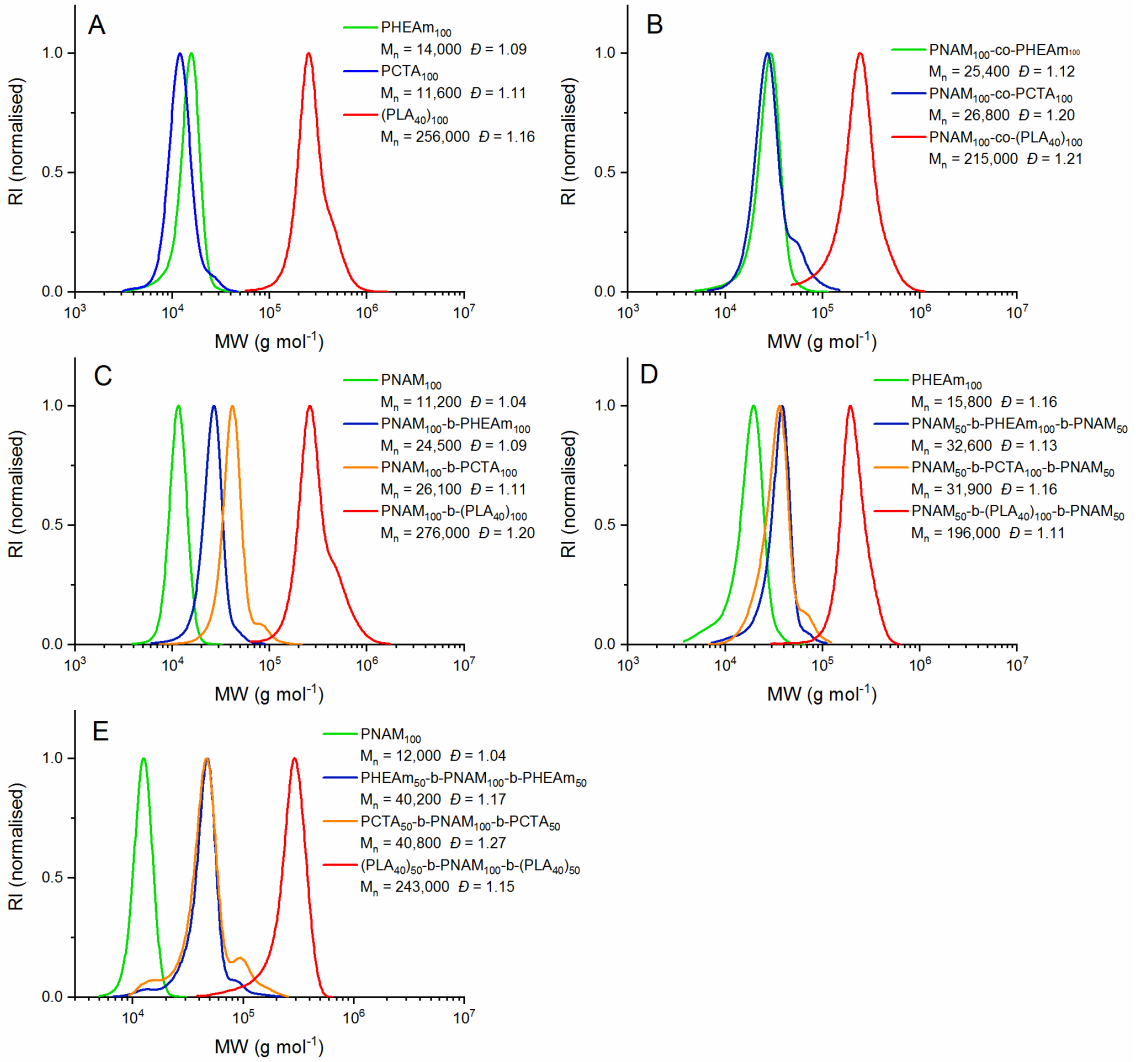

Figure 3.8: SEC molecular weight distributions of A – PLA brush, B – Statisical brush, C – Diblock brush, D – ABA Triblock brush, E – BAB triblock brush. The backbones and PolyCTA polymers were analsyed in DMF SEC conditions, whereas the final PLA bottle-brushes were analysed in $CHCl_3$ SEC due to

differences in solubility. The PLA bottle-brushes contain shuttle CTA derived linear polymer chains which have been omitted for clarity, see Figure B.6 for the full distributions.

SEC analysis of the block copolymer backbones shows relatively narrow dispersities <1.3, although upon esterification to form the PolyCTA intermediate, the formation of a small high molecular weight shoulder was observed (Figure 3.8). ^{1}H NMR analysis confirmed almost full conversion of pendant alcohol groups into esterified CTAs (Figure 3.6) and integration of the PolyCTA monomer unit proton environments with that of PNAM confirmed the desired 1:1 ratio of each block. During the final grafting from step of the PLA side chains, free shuttle CTA was added (0.5 eq. with respect to the backbone CTAs) which improved control of the polymerisation and enabled moderate monomer conversions of ~60% to be reached without the occurrence of substantial bimolecular terminations. This approach means the brush compounds contain ~33 wt. % shuttle CTA derived linear PLA side products (Figure B.6), while undesirable these polymers are not expected to possess substantial friction reduction properties and thus should not interfere with the interpretation of material performance. Additionally a linear PLA of the same molecular weight as the bottle-brush side chain was synthesised to determine its surface activity properties.

Table 3.2: Summary of brush compounds synthesised in this study. Triple detection SEC with dual angle light scattering analysis performed with instrument using $CHCl_3$ eluent at 30 °C with 2 % TEA additive.

Sample	Structure	$M_{n\ theo}$ (g mol^{-1})	$M_{n\ SEC}$ (g mol^{-1})	$M_{n\ DALS}$ (g mol^{-1})	Đ	dn/dc
PLA Brush	$(PLA_{46})_{100}$	1,162,000	256,000	1,168,000	1.16	0.036
Diblock	$PNAM_{100}$-b-$(PLA_{53})_{100}$	1,320,000	276,000	1,466,000	1.20	0.041
BAB triblock	$(PLA_{46})_{100}$-b-$PNAM_{100}$-b-$(PLA_{46})_{100}$	2,338,000	243,000	2,585,000	1.15	0.038
ABA triblock	$PNAM_{50}$-b-$(PLA_{48})_{100}$-b-$PNAM_{50}$	1,212,000	196,000	973,000	1.11	0.041
Statistical	$PNAM_{100}$-co-$(PLA_{44})_{100}$	1,123,000	215,000	1,156,000	1.21	0.038

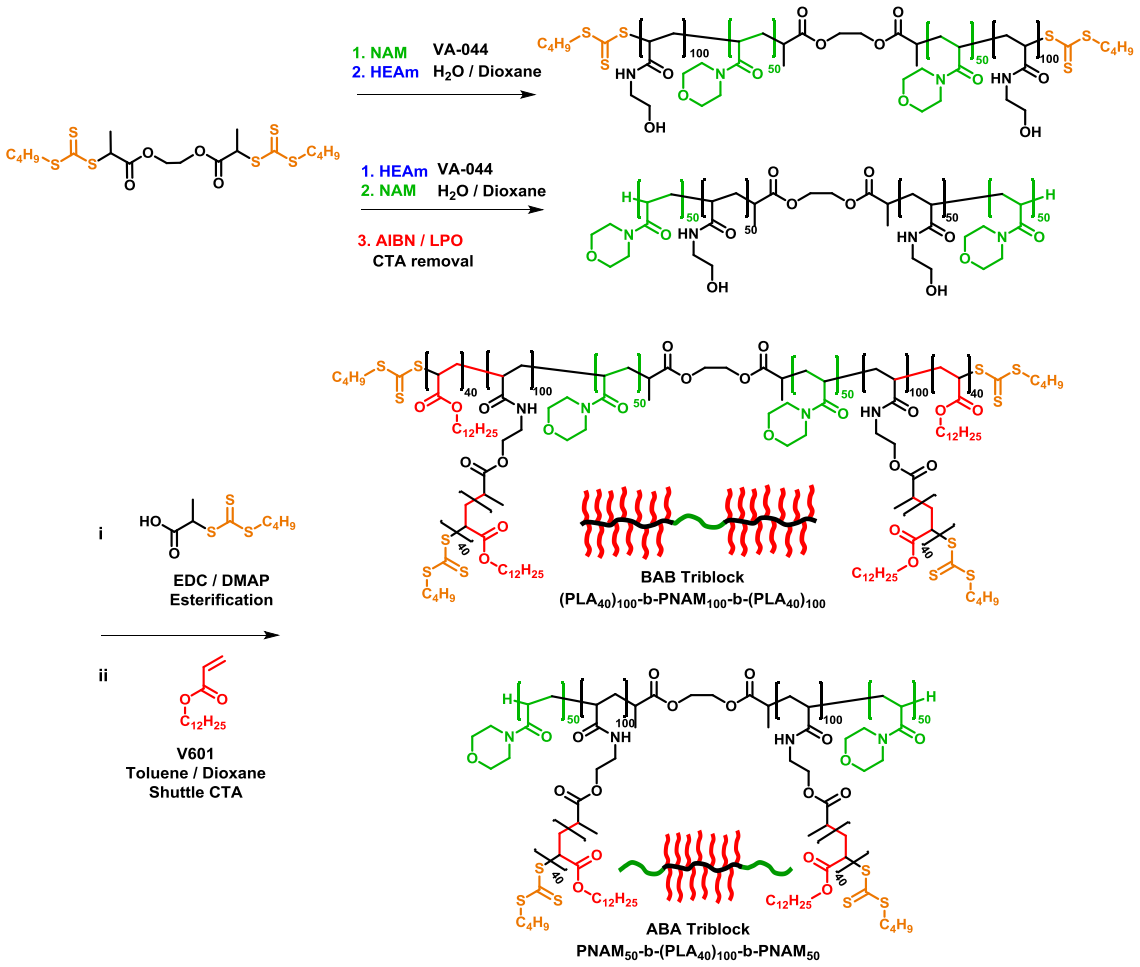

Figure 3.9: Scheme for synthesis of the ABA and BAB triblock backbone bottle-brushes.

In all compounds the DP of the brush backbone (DP100) and PLA side chains units (~DP45) were kept approximately constant and the total amount of NAM anchor group limited to DP100 to provide an architectural comparison between the compounds while ensuring good solubility in oil (Table 1). Initial attempts using higher MW anchor groups of PNAM (DP200-400) on the diblock brush led to difficultly achieving solubility in mineral oil, even at high temperatures, and promoted formation of inverse micelles in organic solvents as evidenced by DLS (Figure 3.10). Upon changing the solvent from toluene to hexane an increase in particle size was observed for the longer DP200 / 400, indicative of aggregation in a more hydrophobic solvent which has poor affinity for the polar PNAM anchor. The DP100 anchor group brush showed significantly smaller size than the other length anchors (20 nm vs >40 nm) in hexane suggesting the shorter polar region disfavours aggregation. Solubility issues in mineral oil were also encountered for an ABA triblock brush with two DP100 PNAM anchor groups therefore this was

shortened to DP50 each in the final material. Previous literature suggests addition of 10% molar polar monomer units into linear friction reducing polymers for good activity,[182] however, in these materials a reduction from this value to 1.40 wt. % was necessary (0.7 wt. % for the BAB compound). As the size of the brush segment is kept at constant MW across all the compounds, the BAB dumbbell has twice the molecular weight of the other compounds. AFM imaging shows an individual PLA brush molecule has a length of ~25nm consistent with the maximum extension of a DP100 backbone (0.25nm per monomer unit).

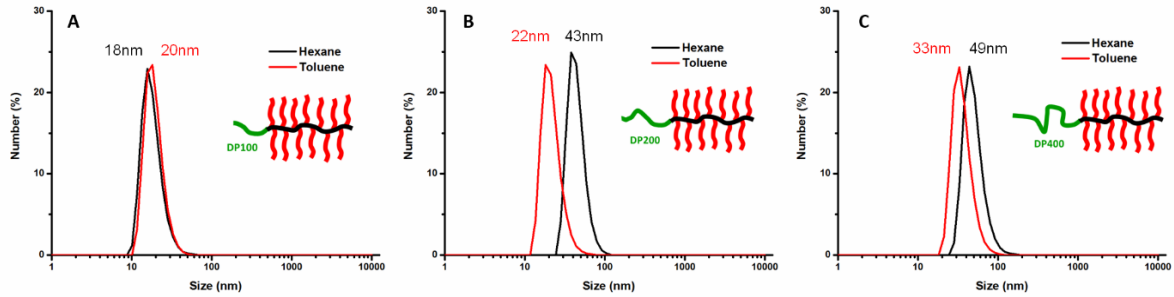

Figure 3.10: DLS analysis of diblock anchor group bottle-brushes with varying DP of the PNAM anchor group. DP = A – 100, B -200, C – 400.

3.2.5 RAFT End group removal

For the ABA triblock an additional CTA removal reaction on the backbone was performed prior to esterification with CTA. If these end groups were retained, during the grafting from step additional PLA blocks would be extended from the PNAM anchor groups which might interfere with their surface activity. In the case of the diblock and BAB triblock compounds the initial CTA groups will chain extend in the same manner described, however, since they are directly attached to the bottle-brush they effectively create additional polymeric bristles which are negligible in context of the 100 side chains of the brush. A number of trithiocarbonate end group removal procedures have been reported in the literature; such as aminolysis, thermal decomposition and Diels-alder modifications.[39] The use of a radical reduction method was particularly appealing, however, due to the introduction of an H end group which should provide a clean method of capping the polymer (Figure 3.11). Introduction of other end groups such as thiols / maleimides (*via* the aminolysis approach) may complicate surface interactions through these species, whereas the H end group should have minimal impact and thus isolate efficacy of the PNAM anchor.

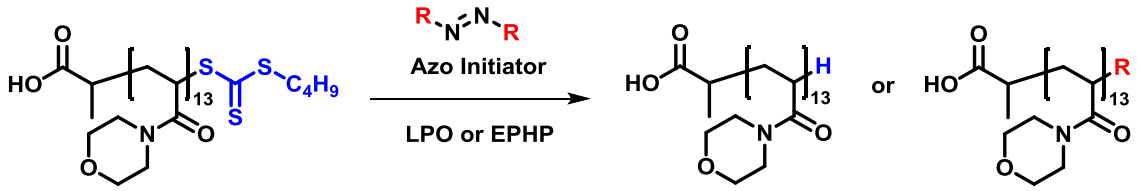

Figure 3.11: Scheme for RAFT agent end group removal by radical reduction leading to two main potential products – either capped with an H or an initiator fragment.

Several reaction conditions for the radical reduction have been reported by Moad et al., including the use of an azo initator with either lauroyl peroxide (LPO)[40] or ethyl piperidne hypophosphite (EPHP).[41] In the case of LPO, the C12 alkyl radical formed as a result of the thermal decomposition of the initiator was suggested to irreversibly add to the trithiocarbonate, causing the intermediate radical to fragment to the polymeric side and thus cleave the RAFT end group. The addition of azo initiator was necessary to inhibit bimolecular termination of the resulting polymeric radical. The study suggests that the polymer is finally capped with an initiator fragment although provides little analytical evidence for this. Alternatively EPHP has been used as an H donor in the radical reduction of xanthates,[42] performing in a similar manner to the reagent tributylstannane but with much lower toxicity and high water solubility. A variety of reaction conditions were explored on a low molecular weight DP13 PNAM to facilitate analysis by MALDI-ToF and characterise end group functionality.

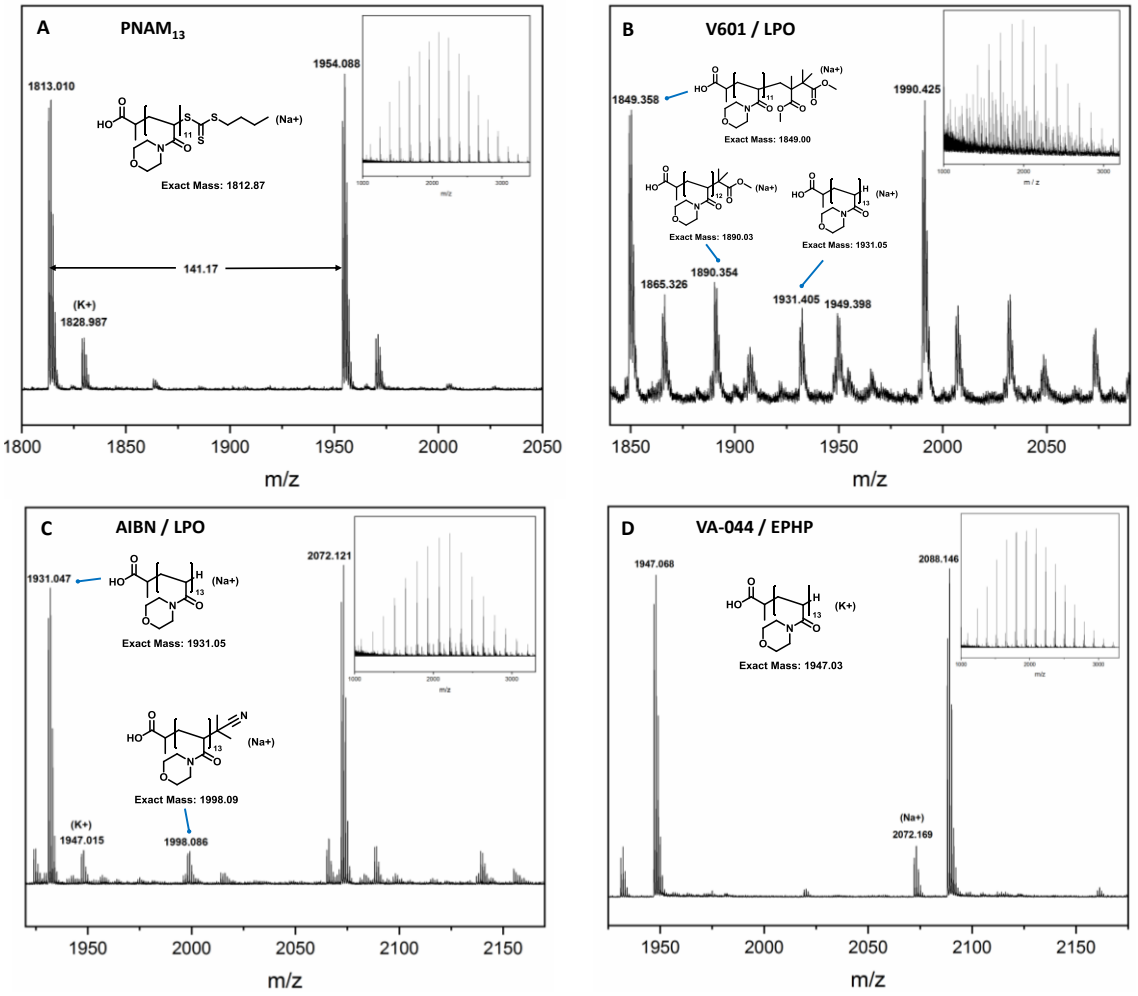

Figure 3.12: MALDI-ToF spectra of PNAM species. A – DP13 PNAM synthesised with PABTC. B – PNAM reacted with V601/LPO reagents. C – Reaction performed with AIBN/LPO reagents. D – Reaction performed with VA-044/EPHP.

Initial attempts using the azoinitiator V601 in combination with LPO lead to the formation of multiple populations, of which included the H terminated compound, presumably formed by disproportionation of a polymeric radical with a fragmented radical of the V601 initiator, and the product of the same termination occurring through a recombination mechanism to yield an initiator fragment end group (Figure 3.12). The presence of several other populations can be explained by the ability of V601 to produce methylmethacrylate (MMA) monomers by self-disproportionation of the decomposed radical (Figure 3.13), which considering the 20 equivalents of azo initiator used with respect to the CTA end group, could lead to the formation of a significant quantity of MMA. Evidence for the introduction of an MMA unit onto the $PNAM_{13}$ starting material was observed (m/z 1849.3). A possible mechanism for the formation of the observed products is outlined in Figure 3.14 where the propagation of MMA monomer onto the

PNAM radical, and subsequent termination, explains the formation of the main population species.

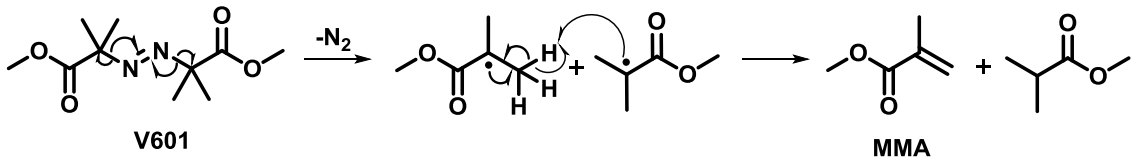

Figure 3.13: Decomposition and termination by disproportionation of V601 to produce methylmethacrylate (MMA) as a side product.

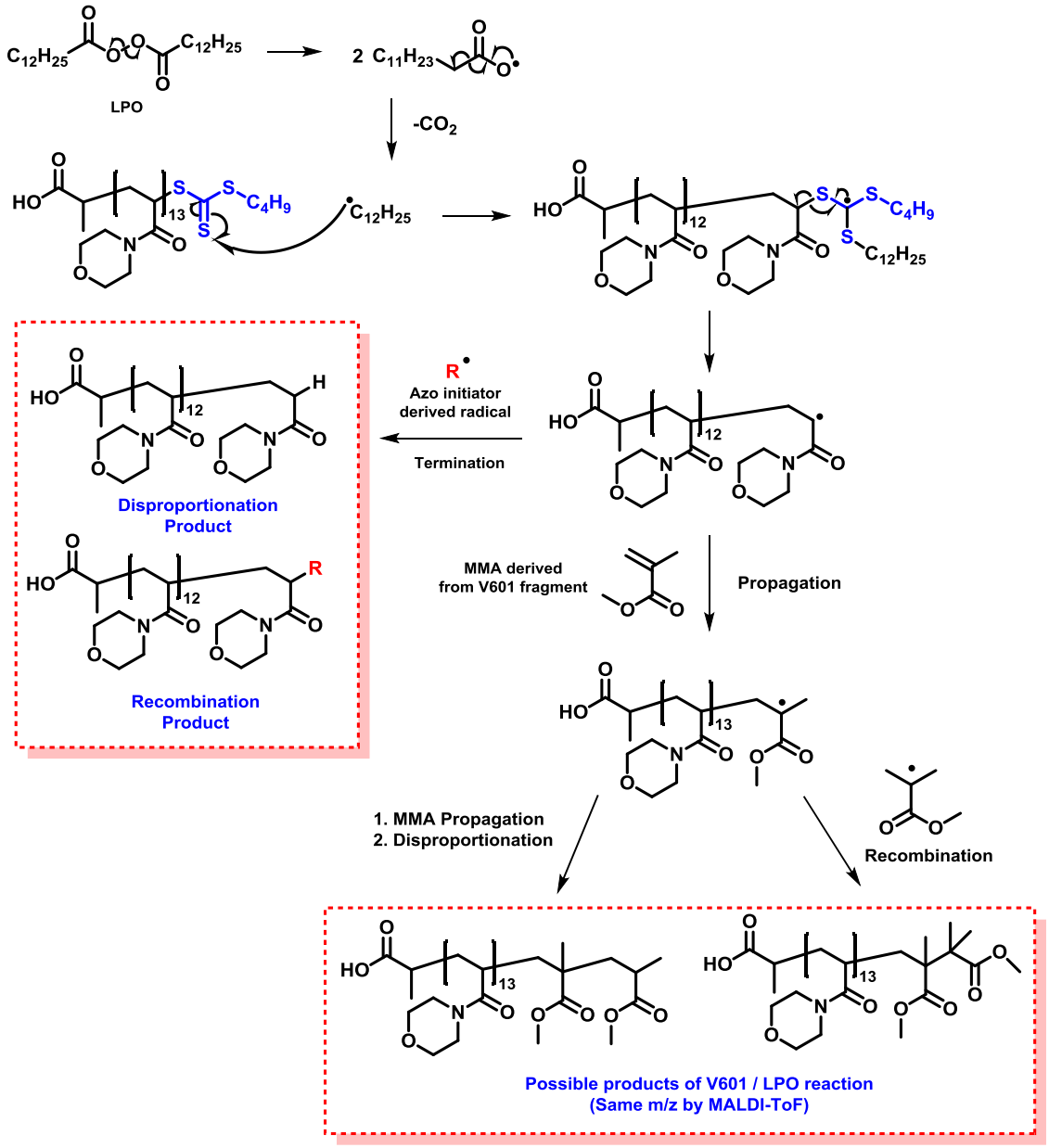

Figure 3.14: Potential mechanism for the RAFT end group removal of the $PNAM_{13}$ with the V601 / LPO reaction conditions. Usage of AIBN / LPO yielded only products in the upper red outlined box.

Under the same conditions with AIBN as the azoinitator, a much cleaner spectra is obtained with predominately H terminated polymers formed and a second minor population incorporating the AIBN derived fragment as the end group, although MALDI-ToF is not a quantitative technique. This demonstrates the large number of populations in the V601 reaction is caused by a side reaction with this initiator specifically, most likely due to the formation of MMA as described. Alternatively the use of EPHP/VA-044 generated entirely the H terminated group with no addition of the initiating species, consistent with the H donor reactivity of the EPHP reagent. The two techniques of AIBN/LPO and VA-044/EPHP were identified as the most effective, offering complementary reaction conditions in terms of solubility and purification options – AIBN/LPO has good solubility in organic solvents whereas the EPHP/VA-044 combination is water soluble. In the case of the ABA backbone the AIBN/LPO methodology was used for the CTA reduction step, whereby analysis by SEC with UV absorption at 309 nm revealed quantitative trithiocarbonate removal (Figure B.4). Precipitation into diethyl ether removed all side products to yield a pure polymer.

3.2.6 Quartz crystal microbalance with dissipation (QCM-D).

QCM-D is a powerful technique to study the interaction of materials with surfaces and was used to assess if the PNAM anchor group promoted adsorption of the polymer bottle-brushes. The QCM is based on the principle of the piezoelectric effect, whereby application of a voltage causes material deformation and *vice versa*.[43] In a QCM instrument an alternating voltage is applied across a thin ~300 µm quartz chip, causing a cyclical oscillation, and by matching the frequency of the voltage to the resonance frequency of the crystal a standing wave is formed. If mass is deposited onto the QCM chip the thickness will be increased by a fractional amount, thus alterating the resonant frequency and by detecting this change the instrument can function as an extremely sensitive mass sensor. This frequency change can be used to calculate mass by the Sauerbrey equation (Figure 3.15), however, this relies on the assumption that the deposited mass behaves as a rigid film. In QCM-D the dissipation is additionally monitored by brief periods of switching off the voltage and examining the decay in oscillation. A rigid layer can be considered an extension of the quartz chip with minimal effect on the dissipation and thus alters the resonant frequency by a readily calculable amount, whereas for a soft, viscoelastic film the oscillations will be dissipated and thus

the Sauerbray model becomes inaccurate. In this case the more complex Voigt model can account for the viscoelastic behviour of the adsorbed layer and uses the measured dissipation to provide more information. Additionally the measured mass of adsorbed film is not purely composed of the tested compond but also includes solvent molecules either as the hydration shell or trapped within the layer which is an additional source of error.

$$\Delta f = -\frac{2\Delta m {f_0}^2}{A\sqrt{(\rho_q \mu_q)}}$$

Figure 3.15: The Sauerbrey equation where Δf = change in resonance frequency, Δm = change in mass adsorbed onto QCM surface, f_0 = fundamental resonance frequency, A = piezoelectrically active area, p_q = quartz density and μ_q = quartz shear-modulus.

Solutions of 0.1 wt. % polymer additive in dodecane were flowed over a quartz crystal chip coated with a steel surface, these conditions provide a similar environment to the desired application as a friction modifier additive in oil based engine fluids. Upon addition of the polymer additive solution a sharp decrease in Δf is observed which plateaus over the course of 1 hour indicating mass adsorption onto the surface (Figure 3.16). After a dodecane rinsing step the diblock material produces a larger final frequency change of -15 Hz in comparison to -10 Hz for the unfunctionalised PLA bottle-brush, suggesting the diblock does indeed lead to increased surface adsoprtion. The reduction in magnitude after rinsing shows a substantial amount of unattached polymer is removed in both cases, perhaps due to build up of multiple layers of weakly attached brush molecules. As a comparison the linear PLA_{50} homopolymer was also analysed, which showed a significantly lower mass adsorption and dissipation change than the bottle-brushes. The smaller molecular size of the linear polymer makes it more likely to form rigid films than the larger bottle-brushes, corrobating with the smaller change in dissipation, which is of sufficiently low value that mass changes could be calculated with the Sauerbrey model. Faster rate adsorption kinetics with a shorter time to reach plateau values can also be attributed to increased mobility of the linear chains and lack of surface conformation rearrangements that may be occuring as for the bottle-brushes.

The observed change in dissipation for the anchor group brush is the largest of all the samples with a value over twice that of the un-functionalised PLA brush. The properties of the polymer layer formed affects the dissipation change and an increase demonstrates

the creation of a viscoelastic film which is expected for a thick layer of bottle-brush polymer. The evolution of the relationship of ΔD vs Δf (Figure 3.15) shows a linear increase to begin with for both brush compounds, implying the initial adsoprtion interaction is similar. For the PLA brush trhe ratio remains roughly constant across the experiment, however, for the diblock an upturn in gradient is observed after ΔD = 2.5. This corresponds to the time point after the sharp decrease in frequency when the value begins to plateau, and is indicative of a slower confromation shift occurring on the surface leading to a change in the nature of the polymeric film. This can be rationalised by the gradual adherence of the polar anchor group onto the surface causing the brush to 'stand up' leading to the formation of a thicker more viscoelastic film, as opposed to the PLA brush which is more likely to lay flat across the substrate and possibly interact *via* the slightly polar PHEAm backbone.

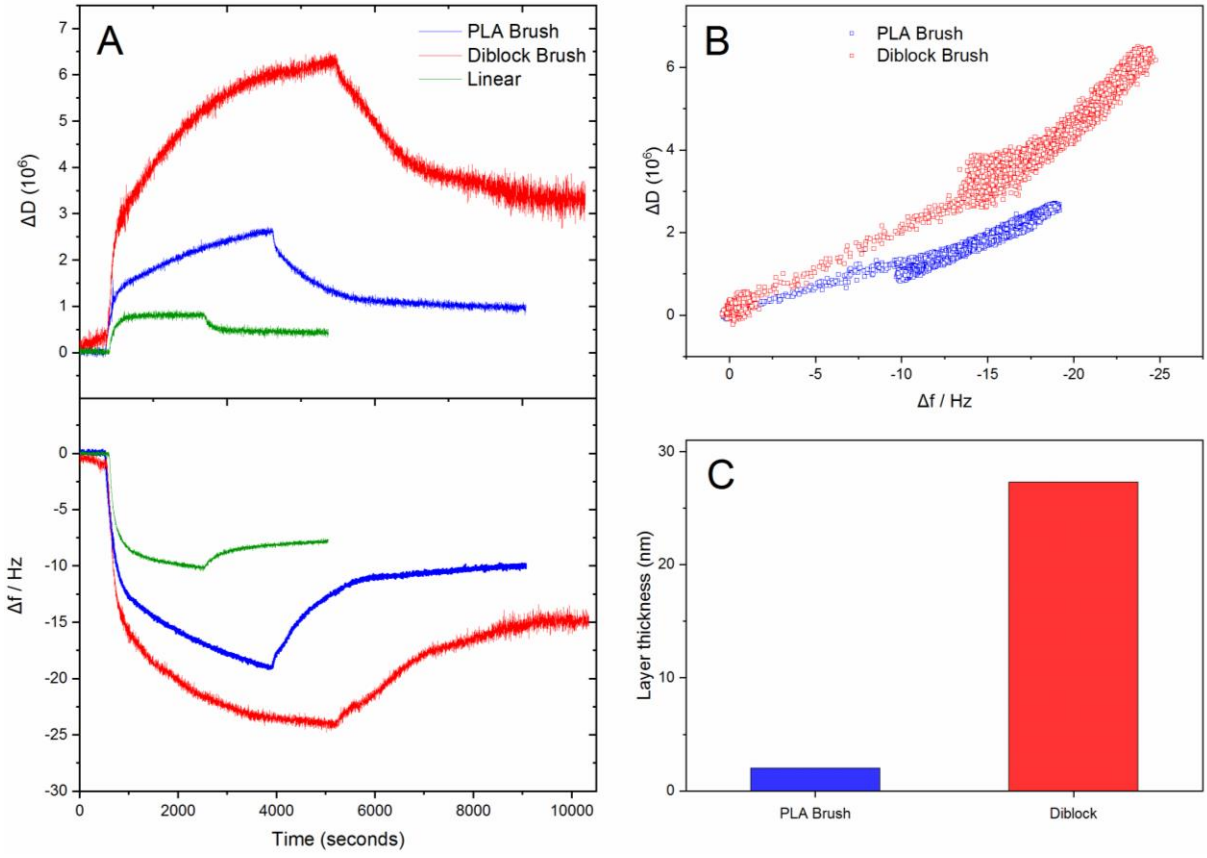

Figure 3.16: A - QCM analysis of the linear PLA, brush PLA and anchor group diblock brush compounds. B – Relationship of ΔD *vs* Δf over time for the brush compounds. C – Layer thicknesses calculated by the Voigt model.

The Voigt model is more suitable for films which cause a significant change in dissipation and therefore was used to calculate the mass of adsorbed material and the layer thickness

for the bottle-brush compounds.[44] The diblock brush forms a significantly thicker film of 27 nm rather than only ~2 nm for the PLA brush, consistent with increased affinity of the polar anchor block. Notably the value is similar to that of the expected length of the backbone at full extension (~25 nm) suggesting a thick surface coverage.

3.2.7 Mini traction machine testing

The friction reduction performance was assessed with a mini traction machine (MTM), which consists of a steel ball loaded in contact with a steel disc where both parts are able to rotate independently to alter the slide/roll speed. Lubricant with the additive is placed in the contact in a controlled temperature environment, and the friction between the two parts at varying entrainment speeds measured by a force transducer. Testing was performed across a temperature range of 40 – 140°C at 1 wt. % treatment rate in a group III oil to generate Stribeck curves for each sample. Since the brush samples contain linear polymer side product the effective treatment of actives is closer to 0.65 %, very low for typical formulations. A representative Stribeck curve is shown in Figure 3.17, which identifies 3 different regimes of lubrication. The boundary regime is defined by direct contact between the asperities of the opposing surfaces with correspondingly high friction, the hydrodynamic regime by a thick layer of lubricant fluid supporting the load between the surfaces and the mixed regime representing a combination of the other two. In the hydrodynamic regime the friction coefficient is primarily affected by the properties of the fluid (viscosity), whereas upon entering the boundary/mixed regime film forming properties of additives and surface interactions become increasingly important.

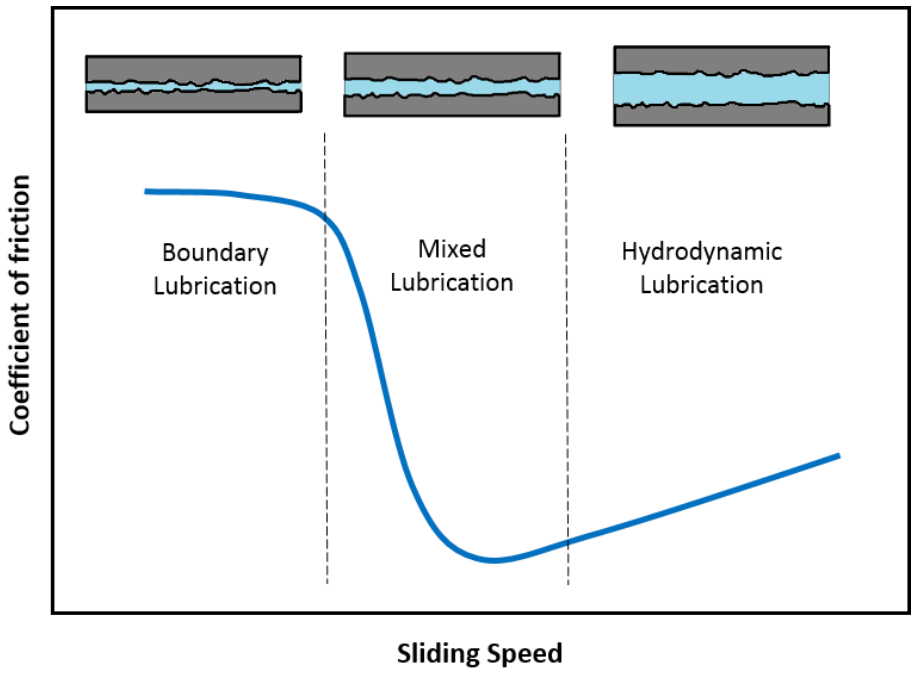

Figure 3.17: Stribeck curve with schematics at top outlining each regime.

Figure 3.18 shows data comparing base oil to test brush samples, the commercially used organic friction modifier glyceryl monooleate (GMO) and an un-functionalised viscosity modifier linear poly(alkylmethylacrylate) (PMA) as controls. In all cases the presence of additive leads to a substantial decrease in friction coefficient, particularly at slow rolling speeds, with excellent performance from the BAB triblock reducing friction by ≈50 % at 120 °C, 10 mm/s rolling speed with respect to the base oil. The PLA brush shows slightly superior performance to that of the linear PMA, although both are quite poor friction modifiers – even the weakly interacting bottle-brushes may be more effective as a result of the increased molecular size compared to that of the linear polymer. The introduction of anchor group evidently is essential for good friction reduction perfomance as demonstrated by the comparison of BAB triblock versus the unfunctionalised polymer brush. This material provides comparable perfomance to that of GMO and in fact the BAB triblock is superior under many condtions. Most noticable is the reduction in traction coefficient at intermediate rolling speeds of 100 – 300 mm/s, in which case the polymeric anchor group brushes maintain lower values than the GMO additive. Organic friction modifiers such as GMO are generally believed to form monolayers on the steel surface, whereas the macromolecular brush materials form much thicker films of ~10 nm that will better support load and prevent direct surface contact. The bottle-brush film should effectively retain oil solvent molecules among the hydrophobic PLA side chains of the

bottle-brush and this thicker tribofilm may prevent entry into the mixed/boundary regime until slower rolling speeds.

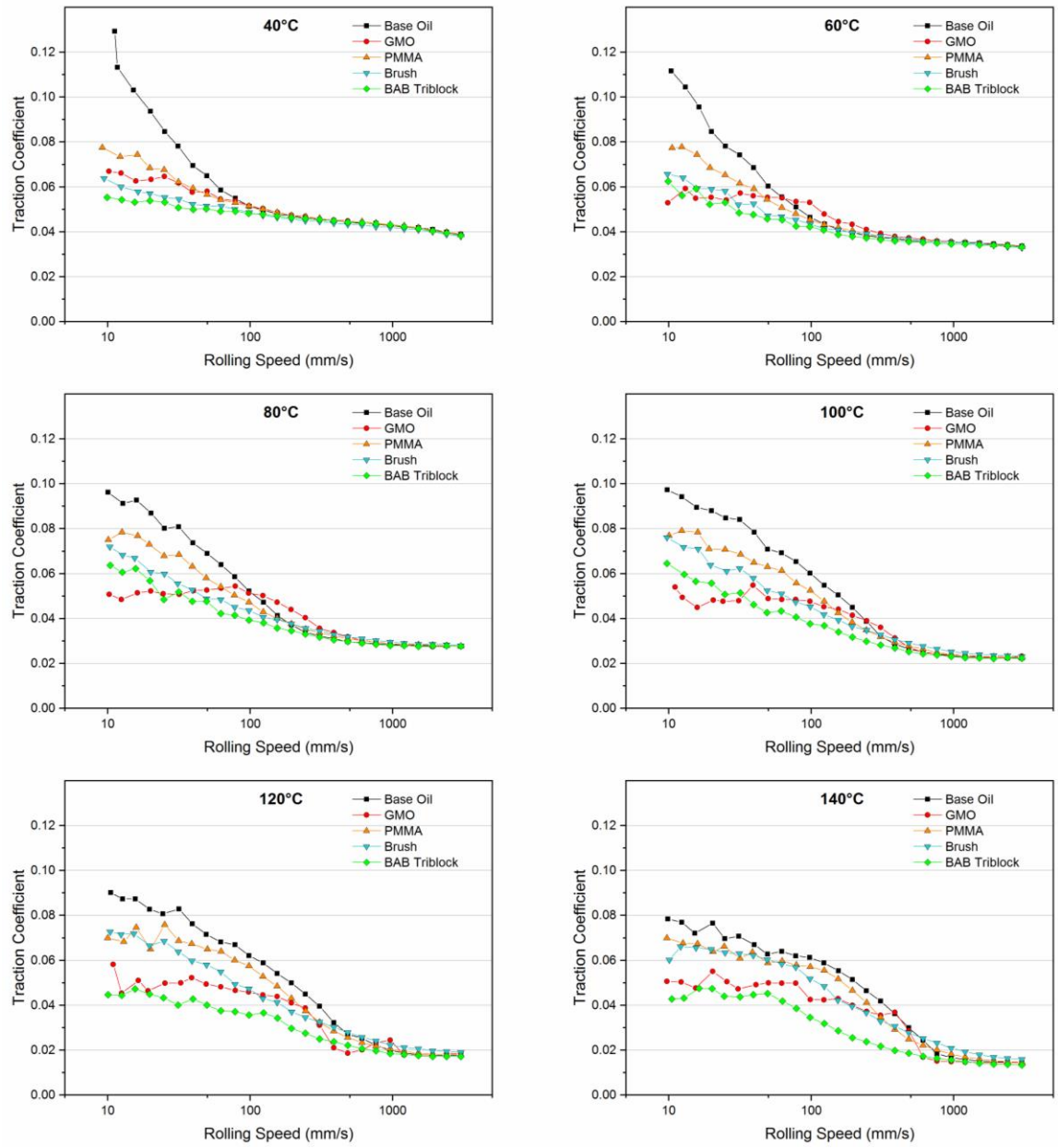

Figure 3.18: MTM testing of compounds at a treatment of 1 wt. % at various temperatures comparing performance of anchor group brushes against base oil, unfunctionalised polymers and the commercial friction modifier (GMO).

The various synthesised brush architectures were analysed under the same conditions by MTM (Figure 3.19). As expected the statistical distribution of polar PNAM monomers causes very poor performance, and in some cases actually leads to an increase in friction with respect to the base oil. Superior performance from diblock materials in dispersion and friction reduction applications has been attributed to the strong interaction of the

numerous adjacent polar monomer units with the substrate, making it unlikely for the anchor to detach from the surface. In a statistical architecture, however, only a small number of neighbouring PNAM monomer units will interact with the surface at a given time and therefore fluctuations may readily detach the entire bottle-brush molecule, disfavouring film formation. Within a bottle-brush architecture this effect may be particularly prevalent as the anchor comonomer is placed in the backbone, where it is highly sterically hindered and therefore reduces the ability of these monomer units to access and bind to the surface. While this explains the lower performance of the statistical bottle-brush it is not clear how this effect could lead to an increase in friction over the base oil. This may instead be caused by a flocculation effect whereby a single brush molecule could have PNAM units interacting with both of the moving substrates leading to increased resistance. Furthermore intermolecular interactions of the amphiphilic macromolecules could contribute to this effect – for the diblock presumably an inverse micelle is formed, which would not be expected to possess surface activity as the polar units are inaccessible, whereas for the statistical bottle-brush weak aggregation between multiple molecules via the PNAM backbone units could form a network like morphology. These larger aggregates would be more prone to flocculation, although would likely be short lived under high-temperature and shear conditions and thus make this mechanism unlikely.

An additional consideration is that the placement of PNAM copolymer into the statistical brush backbone also leads to a reduction in grafting density compared to the other brushes - the lower density of the side chains reduces steric hindrance and thus the grafts are more flexible, which may increase entanglement interactions between the brush molecules, again leading to an increase in friction coefficient. The conformation and behaviour of the bottle-brush macromolecule on the surface would be analogous to the mushroom / dense brush transition found for increasing densities of grafted polymer onto a substrate.[45]

At the lower temperatures, such as 40 °C, the PLA brush polymer shows similar performance to that of the anchor group functional compounds, however, as the temperature increases the gap is widened – at 120 °C the PLA brush displays at traction coefficient of 0.073 whereas the BAB triblock a value of 0.045. The temperature dependence can be rationalised by the shifting towards the boundary regime to higher rolling speeds at the elevated temperature points due to decreasing oil viscosity. Surface

active compounds that form films will provide superior friction reduction in the mixed/boundary regime compared to materials that do not, which explains the increasing discrepancy in performance of the PLA *vs* anchor group brushes.

Among the block anchor group brush architectures the performance of the three compounds is similar, with the BAB triblock marginally displaying the lowest friction reduction across the entire temperature range. This could be due to the surface conformation of the BAB triblock, where the dumbbell structure with two separate brush segments could potentially give a higher surface coverage than a singly segmented bottle-brushes if the treatment rate is insufficient to ensure complete surface coverage. It is worth noting, however, that the amount of linear polymer side product varies slightly between the brush samples making such close performance results difficult to attribute purely to polymeric structural differences. The incorporation of a polar copolymer as a block appears to be the most important factor for lubrication performance.

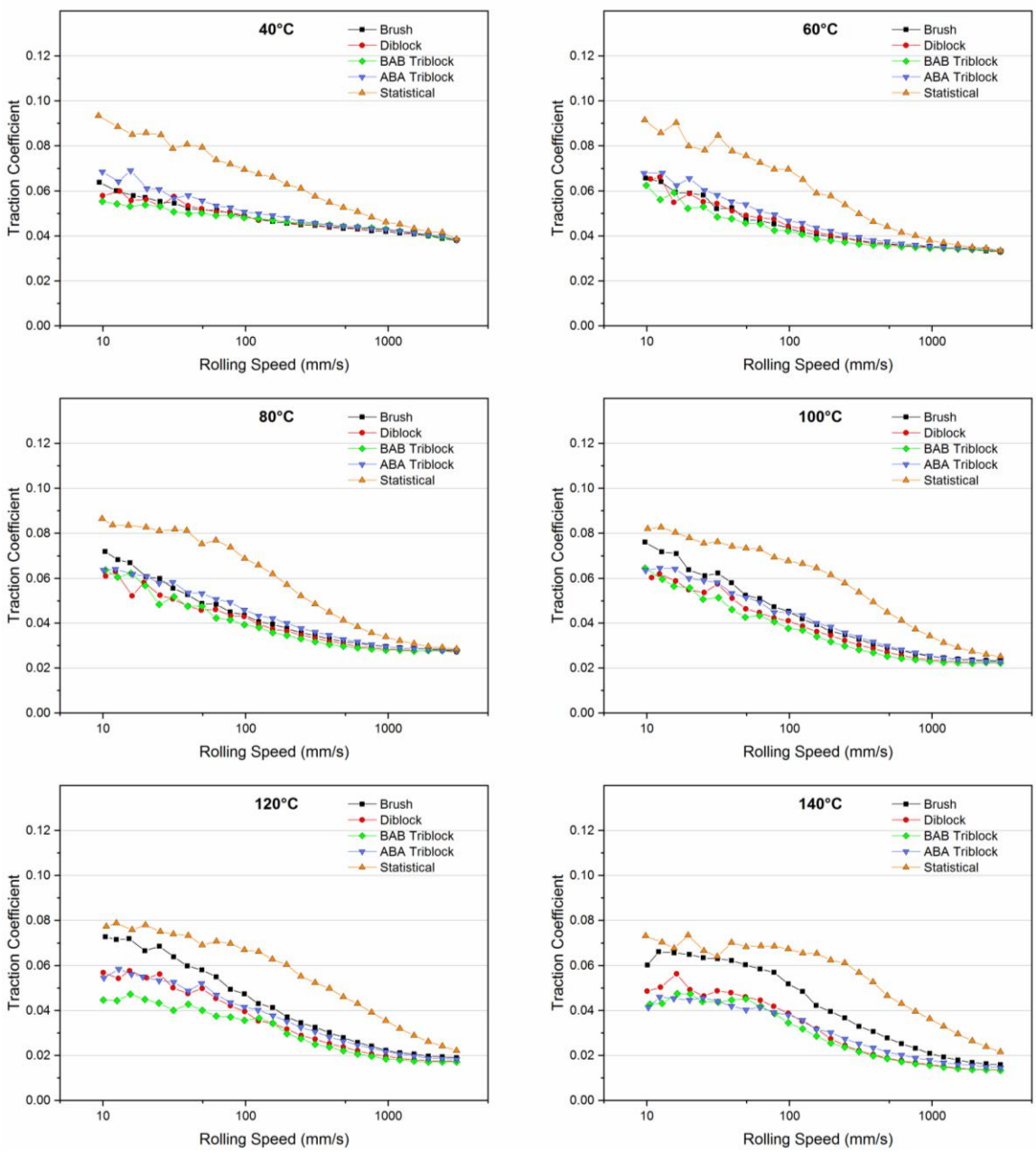

Figure 3.19: MTM testing of polymer at a treatment of 1 wt. % at various temperatures comparing the performance of differing bottle-brush acrhitectures.

3.2.8 Viscosity Testing

Finally, the compounds were also studied to investigate their effects as rheology modifiers. Control of the viscosity index (VI) is an important parameter for affecting friction and wear resistance in lubricant formulations, where a retention of viscosity at elevated operating temperatures and low viscosity at lower temperatures is highly desirable. A possible benefit of the anchor group bottle-brush materials is their usage as dual performance additives – friction reduction from the surface interacting polar block

and viscosity modification as a result of their high molecular weights. To probe these properties, the viscosity of polymer-oil blends at the same 1 wt. % concentration as the MTM testing was determined in Y4 (group III) base oil.

Table 3.3: Viscosity of various polymer-blends at 1wt. % determined at 40 and 100°C.

	Base Oil	PLA Brush	Diblock	ABA	BAB	Stat.	PMA
Viscosity @40 cSt	19.23	26.27	20.43	20.11	20.33	20.54	20.05
Viscosity @100 cSt	4.25	5.4	4.47	4.4	4.46	4.5	4.39
VI	129	146	134	132	133	136	132

In all cases an increase in viscosity index is observed by the addition of polymeric additive (Table 3.3), with the unfunctionalised PLA brush showing the largest effect. The observed increases were only modest, however, even for the commercial viscosity modifier PMA sample. Therefore while the low treatment rate of 1 wt. % appears to be sufficient for friction reduction benefits, a higher concentration would most likely be required for the desirable VI performance and to more accurately assess these materials potential (5 wt. % actives is used a typical formulation). Due to sample quantity limitations higher concentrations could not be measured. These initial data suggest the un-functionalised PLA brush may possess superior performance over the PNAM containing compounds, implying there may be a trade-off with friction performance, although further studies would be required to conclusively determine this.

3.3 Conclusion

This chapter explored the synthesis of a variety of complex bottle-brush polymer architectures incorporating polar poly(*N*-acryloylmorpholine) anchor group blocks onto hydrophobic poly(laurylacrylate) based bottle-brush regions. The RAFT 'grafting from' approach gives good control of diblock / triblock copolymer backbones and the final brush products with narrow dispersities (>1.2). The oil soluble brushes were analysed by QCM-D to demonstrate that the presence of PNAM increased surface adsorption and formed thicker (10 nm), more viscoelastic films than the comparative unfunctionalised brush. MTM testing at a low 1 wt. % treatment rate showed substantial reduction in friction coefficient in the mixed/boundary regime for the block anchor group brushes but not in the case of the statistical copolymer. The polymers display effective friction reduction across temperatures from 40 °C - 140 °C with most significant improvements at the highest temperature ranges. Aside from polymeric architecture, further studies could optimise these materials with respect to side chain length, backbone length, grafting density and nature of the polar anchor group. This presents a broad range of parameters to investigate, which could further improve lubrication efficacy over the promising materials described here.

3.4 Experimental

N-acryloylmorpholine (NAM, 97%), lauryl acrylate (LA, 90%) and *N*-hydroxyethyl acrylamide (HEAm, 97%) were obtained from Sigma-Aldrich and were passed through a basic alumina column before use. Dimethyl sulfoxide-d_6 (99.9% D atom), chloroform-d (99.8% D atom), deuterium oxide (99.9% D atom), methanol, dichloromethane (anhydrous) and 4-(Dimethylamino)pyridine (DMAP) were obtained from Sigma Aldrich and used as received. 1,4-dioxane, toluene and *N*,*N*-dimethylformamide (anhydrous) were obtained from Fisher Scientific and used as received. N-(3-Dimethylaminopropyl)-*N′*-ethylcarbodiimide hydrochloride (EDC) was obtained from Carbosynth and used as received. RAFT agents 2-(((butylthio)carbonothioyl)thio) propanoic acid (PABTC), methyl 2-(((butylthio)carbonothioyl)thio)propanoate (PMBTC) and ethane-1,2-diyl bis(2-(((butylthio)carbonothioyl)thio)propanoate) (DiPABTC) were synthesised according to literature procedures[36, 46]. Initiators lauroyl peroxide (LPO, 97%, Aldrich), 2,2′-azobis[2-(2-imidazolin-2-yl)propane]dihydrochloride (VA-044, >98%, Wako), and dimethyl 2,2'-azobis(2-methylpropionate) (V601, >98%, Wako) were used as received. 2-(((dodecylthio)carbonothioyl)thio)-2-methylpropanoic acid (CTA Acid) and butyl 2-(((dodecylthio)carbonothioyl)thio)-2-methylpropanoate (CTA-1) were supplied by the industrial sponsor, Lubrizol.

^{1}H NMR spectra were ran on either a Bruker DPX-300 or DPX-400 spectrometer using deuterated solvents (deuterated dimethyl sulfoxide, chloroform or water).

Dynamic light scattering

Size measurements were carried out using a Malvern Zetasizer Nano-ZS at 25 °C with a 4 mW He-Ne 633 nm laser at a scattering angle of 173° (back scattering). Measurements were taken assuming the refractive index of butyl acrylate. DLS samples were prepared at a concentration of 1 mg ml^{-1} in toluene or hexane. Samples were incubated for 60 seconds at 25 °C prior to measurement. Measurements were repeated three times with automatic attenuation selection and measurement position. Results were analysed using Malvern DTS 6.20 software.

Mini traction machine testing

Analysis was carried out by Lubrizol, the industrial sponsor of the project. The fluids were evaluated using a mini traction machine (MTM) commercially available from PCS instruments UK. A concentrated contact forms between a steel ball and polished steel disc allowing one to measure the traction of a given fluid. A series of discrete measurements were made at a speed of 2.5 m/s and a Hertz pressure of 1 GPa between 40°C to 120°C in 20°C temperature increments and slide to roll ratio (SRR) of 0-50%.

Quartz crystal microbalance with dissipation

Analysis was carried out by Lubrizol, the industrial sponsor of the project. QCM-D adsorption studies were performed using the Q-sense E4 system equipped with a peristaltic pump (IPC-C, Ismatec) with solvent resistant tubing. Q-sense stainless steel (Grade SS2342) coated QCM chips were used for analysis. Prior to use the chip underwent a cleaning procedure: 10 minutes sonication in toluene, dried under a N_2 stream, 30 minutes sonication in a Hellmanex solution (1%), immediately washed with distilled water and dried under an N_2 stream, 10 minutes sonication in ethanol, dried under an N_2 stream and then treated with an UV ozone cleaner (ProClear plus, Bioforce Nanosciences) for 10 minutes. The chip was loaded into a temperature controlled cell set to 40°C and pure dodecane was passed through the sample cell at a flow rate of 50 µl min^{-1} until a stable frequency baseline was obtained (typically ~1 hour). The sample of interest in a 0.1 wt. % solution in dodecane was then passed over the chip at the same flow rate until the frequency response began to plateau, after which a pure dodecane solvent rinse step was performed. Frequency and dissipation changes were monitored for all tuned overtones with data collection controlled by the QSoft software. Data analysis was performed with the QTools software provided by Q-sense. For the Voigt model all overtones other than the 1^{st} were used for modelling.

Atomic Force Microscopy

Samples were prepared by taking a 0.05 mg ml^{-1} solution of the polymers in hexane and adding one drop onto a highly ordered pyrolytic graphite substrate. The sample was allowed to dry for 2 minutes before analysis. Images were collected using a Bruker-Nano Multimode V instrument in tapping mode.

Rheology Testing

The kinematic viscosity (KV) of the different formulation was measured using a capillary viscometer (Houillon viscometer VH1 – Integrated Scientific LTD) following a standard method (ASTM D7279). The viscosity/temperature relationship, or Viscosity Index (VI), was calculated using the standard method ASTM D2270 by measuring the kinematic viscosity at 40 °C and 100 °C (KV40 and KV100).

Size exclusion chromatography

Analysis was performed on two systems:

DMF-SEC: Agilent 390-LC MDS instrument equipped with differential refractive index (DRI), viscometry (VS), dual angle light scatter (LS) and dual wavelength UV detectors. The system was equipped with 2 x PLgel Mixed D columns (300 x 7.5 mm) and a PLgel 5 µm guard column. The eluent is DMF with 5 mmol NH_4BF_4 additive. Samples were run at 1 ml min^{-1} at 50 °C. Poly(methyl methacrylate) standards (Agilent EasiVials) were used for calibration, MW ranging from 550 to $2.14*10^6$ g mol^{-1}. Analyte samples were filtered through a nylon membrane with 0.22 μm pore size before injection. Respectively, experimental molar mass ($M_{n\ SEC}$) and dispersity ($Đ$) values of synthesized polymers were determined by conventional calibration using Agilent GPC/SEC software.

$CHCl_3$-SEC: Agilent 390-LC MDS instrument equipped with differential refractive index (DRI), viscometry (VS), dual angle light scatter (LS) and two wavelength UV detectors. The system was equipped with 2 x PLgel Mixed C columns (300 x 7.5 mm) and a PLgel 5 µm guard column. The eluent is $CHCl_3$ with 2 % TEA (triethylamine) additive. Samples were run at 1 ml min^{-1} at 30 °C. Poly(methyl methacrylate) standards (Agilent EasiVials) were used for calibration, MW ranging from 550 to $2.14*10^6$ g mol^{-1}. Ethanol was added as a flow rate marker.

Experimental Procedures

Synthesis of PolyCTA – functionalisation with CTA Acid

PHEAm (0.5 g, 4.35 mmol with respect to alcohol groups) and CTA Acid (2.38 g, 6.5 mmol) were dissolved in 30 ml DMF in a dry 100 ml round bottom flask under nitrogen,

cooled with an ice-water bath, followed by the addition of DMAP (0.133 g, 1.09 mmol) then DCC (2.24 g, 10.9 mmol). The reaction mixture was stirred for 30 minutes, the ice bath was removed and then stirred at room temperature for a further 24 h. 30 ml of DCM was added to the reaction mixture and filtered to remove white urea precipitate. The filtrate was precipitated three times in methanol to isolate the PolyCTA (~80 % alcohol groups functionalised by ^{1}H NMR). The PolyCTA was then dissolved in anhydrous DCM in a round bottom flask and the reaction procedure repeated with the addition of the same amount of CTA Acid, DCC and DMAP. The reaction mixture was again filtered and precipitated three times in methanol, the solid collected and dried in a vacuum oven overnight at 45 °C to yield an oily orange solid. ^{1}H NMR (300 MHz, $CDCl_3$): δ 4.4 – 4.1 (2H, C(O)OC<u>H</u>$_2$), 3.6 – 3.5 (2H, C(O)NHC<u>H</u>$_2$), 3.4 – 3.3 (2H, SC<u>H</u>$_2$), 2.2 – 1.2 (3H, C<u>H</u>$_2$C<u>H</u>), 1.62 (6H, s, S(C<u>H</u>$_3$)$_2$), 1.60 (2H, s, SCH$_2$C<u>H</u>$_2$), 1.26 (18H, s, SCH$_2$CH$_2$C$_9$<u>H</u>$_{18}$), 0.94 (3H, t, C<u>H</u>$_3$CH$_2$).

Synthesis of PHEA$_{10}$-co-PLA$_{90}$ backbone

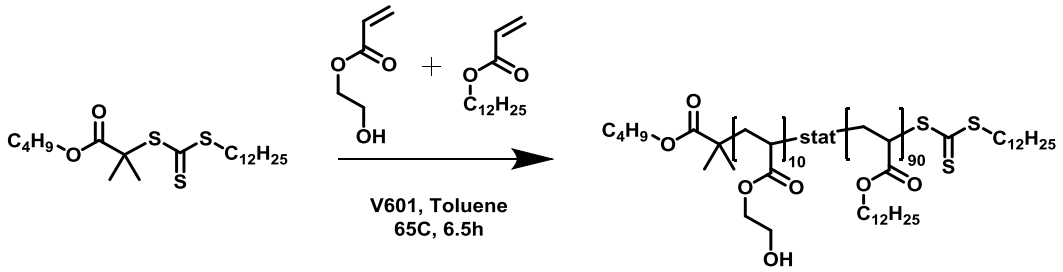

Lauryl acrylate (3 g, 12.48 mmol), hydroxyethylacrylate (145 mg, 1.25 mmol), CTA-1 (52.5 mg, 0.125 mmol) and V601 (2.9 mg, 0.0125 mmol) were dissolved in toluene (1.6 ml) in a glass vial fitted with a stirrer bar and rubber septum. The reaction mixture was degassed with N_2 for 10 minutes and placed in an oil bath set to 65 °C for 6.5 hours. The vial was then removed, cooled under a stream of water, the reaction mixture measured by NMR to determine monomer conversion (93 %) and then precipitated three times into ice cold methanol to yield a yellow oil. . ^{1}H NMR (300 MHz, $CDCl_3$): δ 4.1 – 3.9 (4H, s, C(O)OC<u>H</u>$_2$), 3.8 – 3.7 (2H, OHC<u>H</u>$_2$), 2.2 – 1.2 (3H, C<u>H</u>$_2$C<u>H</u>), 1.62 (6H, s, S(C<u>H</u>$_3$)$_2$), 1.26 (18H, s, SCH$_2$CH$_2$C$_9$<u>H</u>$_{18}$), 0.94 (3H, t, C<u>H</u>$_3$CH$_2$). $CHCl_3$ SEC: $M_{n\ SEC}$ = 20,100 , $Đ$ = 1.18.

Esterification of the PHEA$_{10}$-coPLA$_{90}$ backbone

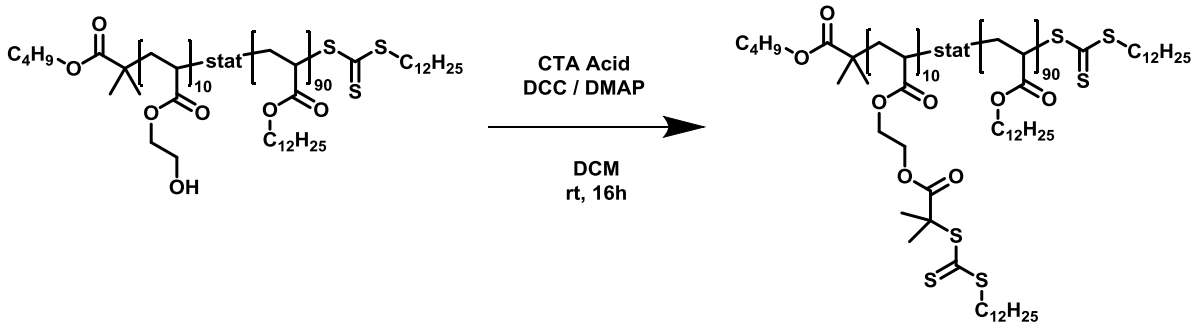

The PHEA$_{10}$-co-PLA$_{90}$ backbone (7g, 3.07 mmol OH groups) and CTA Acid (1.68 g, 4.61 mmol) were dissolved in anhydrous DCM (40 ml) in a round bottom flask under nitrogen. The reaction mixture was cooled with an ice bath followed by the addition of DCC (1.9 g, 9.22 mmol) and DMAP (56.3 mg, 0.461 mmol), and left to stir overnight for a total of 16 hours. The reaction mixture was filtered, the solute concentrated under a stream of nitrogen and then precipitated three times into ice cold methanol to yield the product as a yellow oil. ^{1}H NMR (300 MHz, $CDCl_3$): δ 4.3 – 4.2 (4H , 2s, C(O)OC$\underline{H}_2$C$\underline{H}_2$OC(O)), 4.1 – 3.9 (4H, s, C(O)OC$\underline{H}_2$ PLA), 3.22 (2H, SC$\underline{H}_2$), 2.2 – 1.2 (3H, C$\underline{H}_2$C$\underline{H}$), 1.62 (6H, s, S(C$\underline{H}_3$)$_2$), 1.26 (18H, s, SCH$_2$CH$_2$C$_9\underline{H}_{18}$), 0.94 (3H, t, CH$_2$C$\underline{H}_3$). $CHCl_3$ SEC: $M_{n\ SEC}$ = 23,400 , $Đ$ = 1.11.

Comb polymer synthesis – grafting from step

PCTA$_{10}$-co-PLA$_{90}$ backbone (3.08 g, 0.945 mmol CTA), lauryl acrylate (12.5 g, 52 mmol), V601 (12 mg, 0.052 mmol) and CTA Acid (34.5 mg, 0.0945 mmol) were dissolved in toluene (36.6 ml) in a round bottom flask fitted with a stirrer bar and rubber septum, degassed for 10 minutes with N_2 and placed in oil bath heated to 65 °C for 6 hours. The polymer was isolated by precipitation three times into ice cold methanol and dried in a vacuum oven heated to 40 °C overnight to yield the product as a pale yellow oil. $CHCl_3$ SEC: $M_{n\ SEC}$ = 54,800 , $Đ$ = 1.16.

Synthesis of $PNAM_{100}$-b-$PHEAm_{100}$ diblock backbone

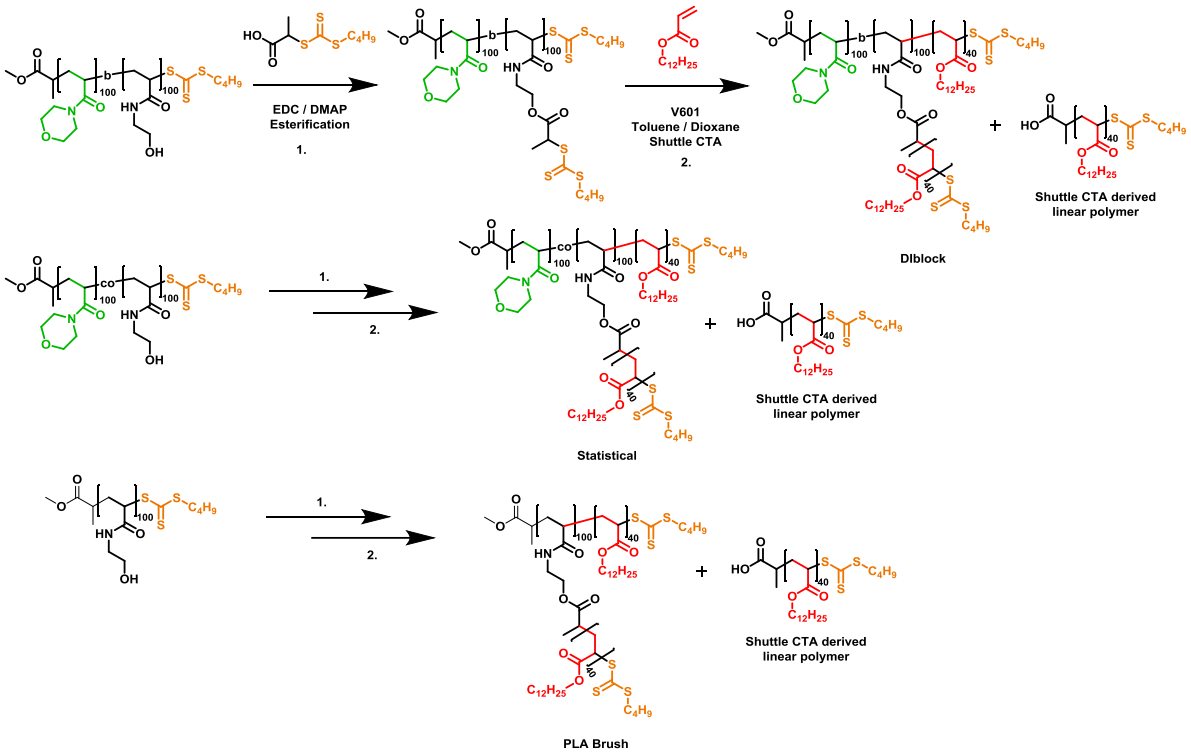

Experimental Scheme 1: Synthetic scheme for synthesis of diblock, statistical and PLA homopolymer bottle-brushes.

NAM (1.0 g, 7.08 mmol), PMBTC (17.9 mg, $7.08*10^{-2}$ mmol), VA-044 (0.6 mg, $1.77*10^{-3}$ mmol) were dissolved in a mixture of water (1590 µl) and dioxane (1060 µl) in a 7 ml vial fitted with a stirrer bar and rubber septum. The reaction mixture was degassed with N_2 for 15 minutes and placed in an oil bath heated to 44 °C for 7 hours. A sample was taken to confirm full consumption of monomer by NMR and the vial stored in the fridge overnight. Then a degassed of HEAm (815 mg, 7.08 mmol), VA-044 (0.6 mg, $1.77*10^{-3}$ mmol) and water (300 µl) was added to the vial, mixed and heated at placed in an oil bath heated to 44 °C for 7 hours. A monomer conversion of 94 % was determined by ^{1}H NMR, the reaction mixture was diluted with methanol and precipitated once in acetone, twice into ethyl acetate and dried in a vacuum oven at 40 °C overnight to yield a pale yellow powder.

For the $PHEAm_{100}$ homopolymer backbone the same reaction conditions as for the first block were used but with HEAm (7.08 mmol) instead of NAM. For the statistical $PNAM_{100}$-co-$PHEAm_{100}$ backbone a polymerisation mixture of NAM (920 mg, 6.52 mmol), HEAm (750 mg, 6.52 mmol), PMBTC (16.4 mg, $6.52*10^{-2}$ mmol), VA-044 (0.5

mg, $1.77*10^{-3}$ mmol), water (2115 µl) and dioxane (1410 µl) was prepared and reacted in the same conditions as described above.

Synthesis of triblock ABA / BAB copolymer backbones

ABA backbone – HEAm (750 mg, 6.51 mmol), DiPABTC (32.8 mg, $6.51*10^{-2}$ mmol), VA-044 (0.7 mg, $2.17*10^{-3}$ mmol), water (397 µl) and dioxane (748 µl) were placed in to a 3 ml vial fitted with a stirrer bar and rubber septum. The reaction mixture was degassed with N_2 for 15 minutes and placed in an oil bath heated to 44 °C for 8 hours. NMR revealed 97 % conversion of monomer, the reaction mixture was precipitated twice into acetone and dried under vacuum at 40 °C. 400 mg of the dried product was then mixed with NAM (490 mg, 3.47 mmol), VA-044 (0.4 mg, $1.16*10^{-3}$ mmol) and water (1300 µl), degassed with N_2 and heated at 44 °C for 6 hours. The reaction mixture was precipitated into acetone and then twice in ethyl acetate and dried under vacuum.

BAB backbone – synthesis was performed without precipitation between blocks using the same procedure as above except addition of the NAM block first and the HEAm second. The monomer conversion of the first NAM block proceeded to >99 % and therefore precipitation was unnecessary and the triblock was synthesised in one pot. Typical ^{1}H NMR spectra of the copolymers (300 MHz, D_2O): δ 3.9 – 3.5 (br, 12H, NHC$\underline{H}_2$C$\underline{H}_2$OH, N(C$\underline{H}_2$C$\underline{H}_2$)$_2$O)), 2.5 (1H, C$\underline{H}_2$C$\underline{H}$-NAM), 2.0 – 1.0 (3H, C$\underline{H}_2$C$\underline{H}$ backbone).

CTA end group removal

The procedure was adapted from previously reported work.[209] The ABA $PNAM_{50}$-b-$PHEAm_{100}$-$PNAM_{50}$ polymer (1 g, 1 eq. with respect to CTA), AIBN (230 mg, 20 eq.) and lauroyl peroxide (40 mg, 2 eq.) were dissolved in 15 ml DMF, degassed for 10 minutes with N_2 and placed in an oil bath heated to 80 °C for 6 hours. The reaction mixture was precipitated three times into diethyl ether and dried under vacuum to yield a colourless powder. Analysis by SEC with a UV detector showed no absorption from the polymer at 309 nm indicating quantitative removal of the CTA end group.

General synthesis of PolyCTA backbones with PABTC

PHEAm copolymer (500 mg, 1 eq. with respect to alcohol groups) was dissolved in 10 ml anhydrous DMF under nitrogen and PABTC (1.5 eq.) added. The reaction mixture

was cooled with an ice bath followed by addition of DMAP (0.15 eq.) then EDC (2 eq.). After two hours the ice bath was removed and left to stir overnight. The reaction mixture was concentrated under a stream of nitrogen and precipitated three times into an ice cold solution of methanol / water (50:50), solubilising in dioxane between precipitations. The precipitate was transferred to a vial and dried under vacuum at 40 °C to yield a sticky orange solid. Example NMR of the diblock copolymer: ^{1}H NMR (300 MHz, $CDCl_3$): δ 4.9 -4.8 (1H, SC<u>H</u>**(**CH_3)), 4.4 – 4.1 (2H, C(O)OC<u>H_2</u>), 3.9 – 3.4 (12H, br, C(O)NHC<u>H_2</u> + O(C<u>H_2</u>C<u>H_2</u>)$_2$N), 3.4 – 3.3 (2H, SC<u>H_2</u>), 2.7 – 2.3 (1H, CH_2C<u>H</u>-NAM), 2.2 – 1.2 (3H, C<u>H_2</u>C<u>H</u>), 1.66 (2H, t, SCH_2C<u>H_2</u>), 1.62 (3H, d, SCH(C<u>H_3</u>)), 1.45 (2H, q, SCH_2CH_2C<u>H_2</u>), 0.94 (3H, t, C<u>H_3</u>CH_2).

General procedure of 'grafting from' step

A DP of 75 was targeted for the side chains with the addition of 0.5 eq. free shuttle CTA with respect to the polymeric grafted CTA units. Lauryl acrylate (9 g, 37.44 mmol), PolyCTA (135 mg, 0.333 mmol), PABTC (39.7 mg, 0.166 mmol), V601 (4.3 mg, $1.87*10^{-2}$ mmol), toluene (13.6 ml) and dioxane (13.6 ml) were placed in 50 ml round bottom flask. For the homopolymer $PCTA_{100}$ backbone the polymerisation was performed in 100% toluene as the solvent at the same overall concentration. The reaction mixture was degassed with N_2 and placed in an oil bath set to 65°C for 7.5 hours, until a monomer conversion of 59 – 70 % was obtained to reach a side chain length of DP46 - 53. The flask was cooled to room temperature and the reaction mixture precipitated three times into ice cold methanol and dried under vacuum to yield a yellow oil. SEC analysis of bottle-brushes including the linear polymer side product shown in Figure B.6. ^{1}H NMR (300 MHz, $CDCl_3$): δ 4.4 – 4.1 (2H, C(O)OC<u>H_2</u>), 3.4 – 3.3 (2H, SC<u>H_2</u>), 2.2 – 1.2 (3H, C<u>H_2</u>C<u>H</u>), 1.60 (2H, s, SCH_2C<u>H_2</u>), 1.26 (18H, s, S$CH_2CH_2C_9$<u>H_{18}</u>), 0.94 (3H, t, C<u>H_3</u>CH_2).

3.5 References

1. H. Spikes, *Tribology Letters*, 2015, **60**, 5.
2. M. Desanker, X. He, J. Lu, P. Liu, D. B. Pickens, M. Delferro, T. J. Marks, Y.-W. Chung and Q. J. Wang, *ACS Appl. Mat. Inter.*, 2017, **9**, 9118-9125.
3. J. Fan, M. Müller, T. Stöhr and H. A. Spikes, *Tribology letters*, 2007, **28**, 287-298.
4. R. A. Wright, K. Wang, J. Qu and B. Zhao, *Angew. Chem. Int. Ed.*, 2016, **55**, 8656-8660.
5. B. T. Seymour, R. A. Wright, A. C. Parrott, H. Gao, A. Martini, J. Qu, S. Dai and B. Zhao, *ACS Appl. Mat. Inter.*,, 2017, **9**, 25038-25048.
6. J. Klein, E. Kumacheva, D. Mahalu, D. Perahia and L. J. Fetters, *Nature*, 1994, **370**, 634.
7. S. Watson, M. Nie, L. Wang and K. Stokes, *RSC Advances*, 2015, **5**, 89698-89730.
8. V. V. Tsukruk, V. N. Bliznyuk, J. Hazel, D. Visser and M. P. Everson, *Langmuir*, 1996, **12**, 4840-4849.
9. J. Graham, H. Spikes and S. Korcek, *Tribology Transactions*, 2001, **44**, 626-636.
10. H. Sakata, M. Kobayashi, H. Otsuka and A. Takahara, *Polym. J.*, 2005, **37**, 767.
11. T. Kreer, *Soft Matter*, 2016, **12**, 3479-3501.
12. P. Mocny and H.-A. Klok, *J. Molecular Systems Design*, 2016, **1**, 141-154.
13. R. M. Bielecki, P. Doll and N. D. Spencer, *Tribology Letters*, 2013, **49**, 273-280.
14. S. Jahn and J. Klein, *Macromolecules*, 2015, **48**, 5059-5075.
15. M. Chen, W. H. Briscoe, S. P. Armes and J. Klein, *Science*, 2009, **323**, 1698-1701.
16. O. Tairy, N. Kampf, M. J. Driver, S. P. Armes and J. Klein, *Macromolecules*, 2014, **48**, 140-151.
17. R. M. Bielecki, E. M. Benetti, D. Kumar and N. D. Spencer, *Tribology Letters*, 2012, **45**, 477-487.
18. R. M. Bielecki, M. Crobu and N. D. Spencer, *Tribology Letters*, 2013, **49**, 263-272.
19. J. W. Robinson, Y. Zhou, J. Qu, J. T. Bays and L. Cosimbescu, *Reac. Func. Polym.*, 2016, **109**, 52-55.
20. A. Martini, U. S. Ramasamy and M. Len, *Tribology Letters*, 2018, **66**, 58.
21. M. Müller, K. Topolovec-Miklozic, A. Dardin and H. A. Spikes, *Tribology Transactions*, 2006, **49**, 225-232.
22. 2011.
23. L. Cosimbescu, J. W. Robinson, Y. Zhou and J. Qu, *RSC Advances*, 2016, **6**, 86259-86268.
24. S. Yamada, A. Fujihara, S.-i. Yusa, T. Tanabe and K. Kurihara, *Langmuir*, 2015, **31**, 12140-12147.
25. W. Fu, W. Bai, S. Jiang, B. T. Seymour and B. Zhao, *Macromolecules*, 2018, **51**, 1674-1680.
26. B. Xu, Y. Liu, X. Sun, J. Hu, P. Shi and X. Huang, *ACS Appl. Mat. Inter.*, 2017, **9**, 16517-16523.
27. G. Olanya, J. Iruthayaraj, E. Poptoshev, R. Makuska, A. Vareikis and P. M. Claesson, *Langmuir*, 2008, **24**, 5341-5349.
28. J. Faivre, B. R. Shrestha, J. Burdyńska, G. Xie, F. Moldovan, T. Delair, S. Benayoun, L. David, K. Matyjaszewski and X. Banquy, *ACS Nano*, 2017.
29. J. Faivre, B. R. Shrestha, G. Xie, M. Olszewski, V. Adibnia, F. Moldovan, A. Montembault, G. Sudre, T. Delair and L. David, *Chem. Mater.*, 2018.
30. A. Dėdinaitė, *Soft Matter*, 2012, **8**, 273-284.
31. B. Zappone, M. Ruths, G. W. Greene, G. D. Jay and J. N. Israelachvili, *Biophys. J.*, 2007, **92**, 1693-1708.
32. X. Banquy, J. Burdynska, D. W. Lee, K. Matyjaszewski and J. Israelachvili, *J. Amer. Chem. Soc.*, 2014, **136**, 6199-6202.

33. X. Liu, A. Dedinaite, M. Rutland, E. Thormann, C. Visnevskij, R. Makuska and P. M. Claesson, *Langmuir*, 2012, **28**, 15537-15547.
34. Z. Zheng, J. Ling and A. H. Müller, *Macromol. Rapid Commun.*, 2014, **35**, 234-241.
35. Y. Wang, Z. Zheng, Z. Huang and J. Ling, *Polymer Chemistry*, 2017, **8**, 2659-2665.
36. A. Kerr, M. Hartlieb, J. Sanchis, T. Smith and S. Perrier, *Chem. Commun.*, 2017, **53**, 11901-11904.
37. I. Lacík, A. Chovancová, L. Uhelská, C. Preusser, R. A. Hutchinson and M. Buback, *Macromolecules*, 2016, **49**, 3244-3253.
38. Z. Tang and S. Li, *Curr. Opin. Solid State Mater. Sci.*, 2014, **18**, 119-139.
39. H. Willcock and R. K. O'Reilly, *Polymer Chemistry*, 2010, **1**, 149-157.
40. M. Chen, G. Moad and E. Rizzardo, *J. Polym. Sci., Part A: Polym. Chem.*, 2009, **47**, 6704-6714.
41. Y. K. Chong, G. Moad, E. Rizzardo and S. H. Thang, *Macromolecules*, 2007, **40**, 4446-4455.
42. D. O. Jang and D. H. Cho, *Tetrahedron Lett.*, 2002, **43**, 5921-5924.
43. I. Reviakine, D. Johannsmann and R. P. Richter, *Anal. Chem.*, 2011, 8838-8848.
44. G. Dunér, E. Thormann and A. Dėdinaitė, *J. Colloid Inter. Sci.*, 2013, **408**, 229-234.
45. T. Wu, K. Efimenko and J. Genzer, *J. Amer. Chem. Soc.*, 2002, **124**, 9394-9395.
46. C. Ferguson, R. Hughes, D. Nguyen, B. Pham, R. Gilbert, A. Serelis, C. Such and B. Hawkett, *Macromolecules*, 2005, **38**, 2191-2204.

Chapter 4

Polymeric nanotubes as drug delivery vectors – comparison of a covalently and supramolecularly assembled construct

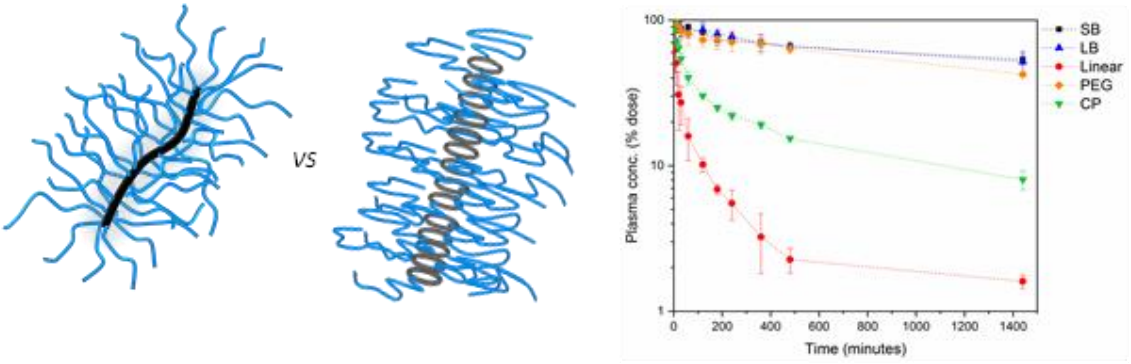

The ability to control the size and architecture of molecular bottle-brushes by RAFT was used to study the effects of aspect ratio on pharmacokinetic and bio-distribution behaviour and thus establish their potential as drug delivery vectors. Additionally they provide an effective control for supramolecular assembled nanotubes of similar dimensions, which have a possible benefit of inherent degradability through their reversible aggregation of cyclic peptide core units. Furthermore there is increasing need for alternatives to PEG as a material for nanomedicine, of which water soluble poly(acrylamides) may be highly suitable and are readily controlled by RAFT polymerisation. It was found PNAM bottle-brushes possessed long plasma circulation times comparable to PEG materials, with the cyclic peptide system displaying a lower half-life, although still elevated over a non-assembling linear control. Use of higher aspect ratios bottle-brushes led to substantial distribution into the liver, whereas the cyclic peptide nanotube was able to mostly circumvent organ accumulation.

4.1 Introduction

Nanomedicine as a means to deliver pharmaceutical actives to the body in a controlled manner has received intense scientific focus over the last few decades. Such an approach is highly appealing for the improvement of medicinal treatments by the loading or conjugation of drug within a nano-sized delivery vector, with advantages including the alteration of pharmacokinetic performance of the drug, changing toxicity profiles, releasing drug over a desired time frame and the targeting of a specific active site in the body.[1]

The development of drug delivery systems for the treatment of cancer has received particular attention, with the discovery of the enhanced permeation and retention effect (EPR) in 1986 demonstrating the preferential accumulation of 10 – 100 nm diameter nanoparticles in tumour sites.[2] Rapid uncontrolled growth within solid tumours leads to poorly regulated, highly permeable vasculature with a lack of lymphatic vessels, varying greatly from healthy tissues.[3] It is believed that nanoparticles within the correct size range are able to permeate though gaps in the epithelial cell walls of cancerous mother vessels, but are unable to do so in healthy vasculature, explaining the increased accumulation as a result of the passive properties of the particle.[4] This presents a route to selectively transporting chemotherapeutics, potentially reducing the harsh side effects of these treatments and increasing the tolerable drug dosage to improve therapeutic efficacy. With the suitable chemistry it is also possible to combine targeting moieties, pharmaceutical actives and labels (fluorescence dyes, MRI contrast agents) into a single macromolecular structure. Such an approach offers benefits in terms of synergistic effects of delivering multiple drugs simultaneously and the diagnostic ability to monitor the fate of the nanoparticle *in vivo*, the combination of which is referred to as theranostics.[5]

Macromolecular chemistry offers many tools by which to design and analyse drug delivery vectors, for example the commonly used PEGylation approach to modifying nanoparticles, drugs and proteins.[6, 7] Conjugation with poly(ethylene glycol) (PEG) has been shown to increase circulation times by imparting a stealth effect to avoid immune system response, while additionally above a certain molecular weight (typically 40 – 50 kDa for hydrophilic polymers)[8] polymers avoid clearance *via* renal filtration and thus conjugation facilitates longer plasma circulation times.[9, 10] There have been increasing concerns, however, of an accelerated blood clearance (ABC) effect in PEG materials,

whereby subsequent administrations of the formulation invoke an immune response leading to dramatically decreased circulation times.[11, 12] This is believed to result from the production of anti-PEG immunoglobulin M antibodies.[13] The ABC effect is potentially problematic for chronic treatments where a reproducible response to each dosage is essential and, therefore, PEG may not be the ideal polymer for these applications.

While relying on the passive EPR effect due to size of the nanoparticle alone can improve performance, further gains in tumour accumulation can be obtained by incorporation of targeting ligands onto the peripheral particle surface.[14] These ligands can be designed to have an affinity for the cancerous tumour itself (e.g. antibodies,[15] peptides such as RGD,[16] and folates[17]) or for the tumour vasculature by targeting the overexpression of vascular endothelial growth factors. A recent review surveyed nanomedicine literature and concluded that on average in a given treatment only 0.6% of untargeted nanoparticles successfully distribute into tumour sites.[18] This is increased up to 0.9% with the use of targeting ligands, however, there is still significant room for improvement of these values especially when considering the typically low drug loading efficiencies of nanoparticle formulations, limiting dosage quantities. Additionally the EPR effect is not always beneficial; inside the tumour microenvironment the disorganised vasculature and heterogeneous nature of the tissues can reduce nanoparticle delivery efficacy.[19] Elevated interstitial fluid pressure as a consequence of the ineffective lymphatic drainage creates pressure gradients and in combination with the dense extracellular matrix the diffusion of nanoparticles into tumour cells is inhibited. Hypoxic and sometimes necrotic areas present in tumour tissue result from lack of blood supply, reducing the ability of nanoparticles to penetrate into these regions. Normalisation of vasculature by treatment with anti-angiogenic therapies can in fact improve delivery of nanoparticles in the smaller size ranges, while reducing the accumulation of lager vectors ~100 nm.[20]

Partly due to the aforementioned issues there has of yet been limited success in translating nanomedicine systems into the clinic with only a small number of approved nanomedicines currently available (eg. Doxil and Abraxane), however understanding of the fundamental requirements of an effective drug delivery system has been vastly improved. Surface charge plays an important role in behaviour with close to neutral zeta potentials generally considered optimal.[21] Increased particle charge, either cationic or

anionic, generally leads to faster clearance from blood circulation, while cationic charge improves cellular uptake but is often associated with increased toxicities. The shape of nanoparticles has been established as an important parameter for controlling nanoparticle properties in terms of circulation time, cell association and tumour penetration.[22-24] Spherical nanoparticles have been most frequently studied, primarily due to ease of synthesis, however discs,[25] rods,[26, 27] filomicelles[28] and nanoneedles[29] have also been investigated. Among studied morphologies rod shaped nanoparticles stand out as possessing excellent potential – when compared to their similarly sized spherical counterparts, rod shaped silica nanoparticles displayed increased rate and concentration of accumulation in tumours.[30] The difference was rationalised by the reduced dimension of tubes in one dimension improving the ability to permeate through pores, this was corroborated by an increased permeation in *vitro* through collagen gels. Polystyrene rod shaped particles also showed higher cellular uptake than spherical / disk morphologies.[31] In nature bacteria and viruses are commonly found as rod or filament shaped, such as the tobacco mosaic virus with dimensions of 18 x 300 nm, lending credence to the benefits of this architecture. Pharmacokinetic analysis of a PEG coated tobacco mosaic virus nanotube showed increased circulation times compared to a spherical equivalent.[32]

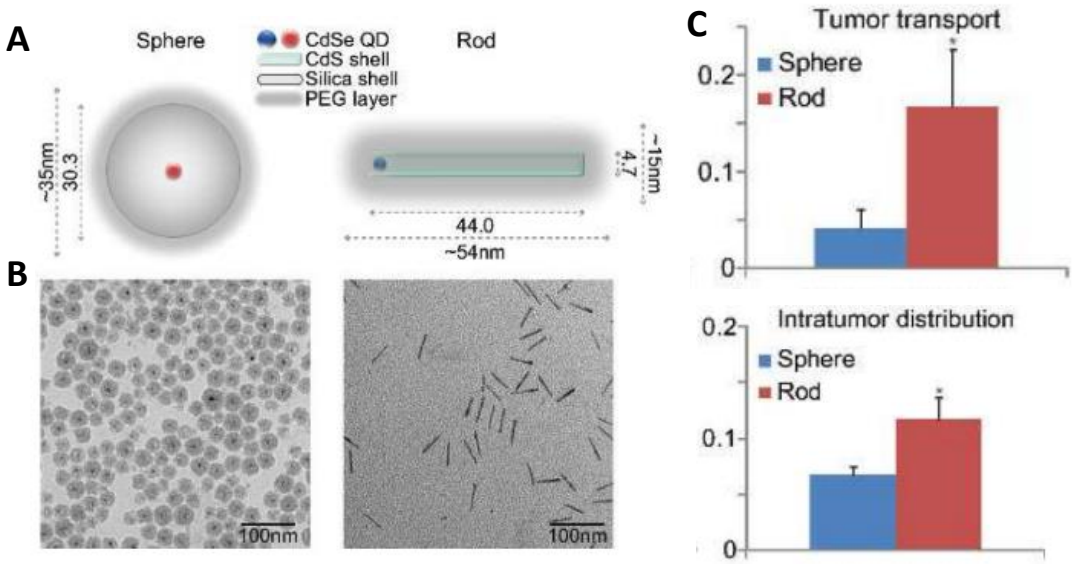

Figure 4.1. **A** – scheme showing dimensions of a sphere and rod shaped silica nanoparticle. **B** – TEM images of each nanoparticle. **C** – Bar charts showing increased tumour transport and distribution of the rod nanoparticle. Adapted from Ref [29].

Bottle-brush macromolecules are an enticing option as drug delivery vectors, however have received relatively little attention in literature,[33] with most research exploring the use of polymer coated organic or inorganic nanoparticles,[34] dendrimers,[35] amphiphilic

block copolymers[36] and nanogel systems.[37] The ability to precisely tune bottle-brush dimensions by modification of the backbone and side chain degree of polymerisation allows for facile synthesis of a range of rod shaped particle sizes and aspect ratios, and therefore provides an effective platform for investigation of morphological effects. Existing as a unimolecular species they do not rely on self-assembly as per worm-like polymer micelles, and thus their chemical compositions and dimensions can be more readily controlled. Additionally chemical functionalisation can be performed at selective positions among the backbone, side chains or end groups of the macromolecule. Bottle-brushes have been studied for use as degradable polymer-drug conjugates and as MRI contrasts agents.[38] [39] PEG based bottle-brushes of varying aspect ratios and with the addition of a hydrophobic crystalline core were investigated to elucidate blood circulation and biodistribution behaviour in rats.[40] It was found the highest aspect ratio materials possessed similar circulation times to the shorter bottle-brushes, but displayed much higher organ accumulation, while the addition of a crystalline core increased rigidity and also contributed to a higher organ uptake.

Alternatively, the synthesis of rod-like nanoparticles through a bottom up supramolecular self-assembly approach may provide advantages due to the inherent degradability of the system, and ability to finely control the chemical structure of each unimer. Potentially toxic long term accumulation of vector could be circumvented by the gradual disassembly of the nanotube into small, readily cleared unimers. A facile route to introducing multiple functionalities could be realised by modifying individual components with numerous drugs / labels and then co-assembling into a single nanotube for simultaneous delivery.

An example of such a system are cyclic peptides consisting of an even number of alternating D and L amino acids, which assemble into nanotubular structures driven through directional hydrogen bonding interactions of the amide groups.[41] The alternation of peptide stereochemistry causes the hydrogen bonding interactions to occur perpendicular to the ring, facilitating face to face stacking aggregation of the cyclic peptides into nanotubes. Cyclic peptides have seen use in a number of biological applications, where they have been identified to possess antibacterial properties. A range of 6-8 unit cyclic peptides displayed high activities against *S. Aureus* and *E. Coli in vitro* and are believed to act through interaction with the bacterial membrane, increasing permeability and disrupting ion potentials.[42, 43] This membrane interaction behaviour was

exploited for drug delivery whereby the cellular uptake of small molecule anticancer drugs was significantly enhanced in the presence of cyclic peptides, leading to reduced IC50 values.[44]

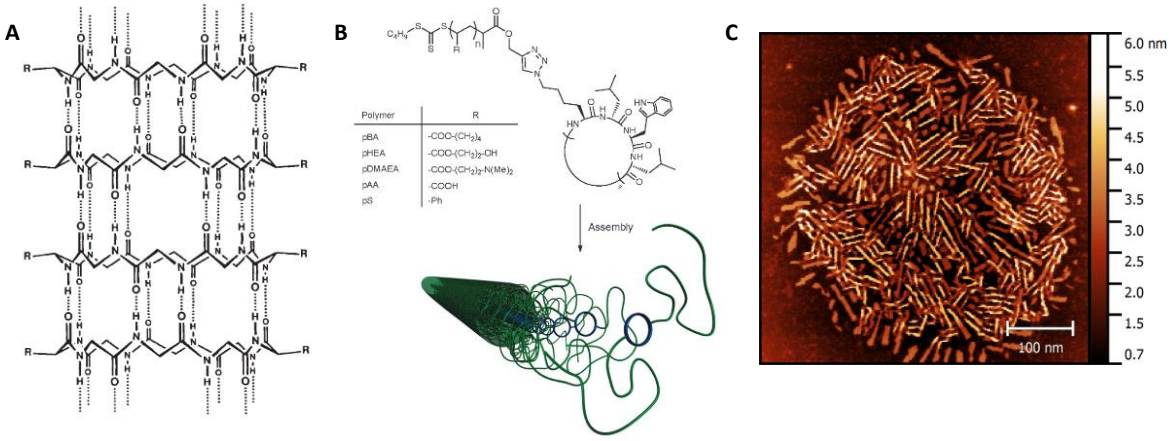

Figure 4.2: A – chemical structure of an octacylic peptide demonstrating the hydrogen bonding interactions between each molecule. Adapted from Ref [40]. **B** – Structure and image of expected morphology of a cyclic peptide polymer conjugate. Adapted from Ref [44]. **C** – AFM image of a PEG-cyclic peptide conjugate dried onto a mica substrate, scale bar = 100 nm.

The cyclic peptides alone, however, tend to possess poor solubility in aqueous solution due to a tendency to form large aggregates and can therefore be challenging to adapt as a drug delivery vectors directly. Modification of the cyclic peptides with polymeric side chains is an effective technique for controlling the material properties, allowing for improvement of solubility, a degree of control of the size of assembly by altering polymer sterics, while also providing a handle for introducing further functionalities.[45] An initial study on the pharmacokinetic properties of cyclic peptide poly(hydroxypropylmethacryalmide) conjugates demonstrated an extended plasma circulation time when compared to a linear polymer of equivalent molecular weight, suggesting the cyclic peptide assembles into a nanotube in the bloodstream.[46] Janus nanotubes can be accessed by conjugation of 2 different polymeric arms to the peptide core,[47] leading to further self-assembly into thicker bundles of nanotubes. Amphiphilic variants of such structures were shown to interact with large unilamellar vesicles to release an entrapped dye, while in *vitro* the janus nanotubes were able to induce escape of small molecules from the lysosomal compartment.[48]

PEG is widely considered the gold standard for biocompatible polymers in nanomedicine, however concerns with the ABC effect make the investigation of alternatives to PEG an

important area of research.[49] Polyacrylamides are a promising class of water soluble materials which typically have low toxicity and some degree of stealth effect *in vivo*, with initial studies revealing they do not display an ABC phenomenon.[50, 51] Of this monomer family Poly(N-acryloylmorpholine) is particularly appealing due to its high solubility in water and a variety of organic solvents, and its well-controlled polymerisation by RAFT,[52] making the synthesis and handling of the material facile. In comparison to PEG, which is typically purchased commercially in a select range of MW and end group functionalities, the polymerisation of NAM proceeds under much less stringent reaction conditions through RAFT allowing for the target MW, multiblock architectures and end group to be precisely modified as required. Furthermore, drug conjugation to PEG can only be performed on the end group, yielding fairly low payload efficiencies, as compared to a monomer such as NAM which could be copolymerised with numerous active linking moieties. As demonstrated in Chapter 2 the grafting from of NAM to access bottle-brushes can be excellently controlled. PNAM has seen use in the modification of membranes to reduce protein fouling[53] and improve hemocompatibility,[54] conjugation with enzymes to increase their solubility[55] and as responsive assembled drug carriers.[56] Therefore current literature suggests PNAM may be a convenient and effective material for a variety of biological applications.

In this chapter the use of PNAM in bottle-brush and cyclic peptide conjugates was evaluated for drug delivery, to assess its potential as an alternative to PEG. The non-degradable covalent backbone of the bottle-brushes means the size can be accurately determined and will presumably be maintained throughout *in vivo* environments, which therefore provides a useful comparison to the dynamic cyclic peptide conjugate system. A greater understanding of the *in vivo* behaviour of the cyclic peptide can be obtained by assessing it against an equivalent low molecular weight linear polymer and the much larger bottle-brush structures.

4.2 Results and discussion

4.2.1 Design and synthesis

As the first step to assessing the biomedical potential of the bottle-brush and nanotube systems, firstly the pharmacokinectic and biodistribution behaviour of the unmodified materials must be studied. Once established the most suitable candidates for loading with active drug molecules could be selected and degradable drug linkages incorporated into the structure to begin determination of treatment efficacies. Therefore within the scope of this study, a method to label the polymers of interest with tracing moieties was established to enable detection during biological experiments.

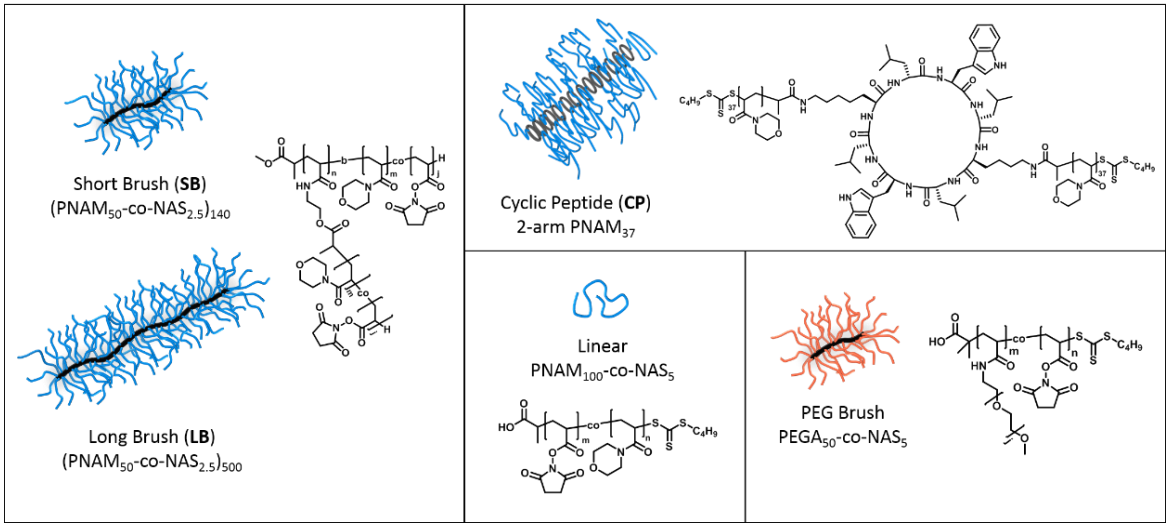

Figure 4.3: Scheme and chemical structures of the 5 compounds studied in this work.

5 compounds were designed for the study – a short and long PNAM composed bottle-brush to probe the effects of aspect ratio, a covalent PEG based bottle-brush to assess PNAM against a known standard, a supramolecular PNAM-cyclic peptide nanotube and finally a short low MW linear PNAM to act a as control.

PNAM conjugated cyclic peptides were synthesised from a RAFT grafting to approach with 1 – 2 polymeric 'arms' per peptide core, by conjugation of an end functional NHS ester RAFT agent to the amino side groups of the cyclic peptide. The PNAM conjugates were found to readily self-assembly into nanotubes (36 nm in length), with a significantly higher aggregation number than the previously studied PHPMA conjugates,[46] and were therefore suitable for testing in biological applications. Assembled cyclic peptide nanotubes possess a 0.47 nm distance between the peptide repeating units, whereas for

vinyl backbone derived bottle-brushes, where every monomer unit displays a side chain, there is a 0.25 nm repeat unit distance between each polymeric graft. Therefore the grafting density of a 2-arm polymer cyclic peptide conjugate should be approximately the same to that of a singly grafted bottle-brush, which lead to the selection of the 2-arm $PNAM_{37}$ compound for further study.

The RAFT R group grafting from approach was used to synthesise two different bottle-brushes with targeted backbones lengths of DP140 and 500, with the same length of side chain (DP50). The side chains were synthesised by copolymerisation of NAM with 5 mol % N-acryloxysuccinimide (NAS), which is known to polymerise in an almost perfectly statistical manner.[57] The incorporation of this monomer was used for functionalisation of dye and radioactive compounds onto the constructs. While the shuttle CTA is effective for improving control of the polymerisation (Chapter 2), in this case the linear polymer side product is undesirable, and therefore the bottle-brushes were synthesised by the standard grafting from approach quenching the polymerisation at ~25 % monomer conversion to mitigate brush-brush coupling terminations. SEC analysis reveals a single population with no low molecular weight linear polymer and narrow dispersities for the bottle-brushes (Figure 4.4).

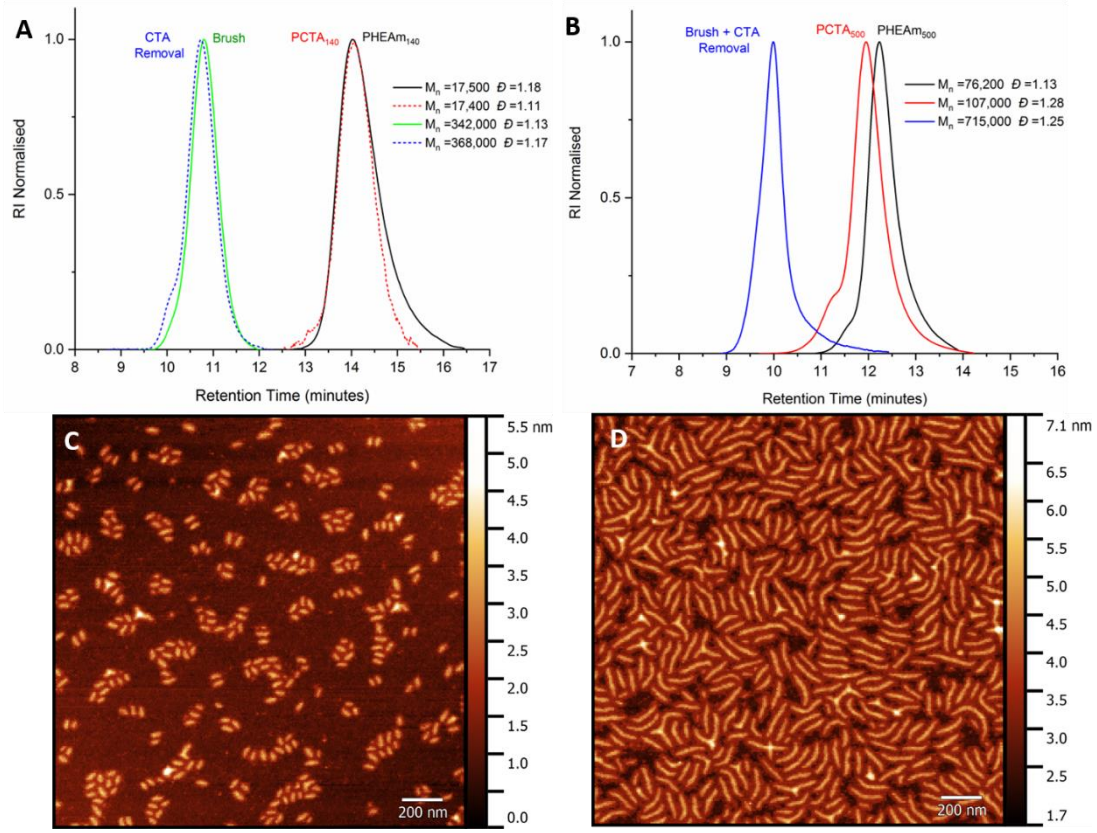

Figure 4.4: SEC molecular weight distributions using DMF eluent system of each synthetic step for **A** – the short PNAM brush, **B** – the long PNAM brush. Atomic force microscopy images prepared for drop casting a dilute aqueous solution onto mica substrate. **C** – SB AFM image, **D** – LB AFM image.

The aqueous solubility of the bottle-brush compounds was initially poor, however, after end group removal of the butyltrithiocarbonate units by radical reduction with ACVA/LPO, the materials were fully soluble. A similar protocol to the earlier described AIBN/LPO removal approach (Chapter 3) was performed, but with the use of ACVA instead as any introduction of the initiator fragment would lead to incorporation of carboxylic acid functionalities, which is advantageous for attaining water solubility. Altering the molar excess of the azoinitator ACVA affected the amount of brush-brush coupling terminations evidenced by a high MW shoulder in SEC, with a larger excess leading to a reduction in formation and optimised conditions of 3 eq. LPO / 30 eq. ACVA were identified (Appendix, Figure C.2). MALDI analysis of a test linear PNAM treated under the same end group removal conditions revealed presence of predominately 'H' terminated chains, with a small number of possible ACVA end groups, although MALDI is not a quantitative technique for the determination of the relative composition of different species (Figure 4.5).

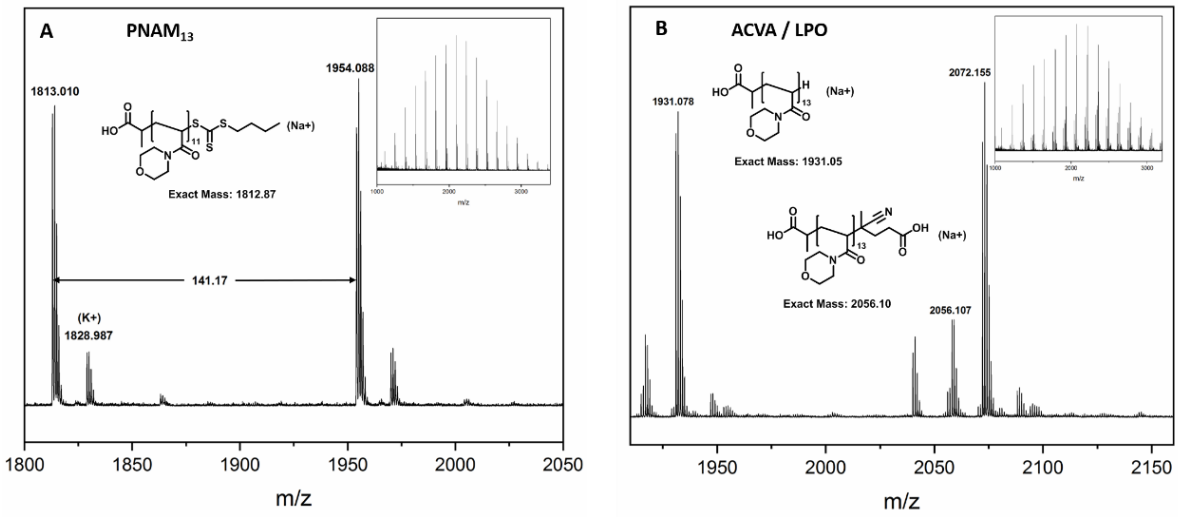

Figure 4.5: MALDI mass spectra of: **A** - $PNAM_{13}$ polymer synthesised with a RAFT agent end group, **B** – $PNAM_{13}$ polymer post reaction with ACVA / LPO revealing full removal of the RAFT end group.

The two PNAM bottle-brushes are useful for providing a controlled comparison of size to the dynamic **CP**, while also offering information on the effect of aspect ratio by transition from a short (40 nm) to long (133 nm) backbone of the particle, as determined by AFM (Figure 4.5). Comparison of the small angle scattering profiles of cyclic peptide PNAM conjugate with the short/long bottle-brush PNAM polymers fitted well with a stiff cylinder + Gaussian chain model (Figure 4.6). The fitted length of the CP cylinder (36 nm) was very similar to the SB compound (41 nm) and thus should provide an effective comparison, while the magnitude of cylindrical radius was comparable for all species (**CP** – 4.1 nm, **SB** – 8.1 nm, **LB** – 8.8 nm).

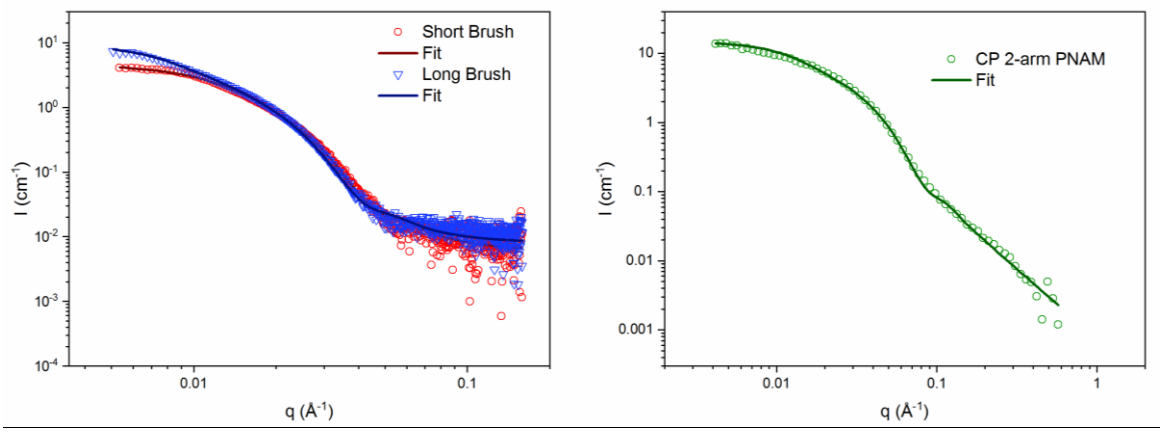

Figure 4.6: Left – SAXS scattering profiles of the SB (red) and the LB (blue) with their fitted models shown as lines. Right – SANS scattering profile of the CP 2-arm PAN conjugate and fit.

A linear polymer of $PNAM_{100}$-co-$PNAS_5$ acts as a control for the cyclic peptide conjugate, with a similar molecular weight but lacking the self-assembly enabling peptide core. Difference in behaviour between this compound and the CP conjugate can therefore be primarily attributed to stacking interactions from the core unit leading to an increased hydrodynamic volume. Finally a PEG bottle-brush was synthesised by grafting through of a 2,000 $gmol^{-1}$ PEG acrylamide macromonomer - 44 PEG repeat units in each side chain is similar to the DP50 PNAM targeted for the other materials and thus is useful as a comparison of changing the polymer composition. Unfortunately targeting higher molecular weights for the macromonomer polymerisation (>DP100) lead to substantial broadening of dispersity (>1.3) (Figure C.9) and therefore a lower MW brush ($M_{n\ theo}$ = 90,000) consisting of a DP50 backbone was studied (Table 4.1). Difficultly in reaching high MWs with good control is a limitation of the grafting through technique, especially for the radical polymerisation of vinyl monomers where the low concentration of vinyl groups and CTA require long reaction times with substantial radical production. Reduction in livingness and thus broader dispersities of the polymer is the likely explanation, demonstrating how the grafting from approach (as used for PNAM brushes) can be superior in some cases. The five compounds were taken forward to *in vitro* / *vivo* study (Table 4.1).

Table 4.1: Chemical strucutre and abbreviations of the synthesised compounds in this study. $M_{n\ SEC}$ and $Đ$ was determined using a DMF eluent system. [a] Activities of the labelled materials were determined after reaction of the NAS units with C14-ethanolamine by liquid scintillation counting.

Compound	Structure	$M_{n\ theo}$ (g mol^{-1})	$M_{n\ SEC}$ (g mol^{-1})	$Đ$	Activity (µCi mg^{-1})[a]
SB	$(PNAM_{50}\text{-co-}NAS_{2.5})_{140}$	987,000	368,000	1.17	1.21
LB	$(PNAM_{50}\text{-co-}NAS_{2.5})_{500}$	3,525,000	715,000	1.25	1.16
Linear	$PNAM_{100}\text{-co-}NAS_5$	15,100	16,400	1.13	0.69
PEG	$PEGAm_{45}\text{-co-}NAS_5$	90,000	64,600	1.32	0.36
CP	$CP\text{-}(PNAM_{37})_2$	12,000	20,600	1.10	-
CP-NAS	$CP((PNAM_{37})\text{-b-}(PNAM_{7.5}\text{-co-}NAS_{7.5}))_2$	16,400	28,900	1.17	6.59

4.2.2 Fluorescence and radioactive tag labelling

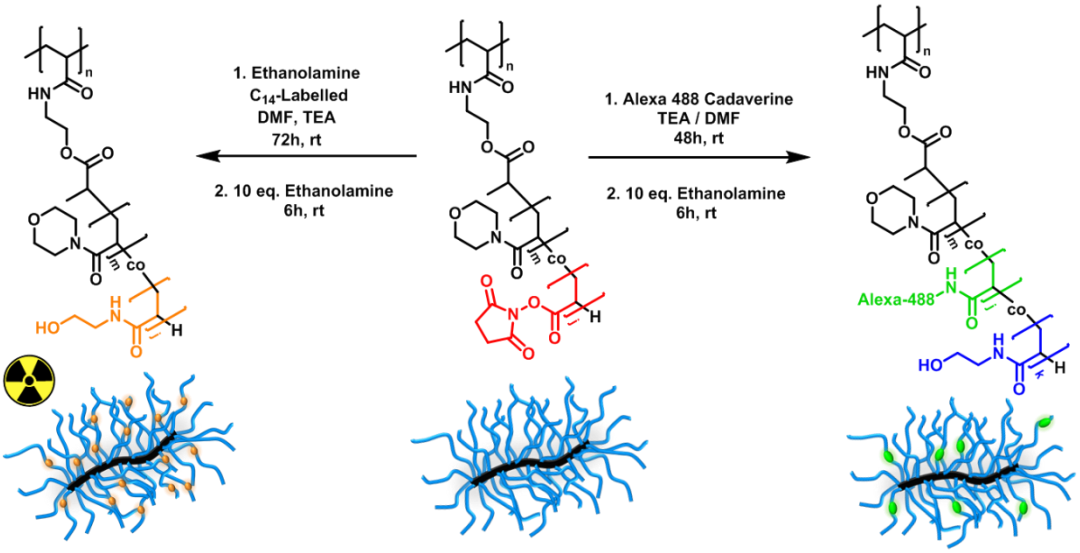

Figure 4.7: Synthetic scheme for the labelling of the short PNAM brush with either a radioacitive or fluorescent tag. The same reaction conditions were used for conjugation of the other 4 polymer materials.

To aid detection of the polymer constructs either C14 radiolabelled ethanolamine or cadaverine Alexa-488 fluorescent dye (excitation 488 nm, emission 502 - 594 nm) were conjugated to the polymer constructs by amide coupling of the amine functional label and NHS ester of the NAS monomer units (Figure 4.7). Stability of amide bonds within the polymeric chains is high *in vivo*, and therefore is an appropriate chemistry for the introduction of tracing labels. If the chemical bond with the polymer construct was labile, it is possible that during biological experiments the behaviour of free label molecule would be followed instead of the vector.

To probe efficacy of the amide coupling reaction, firstly the **SB** was treated with a 2 equivalents excess of benzylamine in DMF with TEA, whereby after 24 h reaction time ^{1}H NMR revealed full consumption of the NHS ester peak at 2.85 ppm and in DMSO-d_6 the introduction of the benzyl group onto the polymer with peaks at ~7.2 ppm is clearly observed (Figure 4.7). Thus the coupling readily occurs to high yield at room temperature and is a suitable approach for introduction of labelling moieties.

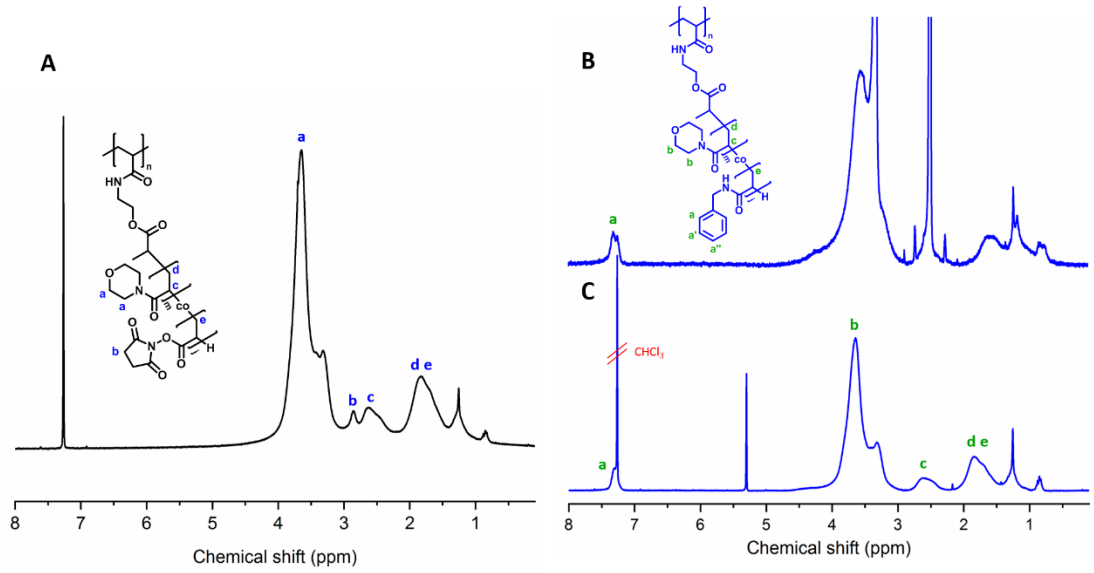

Figure 4.8: A – ^{1}H NMR spectra in $CDCl_3$ of the purified PNAM-co-PNAS bottle-brush. B – ^{1}H NMR spectra in $CDCl_3$ after reaction with benzylamine displaying full consumption of the NHS ester environments. **C** – ^{1}H NMR spectra in DMSO-d_6 of the benzylamine conjugate showing presence of aromatic signals.

For the cyclic peptide an alternate strategy for the incorporation of NAS units was taken - after synthesis of the PNAM CP conjugate the side arms were further chain extended by RAFT polymerisation with a $PNAM_7$-co-$PNAS_7$ block to enable functionalisation. This conjugate was labelled to a higher loading rate and then mixed in a 1:10 molar ratio with the pre-chain extended 2-arm CP starting material, with the dynamic nature of the cyclic peptide stacking interactions ensuring random co-assemble with the unlabelled conjugates. A study on the dynamic co-assembly of cyclic peptides through FRET pair interactions has confirmed this behaviour.[58] The rationale of this approach was to mitigate effects of labelling on the size of CP self-assembly - by decreasing the ratio of labelled conjugates and also by functionalising at the exterior of the side chains, reducing likelihood of altering hydrogen bonding interactions in the peptide core.

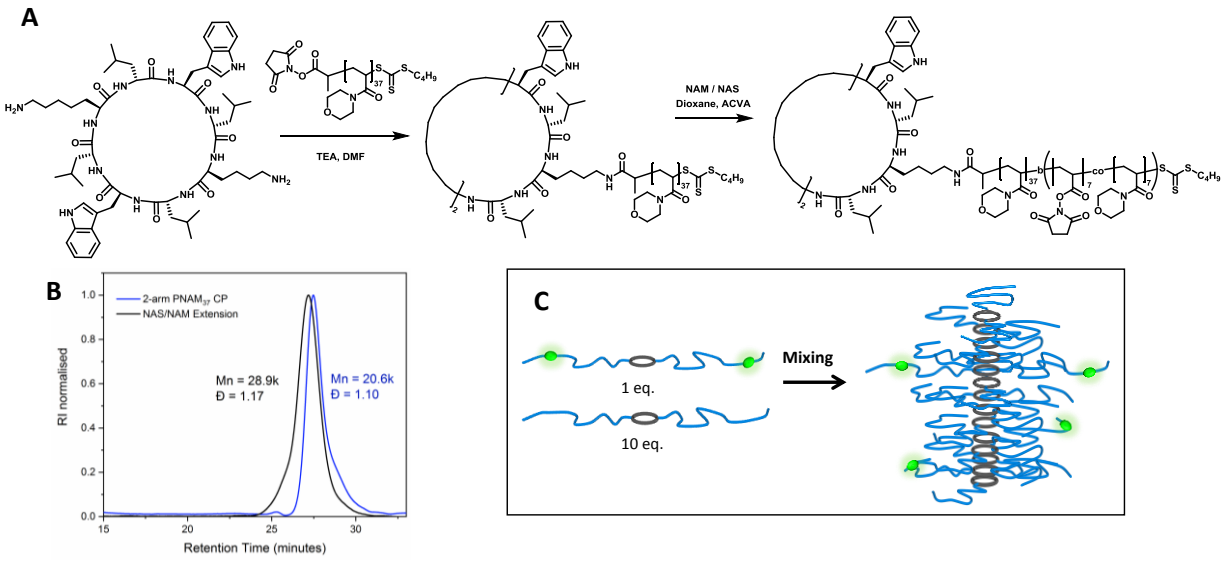

Figure 4.6: A – synthetic approach to the labelling of the 2-arm CP conjugate by chain extension with NAS units. **B** – SEC chromatograms in DMAc eluent system showing clear chain extension of the conjugate with the NAS containing block. **C** – Schematic for the mixing approach of labelled CP with the starting material.

Synthesis of fluorescently labelled compounds was performed with 0.015 equivalents Alexa-488 with respect to NAS units (0.07eq. for **CP**), after which a large excess of ethanolamine (unlabelled) was added to ensure full consumption of NHS ester units and prevent potential side reactions occurring during the biological experiments, while also ensuring the polymer remains fully hydrophilic with no residual hydrophobic NAS units. The low quantity of Alexa-488 moieties (>0.1 % with respect to NAM monomer units) introduced onto the polymers reduces any potential change in properties the dye molecules might endow to a PNAM homopolymer, and therefore the tests *in vitro* should reflect the behaviour of the unmodified materials. HPLC of the Alexa-488 polymer conjugates confirmed fluorescent activity at the desired wavelengths and almost full removal of free dye molecules after dialysis purification (Figure 4.9).

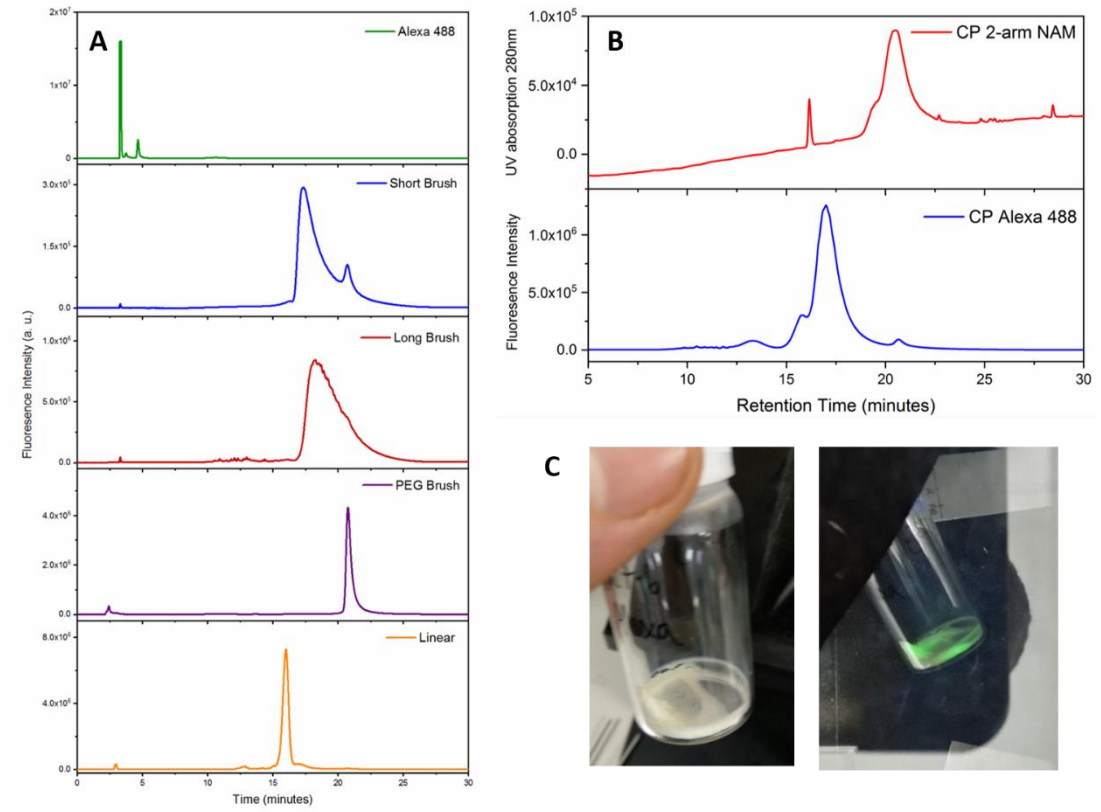

Figure 4.7: A – HPLC traces of polymers after modification with Alexa-488 monitored by fluorescent intensity at the 490 nm / 525 nm excitation/emission wavelengths. **B** – HPLC traces of the CP before and after chain extension and functionalisation with dye. **C** – Image of the dye-labelled SB, under long wavelength UV irradiation a green emission is observed.

Radiolabelling was performed targeting an activity of 1 µCi mg^{-1} by addition of 0.2 equivalents C14-ethanolamine with respect to NAS units. The reaction was assessed by purification with SEC (Sephadex PD10 column) and radioactivity measured by liquid scintillation counting of each fraction. The clear separation of polymer and free radiolabel demonstrates successful conjugation of the radiolabel onto the polymeric constructs (Figure 4.10). Additional dialysis purification was carried out to ensure complete removal of the free radiolabel and indeed further SEC analysis (Sephadex G25 column) showed high sample purity. An inferior conjugation efficiency and thus lower radioactivity was obtained for the PEG compound, presumably due to the lower NAS content by weight (10 mol%, 0.9 wt%) in comparison to the PNAM copolymer (5 mol%, 3.9 wt%), despite the excess of NHS ester with respect to ethanolamine used in both cases would be expected to ensure almost full conjugation of the radiolabel. The mixing strategy for **CP** required higher activities of the labelled conjugate and therefore an increased value was targeted, with the purified conjugated possessing an activity of 6.59 µCi mg^{-1}.

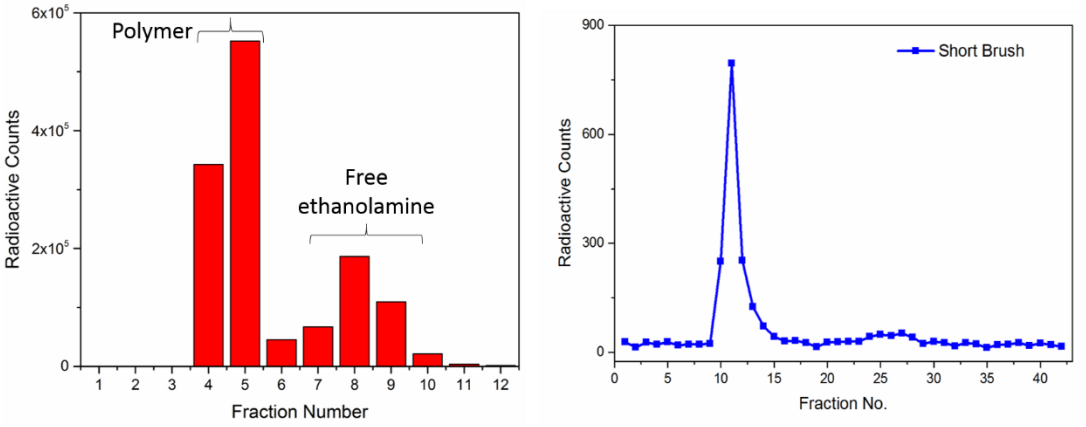

Figure 4.8: Left – PD10 column purification performed of crude reaction mixture showing separation of polymer and the free label. Right – G25 SEC column with PBS eluent of the dialysis purified radiolabelled SB material showing presence of only the high MW brush species. Radioactive counts determined by scintillation counting.

4.2.3 Cell viability

The *in vitro* toxicity of the polymer samples was assessed by an MTT cell growth inhibition assay for 72h on 3T3 fibroblast, MDA-MB-231 breast cancer, HEK-293 and 4T1 mouse breast cancer cell lines. PEG and PNAM are considered biocompatible polymers with low toxicities and as such similar results were expected for the compounds studied here. All five compounds were reacted with unlabelled ethanolamine to remove all NAS units, and instead replaced with poly(hydroxyethylacrylamide) monomeric units, prior to cell testing which has also been identified as a suitable biocompatible polymer.[59] However, some toxicity was observed at higher dosages up to 1 mg ml^{-1} across all compounds (Figure 4.11), most clearly for the 4T1 cell line with cell viabilities dropping to ~75%. For the further flow cytometry and confocal microscopy experiments cells were dosed to a concentration of 0.3 mg ml^{-1} sample, which should minimise detrimental toxicity.

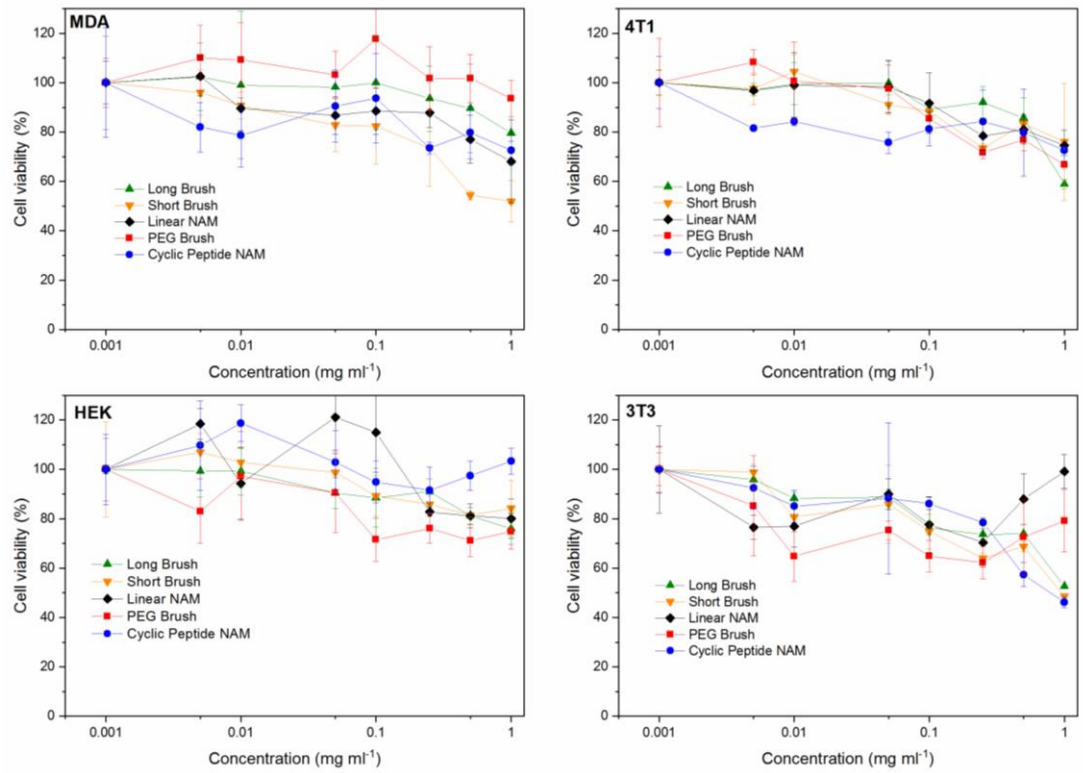

Figure 4.9: MTT assay data for four cell lines for the five compounds studied.

4.2.4 Cell Association

The Alexa-488 labelled polymers were used to determine cellular association by flow cytometry on two cell lines (MDA and 3T3). Cells were incubated with samples for 3 h at either 4 °C or 37 °C, or for 24 h at 37 °C. All compounds showed the trend of significantly increased uptake going from 3 h to 24 h, indicating the accumulation of the compound either adsorbed in the membrane of inside a cell compartment, typical for nanoparticle species. Negligible cellular fluorescence for the 3 h, 4 °C experimental condition implies the uptake proceeds through predominately energy dependent endocytosis pathways (Figure 4.12) rather than passive mechanisms such as membrane diffusion.

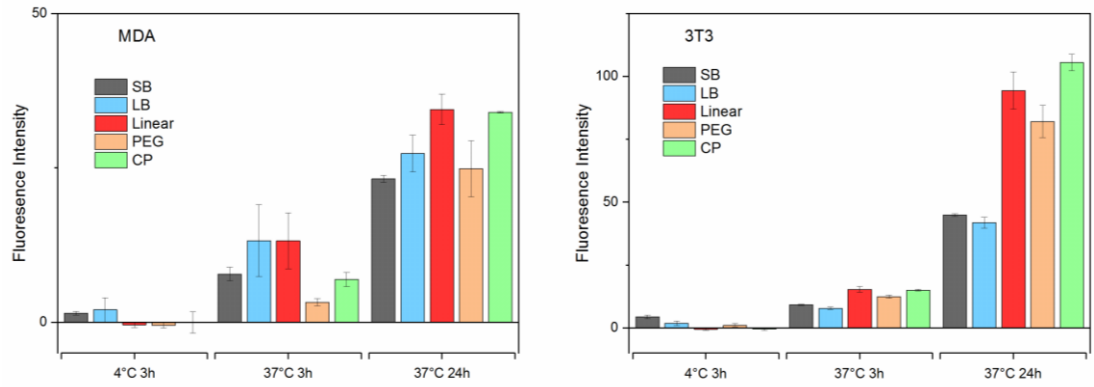

Figure 4.10: Flow cytometry data for left – MDA and right – 3T3 cell lines. Experiments were performed in triplicate for each set of conditions. Error bars show standard deviation.

The **CP** and linear shows the highest uptake rates with comparable values after 3 h and 24 h for both cell lines. Poly(hydroxypropylmethacrylamide) cyclic peptide conjugates have been shown to display increased cell uptakes over an equivalent linear polymer,[46] however it is possible changing the nature of the polymer to PNAM as in this study may change this relationship and under these conditions / cell lines an identical association is observed. As such it is not possible to conclude if the effect of supramolecular stacking into nanotubes has an impact in vitro for the 2 arm PNAM conjugate, however there is a significant increase over the covalently bound backbone bottle-brushes.

The similar chemical composition of the **SB**, **LB** and linear compounds facilitates determination of the polymeric structural effect upon cell association. A stark difference between the linear and higher molecular weight bottle-brush samples is apparent. Despite reports of nanoparticles in the 30-50 nm regime possessing increased cell uptake,[60] in this case the small linear polymer (<10 nm R_h) exhibits the highest uptake, while the effect of increasing MW and aspect ratio between the SB and LB does not appear significant. To fully understand this system further studies would be required to elucidate the effects of polymer composition (PEG / PNAM), the molecular weight and architecture of the polymer. Additionally experiments with the use of endocytic inhibitors could provide information on the predominant mechanism within endocytosis.[61]

4.2.5 Spacial coincidence with Lysosomal tracker

To gain more information on the cell association behaviour and to in particular identify which regions of the cell the compounds interact with, confocal microscopy was

performed. Lystroacker, a pH sensitive fluorescent dye conjugated to dextran, is highly effective as a marker for the lysosomal compartment and was therefore co-treated with the compounds to identify any spatial coincidence of the two. MDA and 3T3 cell lines were incubating for 24 with the fluorescently labelled conjugates and afterwards studied in the confocal microscope. Presence of alexa-488 channel fluorescence confirms uptake of compound inside of the cell, rather than purely through interaction with the membrane (Figure 4.13). Treatment with Lysotracker Red enables assessment of compound colocalisation, and in the merged red and green channels strong evidence of overlaying signal is observed by presence of the yellow coloured regions. For all five compounds across both cell lines uptake seems to occur primarily through the lysosomal compartments, consistent with the energy dependent endocytic pathway as the most probable mechanism for cell association.

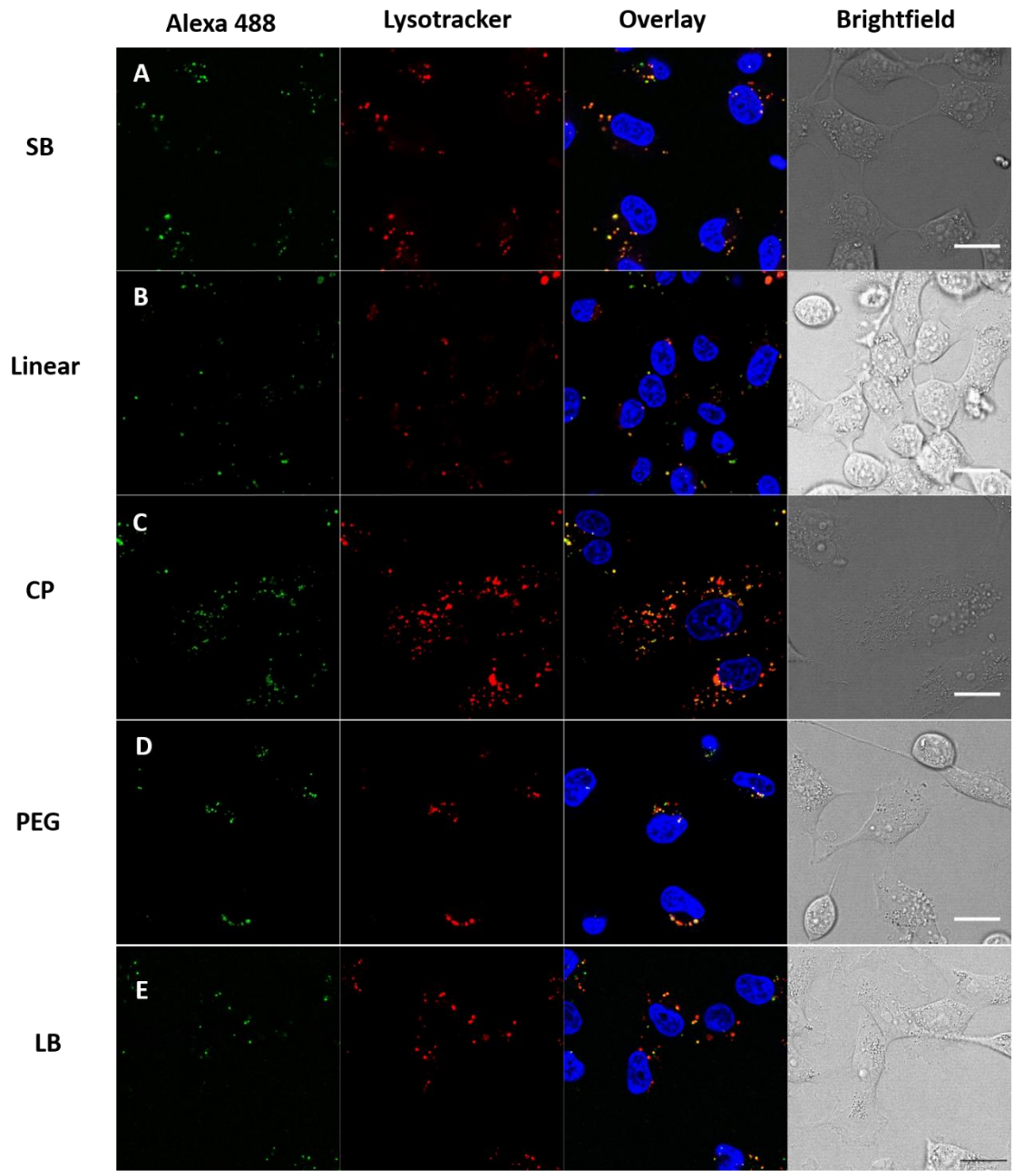

Figure 4.11: Confocal microscopy images of MDA cell cultures incubated with the labelled compounds for 24 h at 37°C prior to imaging and with Lysotracker red / Hoechst blue stains shortly before. Channels show the Alexa-488 labelled compounds at 490 / 530 nm excitation / emission, lysotracker at / nm and Hoechst blue at / nm.

At the recorded settings, the resolution of the confocal microscope was approximately 200 nm and, therefore, it is possible the samples are not truly colocalised but rather happen to be within 200 nm distance. To elucidate this, additionally a time lapse confocal imaging experiment was carried out on the **CP** and **SB** compounds in live cells to clarify coincidence with the lysosome. As demonstrated by still images at various time points (Figure 4.14), the yellow regions, resulting from stacked compound and lystoracker,

remain colocalisied over the course of the time lapse despite motion between frames. This therefore provides further evidence of strong lysosomal compartmentalisation rather than incidental overlay by random fluctuations. It is worth noting after 4 seconds of recording quenching of the red lysotracker dye is observed, causing the red/yellow colour to fade, and therefore longer measurements times could not be performed.

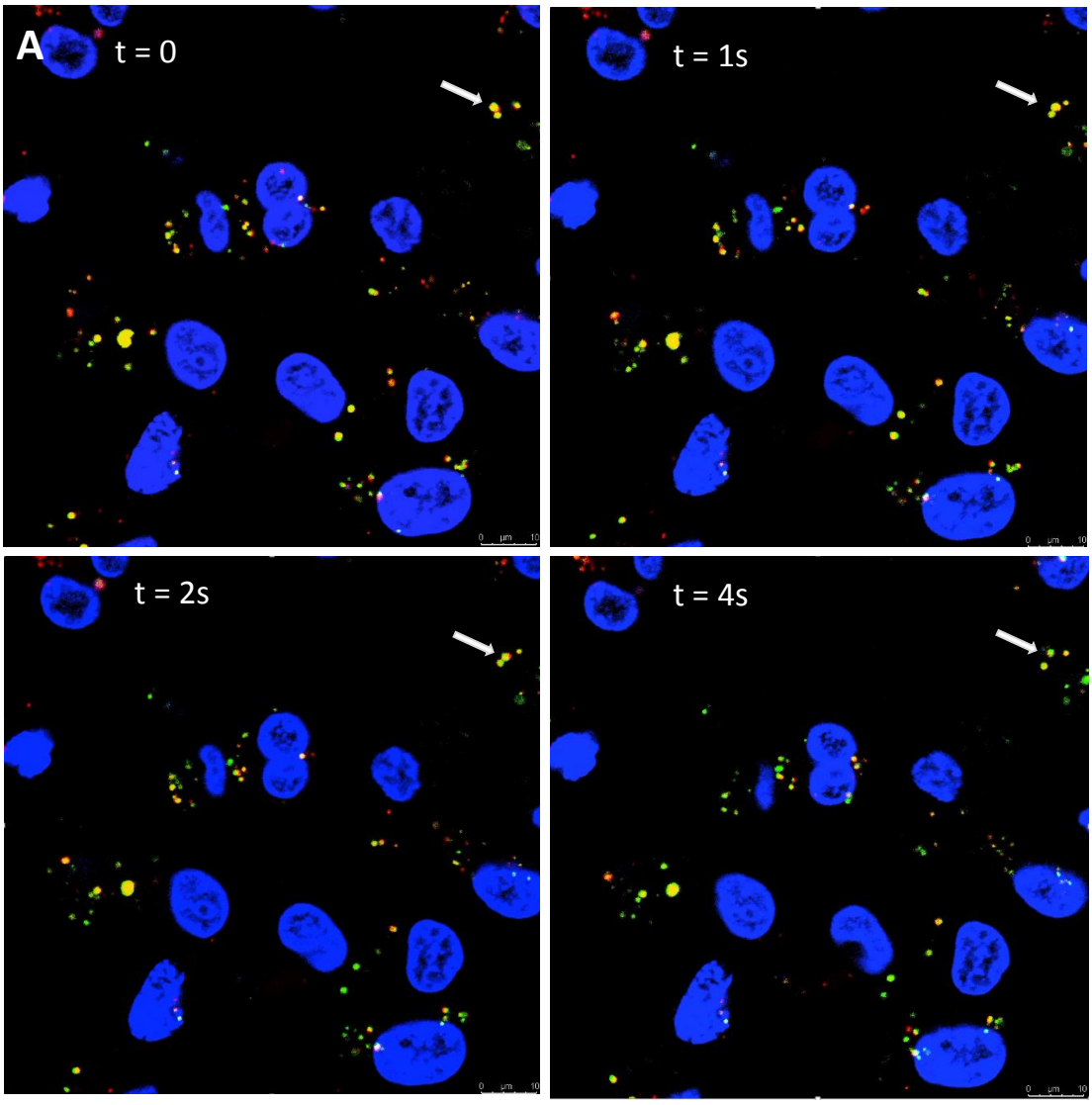

Figure 4.12: Confocal microscopy showing still images of a time lapse experiment at various time points of MDA cells treated with the dye labelled CP conjugate.

4.2.6 *In vivo* pharmacokinetics

The C14-radiolabelled compounds were injected intravenously into male Sprague-Dawley rats at a nominal dose of radioactivity (1 µCi, varying 0.82 – 2.78 mg dose of sample) and blood samples taken over the course of 24 h to monitor plasma concentration

time profiles. Pharmacokinetic parameters were calculated using the non-compartment model, values listed in Table 4.2.

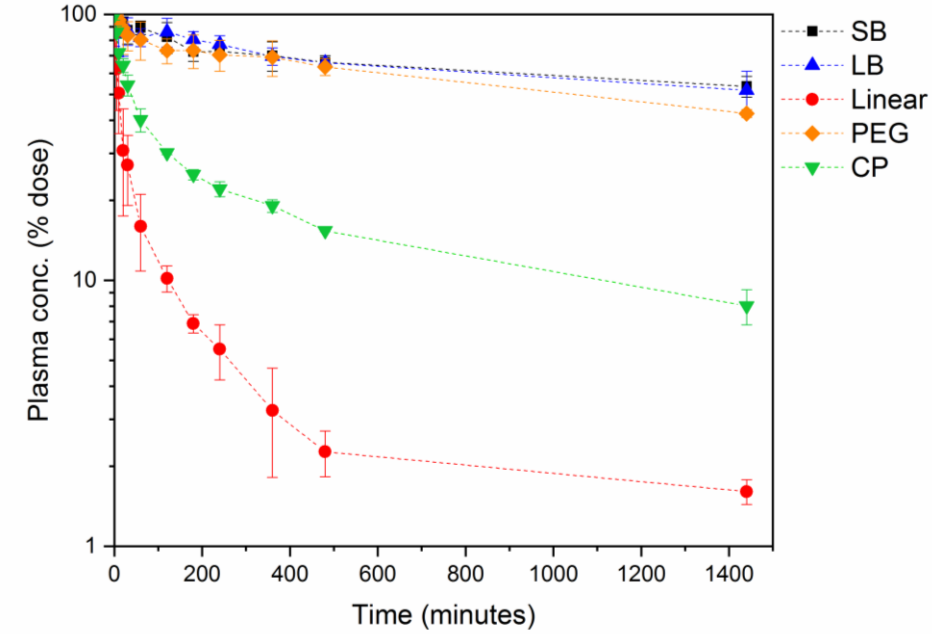

Figure 4.13: Plasma concentration profiles as a % of initial dose against time for the 5 radiolabelled compounds.

Comparing percent dose normalised plasma concentrations (Figure 4.15), the linear polymer was cleared rapidly relative to the high MW bottle-brush polymers which displayed higher exposure over time, with the cyclic peptide possessing an intermediate rate. This was reflected the elimination half-life values of >28 h for the three brushes, 14.6 h for **CP** and only 4.9 h for the linear polymer. The significantly increased half-life of the CP conjugate compared to the linear was hypothesised to be caused by the cyclic peptide core moiety, most likely indicative of stacking interactions occurring in *vivo* leading to a higher MW species that could not be renally cleared. The higher circulation time of the SB (40 nm length) however, suggests the CP conjugate is significantly smaller *in vivo* than the SANS determined length. This effect may be attributed to the vascular environment in *vivo* where hydrogen bonding interactions may occur with blood components in addition to shear flow forces, thereby inducing nanotube disassembly. As a result it is challenging to assess the true length of the nanotube in the circulation system, however a substantial improvement in pharmacokinetics over low MW PNAM is observed. Another consideration is possibility for association of the CP moiety with proteins within the blood stream, to form a corona of different composition than the linear

polymer, which could lead to the altered plasma residence time. Further analysis of plasma samples by SEC could evaluate this.

Table 4.2: Pharmacokinetic parameters determined by the non-compartment model showing the average and standard deviation across n=3 in vivo plasma concentration experiments.

	Short Brush	Long Brush	Linear NAM	PEG	CP
t1/2 (h)	55.6 ± 27.6	35.3 ± 2.7	4.9 ± 3.3	28.6 ± 9.4	14.6 ± 2.9
AUC (µCi ml^{-1} min)	50.75 ± 2.9	78.3 ± 7.1	4.75 ± 0.7	63.5 ± 5.0	20.5 ± 0.8
Vd (ml)	24.3 ± 2.3	14.5 ± 1.7	89.5 ± 54.6	16.8 ± 2.7	38.2 ± 3.5
Cl (ml h^{-1})	0.342 ± 0.102	0.287 ± 0.049	13.6 ± 2.59	0.426 ± 0.065	2.06 ± 0.248
Urine (% dose)	0.62 ± 0.10	0.66 ± 0.40	50.8 ± 18.3	2.52 ± 0.14	28.5 ± 19.3

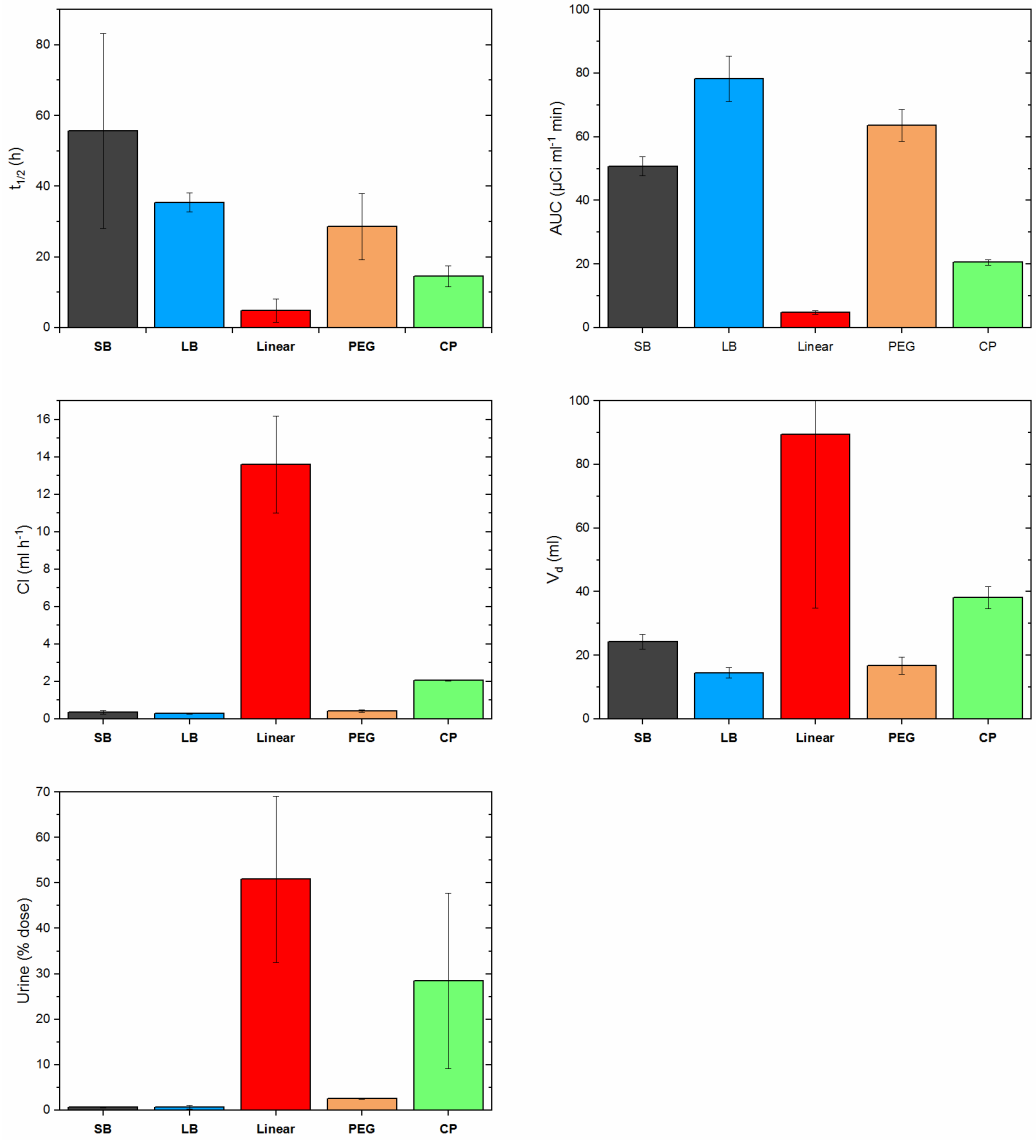

Figure 4.14: The pharmacokinetic parameters listed in table 4.2 visualised in bar chart format.

Profiles appear very similar between the short and long brush, the most important factor for long circulation times in this case may be exceeding the renal excretion limit cut-off (5.5 nm R_h, ~50k g mol^{-1} for a hydrophilic polymer), which both PNAM brushes do substantially (1M / 3.2M g mol^{-1} for SB / LB respectively). The molecular weight cut-off is a rough value, however, and refers to a linear polymer - the highly branched systems studied here may deviate from this. The slightly reduced plasma residence time of the PEG brush is primarily attributed to the lower MW of this compound, which shows a higher % dose excreted into urine (2.5 % vs 0.6 % for SB). The molecular weight distribution of the PEG brush ($M_{n\ theo}$ = 90,000 g mol^{-1}, $M_{n\ SEC}$ = 64,400 g mol^{-1}, $Đ$ = 1.32) indicates a small proportion of species will fall below the excretion limit and thus be cleared at a faster rate.

The apparent volume of distribution (V_d) represents the theoretical volume of dilution required to reduce the concentration of compound administered to the observed value. In the case of the high MW bottle-brush species, the V_d was expected to be close to the total blood volume of the rat (~20 ml), suggesting that, the compound was fully distributed into the central blood compartment and has not undergone significant renal clearance or further distribution to organs or tissues within the initial time points. A V_d significantly larger than the maximum blood volume would indicate the compound is either distributed elsewhere in the body or rapidly excreted, most likely into urine. Indeed, for the **LB**, **SB** and **PEG** close to expected values for V_d were observed (14.5 - 24.3 ml), whereas a much higher (89.5 ml) value is found for the linear polymer indicating the fast removal from the blood compartment. The **CP** system exhibited an intermediate V_d value (39.7 ml), this trend matches with both the clearance rates and dose excreted into urine, which are also highest for the linear polymer and of moderate value for the **CP**. The intrinsic ability of the **CP** to disassemble into unimeric units of low MW allows for potentially beneficial clearance through the renal excretion pathway. The improved circulation time over the linear polymer is promising, however it is significantly lower than the bottle-brush and for drug delivery applications targeting tumours a higher half-life for the **CP** would often be considered desirable.

The significantly higher exposure observed with the PNAM bottle-brushes suggests the material has potential as an alternative to PEG in biomedical applications, although the difference in MW of the PEG brush means it is not possible to conclusively assess

performance of NAM vs PEG through this experiment. However, the data still provides promising results despite the non-ideal comparison.

4.2.7 Biodistribution

The biodistribution of the materials in major organs was determined by harvesting tissues post 24 h dosing and measuring the residual levels of C14 radiolabel. Organs were not perfused and therefore compound present in the blood and vasculature, especially pertinent for the kidneys, heart and lungs, were also included in measurements. The level of accumulation for the linear polymer was very low in all organs (<1.38 % dose) (correlating with the high dose recovery in urine) and suggests that rapid renal clearance reduced distribution into organs. Slightly higher values, particularly for the liver and kidneys (4.06 % and 3.22 %), were observed for the **CP**, with relatively higher accumulation of bottle-brush materials in the organs, attributed to their longer circulation times. The results are consistent with the reasoning of the initially assembled CP nanotube avoiding rapid clearance by virtue of its large hydrodynamic volume, while the gradual disintegration into smaller nanotubes / unimers prevents long term accumulation into organs and ultimately leads to renal excretion. This demonstrates the inherent degradability advantage of the self-assembled CP system, as opposed to the covalently bound bottle-brush approach.

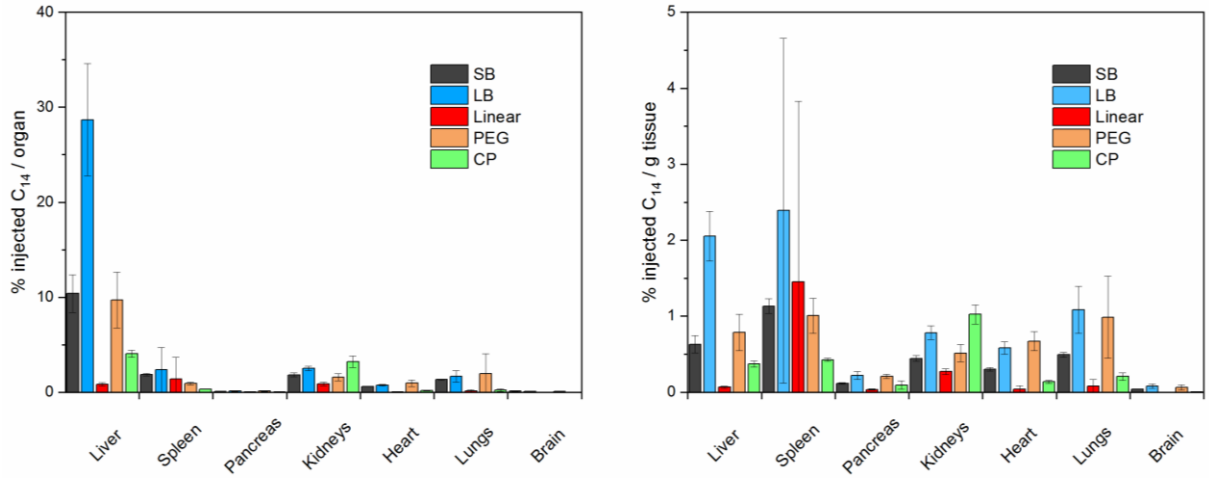

Figure 4.15: Biodistribution data in major organs of the 5 compounds determined after 24 h IV dosage. Blank organs were spiked to determine counting efficiencies. Left - % dose found in each organ. Right - % dose per gram tissue of each organ.

Increasing the aspect ratio and MW of the PNAM bottle-brush from the **SB** to **LB** resulted in significantly higher liver accumulation (10.4 % vs 28.7 % respectively), with the

dosages in other organs showing much smaller differences. The particularly high accumulation in the liver and spleen is indicative of uptake by the mononuclear phagocytic system (MPS), which is known to occur more readily for larger nanoparticles and explains the trend of increased accumulation for the **LB** over **SB**.[62] Similar results for biodistribution of high aspect ratio bottle-brushes was reported by Müllner *et al*.[40] and suggests that the usage of shorter bottle-brushes for drug delivery may be superior than higher aspect ratio materials, as almost identical plasma residence times were obtained without extensive liver accumulation. Additionally, smaller nanoparticles under 15 nm (spherically shaped) have been shown to possess increased penetration than larger particles through extracellular matrix within tumour sites and thus perform better in tumour growth inhibition.[34] Comparable biodistribution was observed for the **SB** and **PEG** systems, indicating similar *in vivo* behaviour for both PNAM / PEG materials, although there may be a molecular weight dependence on biodistribution behaviour. Figure 4.17 (right) shows the % dose per gram tissue, which reveals the bottle-brushes have a high affinity for accumulation into the liver and more so for the spleen, likely as a result of efficient splenic filtration through the MPS clearance mechanism. This effect was particularly high for the **LB** suggesting a correlation between very high molecular weight and this accumulation effect.

4.3 Conclusion

Cyclic peptide PNAM conjugates were found to assemble into 36 nm nanotubes in solution and were compared to two covalently bound bottle-brushes of 40 or 133 nm in length. Confocal microscopy found evidence of endosomal uptake from the high tendency of lysosomal colocalisation for all of the studied compounds. This was corroborated by the low degree of cell association measured at 4°C as opposed to the increased values at 37°C, in these experiments the CP possessed similar uptake to a linear polymer and higher than the bottle-brush materials so may be advantageous for delivery in this regard. Stacking of the CP into nanotubes *in vivo* is the most likely explanation for the increased plasma residence times observed over a comparative MW linear, however, much lower half-life times were found for the CP than both the SB and LB suggesting the nanotube is either significantly smaller than 40 nm or the dynamic self-assembly causes fairly fast degradation. This is reflected in the biodistribution results where the CP shows negligible organ accumulation, likely due to the ability to disassociate into low MW unimers. Usage of CP delivery systems may be promising for targeting of tumours by the EPR effect where initial accumulation is desirable but often smaller polymer / nanoparticles are found to penetrate tissues more effectively. Additionally a PEG bottle-brush was studied to justify the use of PNAM as a biocompatible drug delivery material, and indeed the PNAM brushes were found to perform comparably with plasma half-lifes exceeding 35 h. The ease and flexibility of synthesis of NAM polymers by RAFT make these appealing candidates for further research, especially the short PNAM brush. Future investigations will look into the behaviour of the CP and PNAM brushes in tumour models to further assess their potential in anti-cancer treatments.

4.4 Experimental

Materials

4-acryloylmorpholine (NAM, 97%) was obtained from Sigma-Aldrich and passed through a basic alumina column before use. N-Acrylic acid hydroxysuccinimide ester (NAS, >90%), 4,4′-azobis(4-cyanovaleric acid) (ACVA, >98%), acryloyl chloride (>97%), acetonitrile, trimethylamine, diisopropylethylamine (DIPEA), triisopropylsilane, dimethyl sulfoxide-d_6 (99.9% D atom) and chloroform-*d* (99.8% D atom) were obtained from Sigma Aldrich and used as received. CH_3O-PEG-NH_2 (MW 2000 Da, Rapp Polymere), Alexa-488 Cadaverine (Fisher), C14-Ethanolamine (50-60 µCi/mmol, American Radiolabeled Chemicals), 1,4-dioxane (anhydrous, Acros Organics), N,N-dimethylformamide (anhydrous, Acros Organics), N-methylmorpholine (NMM, Alfa Aesar) and piperidine (Alfa Aesar) were used as received. 4-(4,6-ii(DMTMM·BF_4), O-(1H-6-Chlorobenzotriazole-1-yl)-1,1,3,3-tetramethyluronium hexafluorophosphate (HCTU), 2-chlorotrityl resin, Fmoc-D-Leu-OH, Fmoc-L-Lys(Boc)-OH, Fmoc-L-Trp(Boc)-OH were purchased from Iris Biotech and used as received.

Instrumentation and analysis

NMR spectroscopy

^{1}H and ^{13}C NMR spectra were ran on either a Bruker DPX-300 or DPX-400 spectrometer using deuterated solvents (deuterated dimethyl sulfoxide, chloroform or water).

SEC analysis

SEC analysis was performed on two systems:

DMF-SEC: Agilent 390-LC MDS instrument equipped with differential refractive index (DRI), viscometry (VS), dual angle light scatter (LS) and dual wavelength UV detectors. The system was equipped with 2 x PLgel Mixed D columns (300 x 7.5 mm) and a PLgel 5 µm guard column. The eluent is DMF with 5 mmol NH_4BF_4 additive. Samples were run at 1 ml min^{-1} at 50 °C. Poly(methyl methacrylate) standards (Agilent EasyVials) were used for calibration, MW ranging from 550 to $2.14*10^6$ g mol^{-1}. Analyte samples were filtered through a nylon membrane with 0.22 μm pore size before injection. Respectively, experimental molar mass ($M_{n,SEC}$) and dispersity ($Đ$) values of synthesized polymers were determined by conventional calibration using Agilent GPC/SEC software.

DMAC-SEC was performed on a Shimadzu modular system comprised of a SIL-20AD automatic injector, a RID-10A differential refractive-index detector and a 50 × 7.8 mm guard column followed by three KF-805L columns (300 × 8 mm, bead size: 10 μm, pore size maximum: 5000 Å). *N*,*N*-Dimethylacetamide (DMAc, 0.03% LiBr) was used as the eluent with a flow rate of 1 ml min^{-1} at 50 °C. Samples were filtered through 0.45 μm PTFE filters before injection. The SEC calibration was performed with polystyrene standards ranging from 500 to 2×10^6 g mol^{-1}.

Atomic force microscopy

AFM images were acquired in AC mode on a Cypher S system (Asylum Research). The probes used were AC160TS from Olympus probes with a nominal resonant frequency of 300 kHz and a spring constant of approximately 40 N m^{-1} on a Multimode AFM (Asylum Research). Images were acquired at a pixel resolution of 512 and a scan rate of 1 Hz. Samples were diluted to 1 mg ml^{-1} in water, and samples were prepared by drop casting the solution onto a freshly cleaved mica substrate and drying under stream of nitrogen. The data were analyzed by the Asylum Research software.

Synthesis of linear peptide

A previously described literature procedure was followed.[63] Synthesis of NH_2-L-Lys(Boc)-D-Leu-L-Trp(Boc)-D-Leu-L-Lys(Boc)-D-Leu-L-Trp(Boc)-D-Leu-COOH was performed using a Prelude (Protein Technologies inc.) automated solid phase peptide synthesiser, using a previously described procedure. 2-chlorotrityl resin (0.36 g) was allowed to swell with DCM prior to loading by addition of a solution of Fmoc-D-leu-OH (1.01 g, 2.86 mmol) and DIPEA (0.4 M) in DMF (16 ml) and reacted for 2 h, drained and then treated with DCM / MeOH / DIPEA (17:2:1, 10 ml) to ensure capping of unreacted resin sites. The drained resin was washed with DMF, and 20% Piperdine solution in DMF (15 ml) was added to deprotect the Fmoc groups, followed by further washing with DMF. Subsequent coupling steps were performed by addition of Fmoc-amino acid (2.86 mmol) with an HCTU (0.83 g, 0.20 mmol) and NMM (0.44 ml, 0.4 mmol) solution in DMF (10 ml), left to react for 2 h and then washed with DMF. Further deprotection and addition steps were repeated until the targeted octapeptide was synthesised. After the final Fmoc deprotection step the peptide was cleaved from the resin by addition of HFIP (20 %) in DCM (3 x 10 ml) and washed with DCM. The solution was concentrated under vacuum to yield an off-white solid. ESI MS +ve: Calcd for $[M+Na]^+$ 1503.89. m/z 1503.8 found.

Cyclisation and Boc deprotection of linear peptide

The linear peptide (350 mg) was dissolved in DMF (100 ml), DMTMM·BF_4 (143 mg, 0.44 mmol) added and stirred under nitrogen for 5 days at room temperature. The DMF was removed by concentration under reduced pressure, redissolved in DMF (10 ml) and precipitated into ice cold MeOH/H_2O (1:1), then dried in a vacuum oven overnight.

The solid was dissolved in a mixture of 95 % TFA (5 ml), 2.5 % triisopropylsilane and 2.5 % H_2O, left to stir for 3 h, the reaction mixture transferred to a falcon tube and precipitated by addition of ice cold diethyl ether. The supernatant was discarded, washed with additional diethyl ether, centrifuged (process repeated twice) and then transferred to a vacuum oven and left to dry overnight. The product was isolated as a pale orange powder (260 mg). ESI MS +ve: Calcd for $C_{58}H_{88}N_{12}O_8Na$ $[M+Na]^+$ 1103.7. m/z 1103.6 found. See Figure C.6 for assigned ^1H NMR.

Chain extension of 2-arm $PNAM_{37}$ cyclic peptide conjugate

The PNAM conjugate was prepared by amide coupling of the amine units of the deprotected cyclic peptide and an NHS ester of the end group of a $PNAM_{37}$ polymer synthesised from a NHS functional RAFT agent. The synthesis and SANS analysis of this compound was performed by Dr. Ed Mansfield. This compound (12.5 mg, $1.98*10^{-3}$ mmol) was then chain extended by addition of NAM (2 mg, 0.0149 mmol), NAS (2.4 mg, 0.0149 mmol), ACVA (0.1 mg, $4.72*10^{-4}$ mmol) and DMF (200 µl) in a 1 ml glass vial. The reaction mixture was degassed with nitrogen, placed in an oil bath heated to 70°C and stirred for 6 h, then precipitated twice into diethyl ether, redissolved in water and freeze dried to yield a colourless powder.

Synthesis of PNAM-co-PNAS side chain bottle-brushes

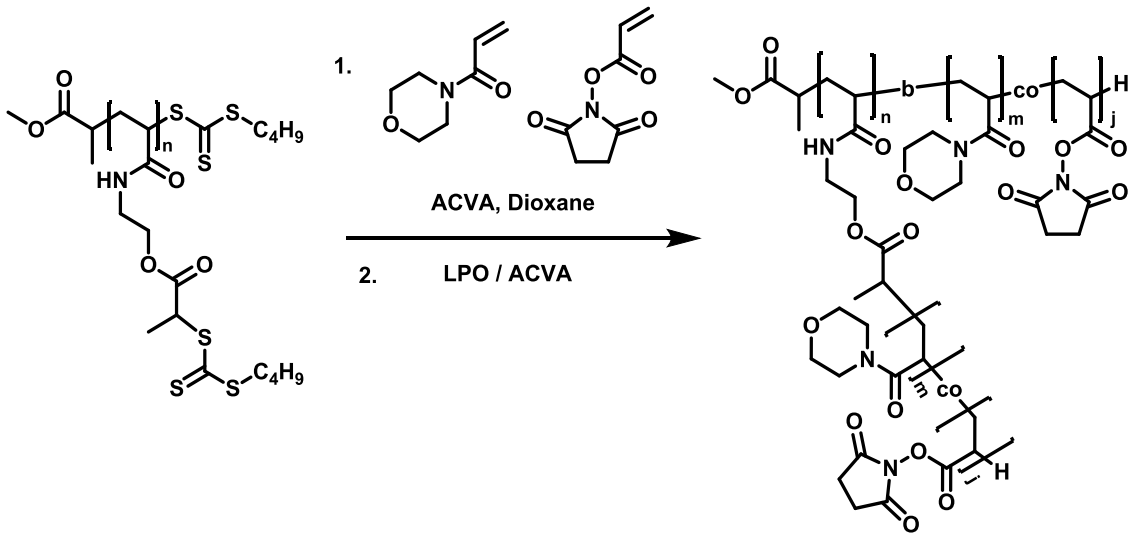

The PolyCTA was synthesised as previously described in chapter 2. PolyCTA (11.9 mg, $3.45*10^{-2}$ mmol, 1 eq.), NAM (1g, 7.08 mmol, 200 eq.), NAS (60 mg, $3.45*10^{-1}$ mmol, 10 eq.), ACVA (0.66 mg, $2.36*10^{-3}$ mmol) and anhydrous dioxane (2.8 ml) were added to a vial fitted with a stirrer bar and rubber septum. The reaction mixture was degassed with nitrogen for 10 minutes and placed in an oil bath heated to 60°C for 2h. The monomer conversion was determined by ^{1}H NMR, the polymerisation was stopped at approximately 25 % conversion to target a DP of 50 for the side chains. The reaction mixture was precipitated 3 times into ice cold diethyl ether and dried under vacuum to yield a pale yellow powder.

The ($PNAM_{50}$-co-$PNAS_{2.5}$) bottle brush (300 mg, $4.0*10^{-2}$ mmol CTA), ACVA (336 mg, 1.2 mmol, 30 eq.), Lauroyl peroxide (47.8 mg, 0.12 mmol, 3 eq.) were dissolved in anhydrous dioxane (15 ml), degassed with nitrogen for 10 minutes and heated in an oil bath at 80°C for 6 h. The reaction mixture was precipitated 3 times into ice cold diethyl ether, then redissolved in water and dialysed for 3 days against a 10k MWCO membrane. The aqueous solution was freeze dried to yield a colourless powder. SEC analysis confirmed removal of the characteristic UV absorption at 309 nm of the trithiocarbonate groups. ^{1}H NMR (300 MHz, $CDCl_3$) δ 4.0 – 3.0 (8H, $(OC\underline{H}_2C\underline{H}_2N)_2$), 2.81 (4H, $C(O)C\underline{H}_2C\underline{H}_2C(O)$), 2.6 -2.2 (1H, $NC(O)C\underline{H}$ (NAM)), 2.0 – 1.0 (3H, $C\underline{H}_2C\underline{H}$ backbone).

Synthesis of linear PNAM-co-pNAS

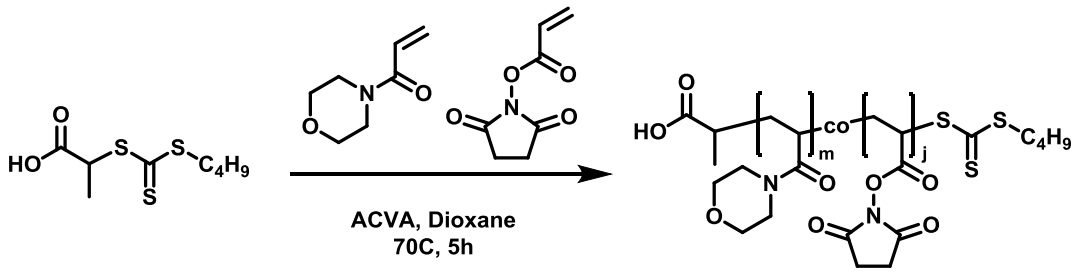

NAM (200 mg, 1.42 mmol, 100 eq.), Acrylic acid NHS (12 mg, $7.08*10^{-2}$ mmol, 5 eq.), PABTC (3.4 mg, $1.42*10^{-2}$ mmol. 1eq.) and ACVA (0.79 mg, $2.83*10^{-3}$ mmol) were dissolved in 0.53 ml anhydrous dioxane in a 3 ml vial fitted with a stirrer bar and rubber septum. The reaction mixture was degassed with nitrogen for 10 minutes, placed in oil bath set to 70°C for 5h and then precipitated twice into diethyl ether, dried under vacuum to yield a pale yellow powder.

Synthesis of PEG acrylamide macromonomer

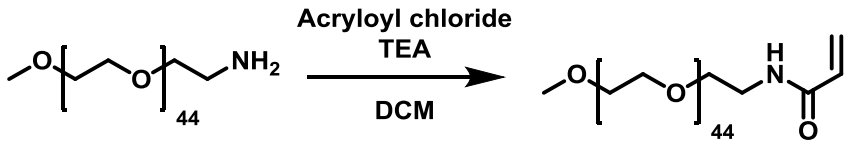

Amino-PEG (4.5 g, 2.25 mmol, M_n = 2,000 g mol^{-1}) was dissolved in 60 ml anhydrous DCM in a 250 ml round bottom flask under nitrogen, triethylamine (364 mg, 3.60 mmol) was added and then the reaction mixture was cooled with an ice bath. Acryloyl chloride (306 mg, 3.375 mmol) was added dropwise to the reaction mixture, after 2 h the ice bath was removed and left to stir overnight at room temperature. The DCM was concentrated under vacuum, the residue redissolved in 0.1 M $NaHCO_3$ solution (30 ml) and extracted twice with DCM. The organic layer was collected, dried, over $MgSO_4$, filtered and concentrated. The crude mixture was then purified by passing through a silica plug using DCM / MeOH 9:1 as the eluent, the collected fractions were concentrated to yield a white powder (3.5 g, 78 % yield). . ^{1}H NMR (300 MHz, $CDCl_3$) δ 6.21 (dd, J = 9.6 Hz, 17.1 Hz, 1H), 6.12 (dd, J = 1.8 Hz, 17.1 Hz, 1H), 5.69 (dd, J = 1.8 Hz, 9.3 Hz, 1H), 3.63 (s, 1H), 3.40 (m, 2H), 3.30 (s, 3H). MALDI analysis confirmed addition of vinyl end group (See Figure C.7).

Synthesis of PEG bottle-brushes

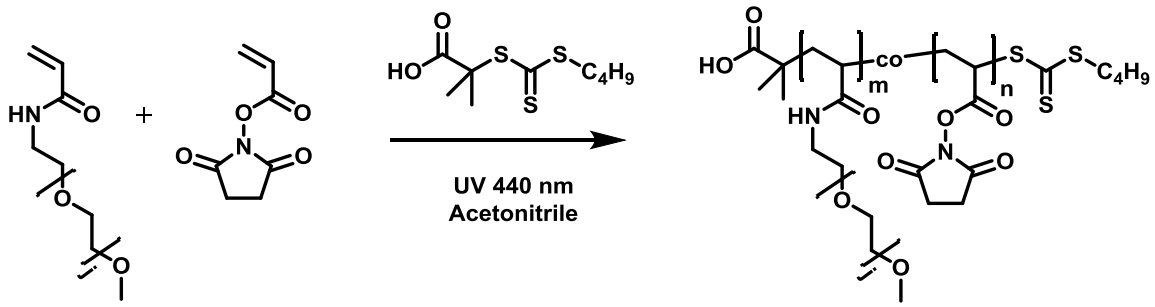

PEG acrylamide (100 mg, $5*10^{-2}$ mmol), BDMATC (0.63 – 0.08 mg, depending on target DP) and NAS (0.8 mg, $5*10^{-3}$ mmol) were dissolved in 300 µl acetonitrile, degassed with nitrogen and placed in a UV curing box (λ = 440 nm) for 48 h. The macromonomer conversion was monitored by size exclusion chromatography reaching >90 %. The reaction mixture was then precipitated three times into ice cold diethyl ether to remove residual macromonomer and dried under vacuum to yield a colourless powder.

Fluorescence labelling by conjugation of Alexa-488 dye

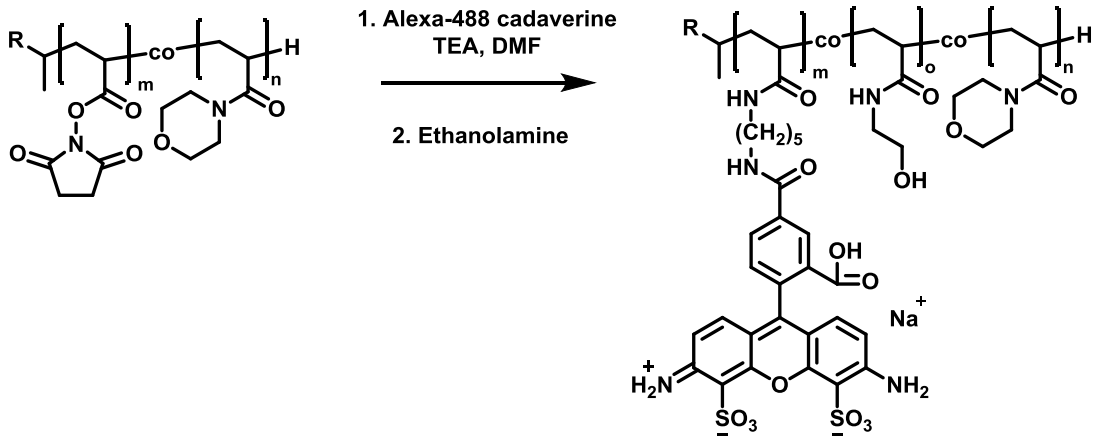

The PNAM-co-PNAS short brush (10 mg, $3.33*10^{-3}$ mmol NAS units), TEA (1 mg, 9.88*10-3 mmol) and Alexa-488 cadaverine (0.03 mg, $4.68*10^{-5}$ mmol) were dissolved in 250 µl anhydrous DMF in a 1.5 ml screw cap vial and stirred for 2 days at room temperature in the dark. After which ethanolamine (2 µl, $3.27*10^{-2}$ mmol) was added and stirred for a further 4 h at room temperature, after which the DMF was removed under a stream of nitrogen, the residue redissolved in water and immediately passed through a Sephadex PD10 column. The fractions were analysed by fluorescence spectrometer to reveal full conjugation of the dye onto polymer. The polymeric fractions were combined, washed three times through a centrifuge dialysis tube (100k MWCO) and freeze dried to yield the compound as a colourless powder.

The same procedure was used for the other polymers, except for the linear in which a lower 10k MWCO of the dialysis centrifuge tube was used. For the cyclic peptide conjugate a different ratio of reagents was used: CP-NAS extended (3 mg, $2.74*10^{-3}$ mmol NAS units) and Alexa-488 cadaverine (0.09 mg, $1.41*10^{-4}$ mmol), otherwise the same reaction procedure was carried out.

Radiolabelling by conjugation of C14-ethanolamine

A typical procedure is described: the PNAM-co-PNAS short brush (20 mg, $6.66*10^{-3}$ mmol NAS units), TEA (0.3 mg, $2.96*10^{-3}$ mmol) and C14-ethanolamine ($1.6*10^{-3}$ mmol, 0.4 ml solution in H_2O/ethanol) were dissolved in DMF (0.5 ml) in a 3 ml screw cap vial, and stirred at room temperature for 48 h, after which an additional unlabelled aliquot of ethanolamine (3 mg, $4.9*10^{-2}$ mmol) was added to the reaction mixture and stirred for a further 4 h. The reaction mixture was concentrated under a stream of nitrogen, redissolved in water and immediately passed through a PD10 purification column collected into 1 ml fractions. These was analysed by liquid scintillation counting to confirm separation of polymer and free radiolabel, fractions 3 – 6 (polymeric species) were mixed and placed in a floatalyzer dialysis device with a 10 k MWCO and dialysed against water for 3 days until no radioactivity in the bulk water was measurable. The solution was transferred to a vial, dried under a stream of nitrogen with heating at 50°C to yield the radiolabelled conjugate as a white residue.

For the cyclic peptide labelling conjugate the C14-ethanolamine was dried under a stream of nitrogen prior to use, the removal of water was found to improve reaction yield presumably by reducing hydrolysis rate of the NHS ester and was necessary for the acquirement of higher radioactivities, as required for the CP conjugate. CP-NAS (4 mg, $3.66*10^{-3}$ mmol), dried C14-ethanolamine ($1.6*10^{-3}$ mmol), and TEA (0.3 mg, $2.96*10^{-3}$ mmol) were mixed in a 3 ml screw cap vial. The same procedure as described above was carried out.

Cells

MDA-MB-231, HEK-293, 4T1, 3T3 were obtained from. MDA, HEK and 4T1 were grown in Dulbecco's Modified Eagle Medium (DMEM) supplemented with 10% v/v foetal calf serum. 3T3 were grown in DMEM supplemented with 20% v/v foetal calf

serum. Cells were grown as adherent monolayers at 37°C in a 5% CO_2 humidified atmosphere and passaged at ~80% confluenece.

Cell Proliferation Assay protocol

Viability of cells in presence of the synthesized compound were assessed by an MTT assay. Cells were seeded in a 96-well plate (5,000 cells per well) and allowed to grow for 24 h, followed by the addition of a solution of compound dissolved in cell culture media. The solutions were made up to give a concentration in the well media to a range of 0.001 – 1 mg ml^{-1}. The cells were incubated for 72 h, after which the wells were treated with MTT compound (12 mM in PBS, 10 uL) and incubated for 4 h. The culture media was then removed by aspiration and DMSO (50 uL) added to each well, the plate was incubated at 37C for 10 min to fully dissolve the purple crystals formed upon the oxidation of the MTT reagent. The UV absorption at 540 nm was measured in a Flexstation 3 plate reader to determine cell viability. The measurements were done by triplicate and the results were normalized with the absorbance coming from the test performed on untreated cells.

Cell association by flow cytometry

Cells were seeded in a 24-well plate (100,000 cells per well) with 0.5 ml culture media and incubated for 24 h. A solution of Alexa-488 labelled compounds (75 µl, 1.5 mg ml^{-1}) in culture media was dosed to the cells in triplicate under 3 experimental conditions: incubation at 37°C for 3 h or 24 h, and incubation at 4°C for 3 h. For the 4°C experiment the 24-well plate and sample solution were cooled on ice for 10 minutes prior to dosage of the compound, and kept on ice for the duration of incubation. After incubation, the culture media was then removed, the cells washed twice with cold PBS, treated with Trypsin and incubated for 10 minutes to harvest cells. A solution of bovine serum albumin (BSA, 10%, 0.3 ml) was added to each well, transferred to a 96-well plate and centrifuged at 350 G for 5 minutes, after which the supernatant was discarded and the cells resuspended in 10% BSA solution. Samples were analysed using a S100EXi flow cytometer (Stratedigm), equipped with 405, 488, 552 and 640 nm solid-state lasers. Forward and side scatter gates were used to exclude debris and dead cells using a viability dye (Propidium iodide). The mean fluorescence intensity for a population of 10,000 cells

was determined with Flowjo v8 for each experimental condition in triplicate. **Spatial Coincidence with Lysotracker marked lysosomes.**

Cells were seeded in an 8-well microscopy slide (20,000 cells per well) with 150 ul culture media and incubated for 24 h at 37 °C. A solution of Alexa-488 labelled compounds (33 µl, 0.3 mg ml^{-1}) in culture media was dosed to the cells and incubated for 8 hours. Lysotracker Deep Red (ex/em: 647⁄668, 2 uL per well, 75 nM in DMEM) and Hoechst 33342 (ex/em: 361⁄497, 1 uL, 1 ug ml^{-1} in DMEM) were added 30 and 5 min before imaging the cells respectively. After that, the cells were washed with media and imaged in a humidified incubation chamber with a regulated temperature of 37 C in a Leica TCS SP8 Laser-scanning confocal microscope with a HCX PL APO 40x (NA 1.30) oil objective. Images were acquired at 1024x1024 with a pinhole set to 1 Airy units, capturing Lysotracker Deep Red (ex 633; em: 650 - 778 nm), AF488-brushes (ex 488; em 502 - 594 nm) and Hoechst 33342 (ex 405, 410 - 460 nm) fluorescence. Image acquisition settings were consistent for samples and controls. Images were processed with the FIJI distribution of Image J.

In vivo pharmacokinetics protocol

All animal experimental protocols were approved by the Monash Institute of Pharmaceutical Sciences Animal Ethics Committee, Monash University, Parkville, VIC, Australia. Male Sprague Drawley rates (250-350 g) were used. Animals were maintained on a 12 h light/dark cycle at all times and after transport were acclimatised for 7 days at the facility prior to *in vivo* studies.

A day prior to compound administration, each rat was anaesthetised under isoflurane (2-5% v/v) and cannulas (polyethylene tubing 0.96 x 0.58 mm, Paton Scientific, Victor Harbour, Australia) surgically inserted into the right jugular vein and carotid artery (to facilitate IV administration and blood collection respectively) as previously described.[46] The rats were transferred to individual metabolic cages (to permit separate collection of urine and faeces) and allowed to recover overnight prior to dosing. Each animal was fasted up to 14 h prior to administration of the IV dose with water provided ad libitum. Prior to injection, blank blood samples (0.2 ml) were obtained from the carotid artery. The compounds were dissolved in phosphate buffered saline (PBS) and 0.5 mL was administered as a slow bolus (1 mL/min) at a dose of 1 µCi (2.8 – 9.1 mg kg^{-1}) via the

jugular cannula. The cannula was then flushed with 0.5 ml of heparinized saline after dose administration to ensure complete infusion of the dose. Blood samples (0.2 ml) were taken prior to dose administration and at 1, 5, 10, 20, 30, 60, 120, 180, 240, 360, 480, and 1440 min after dose administration. Blood samples were placed immediately into tubes containing 10 IU of heparin and centrifuged for 5 min at 3500 g. Plasma (50 µl) was collected, transferred to a separate vial and mixed with 4 ml of Ultima Gold scintillation cocktail prior to scintillation counting. Urine samples were collected at the 24 h time point and a 50 µl sample was transferred to a vial, 4 ml of Ultima Gold added and counted by scintillator. A blank urine sample prior to dosage was also collected and analysed to account for background radiation.

The pharmacokinetic parameters were determined using non-compartmental analysis with Excel software using the PK Solver add-in (NCA IV Bolus model). Since the animals were dosed with varying mass but constant radioactivity (1 µCi), the concentrations in terms of µCi ml^{-1} of plasma were used and area under the curve (AUC) reported as µCi ml^{-1} min^{-1}. AUC_{0-t}, elimination half-life ($t_{1/2}$), volume of distribution (V_d) and clearance rate (Cl) were calculated with this approach.

Biodistribution protocol

After the 24 h blood sample was collected, animals were humanely killed by injection of a lethal dose of sodium pentobarbital via the jugular vein cannula and the liver, spleen, pancreas, kidneys, heart, lungs and brain were harvested. The tissues were frozen and stored in polypropylene tubes prior to processing. The samples were homogenised with MilliQ water (5 ml) using a gentleMACS dissociator. Two triplicates of each organ sample (50 -100 mg) one with and without addition of a known quantity of C14-ethanolamine spike, were mixed with Solvable (2 ml, Perkin Elmer) and the samples heated at 60°C overnight. After cooling to room temperature hydrogen peroxide (200 µl, 30% w/v) was added to each vial, followed by addition of Ultima Gold scintillation cocktail (10 ml), vortexed and stored at 4°C for 3 days prior to counting. A sample of blank organs were also processed and analysed in the same manner to provide a background correction. To account for loss of activity as a result of the processing, an efficiency was then calculated to better determine the true dosage per organ:

$$efficiency = \frac{spiked\ tissue\ dpm - tissue\ dpm}{spiked\ solution\ dpm}$$

Where ‘spiked tissue dpm’ is the average measured degradation per minute of the spiked sample, ‘tissue dpm’ is the average measure of the unspiked sample and ‘spiked solution dpm’ is the known amount of radiolabel spike added. The efficiency was then used to correct for the true C14 content by:

$$tissue\ dpm\ corrected = \frac{tissue\ dpm}{efficiency}$$

This value was then used to determine the total dpm of the organ by taking it account the total organ mass prior to processing of which 50 -100 mg was analysed in each sample. The results are reported as either the % dosage per organ or % dosage per gram tissue.

4.5 References

1. F. Canal, J. Sanchis and M. J. Vicent, *Curr. Opin. Biotechnol.*, 2011, **22**, 894-900.
2. Y. Matsumura and H. Maeda, *Cancer Res.*, 1986, **46**, 6387-6392.
3. H. F. Dvorak, *Cancer Immun. Res.*, 2015, **3**, 1-11.
4. J. Fang, H. Nakamura and H. Maeda, *Adv. Drug Del. Rev.*, 2011, **63**, 136-151.
5. N. Schleich, F. Danhier and V. Préat, *J. Controlled Release*, 2015, **198**, 35-54.
6. J. M. Harris and R. B. Chess, *Nature Rev. Drug Disc.*, 2003, **2**, 214.
7. S. Jevševar, M. Kunstelj and V. G. Porekar, *Biotech. J.*, 2010, **5**, 113-128.
8. L. Seymour, R. Duncan, J. Strohalm and J. Kopeček, *J. Biomed. Mat. Res. Part A*, 1987, **21**, 1341-1358.
9. G. Pasut and F. M. Veronese, *J. Controlled Release*, 2012, **161**, 461-472.
10. J. V. Jokerst, T. Lobovkina, R. N. Zare and S. S. Gambhir, *Nanomedicine*, 2011, **6**, 715-728.
11. T. Ishida and H. Kiwada, *Int. J. Pharm.*, 2008, **354**, 56-62.
12. A. S. A. Lila, H. Kiwada and T. Ishida, *J. Controlled Release*, 2013, **172**, 38-47.
13. T. Ishida, X. Wang, T. Shimizu, K. Nawata and H. Kiwada, *J. Controlled Release*, 2007, **122**, 349-355.
14. T. Lammers, F. Kiessling, W. E. Hennink and G. Storm, *J. Controlled Release*, 2012, **161**, 175-187.
15. M. Sugano, N. K. Egilmez, S. J. Yokota, F.-A. Chen, J. Harding, S. K. Huang and R. B. Bankert, *Cancer Res.*, 2000, **60**, 6942-6949.
16. K. N. Sugahara, T. Teesalu, P. P. Karmali, V. R. Kotamraju, L. Agemy, O. M. Girard, D. Hanahan, R. F. Mattrey and E. Ruoslahti, *Cancer Cell*, 2009, **16**, 510-520.
17. J. Sudimack and R. J. Lee, *Adv. Drug Del. Rev.*, 2000, **41**, 147-162.
18. S. Wilhelm, A. J. Tavares, Q. Dai, S. Ohta, J. Audet, H. F. Dvorak and W. C. Chan, *Nature Rev. Mat.*, 2016, **1**, 16014.
19. F. Danhier, *J. Controlled Release*, 2016, **244**, 108-121.
20. V. P. Chauhan, T. Stylianopoulos, J. D. Martin, Z. Popović, O. Chen, W. S. Kamoun, M. G. Bawendi, D. Fukumura and R. K. Jain, *Nature Nanotechnology*, 2012, **7**, 383-388.
21. T. Stylianopoulos and R. K. Jain, *Nanomed. Nanotechnol. Biol. Med.*, 2015, **11**, 1893-1907.
22. S. Venkataraman, J. L. Hedrick, Z. Y. Ong, C. Yang, P. L. R. Ee, P. T. Hammond and Y. Y. Yang, *Adv. Drug Del. Rev.*, 2011, **63**, 1228-1246.
23. N. P. Truong, M. R. Whittaker, C. W. Mak and T. P. Davis, *Expert Opin. Drug Del.*, 2015, **12**, 129-142.
24. Y. Yang, D. Nie, Y. Liu, M. Yu and Y. Gan, *Drug Discovery Today*, 2018.
25. Y. Zhang, S. Tekobo, Y. Tu, Q. Zhou, X. Jin, S. A. Dergunov, E. Pinkhassik, B. Yan, *ACS Appl. Mat. Int.*, 2012, **4**, 4099-4105.
26. X. Huang, L. Li, T. Liu, N. Hao, H. Liu, D. Chen and F. Tang, *ACS Nano*, 2011, **5**, 5390-5399.
27. S. Shukla, F. J. Eber, A. S. Nagarajan, N. A. DiFranco, N. Schmidt, A. M. Wen, S. Eiben, R. M. Twyman, C. Wege and N. F. Steinmetz, *Adv. Health. Mat.*, 2015, **4**, 874-882.

28. Y. Geng, P. Dalhaimer, S. Cai, R. Tsai, M. Tewari, T. Minko and D. E. Discher, *Nature Nanotechnology*, 2007, **2**, 249.
29. P. Kolhar, N. Doshi and S. Mitragotri, *Small*, 2011, **7**, 2094-2100.
30. V. P. Chauhan, Z. Popović, O. Chen, J. Cui, D. Fukumura, M. G. Bawendi and R. K. Jain, *Angew. Chem. Int. Ed.*, 2011, **50**, 11417-11420.
31. A. Banerjee, J. Qi, R. Gogoi, J. Wong and S. Mitragotri, *J. Controlled Release*, 2016, **238**, 176-185.
32. M. A. Bruckman, L. N. Randolph, A. VanMeter, S. Hern, A. J. Shoffstall, R. E. Taurog and N. F. Steinmetz, *Virology*, 2014, **449**, 163-173.
33. M. Müllner, *Macromol. Chem. Phys.*, 2016, **217**, 2209-2222.
34. K. Huang, H. Ma, J. Liu, S. Huo, A. Kumar, T. Wei, X. Zhang, S. Jin, Y. Gan and P. C. Wang, *ACS Nano*, 2012, **6**, 4483-4493.
35. L. M. Kaminskas, B. J. Boyd, P. Karellas, G. Y. Krippner, R. Lessene, B. Kelly and C. J. Porter, *Mol. Pharm.*, 2008, **5**, 449-463.
36. S. Kaga, N. P. Truong, L. Esser, D. Senyschyn, A. Sanyal, R. Sanyal, J. F. Quinn, T. P. Davis, L. M. Kaminskas and M. R. Whittaker, *Biomacromolecules*, 2017, **18**, 3963-3970.
37. R. T. Chacko, J. Ventura, J. Zhuang and S. Thayumanavan, *Adv. Drug Del. Rev.*, 2012, **64**, 836-851.
38. Y. Yu, C.-K. Chen, W.-C. Law, H. Sun, P. N. Prasad and C. Cheng, *Polymer Chemistry*, 2015, **6**, 953-961.
39. M. A. Sowers, J. R. McCombs, Y. Wang, J. T. Paletta, S. W. Morton, E. C. Dreaden, M. D. Boska, M. F. Ottaviani, P. T. Hammond and A. Rajca, *Nature Comm.*, 2014, **5**, 5460.
40. M. Müllner, S. J. Dodds, T.-H. Nguyen, D. Senyschyn, C. J. Porter, B. J. Boyd and F. Caruso, *ACS Nano*, 2015, **9**, 1294-1304.
41. M. R. Ghadiri, J. R. Granja, R. A. Milligan, D. E. McRee and N. Khazanovich, *Nature*, 1993, **366**, 324.
42. S. Fernandez-Lopez, H.-S. Kim, E. C. Choi, M. Delgado, J. R. Granja, A. Khasanov, K. Kraehenbuehl, G. Long, D. A. Weinberger and K. M. Wilcoxen, *Nature*, 2001, **412**, 452.
43. A. Khalfa and M. Tarek, *J. Phys. Chem. B*, 2010, **114**, 2676-2684.
44. J. Chen, B. Zhang, F. Xia, Y. Xie, S. Jiang, R. Su, Y. Lu and W. Wu, *Nanoscale*, 2016, **8**, 7127-7136.
45. R. Chapman, M. Danial, M. L. Koh, K. A. Jolliffe and S. Perrier, *Chem. Soc. Rev.*, 2012, **41**, 6023-6041.
46. S. C. Larnaudie, J. Sanchis, T.-H. Nguyen, R. Peltier, S. Catrouillet, J. C. Brendel, C. J. Porter, K. A. Jolliffe and S. Perrier, *Biomaterials*, 2018.
47. M. Danial, C. M.-N. Tran, P. G. Young, S. Perrier and K. A. Jolliffe, *Nature Comm.*, 2013, **4**, 2780.
48. J. C. Brendel, J. Sanchis, S. Catrouillet, E. Czuba, M. Z. Chen, B. M. Long, C. Nowell, A. Johnston, K. A. Jolliffe and S. Perrier, *Angew. Chem.*, 2018, **130**, 16920-16924.
49. J. J. Verhoef and T. J. Anchordoquy, *Drug delivery translational research*, 2013, **3**, 499-503.
50. T. Ishihara, T. Maeda, H. Sakamoto, N. Takasaki, M. Shigyo, T. Ishida, H. Kiwada, Y. Mizushima and T. Mizushima, *Biomacromolecules*, 2010, **11**, 2700-2706.

51. P. H. Kierstead, H. Okochi, V. J. Venditto, T. C. Chuong, S. Kivimae, J. M. Fréchet and F. C. Szoka, *J. Controlled Release*, 2015, **213**, 1-9.
52. G. Gody, T. Maschmeyer, P. B. Zetterlund and S. Perrier, *Macromolecules*, 2014, **47**, 3451-3460.
53. J. Liu, X. Shen, Y. Zhao and L. Chen, *Ind. Eng. Chem. Res.*, 2013, **52**, 18392-18400.
54. X. Shen, J. Liu, X. Feng, Y. Zhao and L. Chen, *J. Biomed. Mat. Res. Part A*, 2015, **103**, 683-692.
55. G. R. Chado, E. N. Holland, A. K. Tice, M. P. Stoykovich and J. L. Kaar, *Biomacromolecules*, 2018, **19**, 1324-1332.
56. F. Xu, H. Li, Y.-L. Luo and W. Tang, *ACS Appl. Mat. Inter.*, 2017, **9**, 5181-5192.
57. F. D'Agosto, M. T. Charreyre, L. Veron, M. F. Llauro and C. Pichot, *Macromol. Chem. Phys.*, 2001, **202**, 1689-1699.
58. J. Y. Rho, J. C. Brendel, L. R. MacFarlane, E. D. Mansfield, R. Peltier, S. Rogers, M. Hartlieb and S. Perrier, *Adv. Funct. Mater.*, 2018, **28**, 1704569.
59. C. Zhao and J. Zheng, *Biomacromolecules*, 2011, **12**, 4071-4079.
60. B. D. Chithrani, A. A. Ghazani and W. C. Chan, *Nano Lett.*, 2006, **6**, 662-668.
61. L. I. Selby, C. M. Cortez-Jugo, G. K. Such and A. P. Johnston, *Wiley Inter. Rev.: Nanomed. and Nanobiotech.*, 2017, **9**, e1452.
62. A. P. Johnston, G. K. Such, S. L. Ng and F. Caruso, *Curr. Opin. in Colloid Inter. Sci.*, 2011, **16**, 171-181.
63. S. C. Larnaudie, J. C. Brendel, K. A. Jolliffe and S. Perrier, *J. Polym. Sci., Part A: Polym. Chem.*, 2016, **54**, 1003-1011.

Chapter 5

Conclusion and outlook

Use of the RAFT R group 'grafting from' approach was thoroughly explored during chapter 2, in which the benefits of the addition of sacrificial free ungrafted CTA were studied. In the initial work by Müller the 'shuttle CTA' technique was suggested to improve control of the polymerisation by means of aiding radical transfer between sterically hindered CTA groups, ultimately reducing the polydispersity of the final compound. In the acrylamide system studied in this work, the primary benefit of the shuttle CTA was reduction in bimolecular terminations between bottle-brush macromolecules, substantially reducing the formation of high molecular shoulders present in SEC traces. The mechanism of this prevention of cross-coupling can firstly be attributed to the added possibility of terminations occurring between the lower molecular weight linear polymers, rather than the bottle-brushes, and secondly a dilution effect, whereby in comparative experiments the total CTA concentration was kept constant and therefore the addition of shuttle CTA lowered the quantity of bottle-brush. Such a reduction in bottle-brush concentration will significantly reduce probability of intermolecular terminations of these species. While the shuttle CTA approach can be highly advantageous, it comes with the major downside of the substantial formation of linear polymer side products, although for many polymers this can be removed *via* fractional precipitations. Nonetheless, when high monomer conversions are not required, it appears the more traditional approach of targeting low monomer conversions (10-20 %) in radical 'grafting from' procedures may be more convenient for ensuring effective control.

In the realm of multiblock copolymers, however, the quantitative consumption of monomer to allow for iterative polymerisation steps is essential for facile synthetic conditions. In this regard the shuttle CTA approach is of great benefit, and was demonstrated to enable synthesis of hexablock side chain bottle-brushes without unacceptable degrees of cross-coupling. Such materials are highly challenging to synthesise – in the case of the DP100 backbone bottle-brush, for example, there are 100 times more possible termination sites than for a linear polymer, where hexablock linear

copolymers can already be difficult to access with good control. The wide range of architectures achievable through RAFT was then explored by incorporation of multiblocks into select positions among the ‘x’ and ‘y’ axis of the bottle-brush. The segmented structure formed by the placement of a nonablock copolymer into the backbone was of particular interest, as the individual macromolecules could be imaged by AFM to provide evidence for the theorised architecture. While this work was limited to hexablock side chains, it is quite plausible for even longer multiblocks to be accessed by simply increasing the quantity of shuttle CTA to improve control for the brush, however, this is concomitant with an effective reduction in yield of the brush compound. Overall this chemistry is most suited to the high k_p acrylamide monomers which can be polymerised with high end group livingness and short reaction times. While the formation of compartmentalised macromolecular structures can enable many applications, the introduction of a very high number of blocks is most likely of limited benefit and this study was primarily intended to probe the limits of possible complexity with RAFT.

Chapter 3 and 4 then focused on two very different use of the brushes, to illustrate their potential as materials with wide-ranging applications.

Within chapter 3 the bottle-brush chemistry is tailored to investigate their use as oil additives. The initial aim of the project was to develop densely grafted copolymer architectures with the Lubrizol produced CTA Acid / CTA-1 in a suitable synthetic approach for industrial scale up processes. In this regard the project was met with limited success, as firstly the esterification process with CTA Acid was quite inefficient, and then in the ‘grafting from’ step the slower polymerisation rate of lauryl acrylate made it challenging to reach the desired quantitative monomer conversions. While the addition of a large excess of shuttle CTA could again improve control, this would mean that the composition of the resulting product would be mostly linear polymer by-product. Another consideration is the substantial amount of costly RAFT agent required and thus present in the final material, as increasing regulations on oil purity, in particular of Sulphur content, make minimisation of this important. Optimisation of the radical reduction CTA removal chemistry, with facile purification steps, may provide a useful process to mitigate this. Additionally the improved control observed for the comb polymer makes these architectures appealing for further study, as the lower grafting density allows for higher

monomer conversions of LA to be reached and leads to reduced quantity of RAFT agent in the resulting product.

RAFT mediated synthesis, however, proved highly effective for the investigation of structure-property relationships of oil soluble brushes in friction reduction applications. Incorporation of a polar copolymer could be readily performed at selective positions and complex architectures such as the ABA backbone and dumbbell-like macromolecules were accessed with narrow dispersities. A profound effect on surface activity was revealed upon addition of the polar PNAM anchor, as evidenced by QCM-D analysis and the substantial friction reduction in MTM, and is particularly noteworthy considering only ~1.4 wt. % polar units are required. The need for incorporation of the anchor group as a block rather than statistically was demonstrated, which highlights the benefits of RAFT controlled materials. With the low 1 wt. % polymer concentrations studied here, it is likely that further performance improvements will be obtained at higher, more typical additive compositions - in particular a more substantial increase in VI would be of great appeal. While the products may not be directly viable in commercial applications, they provide extremely valuable information to tailor future investigations and develop new generations of high performance additives, which could simultaneously provide excellent viscosity and friction modification.

The precise control afforded by RAFT was then applied to create bottle-brushes for potential use as drug delivery agents. Size and shape of nanoparticles is believed to have an integral effect on biological interactions, therefore the ability to finely tune nanoparticle dimensions is highly useful for improving understanding in this area. Similar plasma circulation behaviour of a short and long brush were observed, however, increased organ accumulation of the longer, high MW brush suggests that the shorter brush (~40 nm in length) may be more effective as a nanocarrier. Furthermore the brushes provided an effective comparison to study the effects of assembling a nanotube through supramolecular interactions rather than a covalent backbone. A PNAM cyclic peptide polymer conjugate was shown to possess intermediate half-life values between that of a linear polymer and a bottle-brush, indicating occurrence of self-assembly in *vivo*, while also showing faster clearance rates through inherent nanotube degradability.

Future work in this area will focus on studying the biocompatibility of PNAM in more detail, in particular to study inducement of immune responses in a similar manner to the ABC effect observed for PEG. Now the long circulation behaviour of the PNAM bottle-brushes has been established, in *vivo* tumour model studies will be carried out to test if the materials display effective tumour uptake and thus be suitable for anticancer applications, where they will again be compared to the supramolecular cyclic peptide system.

In conclusion this thesis has demonstrated the utility of RAFT polymerisation in bottle-brush synthesis and the ability to access complex architectures *via* the shuttle CTA mediated 'grafting from' technique. The flexibility of the synthetic approach provided a versatile platform for exploring the rich possibilities of bottle-brush materials in advanced applications, as wide-ranging as oil additives and drug delivery vectors.

Appendix A

Supporting information for Chapter 2

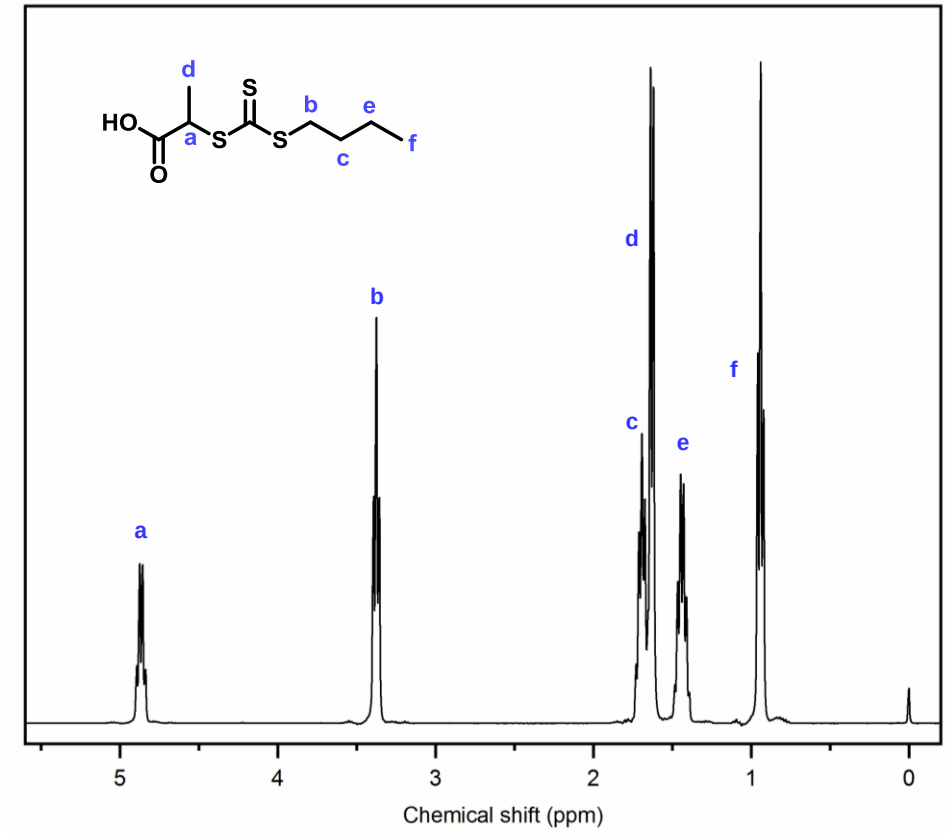

Figure A.1: ^{1}H NMR spectra (400 MHz) of PABTC in $CDCl_3$.

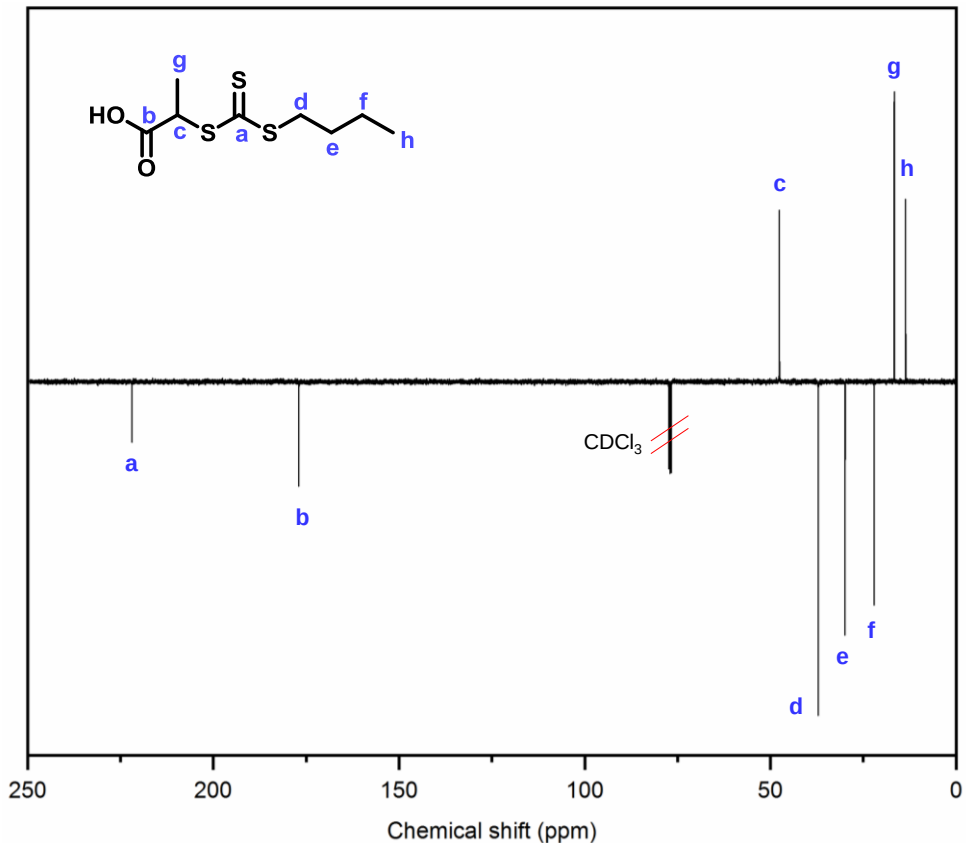

Figure A.2: ^{13}C NMR spectra (101 MHz) of PABTC in $CDCl_3$.

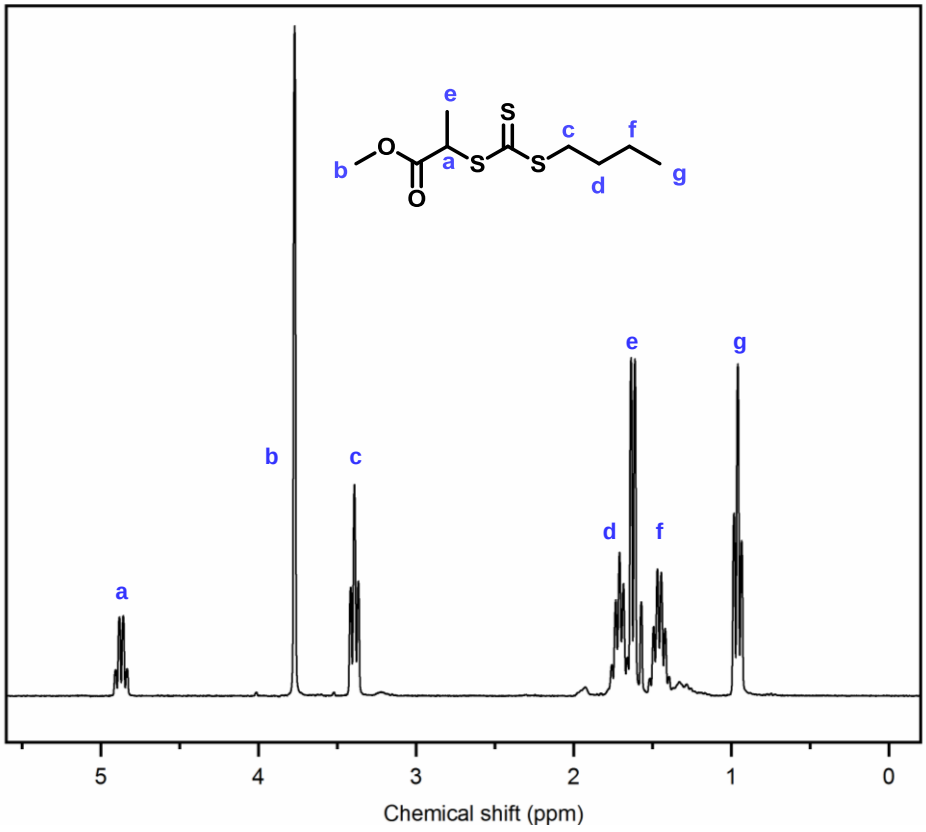

Figure A.3: ^{1}H NMR spectra (300 MHz) of PMBTC in $CDCl_3$.

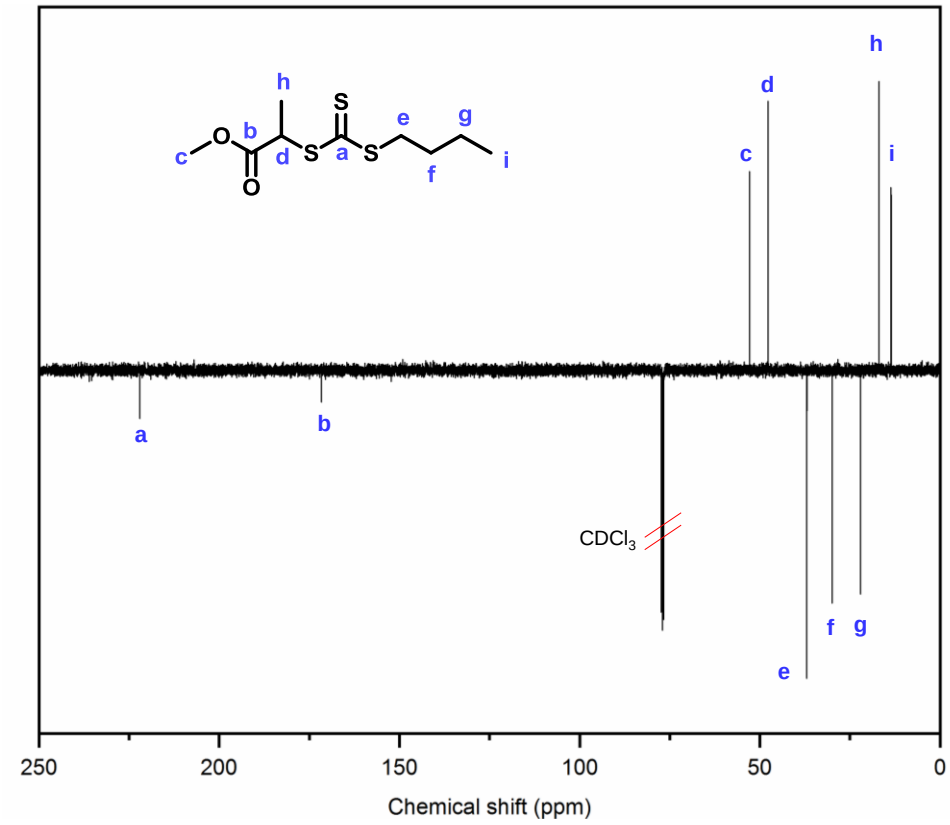

Figure A.4: ^{13}C NMR spectra (101 MHz) of PMBTC in $CDCl_3$.

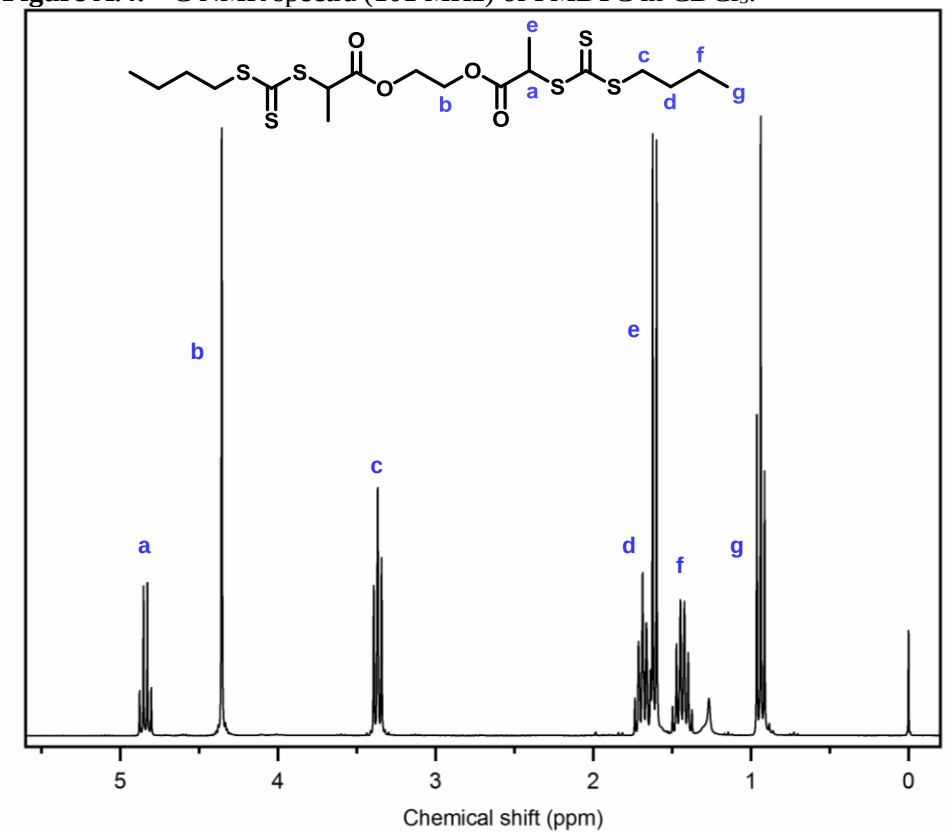

Figure A.5: ^{1}H NMR spectra (300 MHz) of DiPABTC in $CDCl_3$.

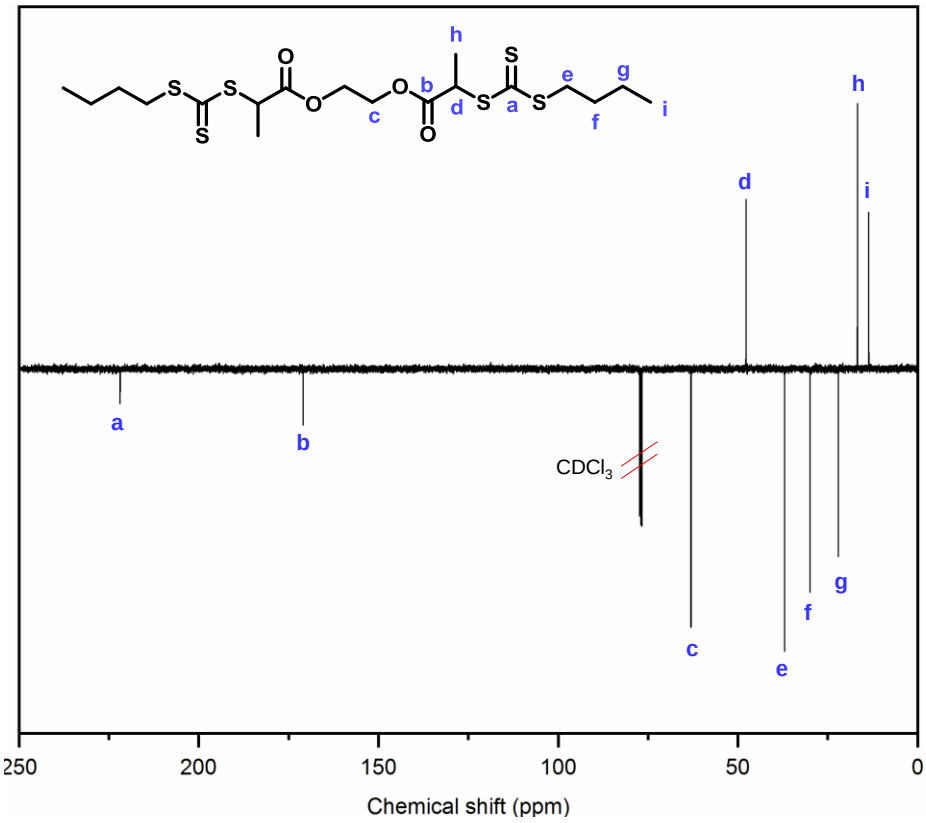

Figure A.6: ^{13}C NMR spectra (101 MHz) of DiPABTC in $CDCl_3$.

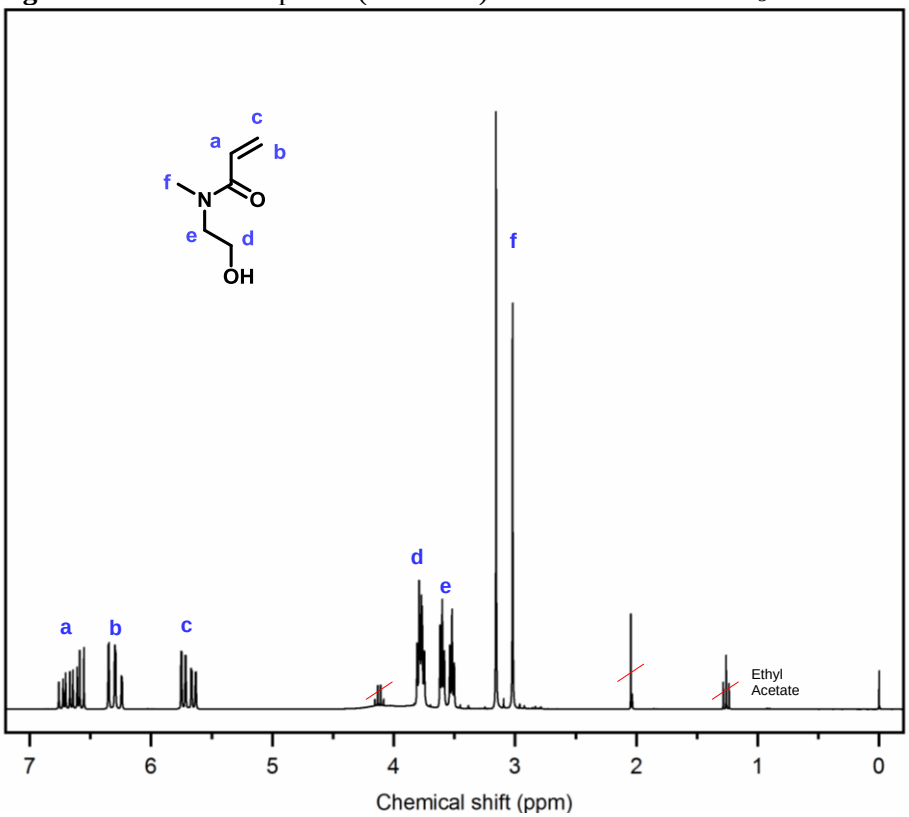

Figure A.7: ^{1}H NMR spectra (300 MHz) of MHEAm in $CHCl_3$. Presence of rotamers

causes splitting for proton environments e and f.

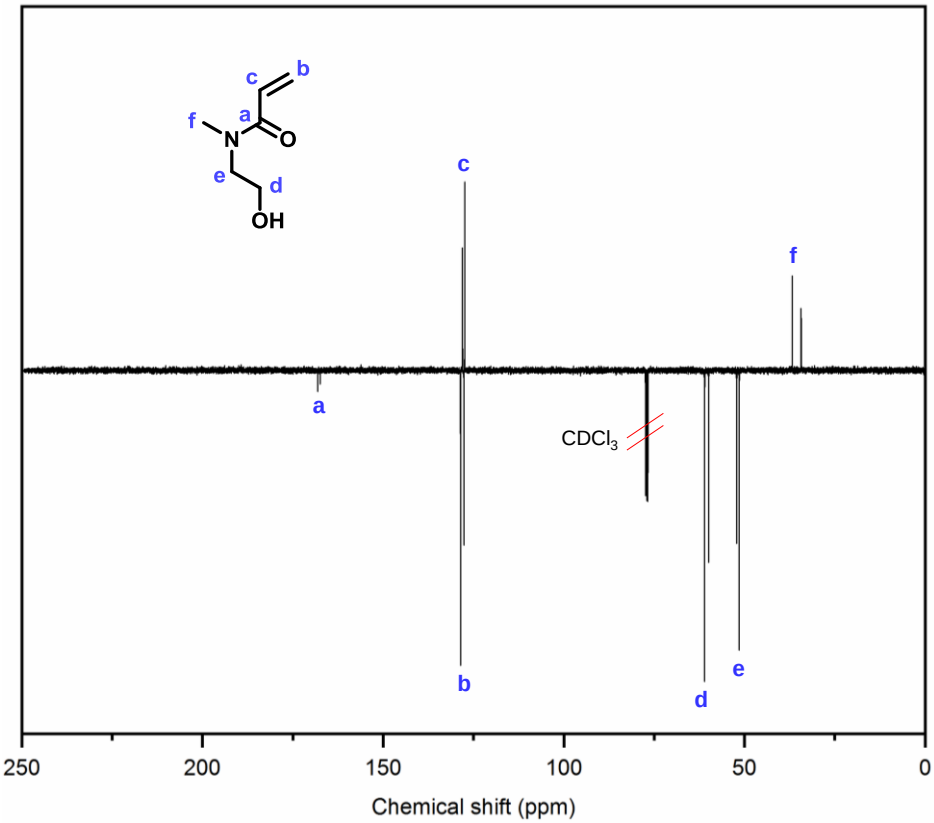

Figure A.8: ^{13}C NMR spectra (101 MHz) of MHEAm in $CDCl_3$.

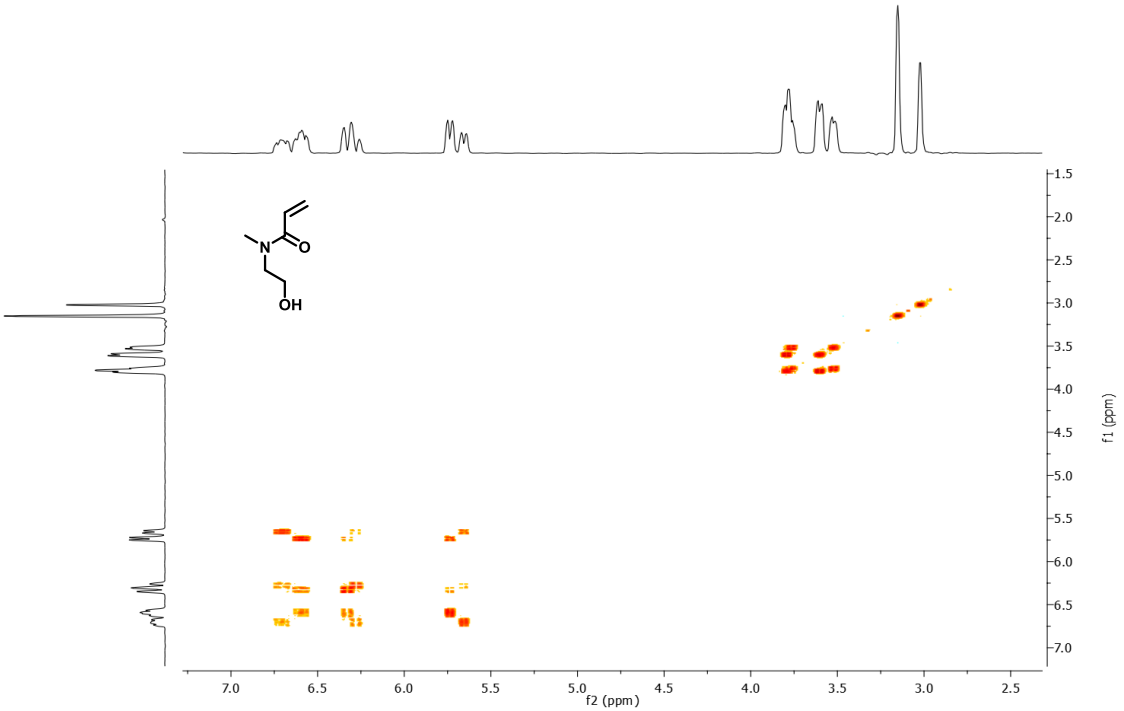

Figure A.9: ^{1}H COSY NMR of the MHEAm in $CDCl_3$.

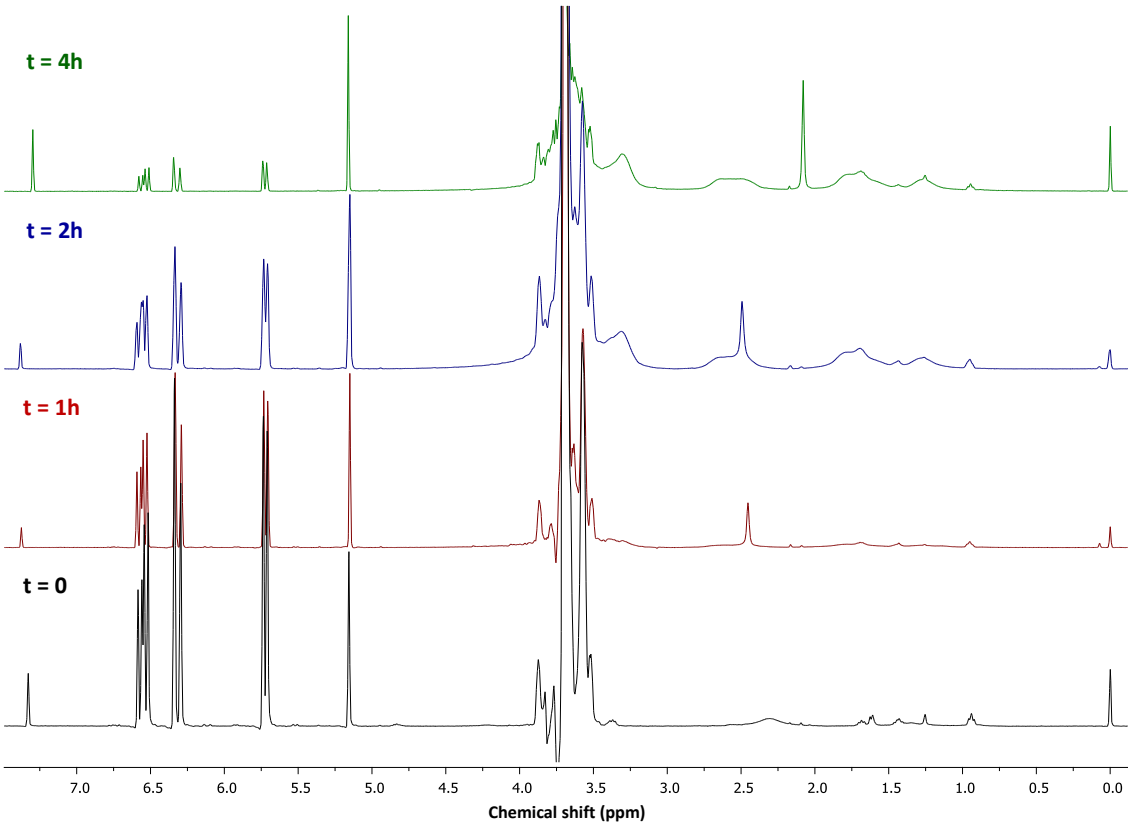

Figure A.10: Typical ^{1}H NMR spectra for the grafting from of NAM from the PolyCTA backbones. Monomer conversion determined by integration of vinyl peak region at 5.5 – 6.5 ppm with an internal standard of trioxane at 5.15 ppm.

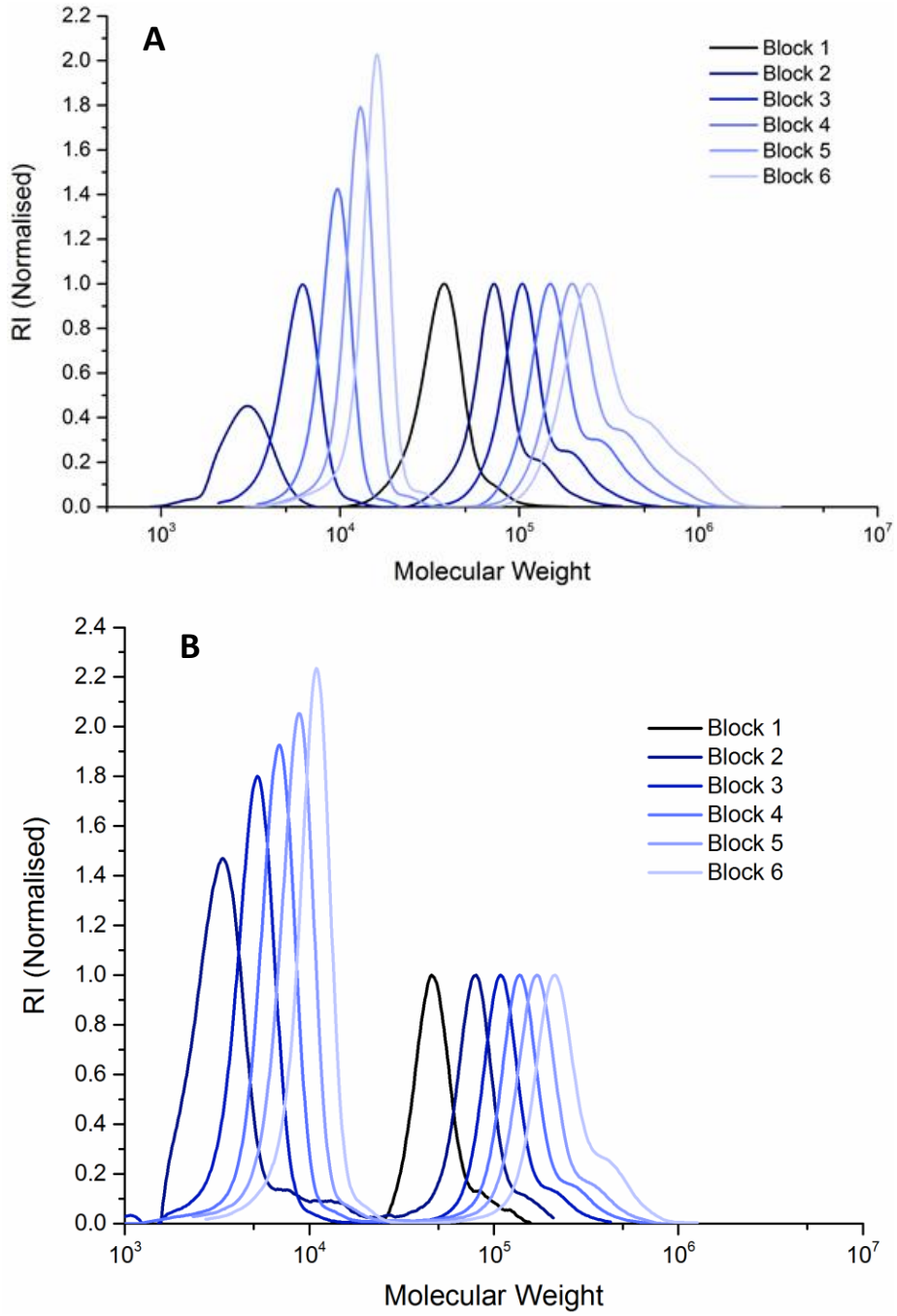

Figure A.11: SEC molecular weight distributions of hexablock side chain bottle-brush including traces of linear shuttle-CTA derived linear polymer. A – DP50 backbone brush compound. B – DP100 backbone brush compound. The linear polymer from block 1 is too low molecular weight and overlaps with SEC system peaks, and is therefore omitted from the figure.

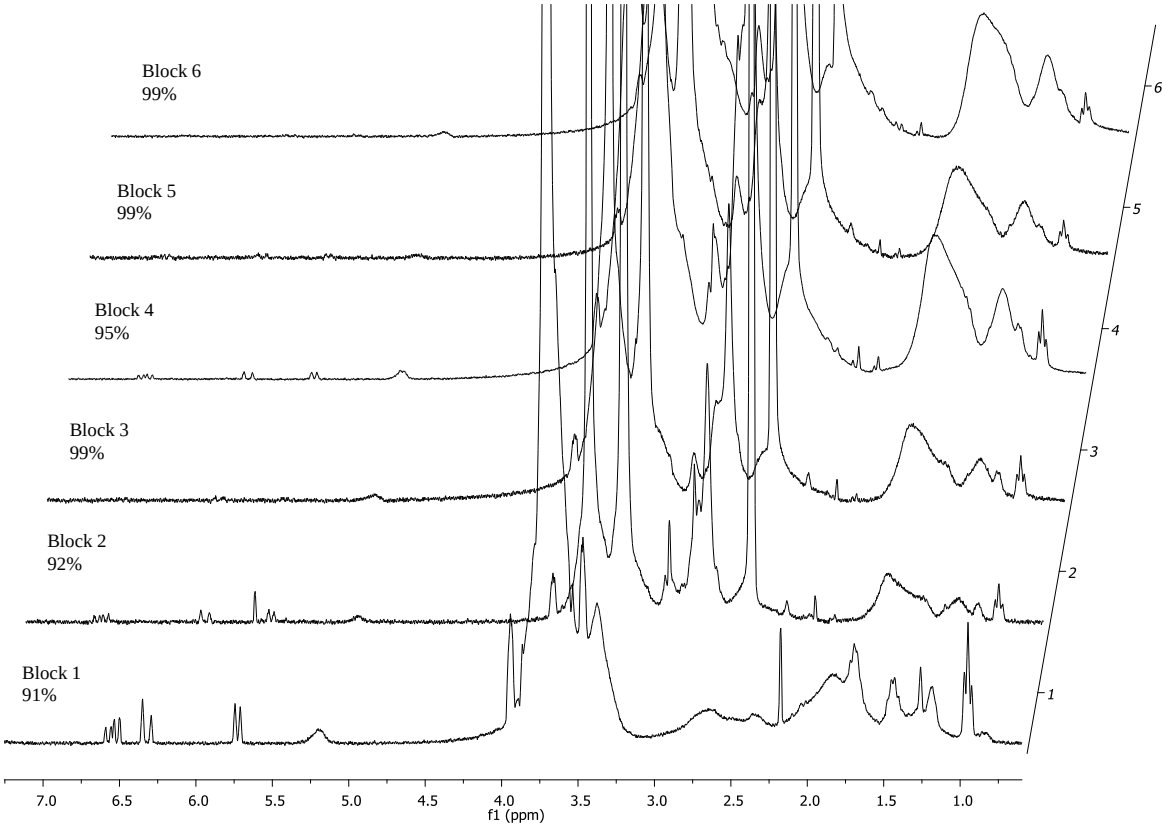

Figure A.12: ^{1}H NMR spectra of the grafting from reaction for hexablock side chains to synthesise compound.

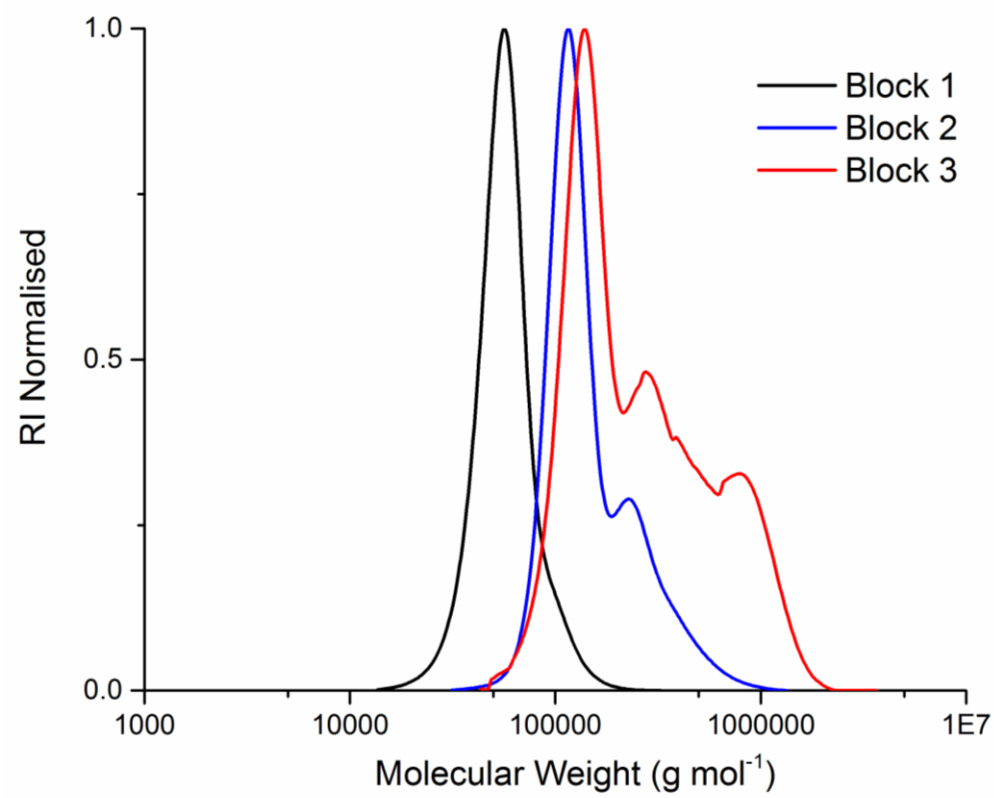

Figure A.13: Attempting to synthesis graft block copolymer side chains of $PCTA_{50}$ backbone in the absence of shuttle CTA leads to extensive brush-brush coupling.

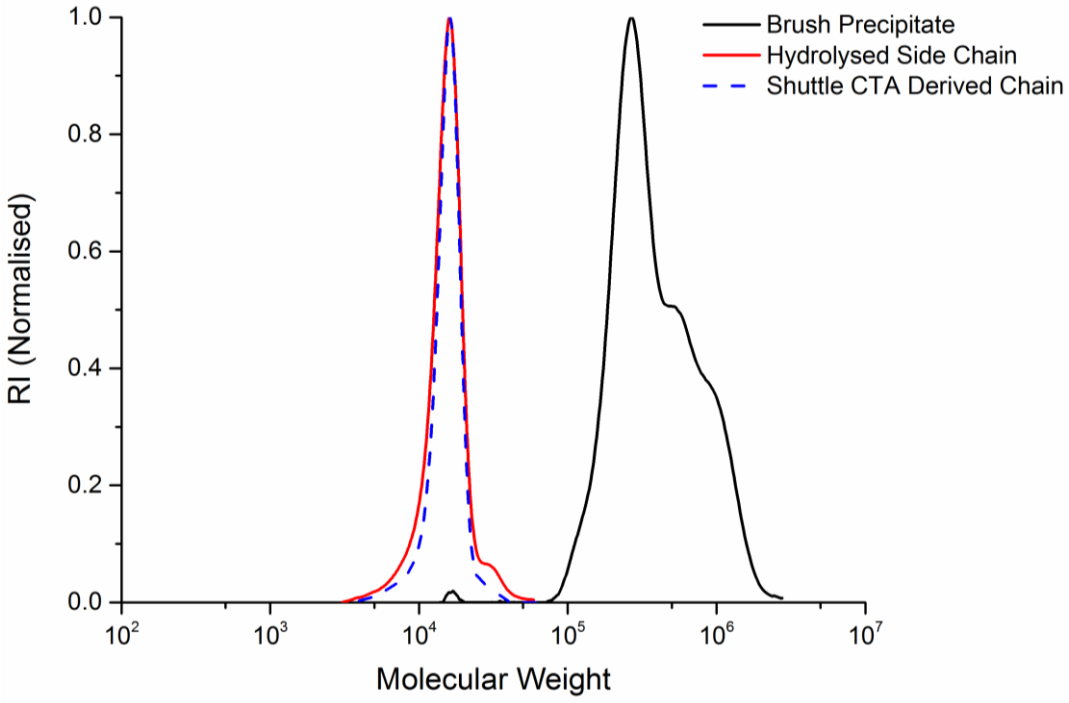

Figure A.14: SEC molecular weight distributions showing hydrolysis of the hexablock side chain leads to an equivalent species to the shuttle CTA derived polymer.

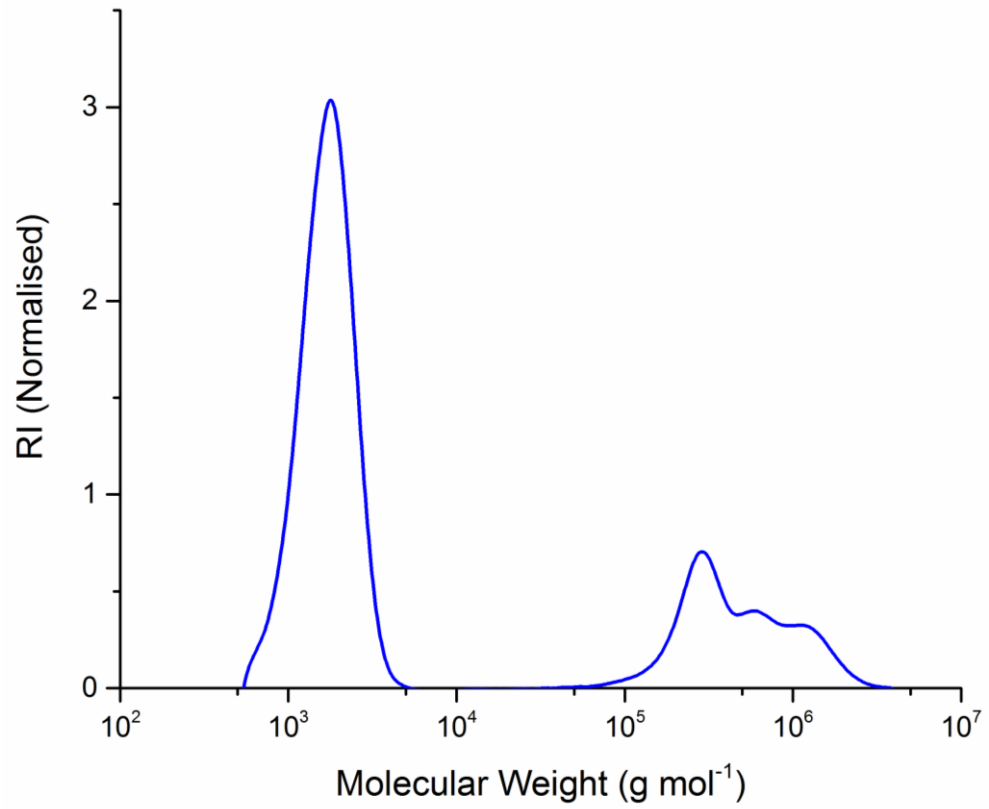

Figure A.15: DMF SEC molecular weight distribution of attempted polymerisation from a DP500 PolyCTA backbone. When reaching full monomer conversion with PNAM side chains, even after one block a broad multimodal distribution is observed for the bottle-brush. 4 equivalents of shuttle CTA were used to try and reduce the rate of cross-coupling, however this was still not sufficient and a large amount of linear polymer is formed compared to bottle-brush.

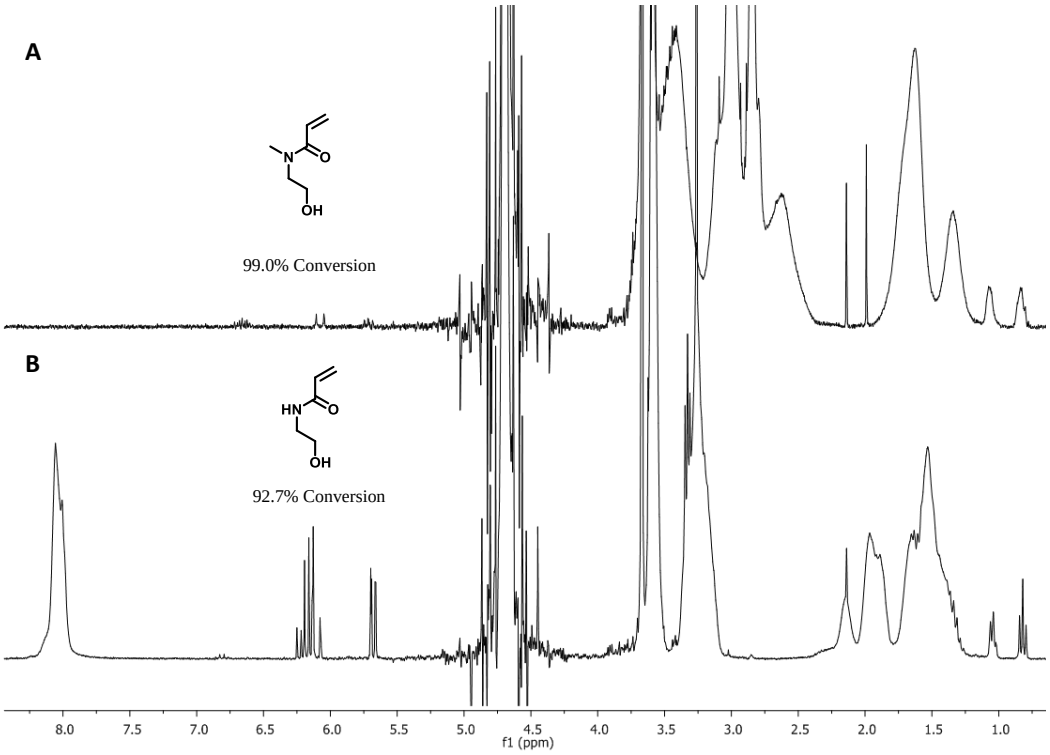

Entry	Monomer	Target DP	CTA/VA-044	Temp. (°C)	Time (h)	Conversion
A	MHEAm	44	120	70	2	99.0
B	HEAm	48	120	70	2	92.7

Figure A.16: Under identical polymerisation conditions the methylated acrylamide monomer reached slightly higher conversions as determined by ^{1}H NMR and was therefore selected for the multiblock backbone synthesis.

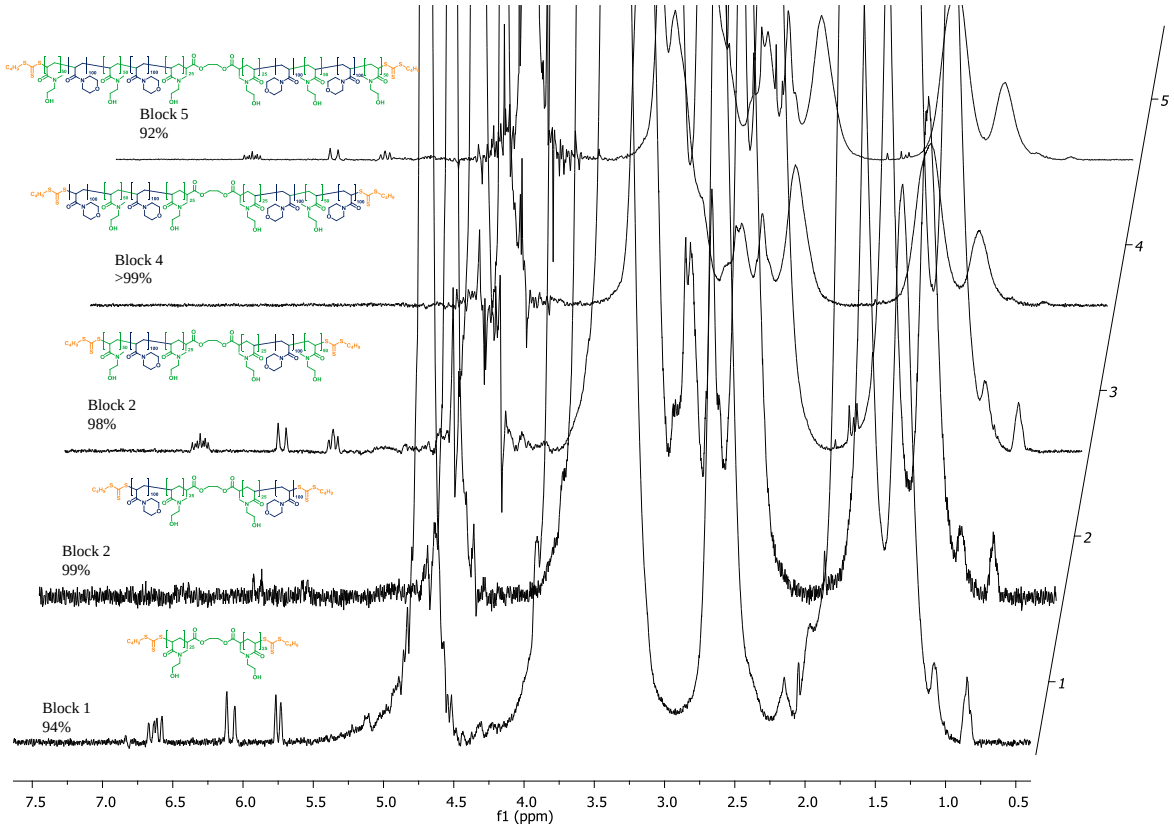

Figure A.17: ^{1}H NMR spectra of the multiblock polymerisation to synthesise the nonablock backbone with MHEAm monomer.

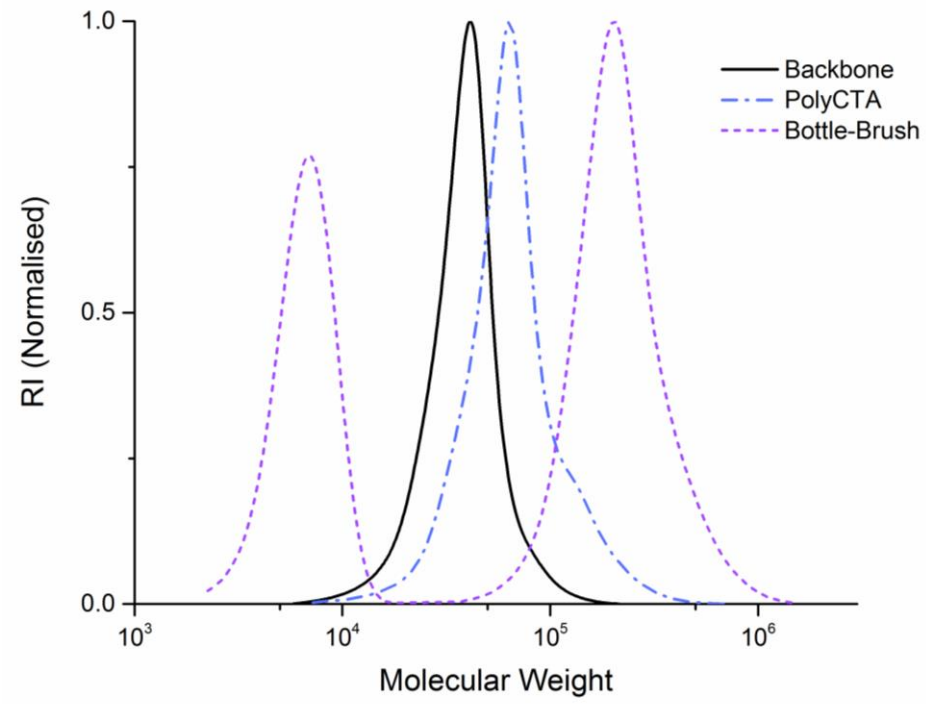

Figure A.18: DMF SEC chromatograms of the nonablock backbone polymer, the PolyCTA and derived bottle-brush. The low molecular shuttle CTA derived polymer is included in the trace.

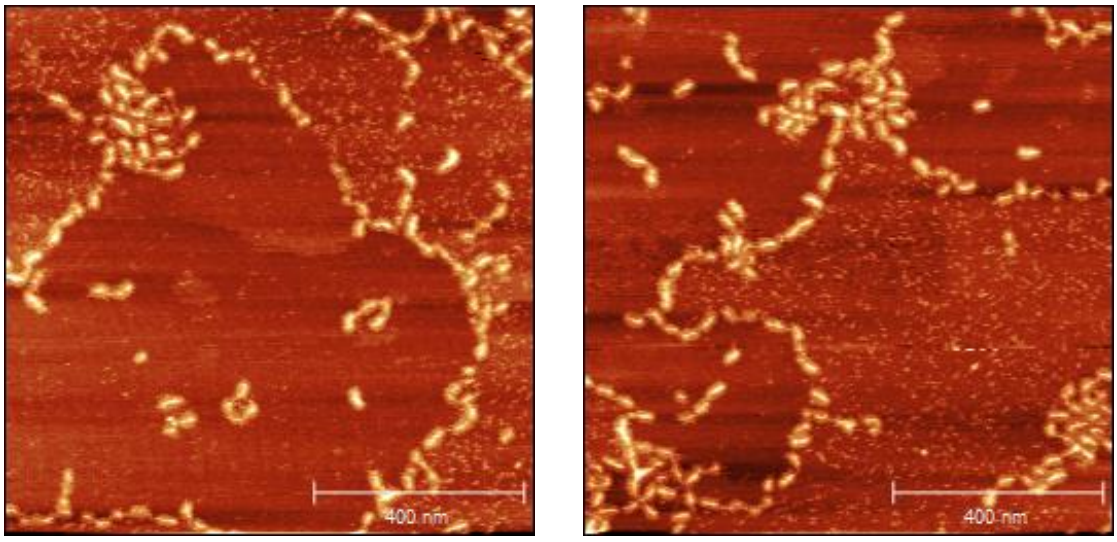

Figure A.19: Additional AFM images of the nonablock backbone bottle-brush polymer.

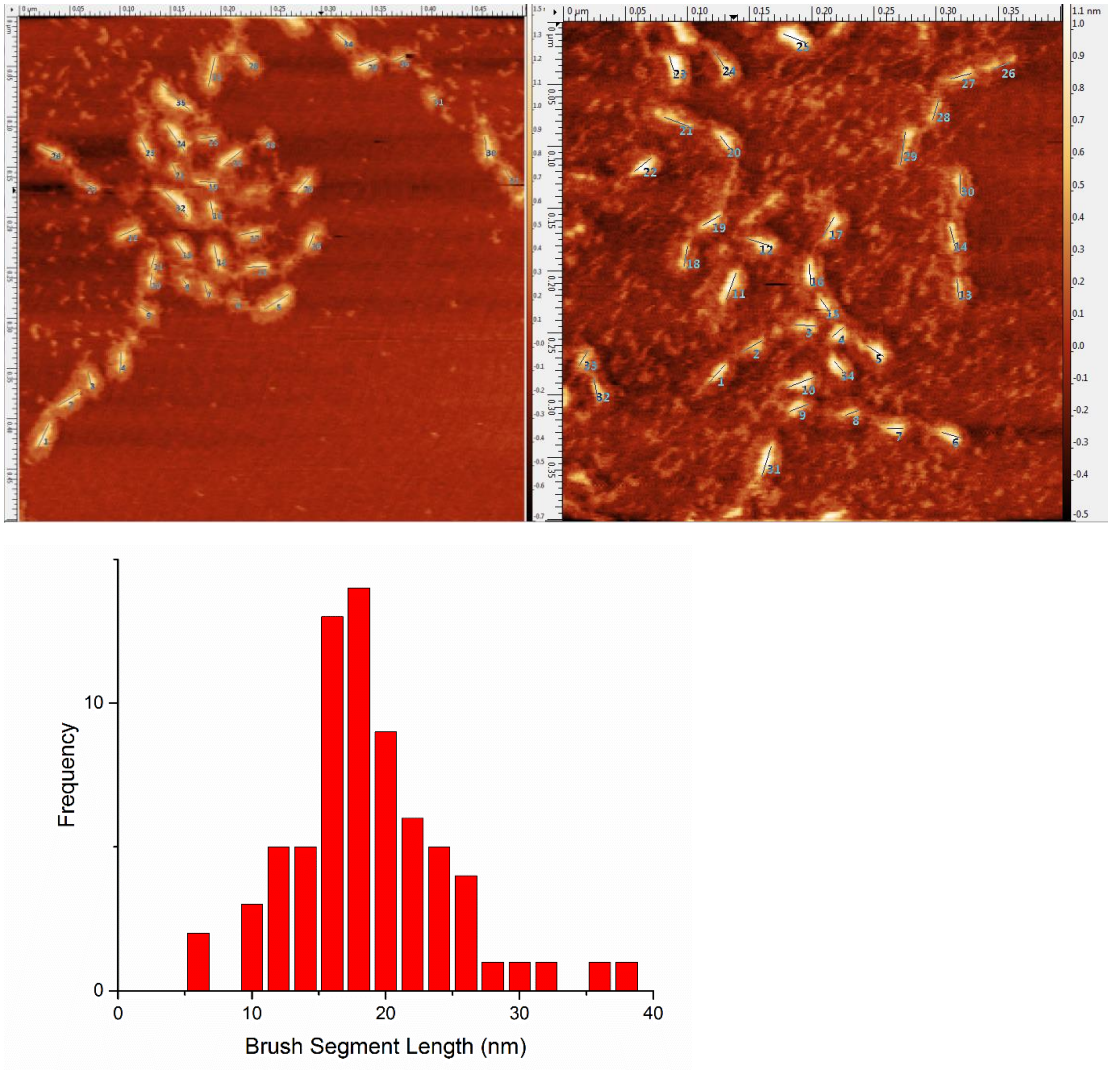

Figure A.20: The length of bottle-brush molecules was measured using Gwyddion software. In total 71 brushes across the two images were measured, the data is shown in histogram to give a mean average of 19 nm.

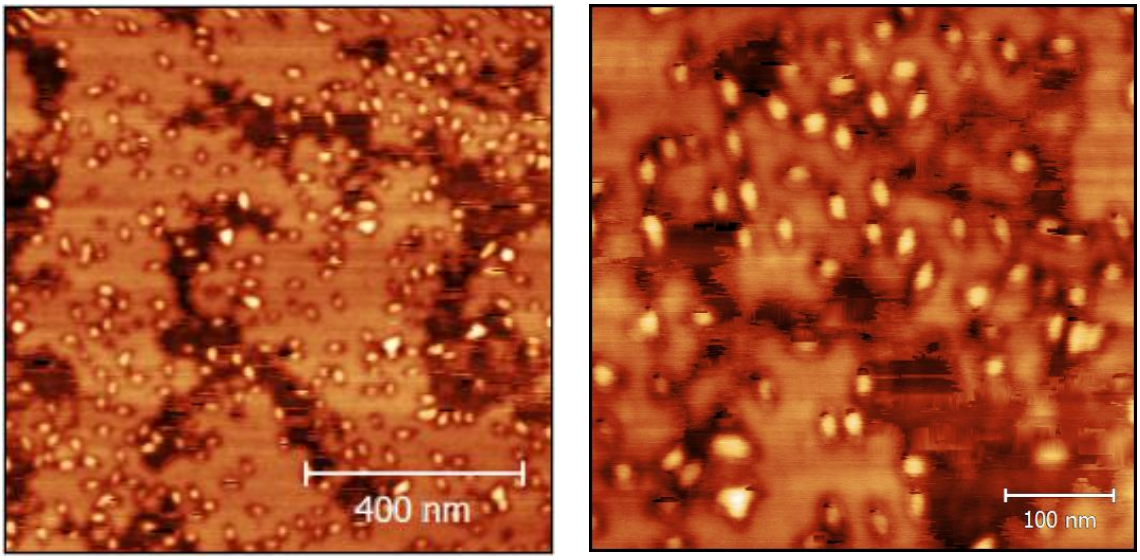

Figure A.21: AFM images of a $[pnBA_{40}]_{100}$ bottle-brush showing presence of short, globular species as opposed to the cylindrical structures observed for the longer DP500 bottle-brush.

Appendix B

Supporting information for Chapter 3

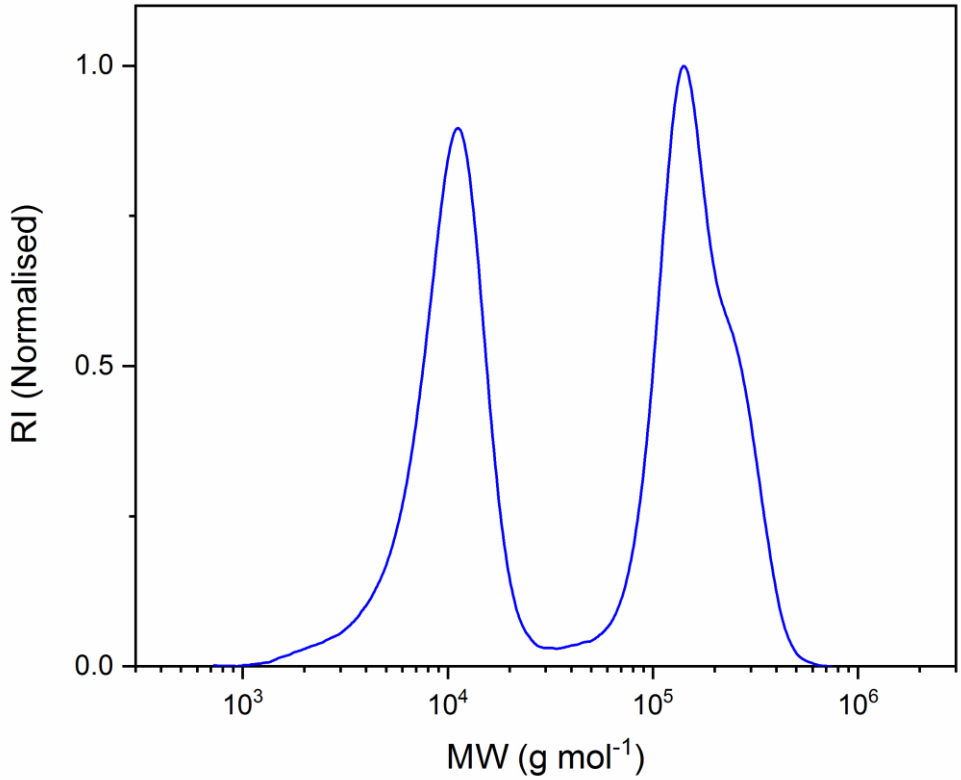

Figure B.1: Example SEC molecular weight distribution of a PLA bottle-brush polymerised up to 92 % monomer conversion with the addition of 0.5 eq. shuttle CTA. In the case of high conversions such as this a high molecular weight shoulder is always formed by the monomer LA. The quantity of linear side product is also relatively high compared to the expected 33 % from the added shuttle CTA, resulting from the increased number of initiator derived chains.

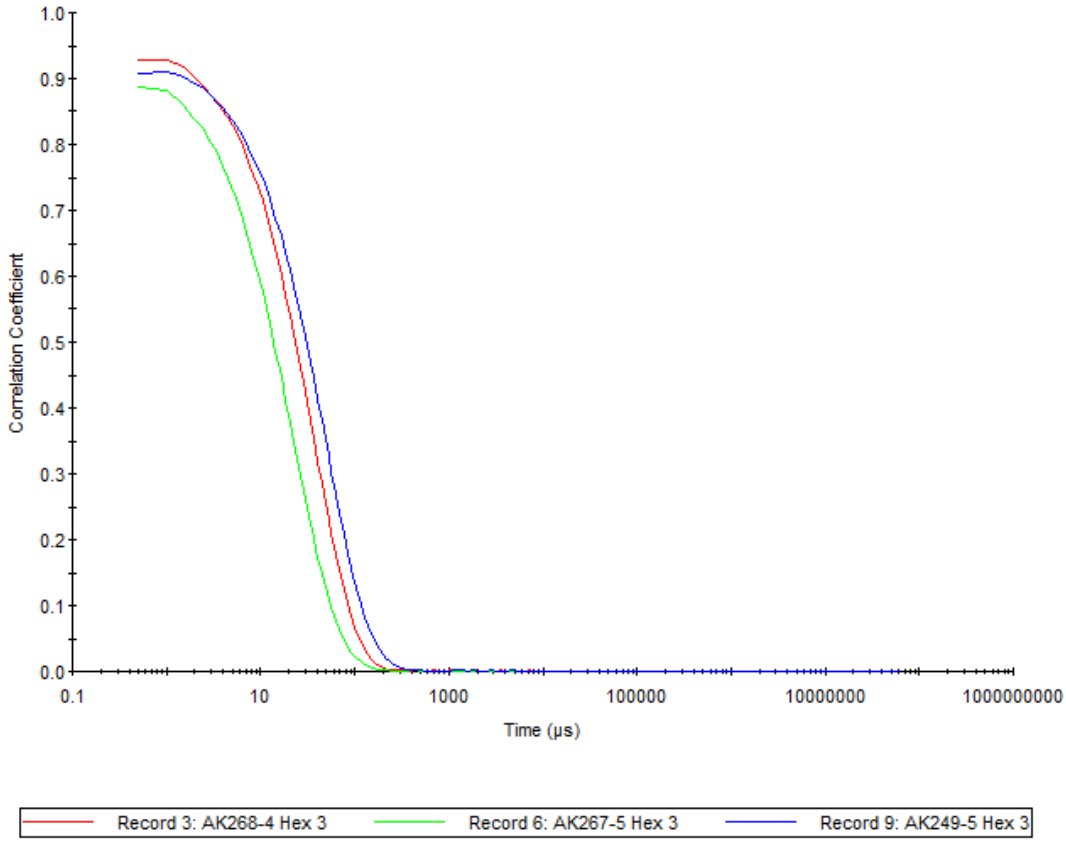

Figure B.2: DLS correlograms of samples in hexane: Green – DP100 PNAM anchor brush, Red – DP200 PNAM anchor brush, Blue – DP400 PNAM anchor brush.

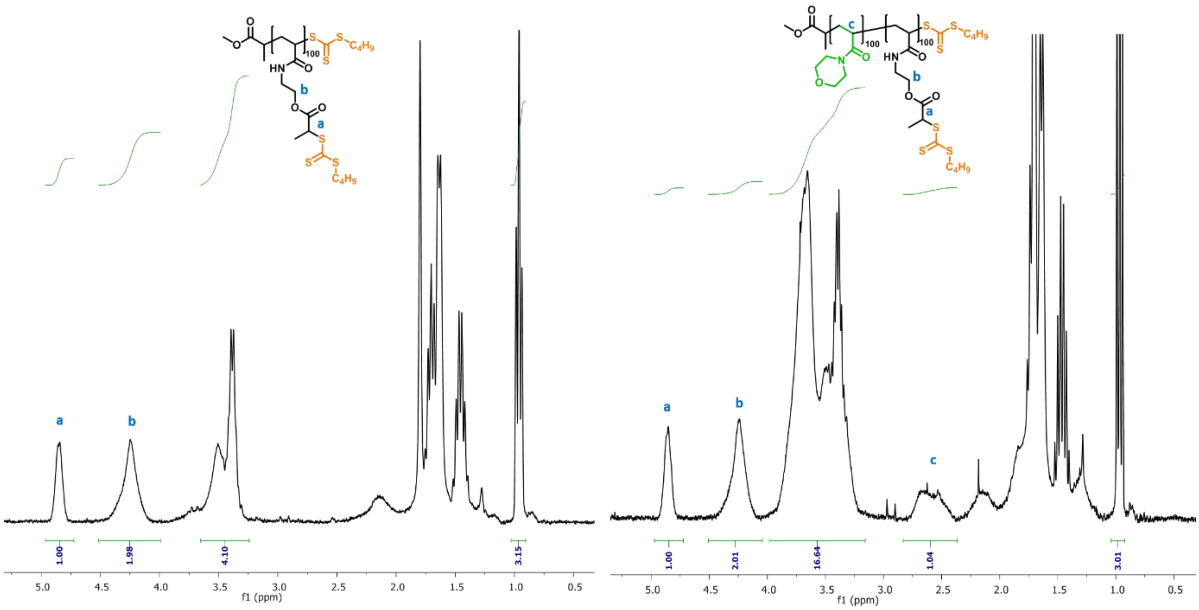

Figure B.3: Left – ^{1}H NMR spectra in $CDCl_3$ (300 MHz) of PCTA derived from homopolymer PHEAm100 backbone. Right - ^{1}H NMR spectra in $CDCl_3$ of diblock PCTA backbone showing integration of 'a' CH adjacent to trithiocarbonate has approximately the same integral as environment 'c' which is consistent with an equal DP100 for the PNAM and PCTA blocks.

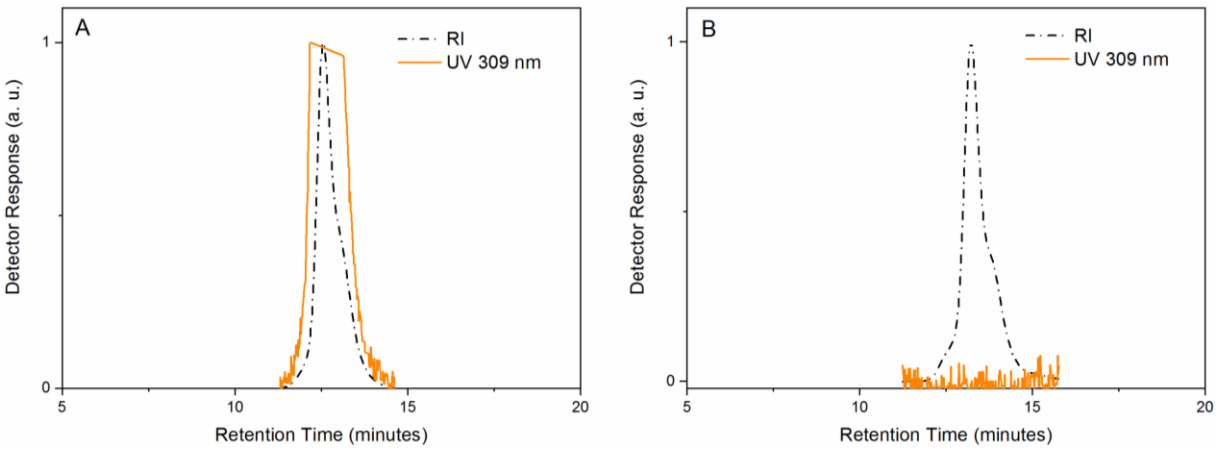

Figure B.4: SEC molecular weight distribution of the $PNAM_{50}$-$PHEAM_{100}$-$PNAM_{50}$ triblock copolymer before (A) and after (B) reaction with AIBN/LPO to remove the CTA end group, characterised by the removal of UV absorption at 309 nm, typical of the trithiocarbonate moiety.

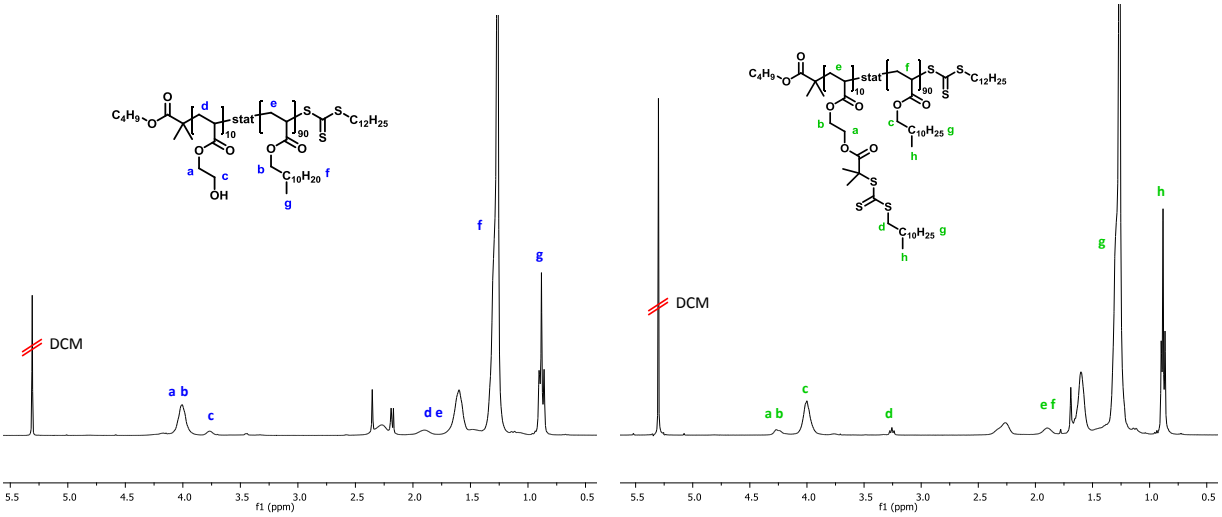

Figure B.5: Left - ^{1}H NMR (300 MHz) spectra in $CDCl_3$ of $PHEA_{10}$-co-PLA_{90} precipitate. Right – ^{1}H NMR spectra of $PCTA_{10}$-co-PLA_{90} PolyCTA backbone used for comb polymer synthesis.

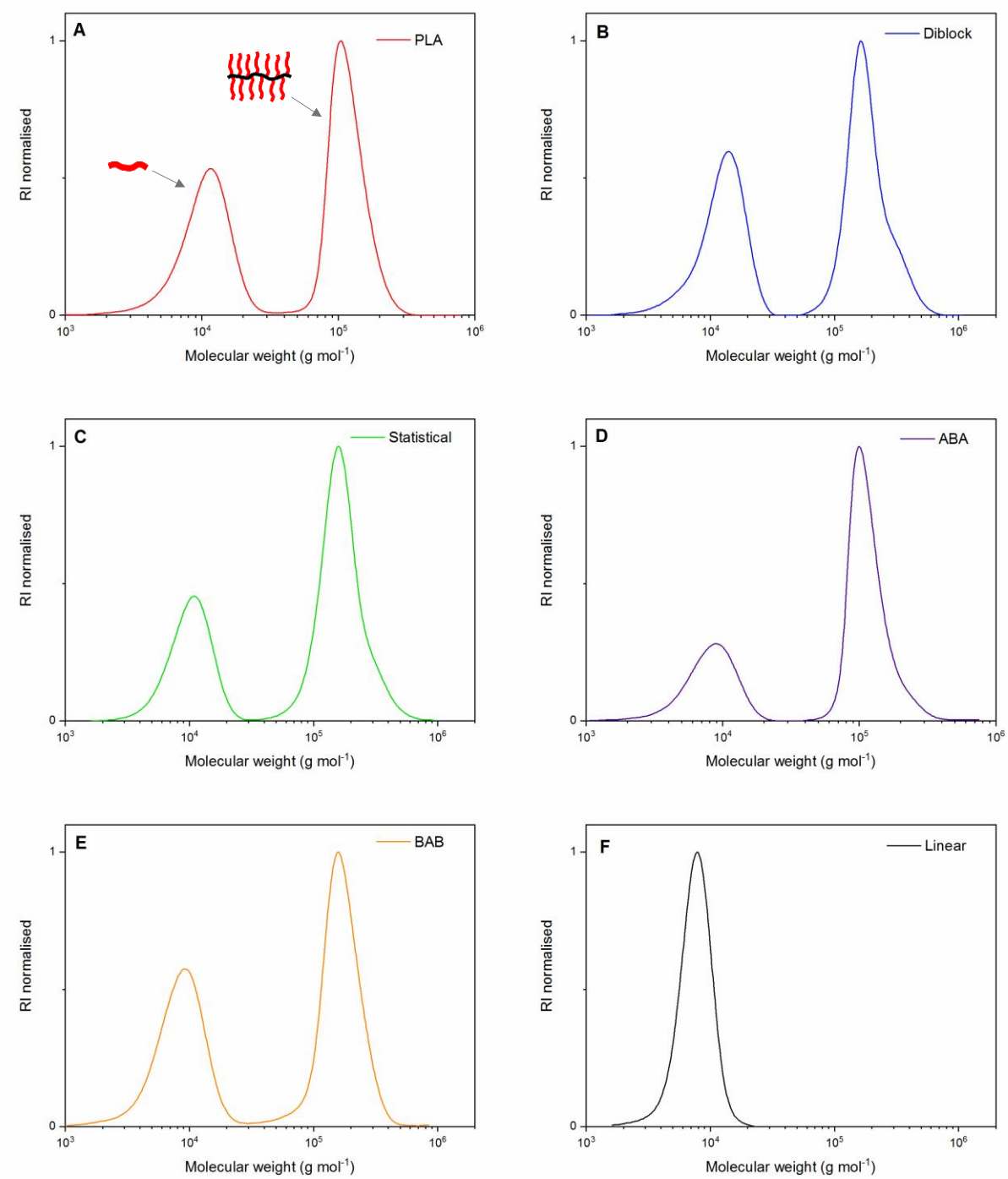

Figure B.6: $CHCl_3$ eluent SEC molecular weight distributions of the bottle-brush samples including the linear polymer species at low molecular weight.

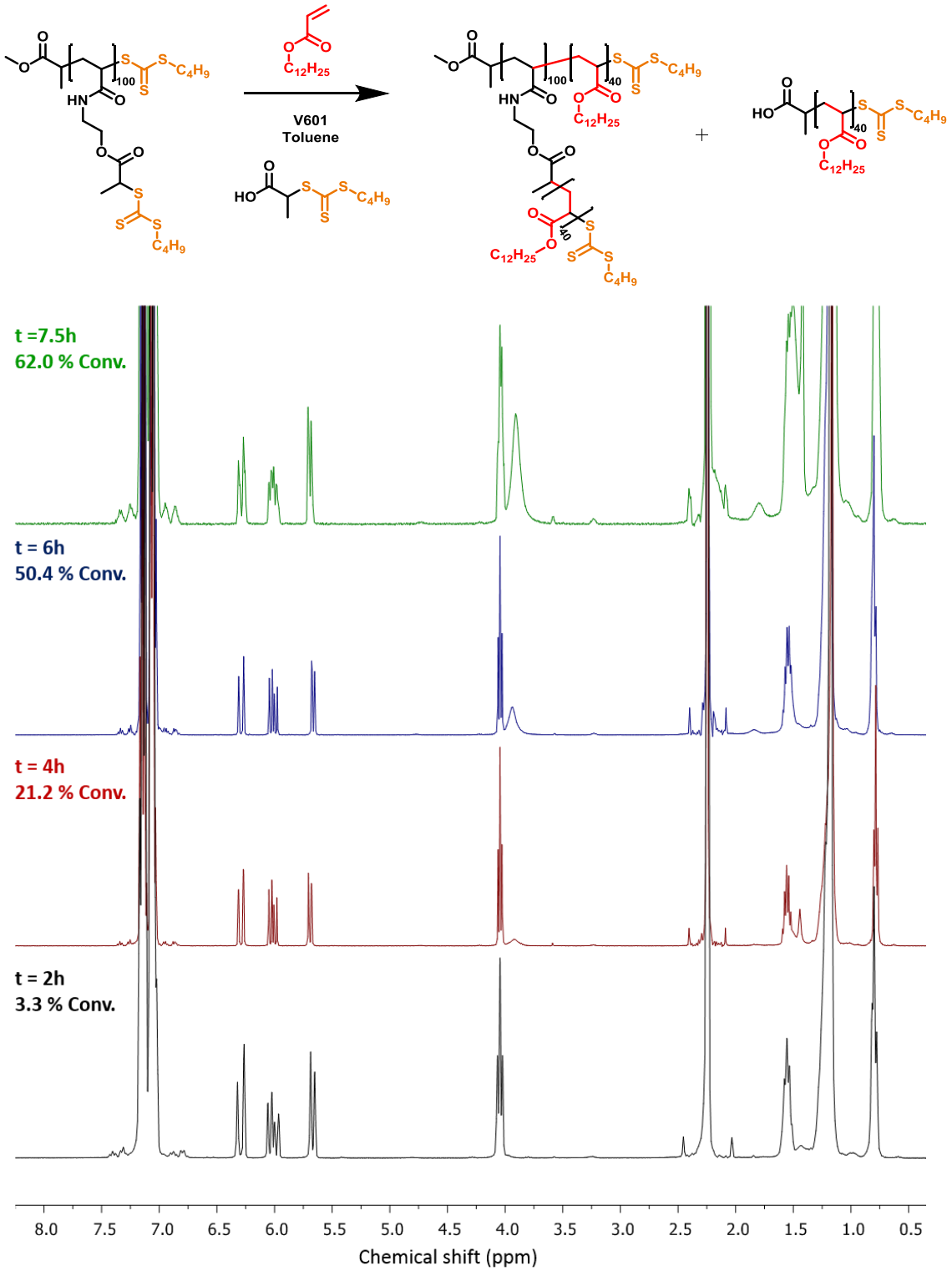

Figure B.7: Top - scheme for grafting from of LA from the DP100 PCTA backbone and the ^{1}H NMR (300 MHz) spectra in $CDCl_3$ used to measure reaction kinetics. Monomer conversions were determined by integration of the CH_2 ester peak of monomer + polymer at 3.8 -4.1 ppm against monomer vinyl peaks at 5.5 – 6.5 ppm.

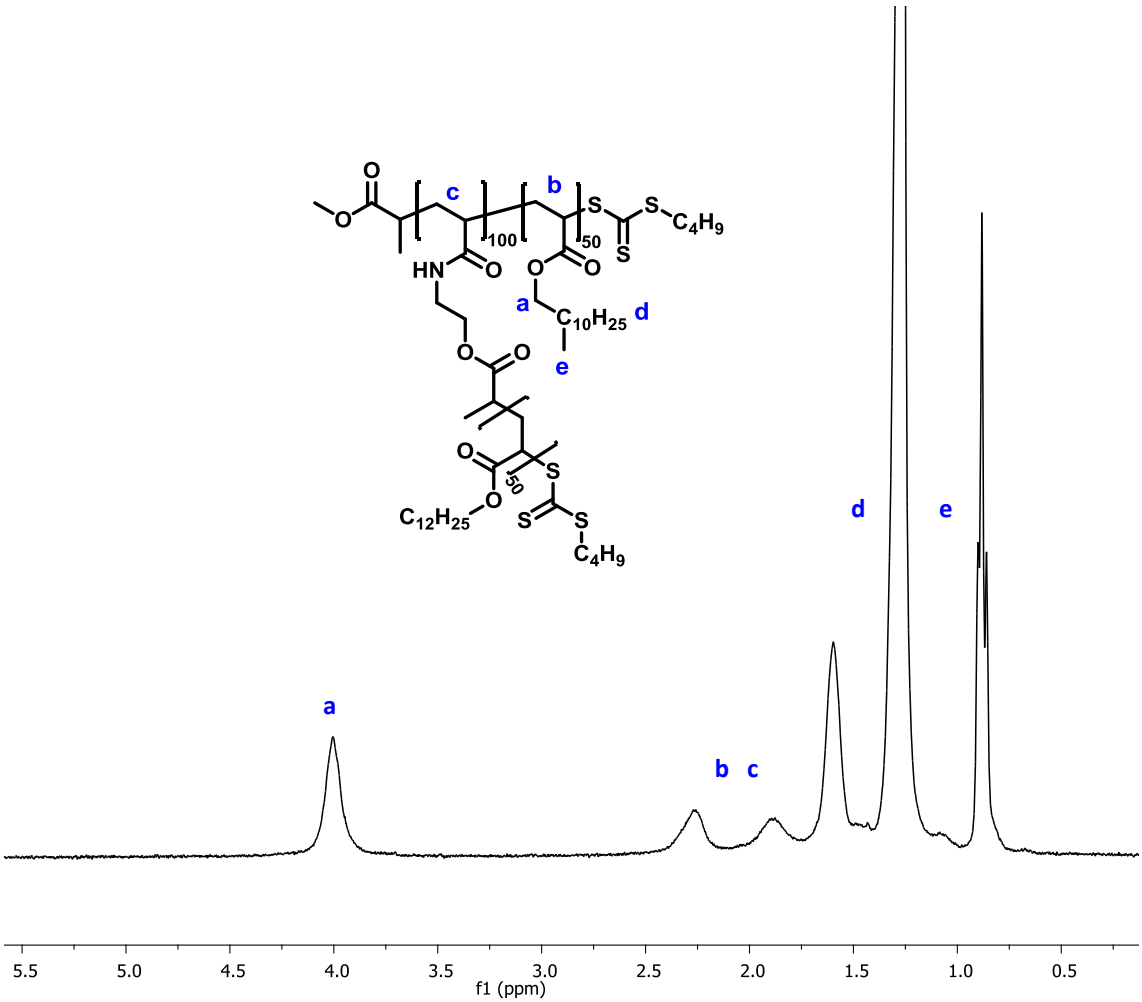

Figure B.8: ^{1}H NMR (300 MHz) spectra in CDCl3 of a PLA bottle-brush polymer.

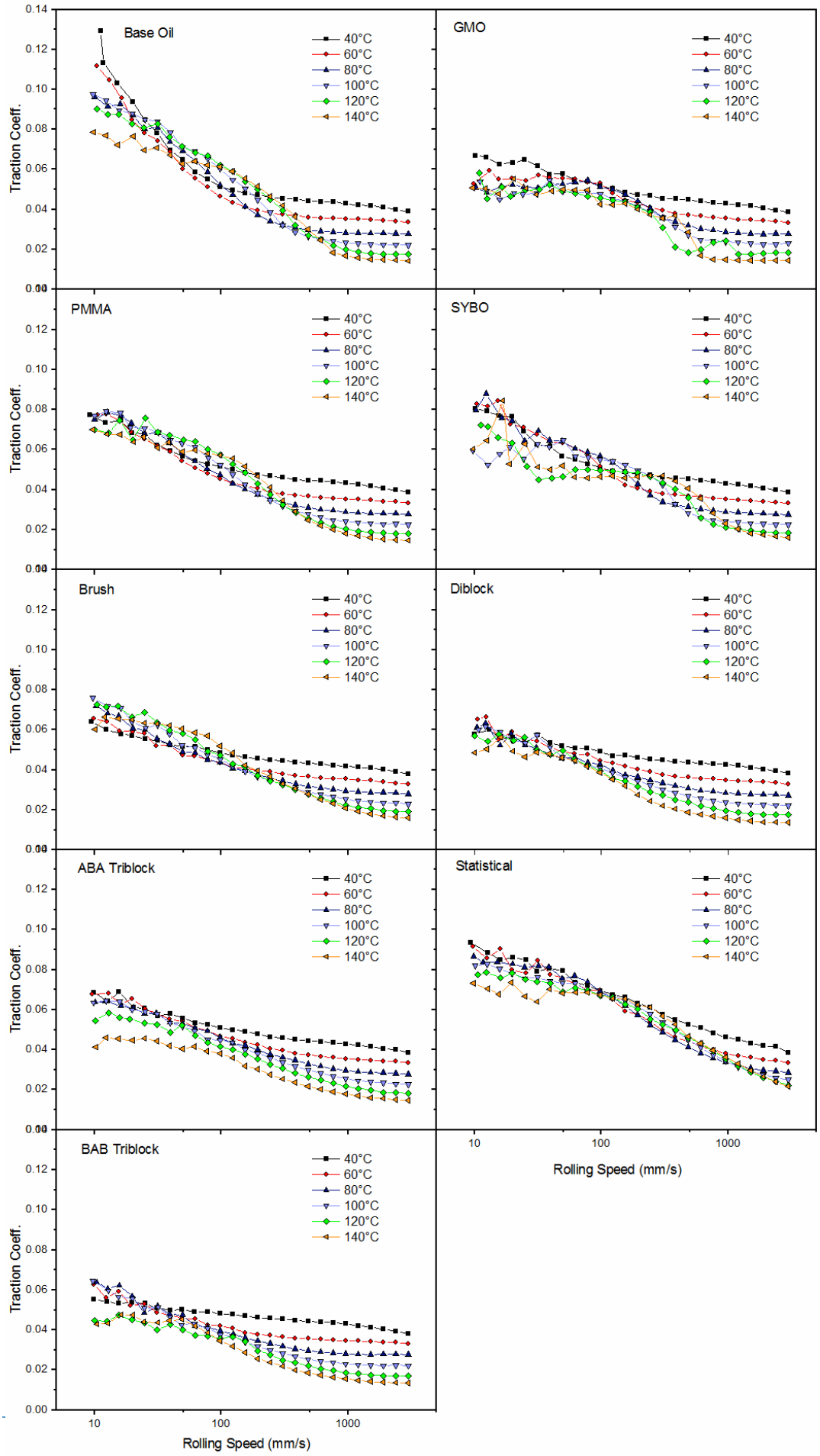
Base Oil
GMO
PMMA
SYBO
Brush
Diblock
ABA Triblock
Statistical
BAB Triblock
40°C
60°C
80°C
100°C
120°C
140°C
Traction Coeff.
Rolling Speed (mm/s)
0.00
0.02
0.04
0.06
0.08
0.10
0.12
0.14
10
100
1000

Figure B.9: MTM testing of each compound performed at 1 wt. % additive in mineral oil, plotted for each temperature ranging from 40 – 140°C

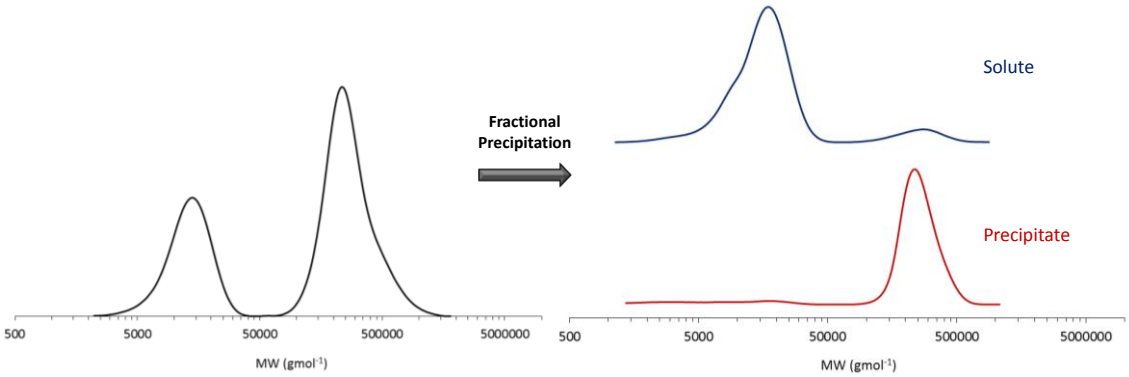

Figure B.10: SEC analysis ($CHCl_3$) shows fractional precipitation procedure is effective for removing linear PLA from the bottle-brush sample. The crude materials was dissolved in THF (50 mg ml^{-1}) and methanol was added dropwise until the solution was significantly turbid. The mixture was heated up until fully dissolved, allowed to cool to room temperature and the residue was collected by centrifugation to yield pure bottle-brush polymer.

Appendix C

Supporting information for Chapter 4

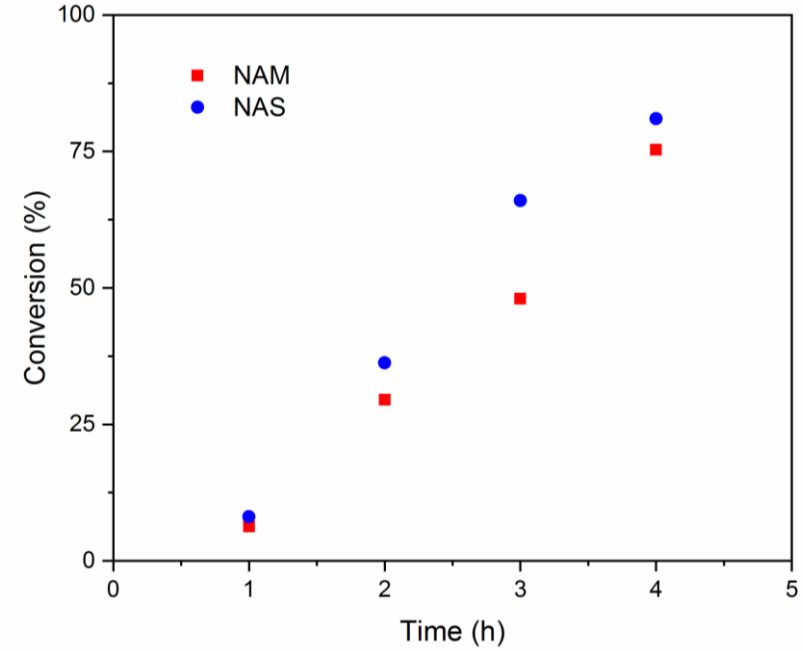

Figure C.1: Kinetics of a NAM / NAS copolymerisation showing similar rate of consumption of both types of monomer, consistent with literature desribing their similar reactivity ratios.

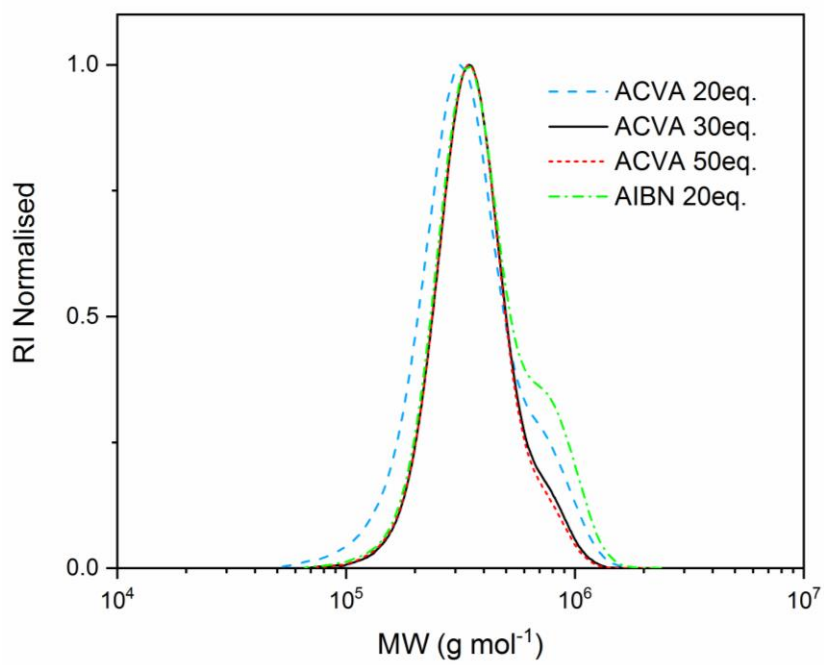

Figure C.2: SEC molecular weight distributions of the CTA removal step performed on the short brush compound with various reaction conditions. Formations of a high molecular weight shoulder is reduced by using a larger excess of ACVA azoinitiator. AIBN was also tested to conifrm the trend was not limited to the use of ACVA in particular.

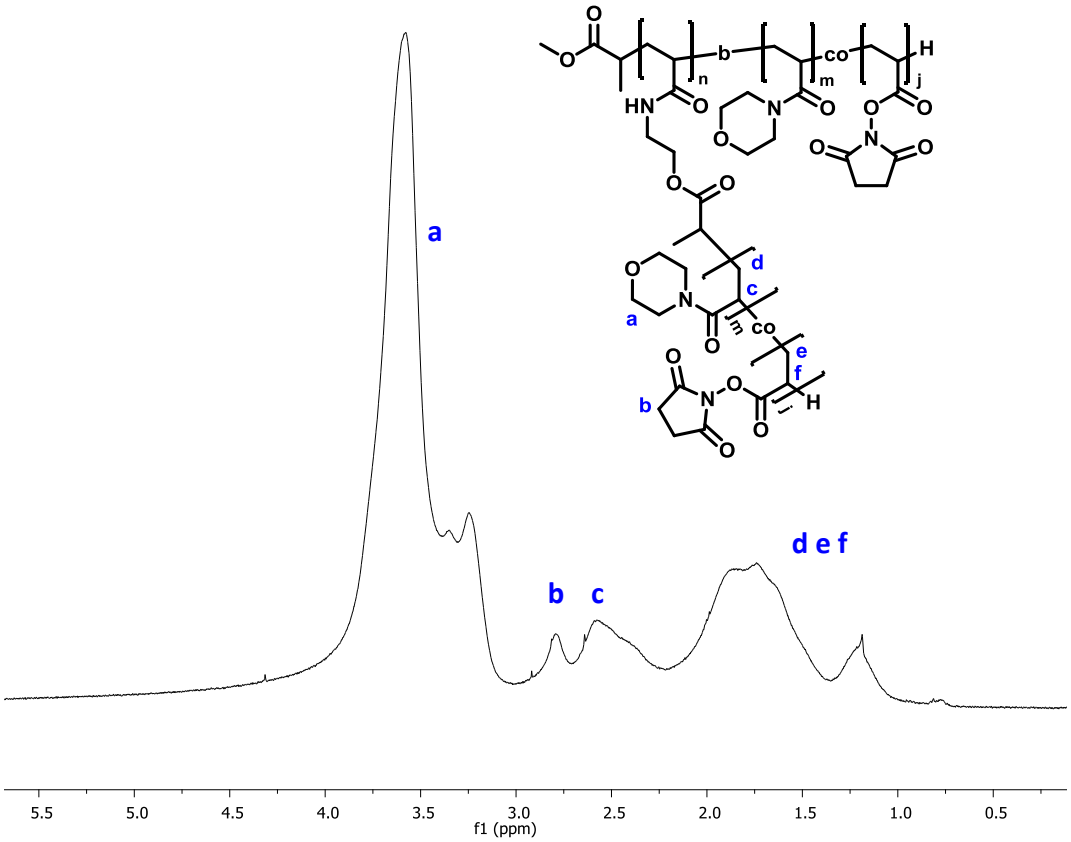

Figure C.3: ^{1}H NMR spectra (300 MHz) in $CDCl_3$ of PNAM-co-PNAS bottle-brush compound.

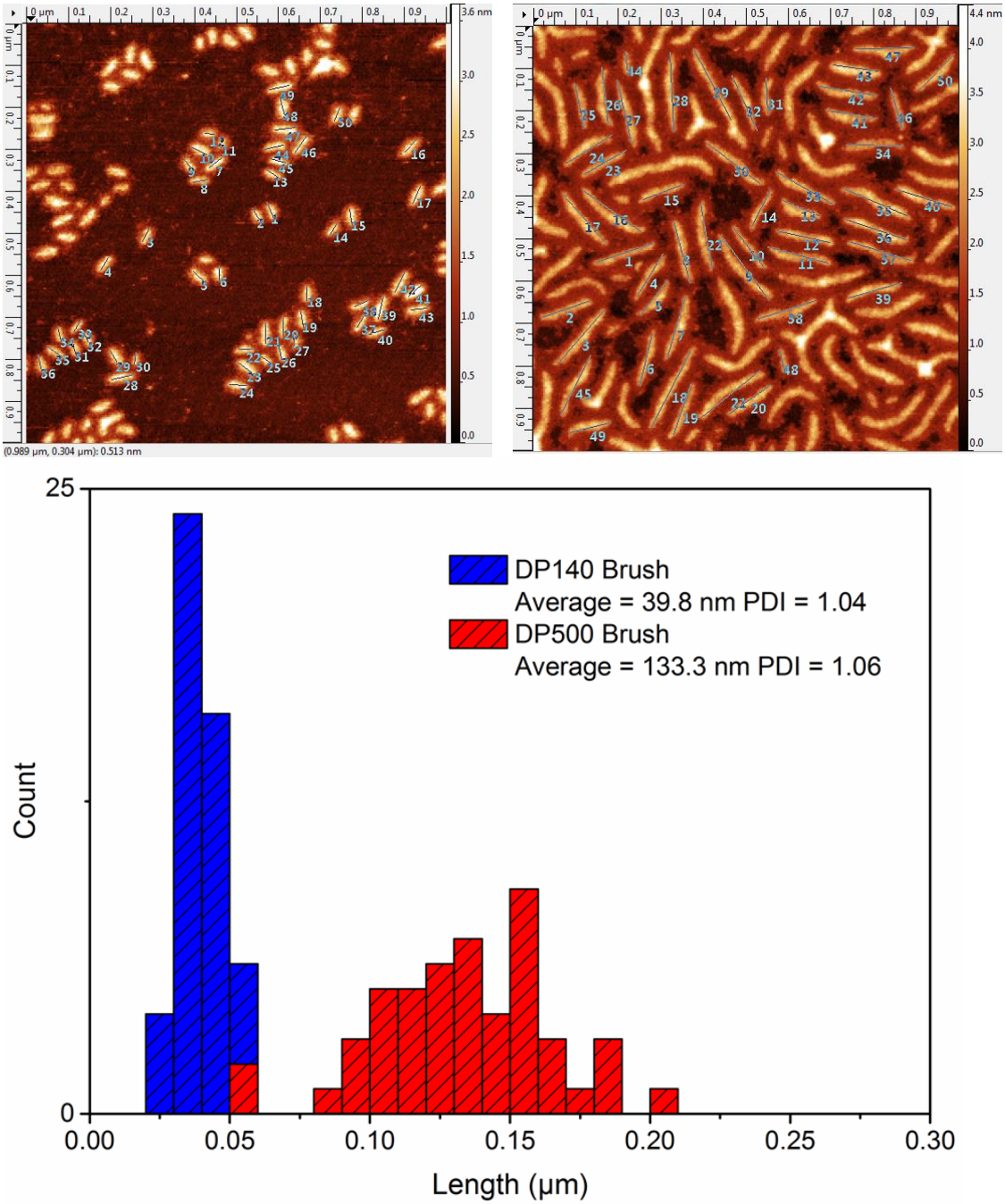

Figure C.4: An approximate size of the each bottle-brush compound was determined by measuring the length of 50 molecules by AFM, the data shown as a histogram.

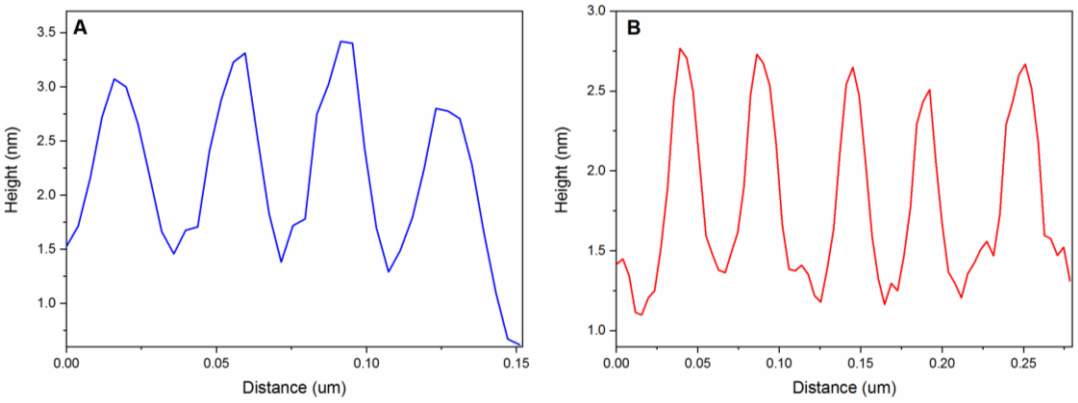

Figure C.5: A – AFM height profile across 4 of the short bottle-brush molecules from above image (Figure) B – AFM height profile of 5 long bottle-brush moelcules.

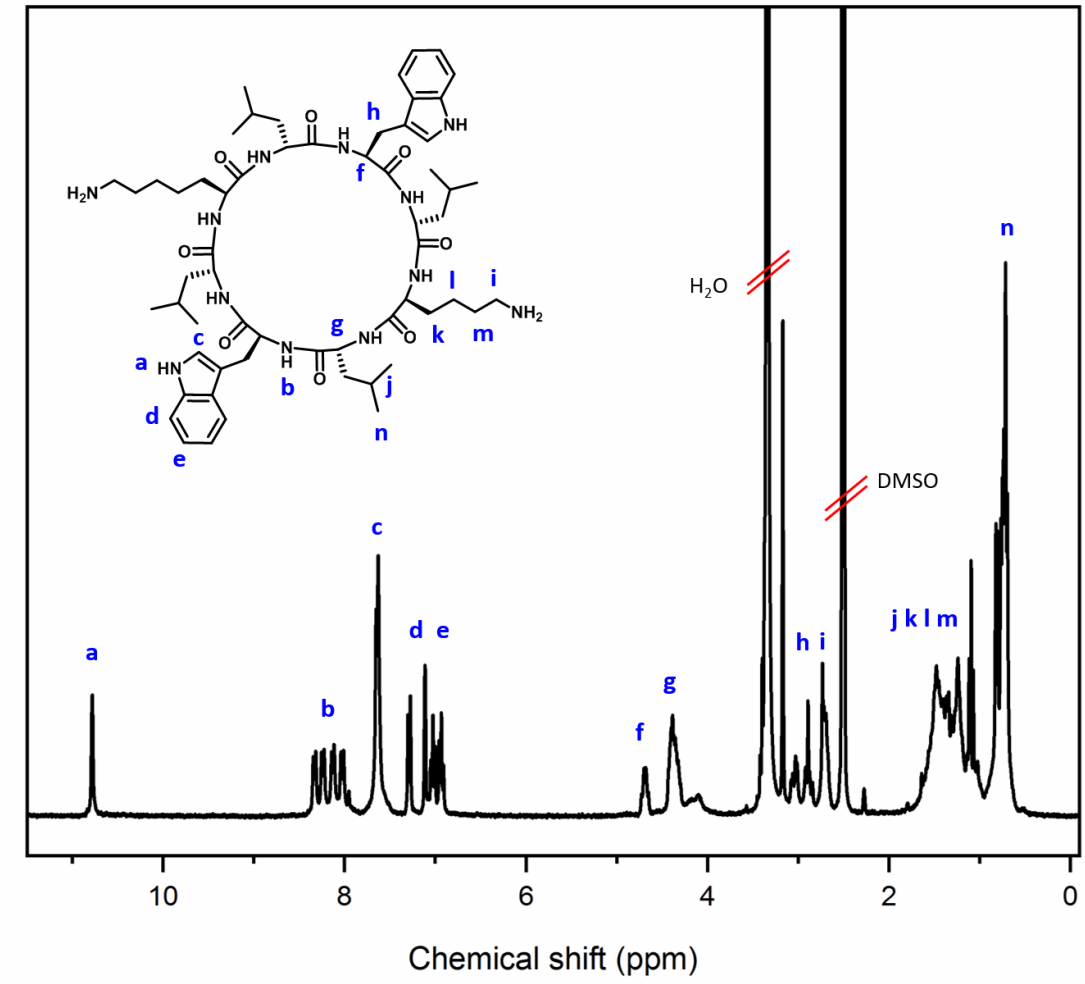

Figure C.6: ^{1}H NMR spectra (400 MHz) of the deprotected cyclic peptide performed in DMSO-d_6.

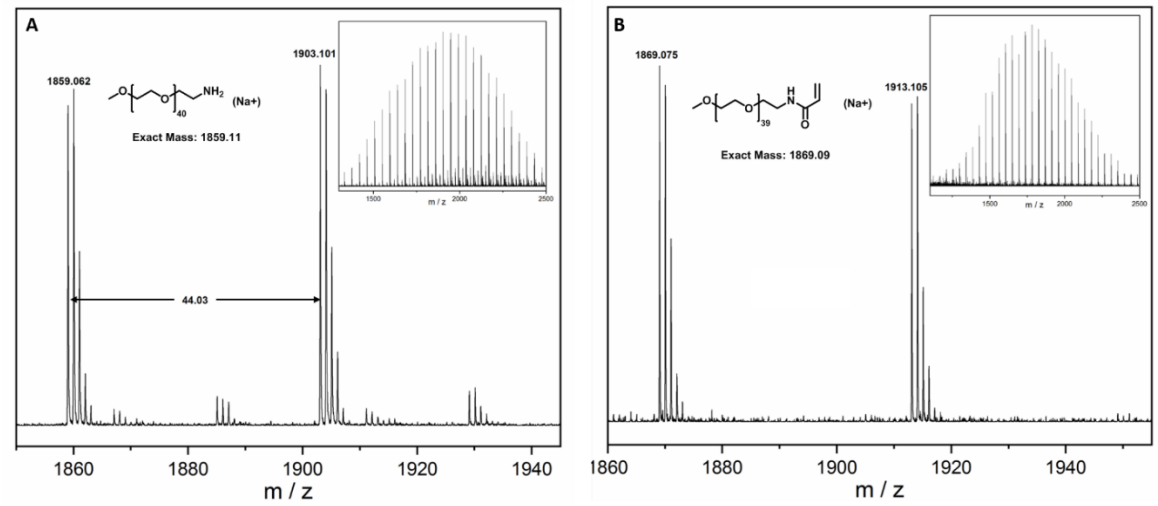

Figure C.7: MALDI-ToF spectra of A - the commerical starting material amine terminated PEG (2,000 $gmol^{-1}$) and B – the synthesised PEG macromonomer.

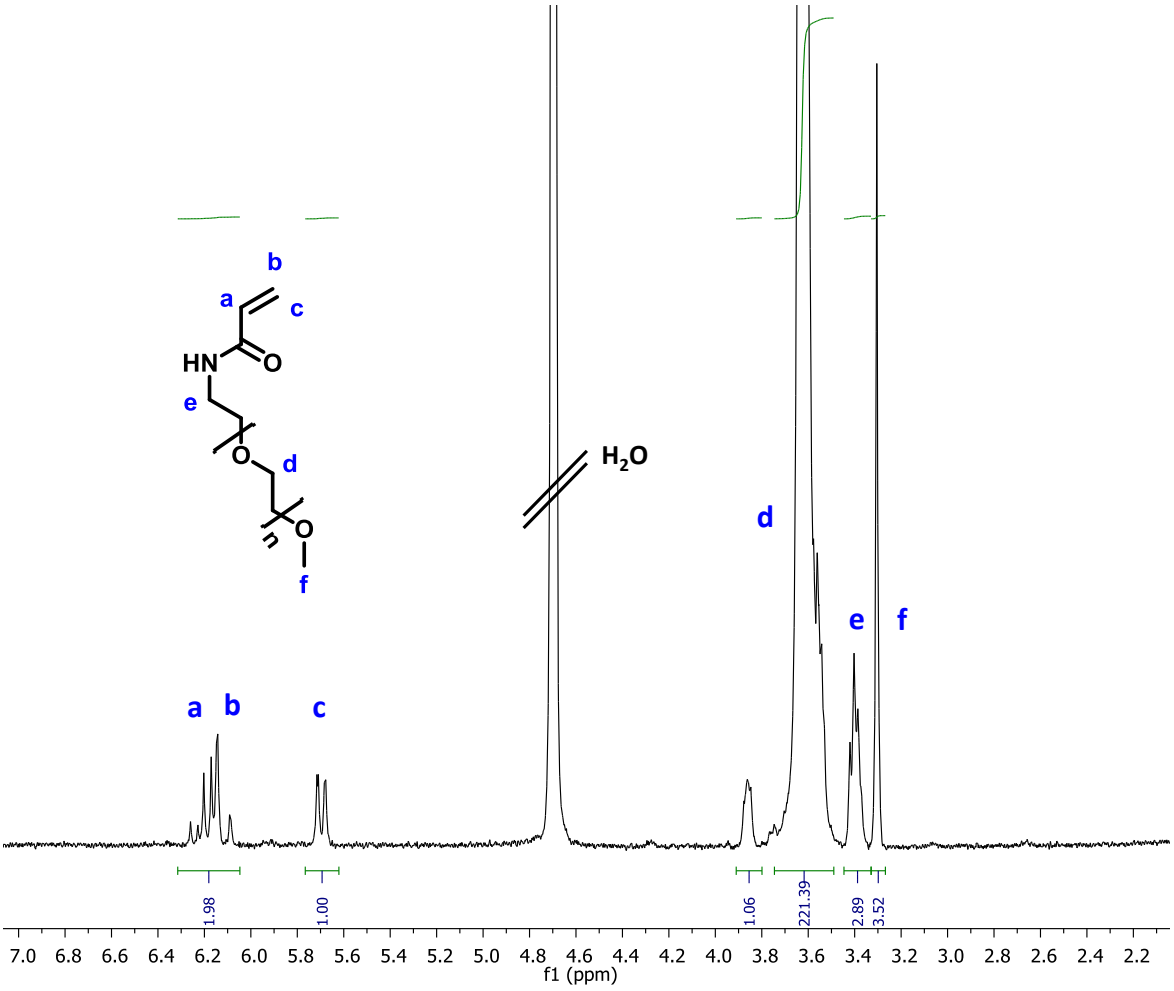

Figure C.8: ^{1}H NMR spectra (300 MHz) of the synthesised PEG macromonomer in $CDCl_3$.

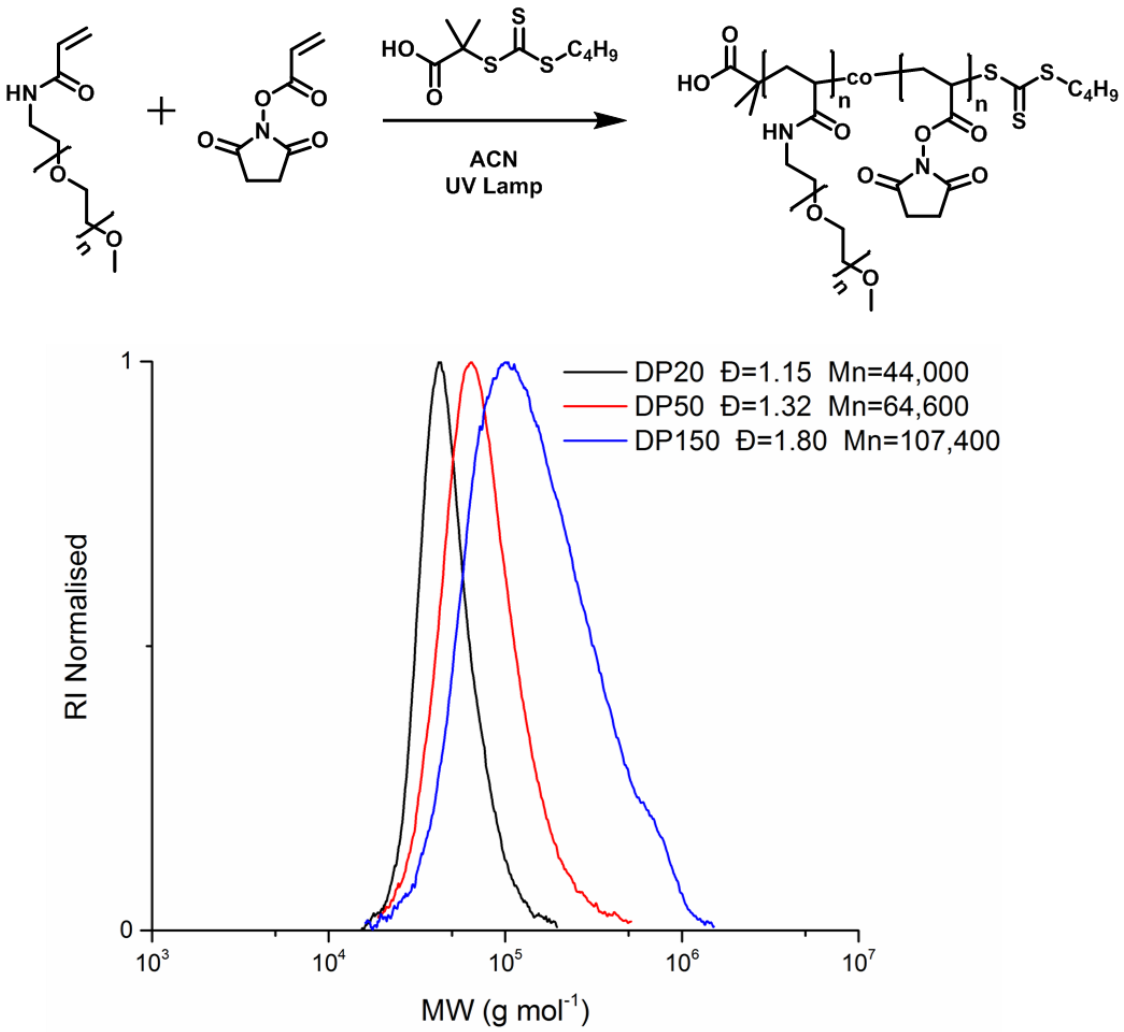

Figure C.9: Top – synthetic scheme of the PEG macromonomer polymerisation to from a bottle-brush. Bottom- SEC molecular weight distributions of the PEG brushes targeting 3 different degrees of polymerisation. Above DP50 a significant increase in dispersity was observed.

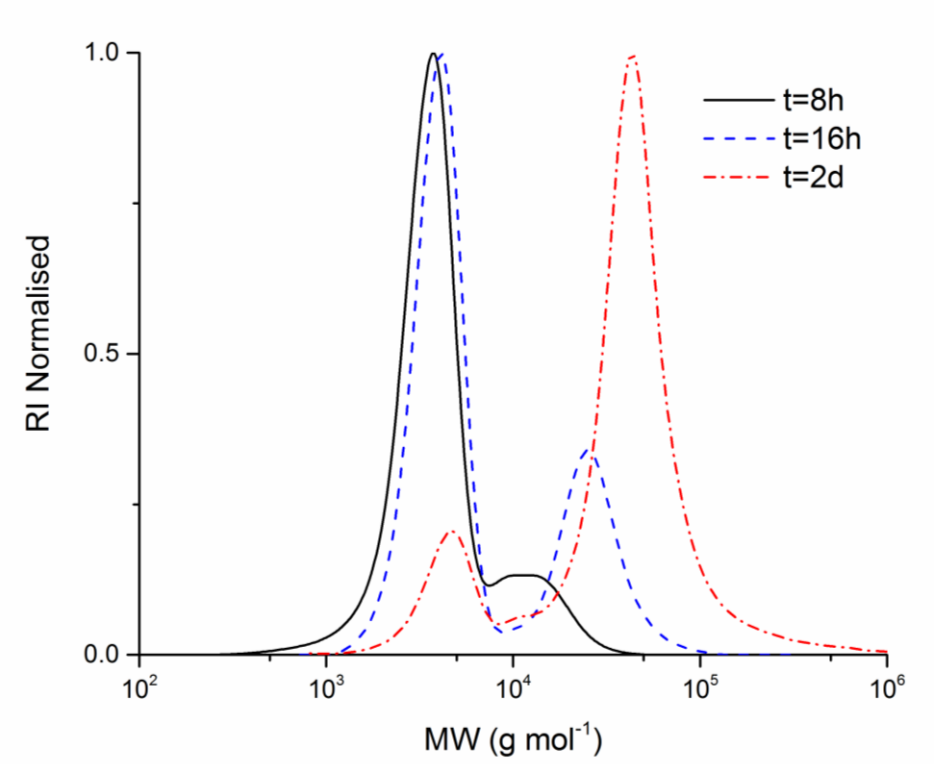

Figure C.10: Kinetic SEC analysis of the PEG macromoner polymerisation, used to determine macromonomer consumption by integration of each peak

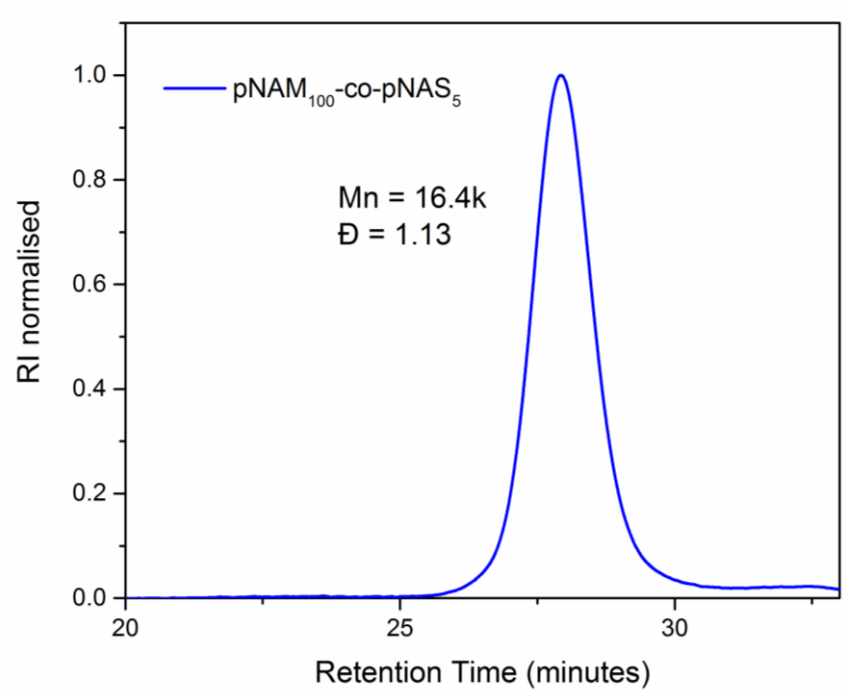

Figure C.11: SEC molecular weight distribution of the linear PNAM-co-PNAS polymer, performed on the DMAc eluent SEC system.

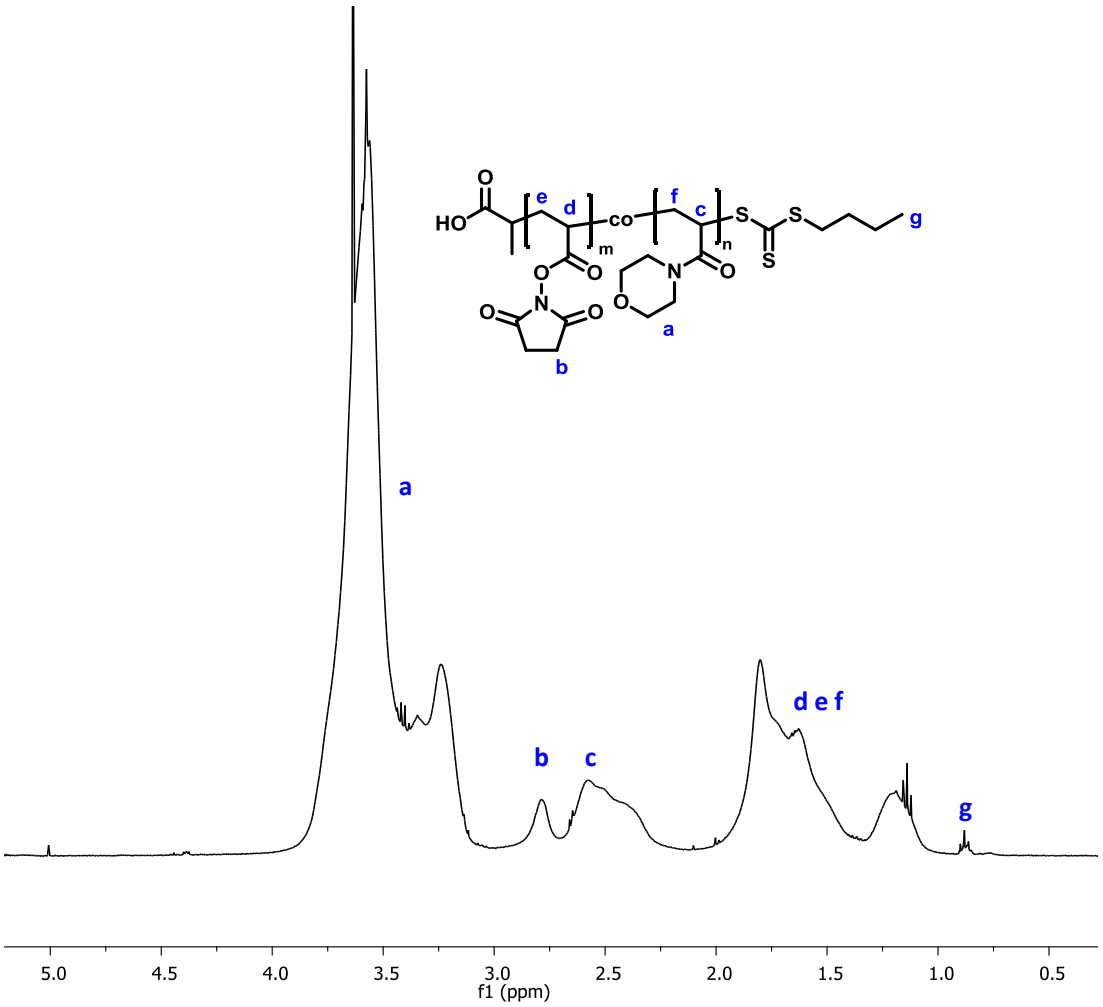

Figure C.12: ^{1}H NMR spectra (300 Mhz) of PNAM-co-PNAS linear polymer compound.

Table C.1: Small angle scattering fitting parameters for the short / long brush (performed with SAXS) and the 2 arm cyclic peptide PNAM (performed with SANS).

	Short Brush	Long Brush	CP 2-arm
Scale	0.060	0.058	0.0025
Cyl. Length (Å)	410	810	360
Cyl. Kuhn Length (Å)	310	436	400
Radius (Å)	81	88	41
Radius Polydispersity	0.1	0.1	0.1
SLD	9.17	9.17	1.12
SLD_solvent	9.47	9.47	6.39
GC I zero	50	50	50
GC rg (Å)	60	60	32
GC Polydispersity	1.1	1.1	1.1

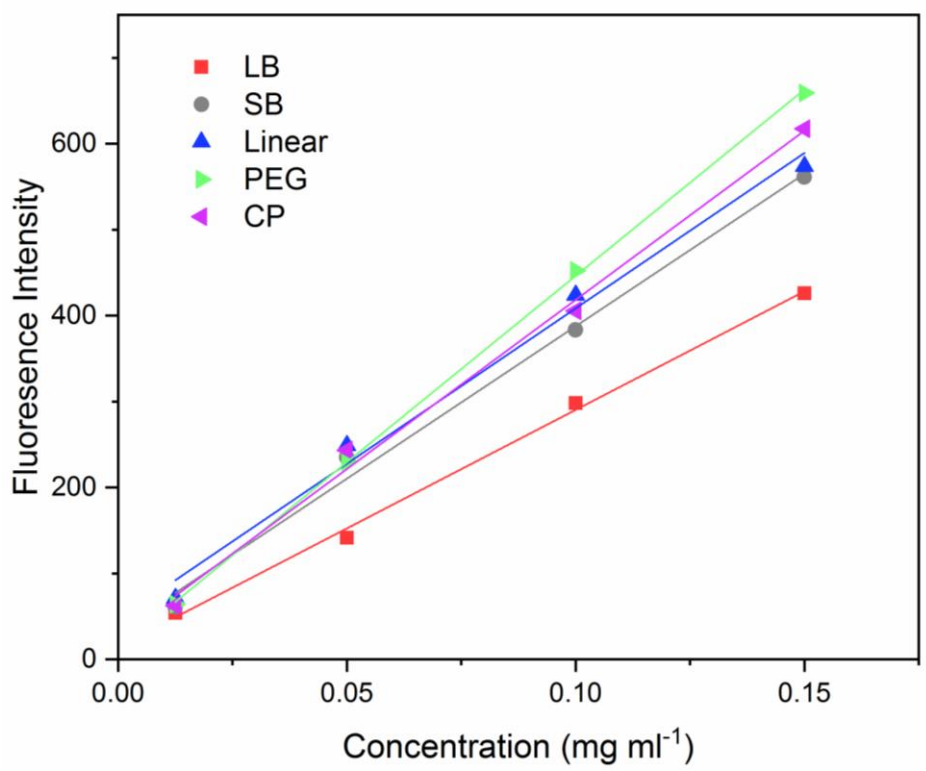

	LB	SB	Linear	PEG	CP	Average
Slope	2758	3547	3615	4336	3936	3638
Correction Factor	1.319	1.026	1.006	0.839	0.924	1

Figure C.13: Top – fluorescence calibration curves the 5 Alexa-488 labelled materials. Table bottom – calculation of correction factors used to process the flow cytometry analysis.

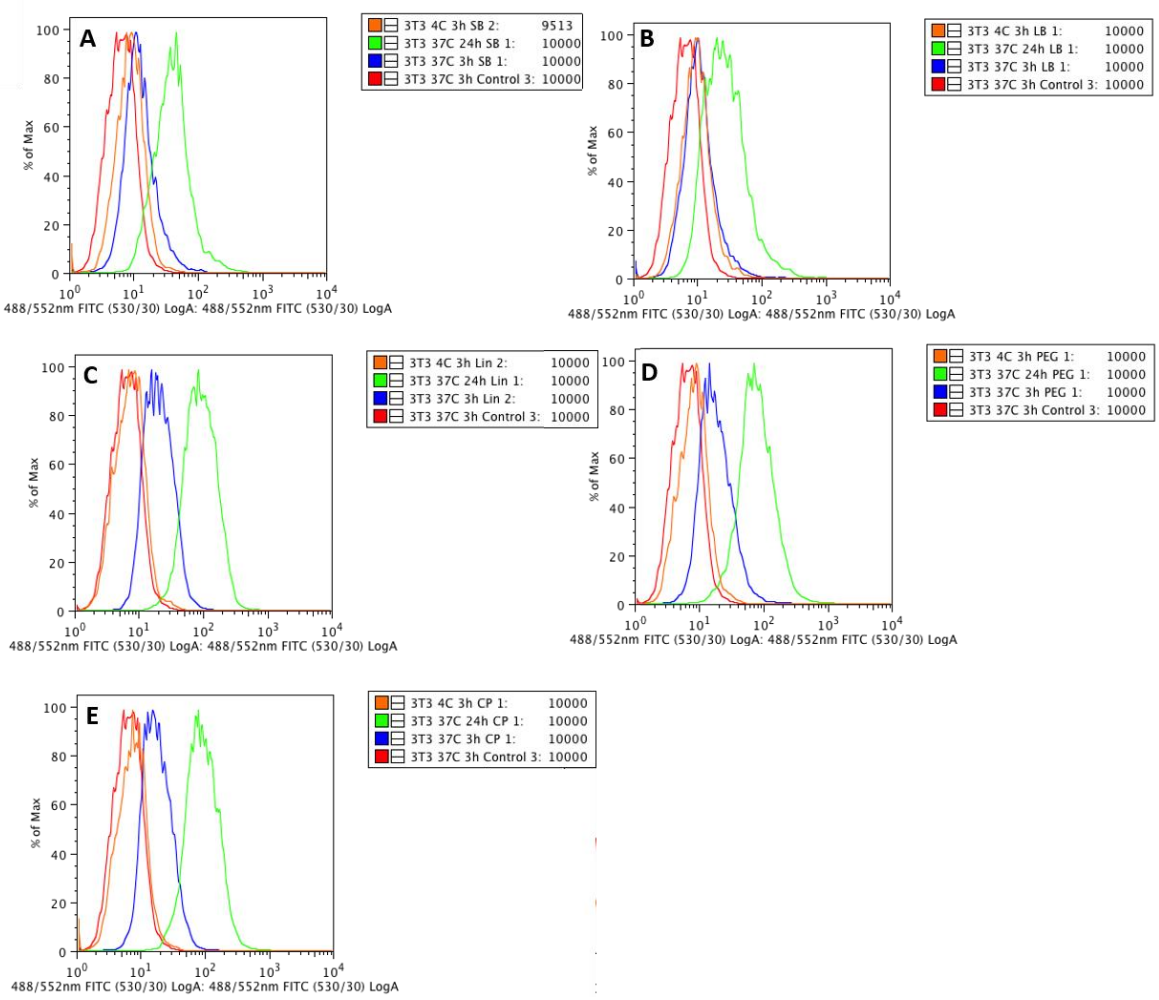

Figure C.14: Flow cytometry histograms of the 3T3 cell lines under 4 experimental conditions for the various compounds: **A** – SB, **B** – LB, **C** – Linear, **D** – PEG brush and **E** – CP.

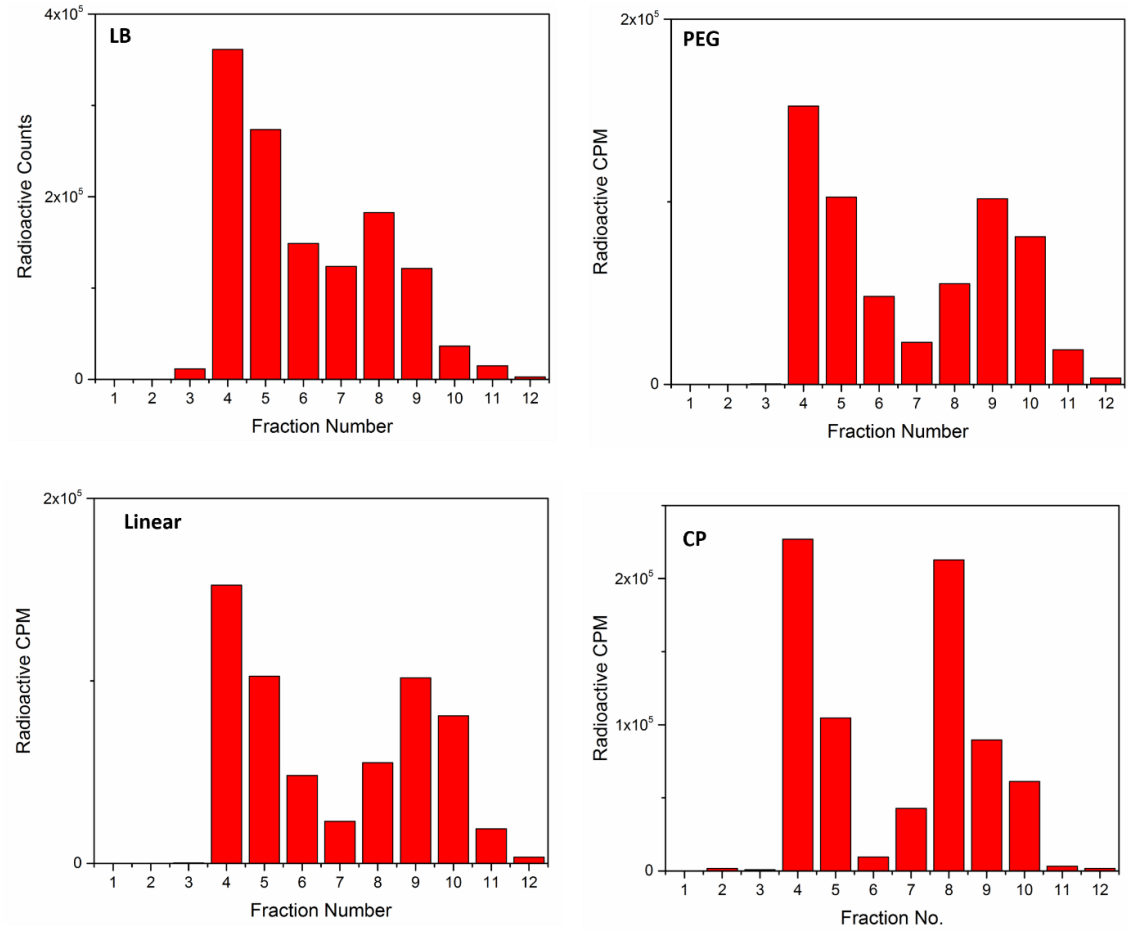

Figure C.15: PD10 purification columns of the crude radiolabelled materials showing separation of the free ethanolamine and the higher fractions numbers 7-10.

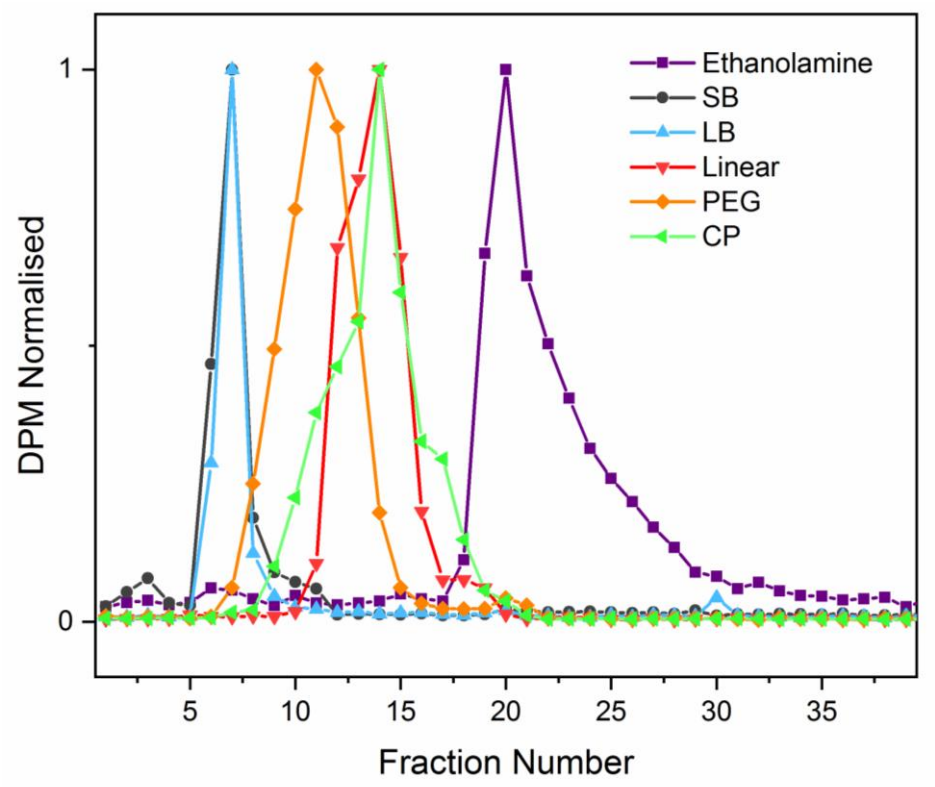

Figure C.16: SEC analysis of the purified radiolabelled compounds, showing all formulations do not contain residual free ethanolamine.

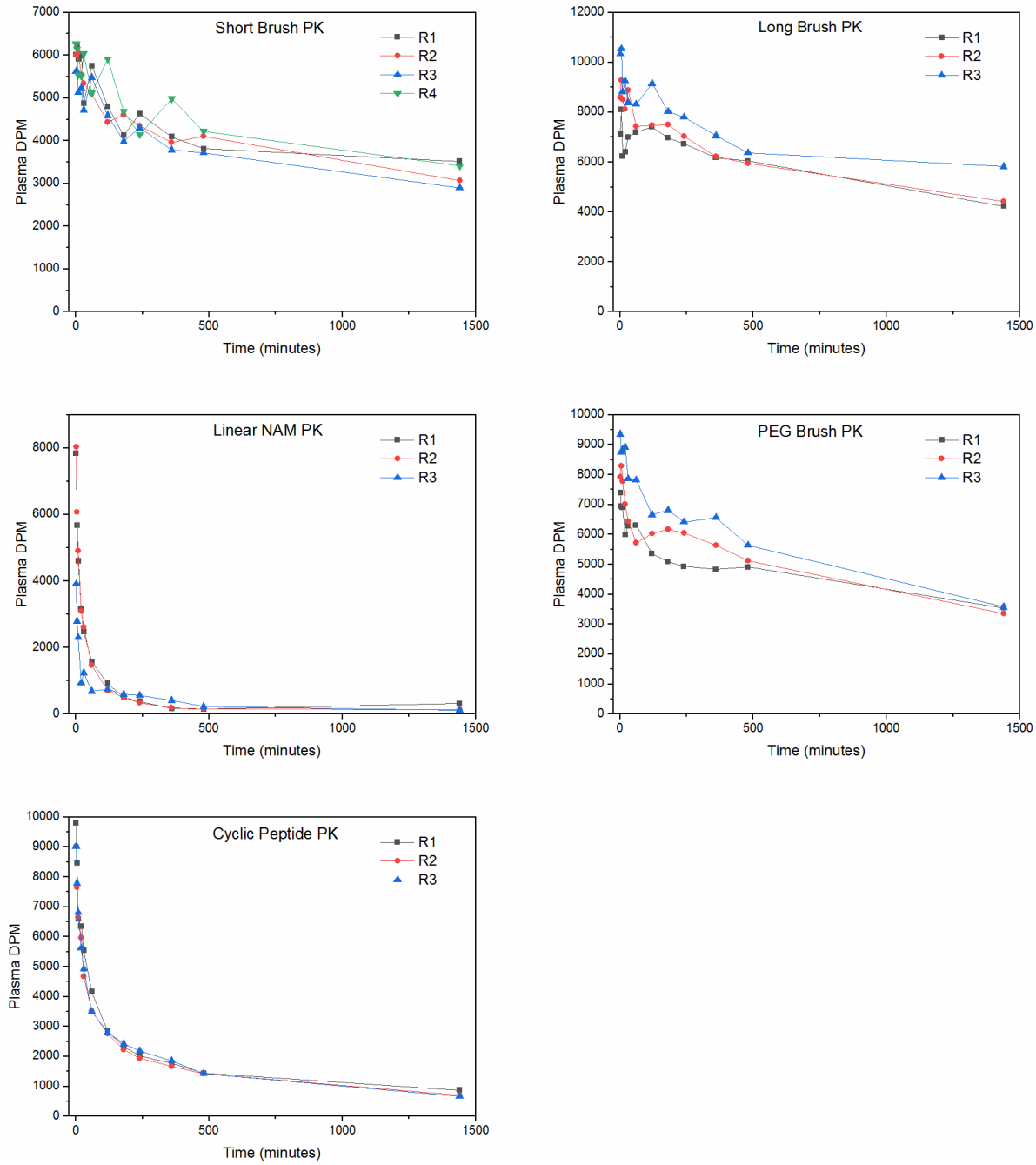

Figure C.17: Uncorrected pharmacokinetic plasma concentrations of radiolabelled materials injected intravenously into rats.

Table C.2: Summary of pharmacokinetic parameters of each repeat.

	Short Brush			
	R1	R2	R3	R4
t1/2 (h)	96.7	41.8	45.8	38.2
AUC (µCi ml^{-1} h)	51.4	50.3	47.1	54.2
V_d (ml)	26.2	23.8	25.9	21.3
Cl (ml h-1)	0.1891	0.3991	0.3974	0.3843
Urine (% dose)	0.51	0.71	0.70	0.56

	Long Brush		
	R1	R2	R3
t1/2 (h)	37.0	32.2	36.9
AUC (µCi ml^{-1} h)	73.3	75.2	86.5
V_d (ml)	15.6	15.5	12.5
Cl (ml h-1)	0.2914	0.3330	0.2357
Urine (% dose)	1.07	0.28	0.62

	Linear NAM		
	R1	R2	R3
t1/2 (h)	1.8	4.4	8.5
AUC (µCi ml^{-1} h)	5.5	4.6	4.2
V_d (ml)	43.3	75.5	149.7
Cl (ml h-1)	16.4839	11.7766	12.2672
Urine (% dose)	48.3	33.9	70.3

	PEG		
	R1	R2	R3
t1/2 (h)	39.4	23.8	22.6
AUC (µCi ml^{-1} h)	59.3	62.2	69.1
V_d (ml)	19.8	16.3	14.4
Cl (ml h-1)	0.3521	0.4764	0.4481
Urine (% dose)	2.66	2.53	2.39

	CP		
	R1	R2	R3
t1/2 (h)	14.8	11.6	17.5
AUC (µCi ml^{-1} h)	21.4	19.8	20.3
V_d (ml)	39.7	34.2	40.6
Cl (ml h-1)	2.1331	2.2562	1.7777
Urine (% dose)	8.34	46.88	30.29